



Contents lists available at ScienceDirect

## Progress in Materials Science

journal homepage: [www.elsevier.com/locate/pmatsci](http://www.elsevier.com/locate/pmatsci)

# Manufacturing of metallic glass components: Processes, structures and properties

Sajad Sohrabi<sup>a</sup>, Jianan Fu<sup>a</sup>, Luyao Li<sup>a</sup>, Yu Zhang<sup>a</sup>, Xin Li<sup>a</sup>, Fei Sun<sup>a</sup>, Jiang Ma<sup>a,\*</sup>, Wei Hua Wang<sup>b,c</sup>

<sup>a</sup> Shenzhen Key Laboratory of High Performance Nontraditional Manufacturing, College of Mechatronics and Control Engineering, Shenzhen University, Shenzhen 518060, China

<sup>b</sup> Songshan Lake Materials Laboratory, Dongguan 523808, China

<sup>c</sup> Institute of Physics, Chinese Academy of Sciences, Beijing 100190, China

## ARTICLE INFO

## Keywords:

Metallic glasses  
Amorphous alloys  
Manufacturing  
Structure characterization  
Mechanical properties  
Functional properties

## ABSTRACT

Metallic glasses (MGs) are out-of-equilibrium metallic systems known for their unique structural and functional properties arising from structural long-range disorder. Despite their attractive properties, practical applications of MGs fabricated by traditional casting strategy face challenges due to size constraints (limited glass-forming ability) and shape complexity issues. Over the decades since the discovery of MGs in the 1960s, significant progress has been made in overcoming these limitations by the manufacture strategy, enabling the fabrication of engineering components with desired sizes, tailored shapes, and intricate geometries. This paper presents a comprehensive assessment of the state-of-art for manufacturing techniques of large MG and MG parts. The advancements in subtractive, formative, and additive manufacturing of MGs, as well as their joining and welding processes, are reviewed. By consolidating the existing knowledge, this review aims to suggest the practical and promising approach to overcome the limited glass-forming ability and size restrictions in cast MGs through the manufacture strategy, offer insights for further advancements in MG manufacturing, address evolving nature of the field and promote a better understanding of the key scientific aspects of structures and properties in processed MG components.

## 1. Introduction

Metallic glasses (MGs) are out-of-equilibrium systems formed when a glass forming metallic liquid is cooled sufficiently fast to suppress crystallization [1]. At the liquid-to-glass transition, the system falls out of metastable equilibrium, solidifying to an amorphous structure with dense packing of atoms but lacking long-range periodicity. The absence of structural defects like grain boundaries, dislocations, and segregation in MGs contributes to significantly enhanced properties and performance compared to traditional crystalline metals [2,3]. These advantages include giant yield stresses and high elastic strain limits [4,5], excellent corrosion resistance [6], superior soft magnetic properties [7–11], good wear resistance [12,13], and impressive electrocatalytic performance [14–17]. These unique characteristics have positioned MGs as a prime choice for a diverse range of innovative high-tech applications across various industries, including aerospace, medical technology, robotics, and e-mobility [18–21].

\* Corresponding author.

E-mail address: [majiang@szu.edu.cn](mailto:majiang@szu.edu.cn) (J. Ma).

<https://doi.org/10.1016/j.pmatsci.2024.101283>

Received 16 June 2022; Received in revised form 13 February 2024; Accepted 10 March 2024

Available online 14 March 2024

0079-6425/© 2024 Elsevier Ltd. All rights reserved.

## Nomenclature

$\Delta T_x$	width of supercooled liquid region
1D	one-dimensional
2D	two-dimensional
3D	three-dimensional
AM	additive manufacturing
ASB	adiabatic shear bands
AWJ	abrasive water jet
BM	base metal
BMG	bulk metallic glass
BMGC	bulk metallic glass composite
BUE	built-up edge
CSAM	cold spray additive manufacturing
DED	directed energy deposition
CT	computed tomography
$D_{\text{formed}}$	minimum forming size
DOC	depth of cut
DSC	differential scanning calorimetry
EBW	electron beam welding
ECMM	electrochemical micromachining
ECR	effective crystallization region
EPMA	electron probe microanalysis
$f$	feeding rate
FEM	finite-element method
FFF	fused filament fabrication
FGM	functionally graded materials
FIB	focused ion beam
FSSW	friction stir spot welding
FSW	friction stir welding
GFA	glass-forming ability
GMG	giant metallic glass
HAZ	heat-affected zone
HE-XRD	high-energy X-ray diffraction
HP	hot-pressing
HRTEM	high-resolution transmission electron microscopy
HSS	high speed steel
LENS	laser engineered net shaping
LFP	laser foil printing
LIFT	laser-induced forward transfer
LPBF	laser powder bed fusion
MD	molecular dynamics
MG	metallic glass
Micro-EDM	micro electrical discharge machining
MP	molten pool
MRR	material removal rate
PCBN	polycrystalline cubic boron nitride
PCD	polycrystalline diamond
PDF	pair distribution function
PEL	potential energy landscape
PM	parent metal
PSZ	primary shear zone
$R_a$	surface roughness
$R_e$	Reynolds number
RFW	rotary friction welding
RSW	resistance spot welding
SAED	Selected area electron diffraction
SEBM	selective electron beam melting
SEM	scanning electron microscopy
SLM	selective laser melting

SLR	supercooled liquid region
SPS	spark plasma sintering
STZ	shear transformation zone
TEM	transmission electron microscopy
$T_{\text{formed}}$	temperature for TPF
$T_g$	glass transition temperature
$T_l$	Liquidus temperature
TPF	thermoplastic forming
TPFA	thermoplastic formability
TRIP	transformation-induced plasticity
TSAM	thermal spray additive manufacturing
TTC	time–temperature–crystallinity
TTT	temperature–time–transformation
$T_x$	crystallization temperature
UAM	ultrasonic additive manufacturing
UVAC	ultrasonic vibration-assisted cutting
UVAM	ultrasonic-vibration-assisted machining
UVIP	ultrasonic vibration-induced plasticity
VFT	Vogel-Fulcher-Tammann
WC	tungsten carbide
XRD	X-ray diffraction
$\Delta H_{\text{rel}}$	relaxation enthalpy
$\Delta H_x$	enthalpy of crystallization
$\mu$ -CT	micro-computed tomography

Like other types of materials, the successful fabrication of MG components plays a crucial role in facilitating their widespread adoption for practical applications [22]. Over time, an increasing number of processing approaches have emerged, enabling the fabrication of MG parts with diverse scales, ranging from micron-scale structures to centimeter-sized 3D structures. These techniques include casting [19,23], thermoplastic forming [23–27], powder consolidation [28], welding and joining [29,30], machining [31–33], and additive manufacturing [34–39]. Each of these strategies offers unique advantages, facilitating the fabrication of MG components in various sizes and shapes, thus significantly expanding their potential applications in diverse industries and fields.

Fig. 1 showcases a selection of 3D printed and net-shape cast bulk MG (BMG) components that have achieved successful commercialization and adoption by different companies worldwide. The figure also serves as a visual representation of the diverse applications of BMG components across different industries, covering both established applications and potential areas for future adoption. Here, we provide a brief overview of a few examples of BMG applications.

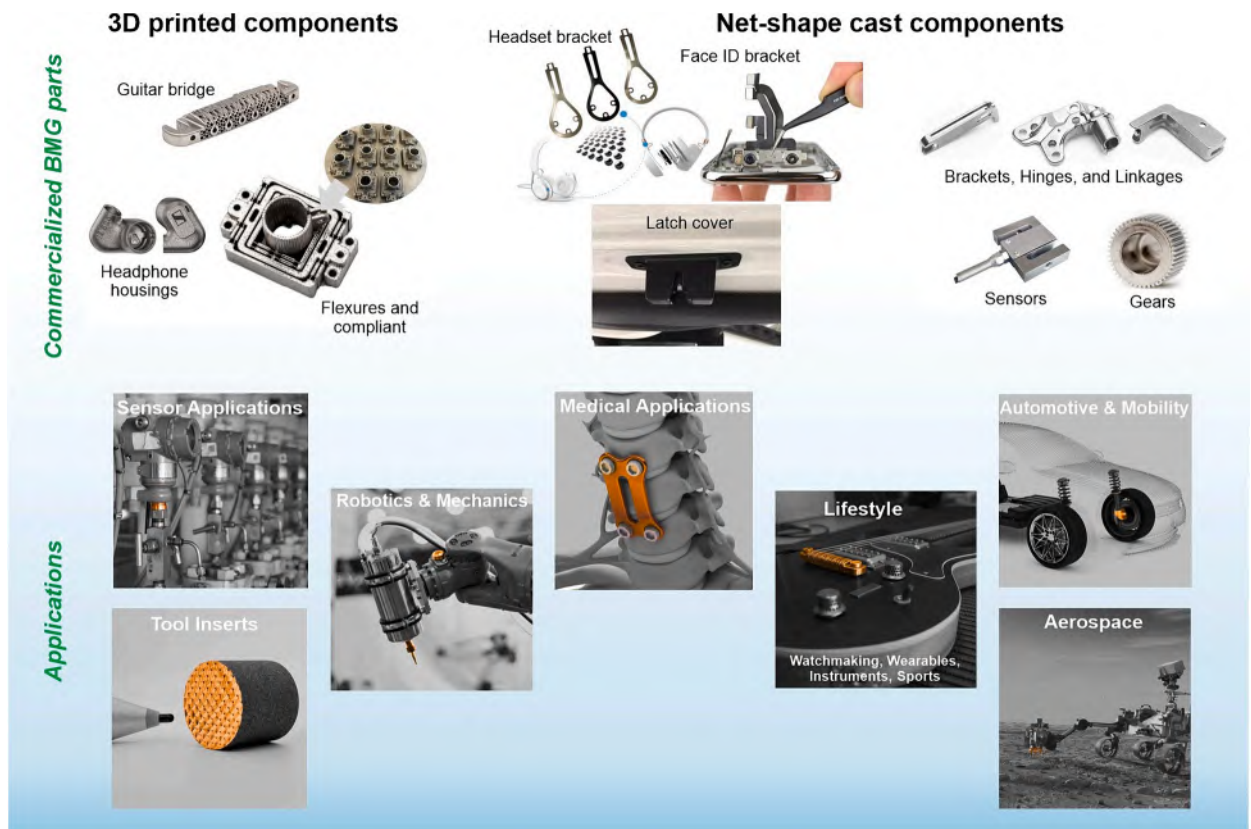
BMGs have proven to be exceptionally advantageous in meeting the stringent demands of medical technology, owing to their exceptional biocompatibility, durability, miniaturization capabilities, and biomechanical properties [43–45]. This distinctive class of materials finds applications as implants (in spine, dental, and traumatology), medical devices and fixtures, as well as surgical and dental instruments [45,46].

Moreover, BMGs have found applications in gears, serving as vital components for torque and power transmission in various machines and devices. MG microgears, in particular, offer several advantages in microassembly, such as zero backlash, excellent repeatability, durability, and compact design [47]. The precision and consistency of MG microgears make them suitable for applications in watches, microactuators, micromanipulators, and microharmonic drives. Compared to microgears made from crystalline metals, MG microgears exhibit superior mechanical strength and wear resistance [48]. Additionally, BMG flexsplines in strain wave gears offer cost benefits for mass production and show potential advantages for sizes below 75 mm in diameter. Their effectiveness in torque transmission has been successfully demonstrated through implementation in a NASA JPL robot [19].

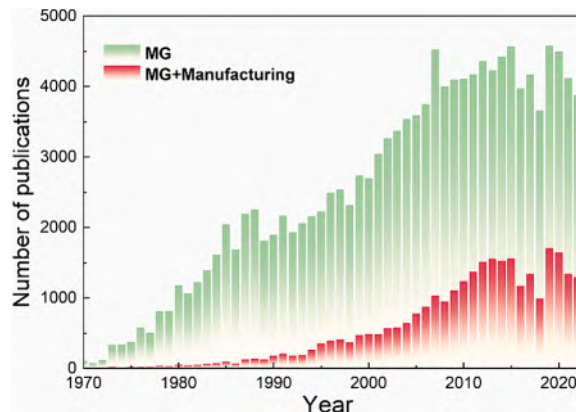
BMGs also find applications in the realm of musical instruments and audio equipment, where components like guitar bridges and pins, as well as headphone housings, represent the remarkable capabilities of these materials [20]. BMG parts efficiently and uniformly conduct sound energy across a broad spectrum of audible frequencies, resulting in amplified acoustic volume and more vibrant harmonics compared to conventional materials [49]. This unique property of BMGs elevates the auditory experience, making them a preferred choice for crafting musical instruments and enhancing audio equipment.

Fig. 2 illustrates a notable upward trend in the number of publications within research fields of MGs and MG manufacturing over the past half-century, indicating a growing interest in both fields. While extensive research has been conducted on the synthesis and characterization of MGs, a comprehensive review encompassing the entire spectrum of manufacturing approaches and associated issues for fabricating MG components, particularly the processes, structures and properties of final products, remains lacking. This review aims to bridge this gap by providing an in-depth analysis of subtractive, formative, and additive manufacturing as well as welding/joining approaches for the manufacture of MG components.

Subtractive manufacturing approaches involve the removal of material from MG to achieve the desired shape and dimensions. Traditional and non-traditional machining techniques have been explored, and their advantages, limitations, and outcomes will be discussed. Formative manufacturing approaches focus on shaping MGs through their viscous behavior at elevated temperatures. These



**Fig. 1.** The commercialized BMG components and applications of BMG components in various industries. The images of 3D printed components and BMG applications are adapted from Heraeus Amloy Technologies, Germany [40]. The images of net-shape cast components at the top center and top right of figure are adapted from Yihao Metal Technology, China [41] and Liquidmetal Technologies, US [42], respectively.



**Fig. 2.** Annual publication trends in the field of MG and MG manufacturing from 1970 to the present. Data sourced from Web of Science, encompassing searches across all databases. The search criteria for MG included topics related to MG or amorphous alloy, while for manufacturing, topics of manufacturing, fabrication, or processing were incorporated in the search parameters.

include techniques such as thermoplastic deformation and powder sintering, which allow for the fabrication of complex geometries and tailored microstructures. Additive manufacturing, also known as 3D printing, has emerged as a promising technique for the production of MG components. The layer-by-layer deposition process offers unprecedented design flexibility and the ability to fabricate intricate structures with enhanced mechanical properties. Various additive manufacturing (AM) methods, such as laser-based AM and ultrasonic AM, will be reviewed in detail. In addition to these approaches, welding and joining techniques play a crucial role in the fabrication of MG components for engineering applications. Different MG welding and joining technologies will be explored along

with structure/property evolution in weldment. It is hoped that this work will be helpful in reconstructing the current state of knowledge about the manufacture of MG components and identifying the research gaps for advancing the field.

## 2. Features and issues of cast MGs and the manufacture strategy of MGs

Since the discovery of Au-Si MGs in 1960 in the form of micron-sized flakes [50], researchers have focused on developing BMGs with centimeter-sized section thicknesses in various alloy systems, including Zr-based, Fe-based, Cu-based, Pd-based, and Ti-based alloys [4,51,52]. The main strategy for fabricating these BMGs has been direct casting, including techniques like suction casting and die-casting [23]. This strategy involves rapidly cooling the alloy to prevent crystallization while simultaneously filling a mold cavity. Fig. 3a illustrates the fabrication of a net-shape BMG rod by suction casting, where the alloy ingot is melted by an arc and then sucked into a water-cooled copper mold, enabling rapid solidification of the material.

BMG compositions for net-shape casting need excellent glass-forming ability (GFA) to prevent crystallization, high hardness or strength for mechanical stability, and superior fluidity for reduced defects and precise complex shapes [53]. However, their higher viscosity and surface tension compared to crystalline alloys present challenges in net-shape casting [54]. Overcoming the trade-off between GFA and fluidity is crucial for producing commercial BMG components with complex shapes during net-shape casting.

Direct casting of BMGs offers advantages such as cost-efficiency, enhanced mechanical properties, and time efficiency. However, the coupling of forming and fast cooling process during casting of BMGs brings limitations, including complexity of mold design, sensitivity to process parameters, and constrains on size and thickness capabilities [23].

On the other hand, cast BMGs are intrinsically brittle due to their disordered atomic arrangement, resulting in limited slip systems and few mechanisms for plastic deformation [55,56], which are crucial for materials to exhibit ductile behavior. As a result, this drawback hinders fabrication of BMG components through conventional metal forming processes at ambient temperatures, such as cold rolling, extrusion bending, and drawing, which require materials to exhibit ductile behavior.

To achieve high GFA or large sizes in cast BMGs, according to Inoue's criteria [57], three essential conditions must be met [4,58]: (1) the system should contain at least three components with specific atomic mismatch and negative enthalpy of mixing, (2) cooling rates must be kept low ( $<10^3$  K/s), and (3) the resultant glass should possess a wide supercooled liquid region (SLR) between the onset temperatures of the glass transition temperature ( $T_g$ ) and crystallization ( $T_x$ ). However, the GFA of cast BMGs is limited due to the critical cooling rate requirements during vitrification (liquid-to-glass transition). The maximum critical size achieved for monolithic BMGs has been only  $\sim 80$  mm in diameter for a Pd-Cu-Ni-P BMG [58,59]. Unfortunately, most of BMG compositions and casting methods developed so far can only satisfy the above conditions when cast parts are restricted to simple shapes with critical diameters smaller than 10 mm, making them impractical for many applications. Consequently, achieving intricate geometries and large-size BMG parts through direct casting remains a challenging endeavor.

A practical and promising approach to overcome the limited GFA and size restrictions in cast BMGs is the manufacture strategy, as schematically shown in Fig. 3b. This method involves using MG feedstocks such as powders, ribbons, foils, or small-sized bulk samples,

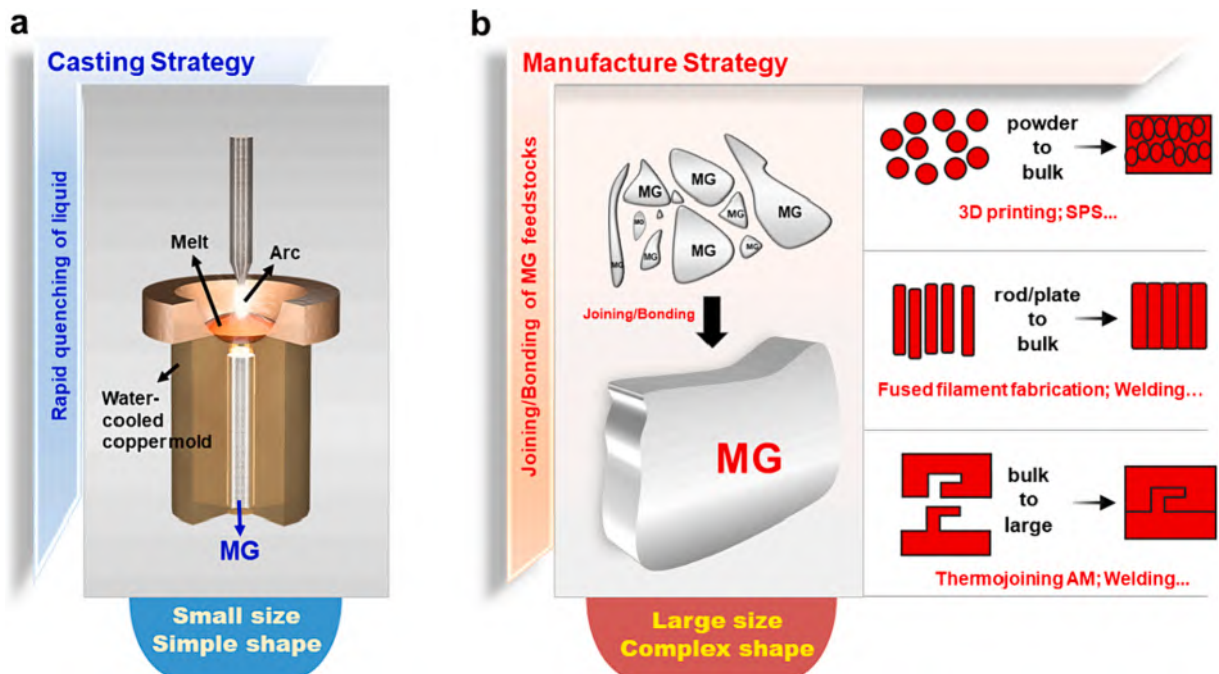


Fig. 3. Casting strategy vs. manufacture strategy to fabricate MG components.

rather than the alloy melt, and employing various processing techniques, like 3D printing and welding, to process them into the desired form. The manufacture strategy encompasses a diverse range of methodologies which will be extensively discussed in this review paper. Metallurgical bonding plays a vital role across many of these techniques, as it allows for joining MG feedstock materials into a unified BMG component. By following this strategy, it becomes possible to obtain larger, and even unlimited-size, BMGs with more complex shapes compared to the traditional casting method. This advancement holds great significance for the entire BMG community.

It is noteworthy that despite six decades of development, the market penetration of MG components remains limited compared to conventional alloys, posing challenges for widespread applications. While MG ribbons find application in power and distribution transformers market, with a global market of \$782 million in 2022 [60], the global BMG market is projected to reach \$246.3 million by 2031 from \$55.9 million in 2021 [61]. This market size is significantly smaller than the extensive steel market of \$928 billion in 2022 [62].

The limitations in the MG market stem from various factors, including size restrictions and the intrinsic brittleness of MGs, as discussed earlier. Additionally, the high raw material cost and elevated production costs associated with traditional metal forming processes further hinder the commercial viability of MGs [22]. Often, the cost of MGs is at least an order of magnitude higher than that of conventional commercial alloys like aluminum alloys and steels. Further, fusion welding of MGs with strong metallurgical bonding poses challenges due to their unique properties and susceptibility to crystallization. While these issues might contribute to the perception that MGs are challenging to work with, they emphasize the need for ongoing research and development to address these issues and discover innovative, cost-effective manufacturing methods as well as exploration of cheaper MG compositions. This imperative is vital for advancing the competitiveness of MGs as advanced engineering materials across various industries.

### 3. MG feedstocks for manufacturing

To implement the manufacture strategy for MGs, the first step involves preparing the feedstock materials. Table 1 provides a comprehensive overview of different types of MG feedstocks and their corresponding characteristics as starting materials for the manufacture of MG components. The table evaluates MG feedstocks based on crucial features, including availability and cost, scalability, compositional diversity, and processability and compatibility for different manufacturing approaches. Utilizing a 0-to-5-star ranking system, each star signifies the degree of relevance for a specific feature. A 0-star rating indicates a lack of relevancy, while a 5-star rating highlights high relevancy. For instance, a 5-star rating implies good availability and reasonable cost, high scalability, a wide range of applicable compositions, and reasonable ease of processing. This scale provides a clear understanding of the strengths and limitations of different forms of MG feedstocks for manufacturing applications.

MG feedstocks are commonly fabricated in various forms, such as one-dimensional (1D) powder, two-dimensional (2D) ribbons/foil, and three-dimensional (3D) BMG rod and sheet, through rapid quenching from the molten alloy at extremely high cooling rates, surpassing  $\sim 10^3$  K/s [63,64]. While other forms of MG, such as  $\mu\text{m}$ -sized wires/fibers [65–67] and BMG pellets [68], do exist, they have seen limited utilization as feedstock materials for manufacturing purposes.

MG powders in micron scales ( $\sim 20\text{--}80\ \mu\text{m}$ ) with spherical and smooth shapes are commonly fabricated by gas atomization. In this process, molten metal is atomized into small droplets by directing it into a cold stream of an inert gas, enabling rapid cooling rates [69]. Alternatively, MG powders with irregular shapes can be obtained through solid-state mechanical alloying, which involves the repeated welding and fracturing of powder particles in a high-energy ball mill [70].

**Table 1**

Summary of MG forms and their features as feedstock for the manufacture of MG components.

Feedstock form	1D feedstock	2D feedstock	3D feedstock
Feedstock features	MG powder	MG ribbon / foil	MG sheet / MG rod
Availability and cost	★★★★☆	★★★★★	★★★☆☆
Manufacturing scalability	★★★★★	★★★☆☆	★★★☆☆
Compositional diversity	★★★☆☆	★★★☆☆	★★★★★
Processability and compatibility			
Subtractive manufacturing	☆☆☆☆☆	★★★★☆	★★★★☆
Formative manufacturing	★★★★☆	★★★★☆	★★★★★
Joining and welding	☆☆☆☆☆	★★★★☆	★★★★★
Additive manufacturing	★★★★★	★★★★★	★★★★☆

MG ribbons/foils with thicknesses ranging between  $\sim 20$ – $100 \mu\text{m}$  are manufactured through the controlled flowing of a molten metal stream onto a rotating chill block surface through free-jet melt spinning [71] and planar flow casting [72,73] techniques. The outcome is a continuous feedstock of MG ribbons/foils, available in a wide range of widths. These ribbons can be as narrow as about 1 mm or extend to several centimeters for MG foils, providing flexibility in selecting the most suitable form for a given manufacturing approach. Additionally, MG ribbons can be transformed into powders via high-energy ball milling technique, where the ribbons are pulverized to produce the desired powdery form [74].

BMG rod and sheet feedstocks are primarily produced through direct traditional casting techniques, including die-casting, copper mold casting, suction casting, and tilt casting [75]. The cast BMG rods typically range in size from  $\sim 1$ – $10 \text{ mm}$  in diameter, while the cast BMG sheets vary in thickness from about 1–5 mm. The specific dimensions depend on the GFA of the feedstock's chemical composition.

MG powder and ribbon feedstocks, boasting industrial-grade purity, enjoy widespread availability and cost-effectiveness, making them attractive options for various applications. In contrast, BMG rods and sheets can face limitations in availability and incur higher costs due to the complexity of their production processes. However, when it comes to high-purity powder feedstocks with notably reduced oxygen contamination, cost-effectiveness may be compromised.

MG powder demonstrates the highest scalability as a feedstock for manufacturing processes, particularly in additive manufacturing techniques. MG feedstocks in the form of ribbon and foil can be moderately scalable but may face some limitations in achieving larger sizes with intricate geometries. On the other hand, BMG rod and sheet feedstocks are the least scalable option, making them more suitable for manufacturing techniques where scalability is not a primary concern.

While cooling rates as high as  $10^6 \text{ K/s}$  are utilized during the fabrication of MG powder and ribbon feedstocks, their compositional diversity is comparatively lower than that of BMG feedstocks, primarily due to technical challenges. The production of fully amorphous MG powder feedstocks from various glass-forming alloys may be challenging due to oxygen entrapment and humidity in the powder feedstock, along with the surface-to-volume ratio influencing oxygen uptake during atomization [76]. Nevertheless, Fe-based and Zr-based MG powders remain among the most widely used alloy systems as feedstock materials.

Further, the preparation of high-quality wide ribbons in various glass-forming systems with uniform thickness and smooth surfaces can be challenging to achieve during planar flow casting, mainly due to the complexity of maintaining melt puddle stability [77,78]. Presently, commercial Fe-based and Co-based MG ribbons and foils are readily available as feedstocks due to their extensive applications as soft magnetic materials [8,79]. Similarly, Ni-based MG foils have found considerable use as brazing feedstock in various industries, such as aerospace metal joining, heat exchangers, metallic catalytic substrates, and preforms [80].

While MG ribbons, sheets, and rods are compatible with subtractive, formative, and additive manufacturing routes, as well as welding and joining techniques, MG powders are primarily suitable for formative and additive manufacturing approaches. However, it is important to note that the GFA of feedstock powders is generally lower than that of cast materials [76]. This reduced GFA increases the risk of nanocrystallization during additive manufacturing, mainly attributed to the complex thermal history arising from laser-material interactions and consecutive remelting steps [81,82]. Furthermore, it has been observed that the use of glass formers characterized by a lower crystal growth rate and sluggish crystallization kinetics holds significant advantages in reducing crystallization during laser-based additive manufacturing (AM) of Zr-based MG powders [83].

Additionally, gas-atomized MG powders often exhibit a broad particle size distribution, which may hinder their efficiency as feedstock materials. To address this challenge, mechanical milling can be employed to transform larger gas-atomized particles into suitable feedstock powder. However, this milling process demands substantial energy input and time. Further, it is worth noting that irregular powders resulting from milling experience a higher increase in temperature compared to the spherical ones directly produced from gas-atomization. This is due to their higher surface-to-volume ratio, which enhances heat exchange [84]. Consequently, the milled powder may become overheated, leading to a higher likelihood of oxygen pick-up from the atmosphere during manufacturing processes that involve elevated temperatures, such as laser-based AM.

## 4. Subtractive manufacturing of MG components

The subtractive manufacturing process for MGs involves starting with MG feedstock and selectively removing unwanted portions to obtain the desired shape, dimensions, and surface finish. Subtractive manufacturing allows for precise shaping, finishing, and customization of MG components. In this section, an overview of subtractive manufacturing approaches for MG components is provided, covering traditional machining methods, such as turning, milling, and drilling, and discussing their effects on surface quality, chip formation, tool wear, and MG structural characterization. Additionally, non-traditional machining techniques, including micro electrical discharge machining (micro-EDM), electrochemical micromachining, laser micromachining, and ultrasonic-vibration-assisted machining are explored. Lastly, shear punching techniques, both traditional and ultrasonic-vibration-assisted, and their impact on structural characterization and surface morphology are examined. This comprehensive analysis sheds light on the various methods employed in subtractive manufacturing of MG components and their implications for final product.

### 4.1. Traditional machining

#### 4.1.1. Machining methods

The manufacturing of BMG parts, which require high precision in terms of dimensional accuracy and surface roughness, often relies on machining as a crucial process. Traditional machining can be broadly categorized into three primary types: turning, milling, and drilling. Fig. 4 shows experimental setups of all three kinds as well as typical BMG workpieces processed. Turning involves rotating the

workpiece while a cutting tool removes material to create cylindrical shapes or features. Fig. 4a shows an ultra-precision lathe machine used for end face dry turning of  $Zr_{55}Cu_{30}Al_{10}Ni_5$  BMG [85]. Recently, turning technique was employed to fabricate surface screw thread shaped structure on a Zr-based BMG rod (Fig. 4b), yielding macroscopic tensile ductility and serrated flow behavior [86].

Milling is a widely adopted manufacturing process, commonly employed by producers to fabricate intricate parts and molds with exceptional dimensional accuracy and surface quality. During the milling process (Fig. 4c), material removal from the workpiece is achieved by a rotating cutting tool equipped with multiple teeth. The tool engages with the MG workpiece, resulting in the formation of chips as material is removed. The cutting action encompasses both shearing and plowing of the material, with the teeth of the milling cutter continuously interacting with the workpiece surface, producing a sequence of interrupted cuts. This milling process enables the creation of diverse shapes, contours, and features on the MG component. The apparatus in Fig. 4c was used for micro-milling of  $Zr_{41.2}Ti_{13.8}Cu_{12.5}Ni_{10}Be_{22.5}$  BMG using a coated two-tooth cemented carbide tool [87]. Optimized micro-milling produced good surface quality and minimal burr width in the machined Zr-based BMGs (Fig. 4d) [87,88].

Hole making through drilling is a commonly employed machining technique. The drilling process (Fig. 4e) involves the creation of holes or cavities in the material using a rotating cutting tool (drill bit). The cutting edge of the drilling tool is primarily responsible for generating the majority of the thrust force during the drilling process. Drilling involves more intricate tool geometry and material deformation compared to the turning process. During chip formation in drilling, the cutting speed and rake angles vary along the cutting edges of a twist drill. In the center web of the drill, the work material is subjected to high negative rake angle, resulting in plowing action. Apart from the tool's geometry, factors such as the workpiece material, process parameters (feed rate, spindle speed), and machine tool vibrations can also influence the quality of the resulting hole [91]. Fig. 4(f) demonstrates that when utilizing a micrograin tungsten carbide (WC) tool to drill a  $Zr_{52.5}Ti_5Cu_{17.9}Ni_{14.6}Al_{10}$  BMG hole at feed rate of  $2 \mu\text{m}/\text{rev}$ , the formation of burrs is virtually negligible [90].

#### 4.1.2. Surface quality of machined workpieces

The surface quality of a BMG workpiece plays a critical role in determining its assembly accuracy and subsequent performance. During the machining of BMGs, process parameters such as the cutting/spindle speed, feed rate, depth of cut, tool geometry, coolant/lubrication, and tool material should be carefully adjusted and optimized to ensure efficient material removal and produce high-quality BMG components with the desired surface finish and dimensional accuracy while keeping their amorphous nature.

Some studies have reported minimal effects of cutting speed and depth on surface roughness ( $R_a$ ) values in machined Zr-based and Pd-based BMGs [92,93]. In Fig. 5a,  $Zr_{57}Cu_{20}Al_{10}Ni_8Ti_5$  (Zr57) BMG,  $Zr_{48}Cu_{47.5}Co_{0.5}Al_4$  (Zr48) BMG composite (BMGC), pure zirconium (Zr702), and titanium alloy (TC4) exhibited stable  $R_a$  values below  $0.75 \mu\text{m}$ , while 45 steel had higher roughness that decreased with increasing speed. Similarly, Fig. 5b demonstrated similar trends with cutting depth, with Zr57 BMG exhibiting the lowest roughness. In contrast, Xiong et al. [94] discovered that as the spindle speed increased in ultra-precision machining of a Pd-based BMG,  $R_a$  initially decreased and then increased, with the minimum value observed at 2000 rpm. This behavior was attributed to the

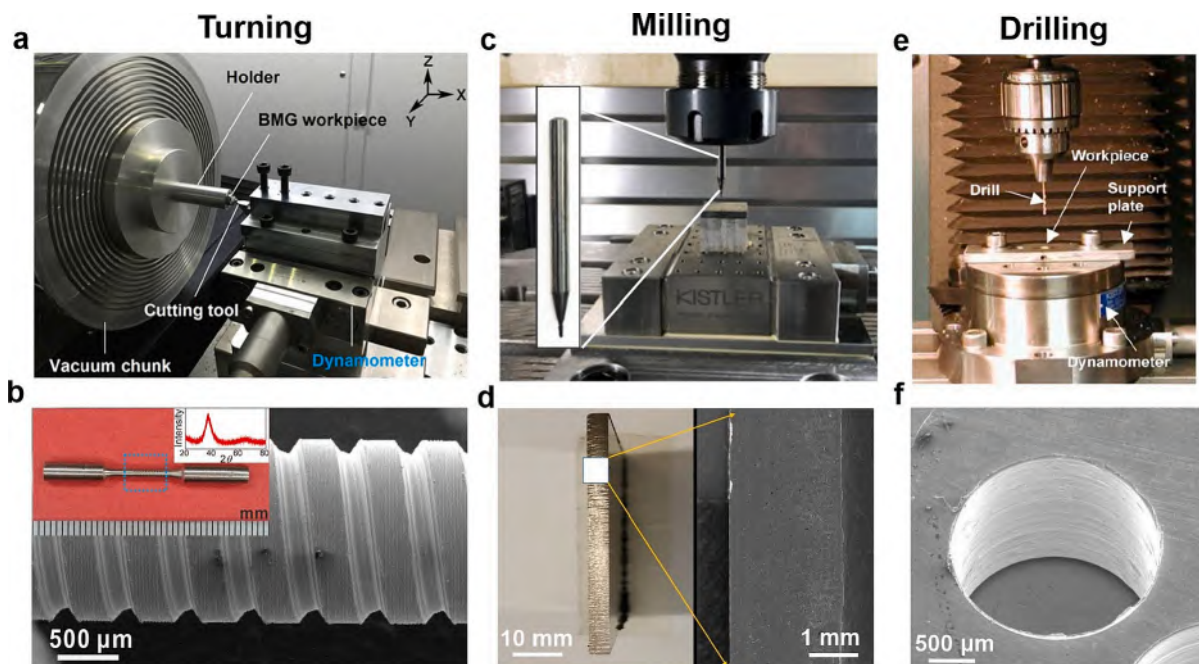
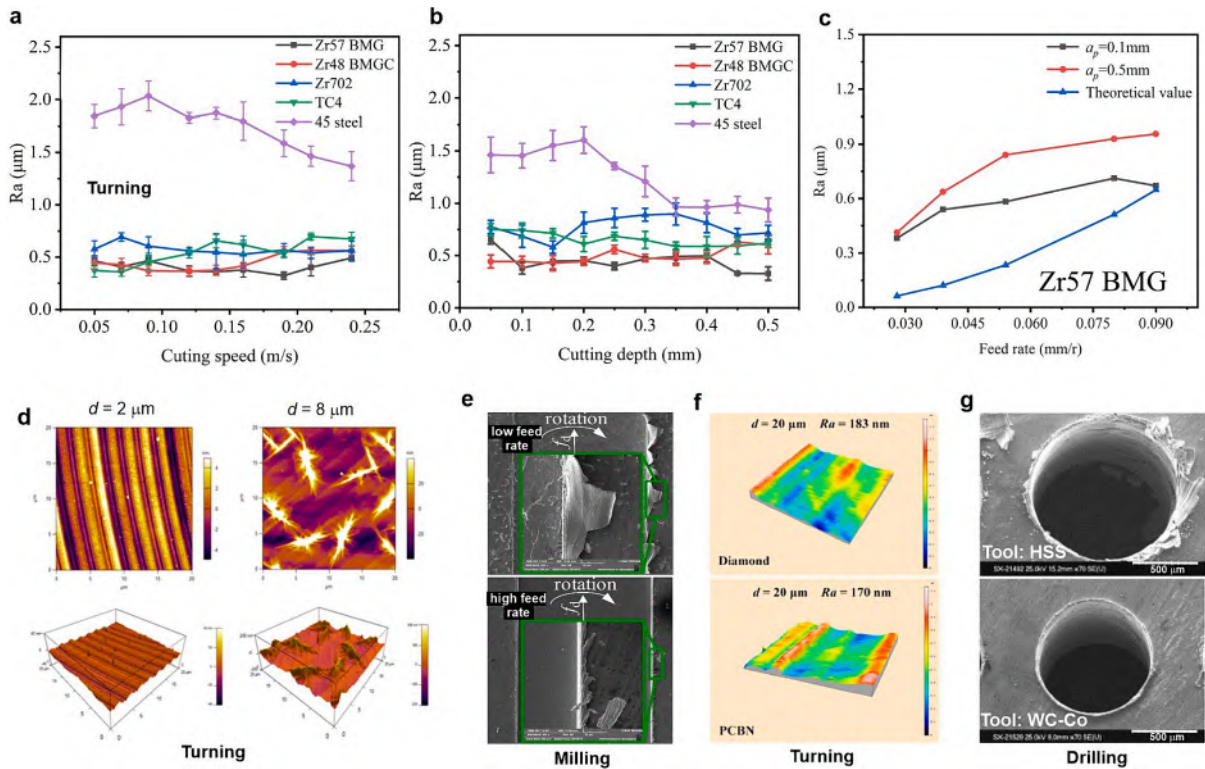


Fig. 4. (a) Setup of turning machining (Adapted from [85]). (b) A machined ( $Zr_{64.13}Cu_{15.75}Ni_{10.12}Al_{10}$ ) dog-bone shaped BMG sample (Adapted from [86]); (c) A micromachining setup for milling process [87]. (d) the visual and magnified images of the milled Zr-based BMG surface (Adapted from [88]). (e) Setup of a drilling test (Adapted from [89]). (f) Exit burrs in a Zr-based BMG drilled by micro-grain WC tool [90].



**Fig. 5.** Variation of surface roughness with (a) cutting speed, (b) cutting depth, and (c) feed rate (Adapted from [93]). (d) AFM images of machined surface cut at depths of 2  $\mu\text{m}$  and 8  $\mu\text{m}$  (Adapted from [94]). (e) The burr morphologies under different feeding rates (Adapted from [87]). (f) Morphology of machined surfaces cut by different tools (Adapted from [85]). (g) Morphology of entry burr drilled by HSS and WC-Co tools (Adapted from [89]).

superplastic characteristics of the BMG resulting from temperature elevation and machining within the SLR. Furthermore, atomic force microscopy (AFM) studies indicated that at depths of cut (DOCs) slower than 6  $\mu\text{m}$ , noticeable tool marks were observed on the machined surface, as shown in Fig. 5d for a DOC of 2  $\mu\text{m}$  [94]. However, at a cutting depth of 8  $\mu\text{m}$ , irregular micro/nanostructures appeared due to oxidation, contributing to an increased surface roughness that negatively impacted overall quality. In a separate study focusing on ultra-precision cutting of  $\text{Zr}_{55}\text{Cu}_{30}\text{Al}_{10}\text{Ni}_5$  BMG, a different trend was observed. As the spindle rate increased, the surface roughness initially increased and then decreased. Specifically, a spindle rate of 3500 rpm was associated with the poorest surface quality. However, increasing the DOC gradually led to an increase in surface roughness ( $R_a$ ) [85].

The spindle speed in high-speed milling processes can significantly affect the surface roughness of BMG surfaces [95]. In the case of Zr-based BMG, an increase in spindle speed led to a gradual reduction in the arithmetic mean height of the milling groove bottom surface, resulting in surface roughness values ranging from 0.8 to 1.6  $\mu\text{m}$  at spindle speeds above 40000 rpm. However, during low-speed milling of  $\text{Zr}_{41.2}\text{Ti}_{13.8}\text{Cu}_{12.5}\text{Ni}_{10}\text{Be}_{22.5}$  BMG at spindle speeds below 16000 rpm, the impact of rotation speed on surface roughness was found to be negligible, while an increase in axial depth of cut (DOC) resulted in gradual surface roughness increase [96]. Conversely, during micro-milling of the same BMG composition, an increasing trend in surface roughness was observed with increasing rotation speed from 10,000 to 18000 rpm, particularly at higher feeding rates [87]. This increase was attributed to the softening of Zr-based BMG caused by elevated cutting temperatures, resulting in decreased viscosity and the formation of wave patterns that increased surface roughness. Similar softening phenomena were also observed by Fujita et al [92] in Zr-based and Pd-based BMGs. Additionally, Wang et al. [87] noted that the axial DOCs within the range of 10 to 45  $\mu\text{m}$  had little influence on the surface roughness of micro-milled Zr BMG, but a significant increase in roughness occurred at a DOC of 60  $\mu\text{m}$ , potentially due to higher forces resulting from the increased axial DOC.

The feeding rate ( $f$ ) is another significant cutting parameter that affects the surface quality of machined BMGs [85,87,96]. The surface roughness ( $R_a$ ) can be theoretically calculated using equations such as  $R_a = f^2 / 8R$  [85] or  $R_a = 0.032 f^2 / R$  [93], where  $R$  represents the tool nose radius. Although the precise calculation of surface roughness is hindered by the deformation and recovery of machined workpieces, an increase in  $f$  is expected to result in a notable rise in  $R_a$  [95,96]. However, an inverse relation between  $f$  and  $R_a$  was reported during micro-milling of  $\text{Zr}_{41.2}\text{Ti}_{13.8}\text{Cu}_{12.5}\text{Ni}_{10}\text{Be}_{22.5}$  [96] and  $\text{Zr}_{55}\text{Cu}_{30}\text{Al}_{10}\text{Ni}_5$  [85] BMGs when the  $f$  dropped below a critical value.

Fig. 5c demonstrates the consistent increasing trend of  $R_a$  with higher  $f$  during low-speed machining of Zr57 BMG, despite the difference between experimental and theoretical values. These variations may arise from additional factors that influence surface

quality, including material characteristics, cutting tools, and lathe conditions. Consequently, Zr57 BMG can achieve low surface roughness, with the influence of cutting depth on surface roughness becoming more pronounced at higher feed rates [93]. Furthermore, a higher feed rate often increases the risk of sample fracturing, resulting in the presence of small burrs on the machined parts (Fig. 5e). Wang et al. [87] have indicated that when the ratio of feed rate ( $f$ ) to the cutting edge diameter ( $r_e$ ) exceeds a critical value of 0.6, the surface roughness demonstrates a positive correlation with this ratio. Specifically, reducing the  $f/r_e$  ratio typically leads to a decrease in surface roughness. Additionally, high feed rates during micro-milling of Zr-based BMG workpieces have been observed to lead to the formation of surface cracks and voids [88,97]. The elevated temperature associated with higher feed rates can induce material melting, contributing to void formation and fluctuating the milling forces. These voids arise from the dynamic solidification process and can potentially impact the mechanical properties of the machined components, leading to degradation.

The achievement of low surface roughness can be attributed to several factors. Firstly, it is influenced by the optimized movement of feeding and rotation, as well as the initial surface profiles. Secondly, the superplasticity exhibited by certain MGs, such as Zr-based BMG, and the collapse effect caused by gravity on the formed peaks play a role in achieving smooth surfaces. Lastly, the characteristics of deposition and scratching between the workpiece materials and milling tools also contribute to the reduction of surface roughness [87].

The choice of tool's material and geometry also plays a significant role in determining the surface roughness of machined BMGs. For instance, at a fixed feed rate of  $5 \mu\text{m/r}$  and DOC of  $10 \mu\text{m}$  (Fig. 5f), the surface roughness is  $183 \text{ nm}$  for a diamond tool and  $170 \text{ nm}$  for a polycrystalline cubic boron nitride (PCBN) tool, indicating the superior performance of the PCBN tool [85]. Further, drilling holes using different high speed steel (HSS) and WC in cobalt matrix (WC-Co) tools result in varying burr sizes (Fig. 5g) [89]. The HSS tool produces larger irregular roller-shaped burrs, attributed to rubbing and more pronounced margin wear, while the WC-Co tool produces relatively smaller burrs due to its higher thermal conductivity and hardness compared to HSS. The shape and size of the entry and exit burrs depend on factors such as tool wear, drill run-out, and the unique ductility of the machined BMGs.

According to Bakkal et al. [90], the use of micro-grain WC tools offers better surface roughness compared to solid WC tools under

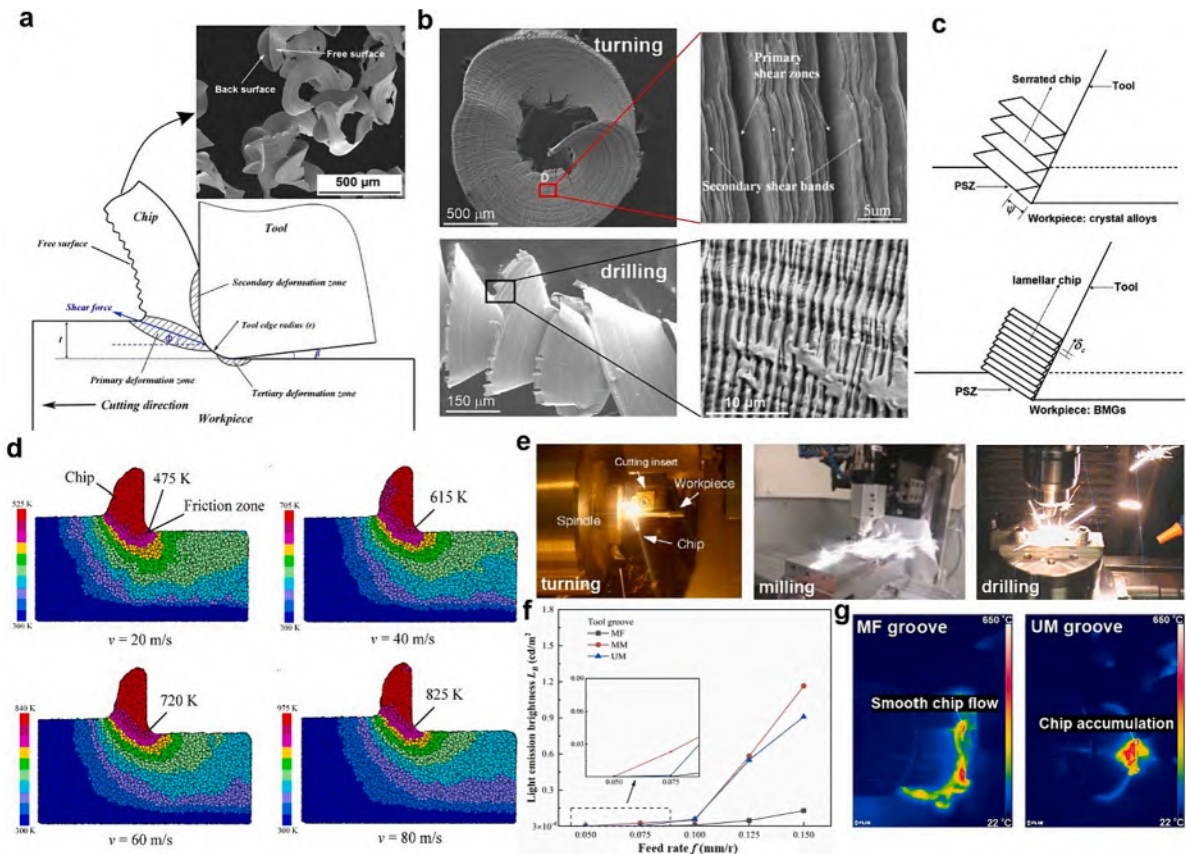


**Fig. 6.** (a) Schematic illustration of cutting process and SEM image of chips cut as a spindle speed of 3000 rpm and feeding rate of  $5 \mu\text{m/r}$  (Adapted from [85]). (b) Chip morphology during turning and drilling of Zr-based BMGs (Adapted from [89,99]). (c) 2D schematics of lamellar chip formation in BMGs (upper) and serrated chip formation in conventional crystalline alloys (lower). Adapted from [99]. (d) Simulated temperature profile during nanometric cutting of MG at different cutting speeds (Adapted from [94]) (e) Light emission during high-speed turning [100], milling [97], and drilling [89] of BMGs; (f) Effect of tool groove on light emission brightness at cutting speed of  $50 \text{ m/min}$ . (g) Infrared thermal images of Zr-based BMG cutting in case of MF and UM tool grooves (Adapted from [101]).

similar processing conditions. The micro-grain WC tool generates smaller thrust forces during BMG drilling compared to the solid WC tool. Additionally, Liu et al. [95] found that the coating of the milling cutter has minimal influence on the surface roughness of the bottom surface of a Zr-based BMG milling groove. However, the number of cutting edges on the milling cutter significantly affects the surface roughness. To achieve lower surface roughness in the milling groove, it is recommended to use a four-edge milling cutter with a nanocomposite coating.

The choice of cooling medium has also an impact on the surface roughness of machined BMGs. Sakata et al. [98] investigated the influence of cutting atmosphere using air-blow and kerosene as coolants. Air-blow resulted in a surface roughness of 51 nm with irregular cutter marks. In contrast, the use of kerosene reduced roughness to 44 nm, prevented micro burr formation, and improved groove depth uniformity in the diamond turning of Zr-based BMG.

Based on the literature review, achieving controlled surface roughness in the machining process of BMG is a complex task due to the influence of various factors such as cutting speed, DOC, feed rate, tool material, and physical/mechanical properties of the BMG workpiece. The determination of optimal parameters that yield desirable surface roughness is challenging, as it requires identifying the combined optimal factors.

#### 4.1.3. Chip formation and cutting mechanism

In contrast to crystalline metals and alloys characterized by long-range order atomic structures, BMGs possess disordered atomic structures. Consequently, the material deformation during machining of BMGs is expected to exhibit distinct behavior compared to that of conventional metals and alloys [92].

The formation of chips during continuous machining is crucial for determining surface quality, including surface roughness. The cutting process generally involves three distinct deformation zones (Fig. 6a) [85]. The primary deformation zone, located in the core cutting region, undergoes severe plastic deformation due to the shear force from the tool edge. This results in the extrusion of materials along the shear force direction. When the plastic deformation reaches its limit, the materials separate from the workpiece, forming the cutting chips, while the remaining materials create a fresh surface. As a result, the upper side of the chips exhibits an uneven and rough free surface due to the movement of extruded materials onto the original workpiece surface. The chips, subjected to high contact stress and friction from the tool rake face, flow out with a curled shape, leading to a smoother back surface compared to the free surface. This active region between the chip and the tool rake face is referred to as the secondary deformation zone. At the same time, the fresh surface is pressed and rubbed by the tool flank face, shaping the machined surface, which represents the tertiary deformation zone. The plastic deformation decreases progressively within these three zones.

Despite the brittleness of BMG at room temperature, the chips formed during machining exhibit a continuous spiral or ribbon-like morphologies (Fig. 6b and c) [85,89,99,102]. This suggests that the material removal process follows a ductile mode, similar to what is frequently observed in cutting of many crystalline metals [103–105]. Bakkal et al. [106] suggested that the chip formation mechanism in high-strain-rate cutting of Zr-based BMG is akin to the formation of serrated chips in crystalline metals. Due to the low thermal conductivity of the BMG, the cutting heat cannot dissipate quickly, resulting in thermal instability of the work material and the formation of adiabatic shear bands (ASB). The ASB mechanism stands as the prevailing formation mechanism of chips during machining of BMGs [107,108], and has been applicable to high-strain rate deformation in other crystalline alloys such as in stainless steels and titanium, aluminum, and copper alloys [109].

As shown in Fig. 6b, the BMG chip surfaces appear smooth, but they contain periodic shear bands with consistent micrometer-scale spacing. A distinct lamellar structure emerges within the BMG chip, indicating its discontinuity. Surprisingly, no characteristic fracture patterns are observed, suggesting fracture mechanisms such as meniscus instability do not occur [99]. The chip lamella presented during machining of Zr-based and Fe-based is likely formed through periodic shear banding within the primary shear zone (PSZ) [89,99,106,108].

Lamellar chip formation in BMG machining shares similarities with serrated chip formation in crystalline alloys (Fig. 6c). Both involve inhomogeneous material flow and shear band formation in the PSZs due to tool-workpiece interaction. However, distinct features of lamellar chips include [99]: (i) smaller scales and spacing ( $\delta_c$ ) of shear bands and PSZs; (ii) relatively smoother free surface or weaker chip serration, indicating smaller shear displacement ( $\Psi$ ) triggers shear banding in BMGs; (iii) presence of secondary shear bands between PSZs on the free surface (see Fig. 6b), suggesting shear localization even at low cutting speeds in BMG machining.

Although shear band formation may contribute to the formation of both lamellar chips and serrated chips, the underlying mechanisms can vary. Jiang and Dai [99] performed a theoretical analysis using a nonlinear dynamic model and proposed that in BMG cutting, the formation of lamellar chips is driven by the collapse of static equilibrium in the free volume flow. On the other hand, in conventional metal cutting, the formation of serrated chips is predominantly influenced by the collapse of static equilibrium in the heat flow. Later, Zeng et al. [110] developed a theoretical model explaining the behavior of shear bands during machining. The model establishes a correlation between atomic-scale dilatancy and shear band evolution and reproduces the ductile-to-brittle transition of shear bands, which influences chip formation. At small cutting depths, ductile shear bands result in serrated chips, while at larger depths, brittle shear bands create discontinuous chips. The model identifies a critical local volume dilatancy of 16.7 % for the transition. This finding demonstrates the role of intrinsic dilatancy in shear band behavior and provide insights into chip formation.

The formation of chips is influenced by several parameters, including cutting speed, feeding rate, and cutting depth [85,94,98,102,111]. Bakkal et al. [100] reported that at low cutting speeds of 0.38 and 0.76 m/s, larger shear lamella chips were typically observed. As the cutting speed increased to 1.52 m/s, various chip types, including irregular lamellar segments, were observed. During spiral milling, chip deposition along the slot edges got more pronounced with higher feed rates [90]. Additionally, lower cutting feed rates tend to produce C-shaped and spiral chips, with the prevalence of C-shaped chips decreasing as the feed rate increases, eventually disappearing at a feed rate of 0.09 mm/r [93]. The cutting depth also influences chip morphology, with cutting

depths ranging from 0.05 to 0.1 mm resulting exclusively in C-shaped chips. Increasing the cutting depth reduces the occurrence of C-shaped chip formation. More recently, Deng et al. [112] found that as the cutting length increases during orthogonal cutting of Vitreloy 1 (Vit.1) BMG, the chips undergo a transition from a laminated structure to a viscous flow state. This transition is accompanied by a change from a relatively smooth surface to a vein-like pattern in the PSZ.

Numerous simulation studies have been also conducted to investigate various aspects of material removal in nanometric cutting of BMGs, such as cutting force, cutting temperature, and chip morphology [113]. For example, Avila et al. [114] conducted a study to investigate the effect of rake angle, from positive 45° to negative 45°, on shear band formation in the MG chip. The findings revealed that the shear band in the chip underwent a transition from sparse to thicker, eventually merging together. A more negative rake angle led to an increase in tool thrust and enhanced pressure at the cutting point, resulting in chip compression and shrinkage. Moreover, Zhu et al. [115] showed that in nanometric cutting of Cu<sub>50</sub>Zr<sub>50</sub> MG, material is mainly extruded rather than sheared at the macroscale, driven by the formation of shear transformation zones (STZs) indicating inhomogeneous plastic deformation. Workpiece pile-up is cutting depth-dependent, reduced by larger tool edge radius, and minimally influenced by cutting speed. In a simulation study of nanometric cutting on Pd<sub>40</sub>Ni<sub>10</sub>Cu<sub>30</sub>P<sub>20</sub> MG alloy, it was observed that increasing the cutting speed led to higher temperatures at the friction zone (Fig. 6d) [94]. At cutting speeds of 20 and 40 m/s, the temperature rise remained below  $T_g$  of 670 K. However, at a cutting speed of 60 m/s, the temperature in the cutting zone reached 720 K, exceeding the  $T_g$ . Further increasing the cutting speed to 80 m/s resulted in temperatures surpassing the  $T_x$  of 720 K, leading to the initiation of crystallization. Hence, controlling the cutting speed becomes necessary to mitigate temperature rise in the friction zone and prevent detrimental effects of crystallization on chip formation.

Light emission is a distinct phenomenon observed during high-speed machining of Zr-based BMGs (see Fig. 6e), negatively impacting the machining process BMG workpieces. This unique feature, which sets BMGs apart from crystalline alloys during mechanical tests, has also been observed during fracture of BMGs under mechanical loading [116–118]. Bakkal et al. [119] recorded flash temperatures ranging from 2400 K to 2700 K during high-speed cutting of a Zr-based BMG, associated intense emission of visible light and oxidation of processed chip. This was mainly attributed to significantly low thermal conductivity of the Zr BMG (~4 W/m K) which causes retaining heat within the chip, leading to the initiation of exothermic oxidation and subsequent light emission on the surface of the chip [100,106]. Due to the increase in temperature and partial melting of the work material, the original lamellar structure of shear band undergoes significant disruption and deformation surrounded by regions of molten and solidified material, exhibiting a viscous-like behavior [100].

Light emission during chip formation is a multifaceted phenomenon influenced by various factors. It has been observed that the intensity of light emission during machining of BMGs tends to increase with higher cutting speeds and feeding rates [88,89,92,106,120], smaller tool rake angles, and the use of tools with lower thermal conductivity such as PCBN [106].

Ding et al. [101] recently investigated light emission in high-speed cutting of Vit. 1 BMG. Friction energy on the tool-chip interface was identified as the primary trigger, with a critical energy threshold of ~ 43 W for visible light emission. The study compared groove tools labeled as MF, MM, and UM, each representing distinct rake angles and front chamfer characteristics. The results revealed similar light emission brightness at feed rates  $f < 0.1$  mm/r (Fig. 6f), and no visible light emission at  $f = 0.05$  mm/r. However, at  $f \geq 0.1$  mm/r, MM and UM groove tools with larger rake angles and chamfered structures hindered chip flow, resulting in chip accumulation and higher cutting temperatures (Fig. 6g). This led to increased wear, friction energies, and stronger light emission compared to the MF tool. The chamfered structure on the cutting edge contributed to higher light emission due to poor chip evacuation, adhesive wear, and increased friction energy. Additionally, the use of a wear-resistant TiAlN/TiAlN coating demonstrated lower light emission compared to TiN/Al<sub>2</sub>O<sub>3</sub>/Ti(C,N) and Al<sub>2</sub>O<sub>3</sub>/Ti(C,N) coatings. Further, cutting oil can help avoid light emission at cutting speeds below 100 m/min, while liquid nitrogen is not recommended due to increased tool wear and adhesive wear.

#### 4.1.4. Tool wear

BMGs are generally considered as difficult-to-cut materials due to their high strength, high hardness, and lacking ductility. For example, Fe-based [121], Co-based [122], and Cr-based [123] BMGs show Vickers hardness values exceeding 1200 HV. Further, the newly discovered Fe-Nb-B MG alloys exhibit hardness and wear resistance levels that are 2–4 times higher than hardened stainless steel and comparable to nitride coatings [124]. The wear of the cutting tool significantly influences the surface quality and dimensional accuracy of machined BMGs [95]. Excessive tool wear is correlated with elevated cutting forces, posing a risk of damage to the part, fixture, and machine tool. As a result, tool wear during machining of BMGs should be taken into consideration.

Bakkal et al. [125] conducted a study on the wear of major and margin cutting edges in HSS and WC-Co tools during drilling process of a Zr-based BMG. They observed substantial wear in both tools when drilling was accompanied by intense light emission from the BMG chips. However, when no light emission was present, the wear on the drills was visible but less severe. The study demonstrated that WC-Co tools, which offer superior mechanical and thermal properties, are a preferred choice for drilling BMG materials. In addition, Bakkal et al. [106] observed welding of the BMG chip to WC-CVD tool having three layers of chemical vapor deposition (CVD) coatings, with noticeable melting taking place on the chip surface during machining. This welding phenomenon, likely observed towards the end of the cutting process, facilitated the adhesion of the chip to the tool tip.

To gain a comprehensive understanding of tool wear, it is important to investigate wear mechanisms. Wang et al. [102] identified different wear mechanisms, including abrasion, adhesion, and fatigue, during machining of Fe-based as-deposited MG overlay at various cutting parameters. A minor occurrence of chemical dissolution wear was noted due to the presence of built-up edge (BUE). Tool failure modes encompassed flank wear, plastic deformation at the minor edge, and catastrophic chipping at the tool nose. Recently, Liu et al. [95] analyzed tool wear during milling of Zr-based BMG and other materials and categorized tool wear into mechanical friction wear, bonding wear, diffusion wear, frictional oxidation wear, and fatigue damage. Deng et al. [112] recently

found that when using a WC-Co cemented carbide grooving tool to orthogonally cut Zr-based BMGs, the adhesion process on the cutting edge can lead to unstable adhesion and subsequent adhesive wear. Once stable adhesion occurs, chips in the sticking area cold-weld to the cemented carbide under high stress. The loss of the Co phase, which has a strong chemical affinity, gradually removes the hard WC phase as the chip flows, resulting in abrasive wear. However, in the sliding area of the tool-chip contact interface and the flank face, the viscous-fluid chips that adhere at high temperatures act as a protective layer, effectively mitigating severe tool wear in those regions.

Fig. 7a and b present a comparison of cutting wear between two types of tools, namely the diamond tool and PCBN tool, after machining BMG workpieces [85]. From the figures, it is evident that the wear of the PCBN tool edge is more severe compared to the diamond tool, while the latter exhibits worse adhesion. In another study by Bakkal et al. [106], it was observed that chipping occurs at the cutting edge of the PCBN tool during lathe machining of Vit. 1 BMG. This chipping was observed near the tool tip and in the tool nose radius region, likely due to the impact of the BMG chip with the tool edge during machining. Furthermore, chemical reactions and oxidation of tool have been demonstrated to occur due to the high temperatures generated during machining of BMGs [85,102,112]. The diamond tool experiences chemical reactions of Zr-C and Zr-O, while the PCBN tool undergoes Zr-O reaction (oxidation) [85]. These chemical reactions significantly limit the application of diamond tools for machining of BMGs, whereas PCBN tools exhibit superior chemical stability when cutting materials.

The cooling condition has also a significant effect on tool wear during machining. Proper cooling helps dissipate heat generated during the cutting process, reducing the temperature at the tool-chip interface. Fig. 7c illustrates the tool wear under different cutting atmospheres: dry cutting, cutting oil, and liquid nitrogen. The worn tool face is observed in the dry cutting and lubrication conditions, while cutting oil can lead to significant chip adhesion instead of reducing friction as expected [101]. The authors suggested that the high cutting speed limits the penetration of oil into the tool-chip interface, resulting in reduced adhesion with a decrease in cutting speed. However, dry cutting also presents similar issues to oil cutting. Liquid nitrogen, on the other hand, reduces light emission by rapidly cooling the temperature and suppressing the exothermic oxidation reaction rate. However, chip adhesion in the liquid nitrogen atmosphere is more severe than in the dry and oil cutting atmospheres. In addition, Maroju et al. [88] conducted a study demonstrating that dry cutting results in a higher level of tool wear compared to cutting with coolant (Fig. 7d). Specifically, the width of tool wear progressively increases with cutting distance. However, in the case of dry cutting, the initial width of tool wear is relatively high, and it becomes significant when the cutting distance reaches 1250 mm.

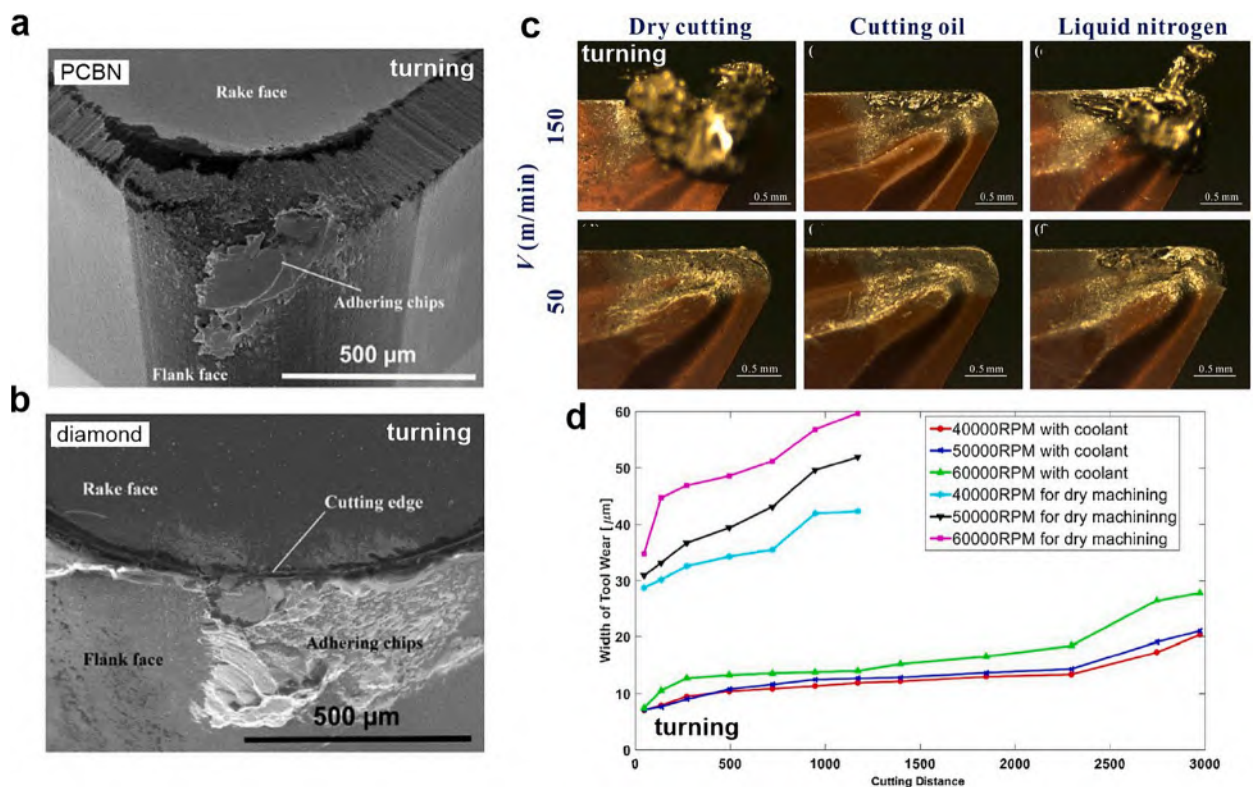


Fig. 7. (a-b) Micrographs showing wear of diamond and PCBN cutting tools (Adapted from [85]). (c) Optical images of a worn coated tool under various cooling and lubrication conditions ( $f_r = 0.15 \text{ mm/r}$ ; MF groove; TiAlN/TiAlN coating). Adapted from [101]. (d) Comparing tool flank wear between dry machining and machining with mist coolant (Adapted from [88]).

#### 4.1.5. Structural and mechanical property characterizations

Numerous studies have indicated that, under optimized cutting conditions, traditional machining of BMGs does not result in crystallization within the machined workpiece and formed chips [85,87,92,93,96,100,108,112]. Nonetheless, the high temperatures generated during machining of BMGs can induce crystallization and oxidation [89,100]. In a study by Bakkal et al. [119], broad amorphous peaks were observed on Zr-based BMG surfaces machined at different cutting speeds as well as the chips cut at the lowest cutting speed (0.38 m/s), as shown in Fig. 8a. However, sharp diffraction peaks appeared on the BMG chip surfaces machined at higher cutting speeds of 0.76 and 1.52 m/s accompanied by visible light emission, indicating the presence of monoclinic  $ZrO_2$  as a crystalline phase. Scanning electron microscopy (SEM) micrographs of chips cut at 1.52 m/s (Fig. 8b) revealed distinct regions with varying gray levels, representing different crystalline structures. These included the oxide layer (O) surrounding the chips, leaf-shaped dark gray crystalline phases (G), amorphous regions inside the chips (A), and eutectic crystalline regions (E). The EDS analysis confirmed varied chemical compositions in different contrast regions. Moreover, under milling conditions, the XRD spectrum showed the crystallization growth with more distinct sharp peaks, especially when material melting occurred at higher feed rates. This confirms that the stress and temperature increase during milling lead to crystallization. If material melting does not occur, the BMG surface remains mostly amorphous [88]. These findings emphasize the importance of controlling cutting parameters to prevent substantial temperature increase.

Another structural feature during machining of BMGs is noticeable changes in the interatomic distances. Chen et al. [85] observed a slight shift of the main XRD amorphous peak of the  $Zr_{55}Cu_{30}Al_{10}Ni_5$  chips towards higher angles compared to the as-cast and machined BMG samples (Fig. 8c). A similar trend was observed in the XRD patterns for machined Vit.1 BMGs with different turned lengths [112]. These shifts in peak position indicate a change in the average interatomic distance in MGs [126]. The atomic pair distribution function (PDF) analysis conducted by Maroju et al. [88] revealed that the radial distance of highly structured atomic arrangement decreases with increased feed rate. This radial distance further decreases with intermittent light emission associated with material crystallization. This is because MGs have a larger volume compared to crystalline materials, where atoms are arranged closely and regularly. Upon heating, the relaxation process annihilates the free volume in the microstructure of MGs [127,128], leading to a reduction in the average interatomic distance [129]. As a result, the main diffraction peak shifts to higher angles according to Bragg's equation [130]. In the machining process of BMGs, the chip formation primarily occurs in the deformation zones, generating significant cutting heat. This heat induces structural relaxation in the BMG chips and machined workpieces, resulting in shorter interatomic distances and increased structural ordering.

Transmission electron microscopy (TEM) characterizations provide additional insights into the structural characteristics of

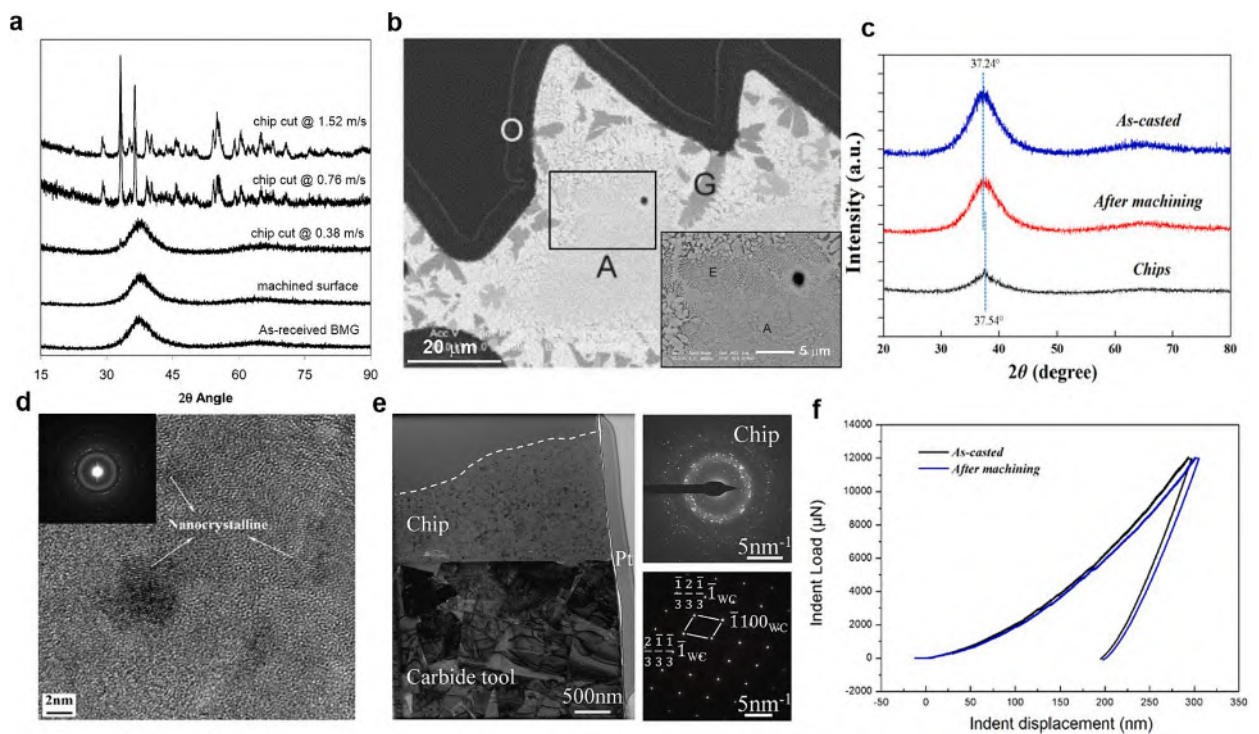


**Fig. 8.** (a) XRD patterns of as-received, machined surface, and chips of Zr-based BMG cut at various speed and in machined surface as well as as-received BMG. (b) SEM micrographs of chip cross-section. Adapted from [119]. (c) XRD patterns as-cast, BMG after machining state, and chips. (d) TEM image of surface microstructure of the machined BMG. Adapted from [85]. (e) TEM image of tool-chip interface and the corresponding SAED patterns of chip and carbide tool (Adapted from [112]). (f) Nano-indentation load-displacement curves of as-cast and machined Zr-based BMG (Adapted from [85]).

machined BMG workpieces and chips, confirming the occurrence of nanocrystallization. In the high-resolution TEM (HRTEM) image from the surface microstructure of a machined Zr-based BMG (Fig. 8d), the orderly arrangement of atoms allowed for the easy distinction of nanocrystalline regions within the amorphous MG matrix. The corresponding selected area electron diffraction (SAED) pattern exhibited numerous spots forming concentric rings, characteristic of nanocrystalline structures. Further, Similarly, the microstructure of a machined Fe-based overlay MG consisted of an amorphous matrix containing nanocrystalline particles with sizes ranging from 30 to 100 nm [102]. The nanocrystalline grains were identified as body-centered cubic (bcc) Fe-based structures.

In another study, Deng et al. [112] conducted a detailed investigation of the microstructure of the adhered chip by examining the tool-chip interface in the sticking area using TEM observations. Fig. 8e showed obvious nanocrystallization of the amorphous material adhering to the tool surface at the chip interface, with a width ranging from 0.9 to 1.7  $\mu\text{m}$ . The fast Fourier transformation (FFT) image contained diffuse halo rings and several spots, confirming the presence of nanocrystals. Additionally, the EDS analysis revealed phase separation within the nanocrystallized region, while the free chip surface remained amorphous with a uniform composition distribution. It was concluded that the chip at the tool-chip interface exhibits a complex composition of multiple crystalline phases and quasi-crystals under high temperature and strain rate conditions during cutting.

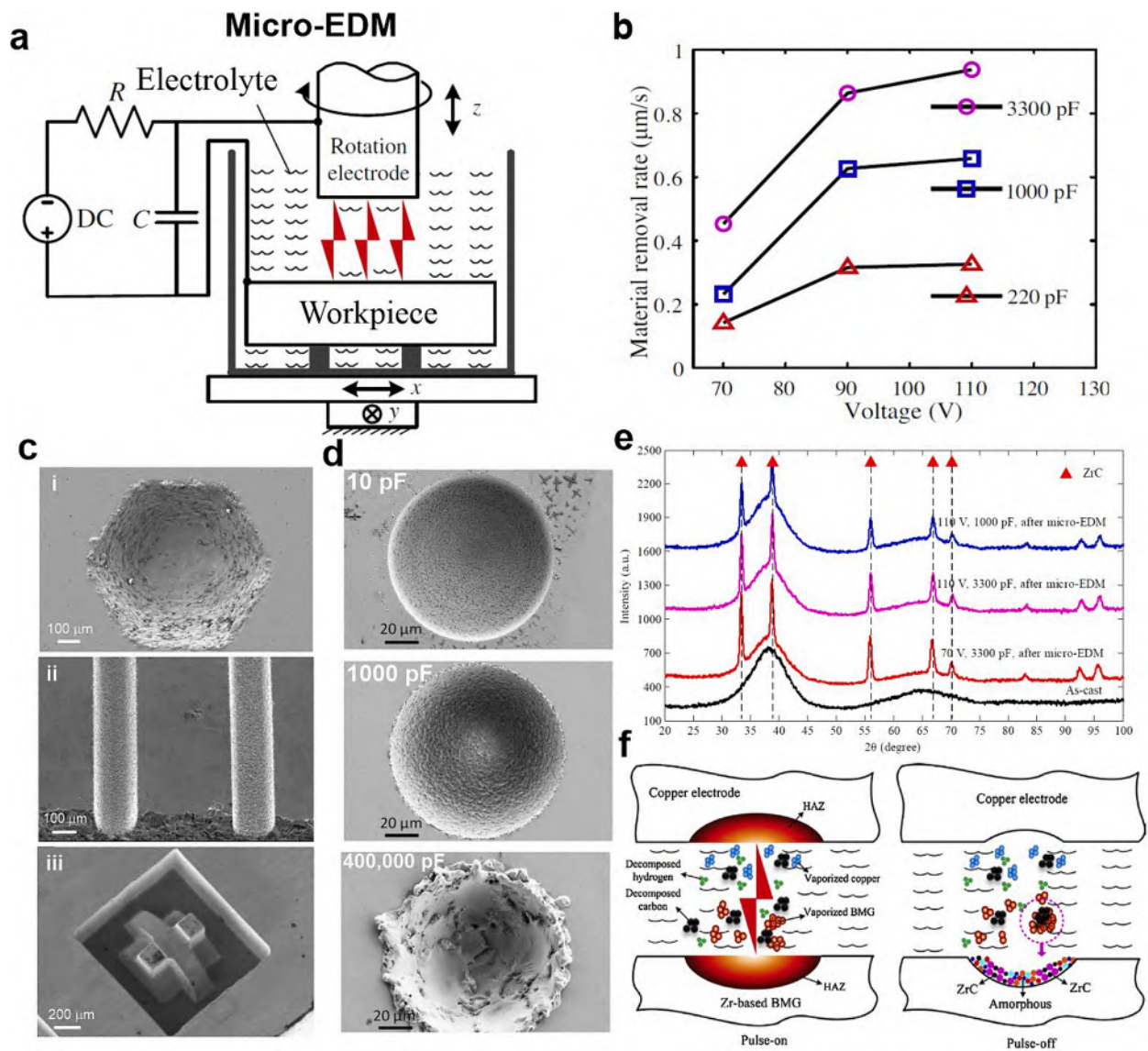


**Fig. 9.** (a) Schematic diagram of the EDM experimental setup. (b) Vit. 1 BMG removal rate at various voltages and capacitances. Adapted from [143]. (c) SEM image for three dimensional microstructures machined on the  $\text{La}_{62}\text{Al}_{14}\text{Ni}_{12}\text{Cu}_{12}$  (i), Zr-based micro-channels (ii), and 3D Pd-based micro-mold. Adapted from [150–152]. (d) Effect of different capacitances on the surface finish of the Zr-based BMG blind micro-holes (Adapted from [153]). (e) XRD patterns of the as-cast BMG surface and micro-EDMed surfaces under various voltage and capacitances (Adapted from [154]). (f) Schematic of spark representing the mechanism of partial crystallization (Adapted from [143]).

The primary factor contributing to nanocrystallization in the microstructure of machined BMGs is the elevated temperature. As previously discussed, the frictional contact between the BMG workpiece and the cutting tool can raise the surface temperature above  $T_x$ , resulting in the precipitation of nanocrystals. Additionally, the severe plastic deformation associated with cutting process of BMGs can also induce nanocrystallization [131,132]. Therefore, both thermal energy and mechanical energy act as driving forces for atomic diffusion and rearrangement, ultimately leading to the formation of nanocrystals.

Limited research has focused on the characterization of mechanical properties in machined BMGs. By performing nanoindentation tests, Chen et al. [85] found larger indentation depths for the machined Zr-based BMG (Fig. 8f), denoting that the hardness of the machined workpiece is lower than that of the as-cast state. This phenomenon of work softening, unlike the work hardening observed in machining crystalline metals, is similar to the hardness decrease observed during structural rejuvenation of BMGs using various thermomechanical processing routes [133], such as cryogenic rejuvenation [134,135], elastostatic compression [136–138], ultrasonic hammering [139], and plastic deformation [140,141]. The decrease in hardness can be attributed to the increase in free volume within the microstructure, resulting in higher energy (less relaxed) states. During the cutting process, the plastic deformation zones (see Fig. 6a) indicate that the newly formed surface experiences plastic deformation induced by the tool flank face. This leads to the formation of numerous shear bands and an increase in free volume at the machined surface, ultimately causing a reduction in hardness. The final hardness value and structural state in machined BMG workpieces are determined by a trade-off between relaxation induced by temperature rise and rejuvenation induced by plastic deformation.

## 4.2. Non-traditional machining

### 4.2.1. Micro-EDM

Micro-EDM has emerged as an advanced machining technique renowned for its precision in shaping complex geometries and fabricating micro-components and parts with intricate features [142]. Throughout the micro-EDM process, controlled sparks generated by electric discharges effectively vaporize and erode the workpiece material, ensuring precise and intricate machining. Key features of micro-EDM include its high energy density, non-contact nature, and the capacity to machine intricate features, rendering it highly suitable for microscale applications.

The micro-EDM encompasses two primary methods: die-sinking and wire EDM. In die-sinking micro-EDM, as depicted in Fig. 9a [143], electric discharges occur between a specially shaped tool electrode and a workpiece submerged in a dielectric fluid. Conversely, wire EDM employs a thin, electrically conductive wire electrode, such as copper and molybdenum wires in the case of EDM of MGs [144]. EDM has also been employed for machining Zr-based BMGs at the macroscale [145–149].

The material removal rate (MRR) during EDM primarily depends on discharge voltage, capacitance, and pulse duration. A systematic study conducted by Huang and Yan [143] showed that the micro-EDM of Vit. 1 BMG at various discharge voltages and capacitances demonstrate a consistent trend (Fig. 9b): an increase in capacitance leads to higher MRR at a given voltage, while an increase in voltage results in increased MRR for a constant capacitance. This phenomenon can be explained by the discharge energy equation,  $E = 1/2CV^2$ , where  $C$  represents the capacitance and  $V$  represents the voltage. As per this energy law, higher voltages and capacitances generate greater discharge energy, consequently enhancing the MRR. Regarding MRR variations with pulse duration, Hsieh et al. [147] found that for various discharge currents ranging from 1 A to 10 A, the material removal rate initially increased and then decreased with an increase in pulse duration. The peak material removal rate was achieved at a pulse duration of 30  $\mu$ s.

Fig. 9c displays the morphologies of different micro-structured BMGs, including a 3D micro-structured  $\text{La}_{62}\text{Al}_{14}\text{Ni}_{12}\text{Cu}_{12}$  BMG (i) [155], a microchannel structure fabricated on Vit. 1 BMG (ii) [151], and a 3D micro-mold manufactured by micro-EDM of  $\text{Pd}_{40}\text{Cu}_{30}\text{P}_{20}\text{Ni}_{10}$  BMG [62]. The micrographs reveal variations in surface quality, with the presence of craters and recast layers in micrographs (i) and (ii). Yeo et al. [151] found that microchannels fabricated using micro-EDM tend to have larger surface roughness compared to those produced by micromilling. This is attributed to the presence of overlapping craters on the surface, which limits achieving the minimum surface roughness. In the EDM process, a crater is the material that is removed by the discharge energy per pulse [153]. On the other hand, the 3D Pd-based micro-molds demonstrated good surface quality by optimizing processing parameters such as time and machining depth [152].

In general, using lower discharge voltage, discharge capacitance, and pulse duration in EDM of BMGs results in smaller craters, thinner recast layers, and reduced burr widths, yielding improved surface quality and reduced surface roughness [143,144,146,147,151,153,154]. The influence of EDM process parameters on surface roughness varies [145,151], with voltage and electrode rotational speed having minimal impact, while capacitance plays a critical role in determining crater sizes, recast layer, and overcut. In wire EDM of BMGs, the surface roughness is mainly influenced by the pulse type and pulse-on time [148]. By carefully selecting these parameters, there is a greater potential to achieve high cutting efficiency and low surface roughness. In micro hole drilling of BMGs using micro-EDM, the electrode rotational speed stands out as the most influential factor [156,157]. While tool rotation negatively affects overcut, edge deviation, and taper angle, it plays a crucial role in significantly reducing machining time, with potential time savings of 5–10 times.

The study performed by Liu et al. [153] showed that at a constant voltage and electrode rotational speed, increasing the capacitance during EDM of blind holes on a Zr-based BMG results in a sharp increase in surface roughness (Fig. 9d). At a capacitance of 400 nF, the surface becomes very rough, with significant recast layer and debris. Higher capacitance also leads to an increase in recast layer at the edge of lower micro-holes. By reducing the capacitance at a voltage of 80 V, the heat-affected zone (HAZ) around the micro-hole edge was minimized, which is crucial for reducing crystallization during BMG machining. Additionally, significant improvements in surface roughness and burr width were observed in the micro-EDM of  $\text{Zr}_{57}\text{Nb}_5\text{Cu}_{15.4}\text{Ni}_{12.6}\text{Al}_{10}$  BMG by reducing the input energy from 13.4  $\mu$ J to 0.9  $\mu$ J [151]. The surface roughness was reduced by 43%–51%, and the burr width decreased by 63%. These improvements were

attributed to the generation of smaller craters and a reduction in the amount of molten material.

The electrode material and size can also affect the surface quality of EDMed BMGs. By using tungsten rod electrode and copper and brass tube electrodes, Yeo et al. [151] found that electrode material melting point had a stronger influence on the tool wear rate at higher input energy, while thermal conductivity had a greater impact at lower input energy. Further, tube-shaped electrodes were more suitable for machining BMG at low input energy due to enhanced heat transport and reduced tool wear. Additionally, using a larger diameter copper rod electrode (200  $\mu\text{m}$ ) with low settings of capacitance, voltage, and discharge energy in micro-EDM resulted in surface porosities [153]. This was likely due to unstable sparking at smaller spark gaps caused by reduced discharge energy. However, using a smaller diameter electrode (75  $\mu\text{m}$ ) resolved the surface defects. Therefore, smaller electrodes and appropriate discharge energy are necessary for stable machining and improved surface finish.

Surface carbonization and crystallization pose challenges in the EDM of BMGs. The wire EDM at macroscales utilizes a high discharge energy that leads to extensive melting and vaporization of the workpiece surface, creating a substantial HAZ. This process often results in significant crystallization of BMG [147], but the extent of crystallization can be mitigated by optimizing EDM parameters [148]. In contrast, micro-EDM offers a promising alternative for machining BMGs while preserving their amorphous characteristics. This is due to the relatively lower discharge energy employed in micro-EDM, which helps minimize the temperature rise and maintain the amorphous structure of the BMGs, resulting in minimal crystallinity.

Huang and Yan [143] analyzed Zr-based BMGs machined by EDM using different discharge capacitances (220 pF, 1000 pF, and 3300 pF). XRD patterns showed broad amorphous peaks, indicating the predominantly amorphous structure of the machined BMGs. However, small crystalline peaks were also observed, with the lowest intensity at a capacitance of 1000 pF. Interestingly, varying the voltage from 70 V to 110 V had a minimal impact on surface crystallization. Furthermore, the microstructures and crystallization characteristics differed between the center and outer regions of the EDMed holes due to factors like sparks, dielectric circulation, thermal dissipation, and debris. In another study, the EDS analysis on the 3D Pd-based micro-mold surface revealed an increase in carbon content from 0.5 % to 5.8 % with increase in processing depth [152]. Also, the XRD analysis showed the presence of  $\text{Cu}_3\text{P}$  and  $\text{Ni}_{12}\text{P}_5$  phases on the MG surface after micro-EDM, with their relative proportions changing as the depth increased. Excessive discharge energies employed during wire EDM can result in higher carbon content on the workpiece surface [145]. This, in turn, can lead to the formation of thick carbonization layers on the surface of the BMG.

Fig. 9e presents a comparison of XRD patterns between the as-cast Zr-based BMG surface and surfaces of samples machined using micro-EDM under various voltages and capacitances, employing a sintered polycrystalline diamond (PCD) electrode [154]. The micro-EDMed sample surfaces exhibit peaks indicating crystallization, specifically the presence of the ZrC phase and unknown phases, in contrast to the amorphous state of the as-cast samples. This surface crystallization is attributed to reactions between MG elements and the carbon-rich PCD electrode and EDM oil during micro-EDM. Notably, another crystallization behavior was observed in the shallow subsurface region of EDMed Zr-based BMG, approximately 20  $\mu\text{m}$  deep, primarily associated with the formation of internal crystalline phases, suggesting a hierarchical pattern along the depth. The variation in crystallization behavior along the depth direction is attributed to the distinct thermal processes occurring in the top surface layer and the subsurface region during the micro-EDM process.

Huang and Yan [143] proposed a mechanism for the partial crystallization of EDMed surfaces in Zr-based BMG (Fig. 9f). During micro-EDM using a copper electrode, sparks are generated between the electrode and the BMG during pulse-on, resulting in the melting, vaporization, and suspension of copper and BMG in the EDM oil. Decomposed hydrogen and carbon are also present in the EDM oil. In certain regions, the vaporized BMGs and decomposed carbons may combine, forming a mixture. During the pulse-off time, the vaporized materials undergo re-solidification. The strong chemical affinity between C atoms and Zr atoms leads to the formation of nanocarbitides, such as ZrC, during the cooling and re-solidification processes. Additionally, the use of different dielectric fluids, such as EDM oil and deionized water, leads to the production of distinct decomposition products during the pulse-on time in EDM, which results in different crystallization phases on the machined surfaces.

#### 4.2.2. Electrochemical micromachining (ECMM)

ECMM is a non-contact subtractive method that utilizes electrochemistry for controlled material removal. It involves submerging a workpiece in an electrolyte and using a nearby tool electrode. Applying a DC current triggers precise material removal through electrochemical reactions. The material removal mechanism in ECMM involves the dissolution of anodic material at the ionic level under an applied electric field. The process creates accurate micro-sized features with high surface quality. However, managing various process parameters, such as electrolyte selection, micro-tool electrode shaping, tool-workpiece distance, and pulse parameters, adds complexity to the method [158].

Kosiba et al. [159] reported the first ECMM of a Zr-based BMG surface using micro-tool electrodes and ultra-short voltage pulses to create micro-hole structures. The choice of process parameters, especially the electrolyte chemistry, was found to be crucial. Aqueous  $\text{NaNO}_3$  was unsuitable due to the formation of thick corrosion product layers. Methanolic  $\text{HClO}_4$  electrolyte allowed for micro-hole structures with aspect ratios of about 1. The pulse voltage significantly affected the morphology, with lower voltages producing porous structures and higher voltages leading to smoothing. ECMM experiments at the pulse voltage 6 V and 100 ns on-time pulse showed the most homogeneous and smoothest micro-hole morphology. Later, Cole et al. [160] designed a novel waveform by combining specific voltage thresholds/regimes for pitting and repassivation, which effectively minimized the adherence of corrosion products and dense oxides to the surface and enabled ECMM of  $\text{Zr}_{57}\text{Ni}_{20}\text{Al}_{15}\text{Cu}_{5.5}\text{Nb}_{2.5}$  in aqueous 2.98 M  $\text{NaNO}_3$ . Precise dimensional tolerances and accuracy were achieved by applying optimal ECMM parameters to pattern lines on the surface. To create more intricate shapes and components, the lines could be improved by utilizing shorter pulse times and slower movement speeds.

Additionally, Horn et al. [161] fabricated complex microstructures with high precision on Fe-based glassy  $\text{Fe}_{65.5}\text{Cr}_4\text{Mo}_4\text{Ga}_4\text{P}_{12}\text{C}_5\text{B}_{5.5}$  BMG surface by ECMM. This was achieved by employing an aqueous electrolyte containing 0.1 M  $\text{H}_2\text{SO}_4$  with up to 0.1 M

$\text{Fe}_2(\text{SO}_4)_3$  addition and applying ultrashort voltage pulses. The study found that increasing pulse lengths (50 to 500 ns) or raising pulse-on voltages (5 to 9 V) led to larger hole diameters and depths due to an enlarged gap between the workpiece and tool electrode. Higher pulse-on voltages also caused corrosion of the surrounding workpiece surface. Machining parameters influenced local transpassive dissolution, but also negatively impacted machining resolution. Adjusting pulse-off voltages and tool feed rates did not improve resolution. High pulse-off voltages increased pitting corrosion, while too small values hindered material dissolution. A slower tool feed rate than the local dissolution rate prevented unwanted tool-workpiece contact but prolonged the process. For example, Fig. 10a (a complex smiley shape) took 3 h to machine.

One of the main challenges in ECMM is to control the electrode reactions in order to prevent the formation of unwanted passive layers on the machined surface regions. Gebert et al. [162] analyzed comparatively the anodic behavior of three Zr-based BMGs with variation in the Cu:valve metal (VM) ratio in the concentrated  $\text{NaNO}_3$  solution (Fig. 10b). Valve metal refers to the metallic elements possessing a stable oxide layer on their surface when exposed to air or oxygen, including Zr, Ti, and Al. Similar polarization behavior was observed for all glassy alloys, with a slightly higher reactivity observed in  $\text{Zr}_{55}\text{Cu}_{30}\text{Al}_{10}\text{Ni}_5$ , which has the highest Cu:VM ratio (0.462), compared to  $\text{Zr}_{57}\text{Ti}_3\text{Cu}_{20}\text{Al}_{10}\text{Ni}_8$  (0.278) and  $\text{Zr}_{57}\text{Cu}_{15.4}\text{Al}_{10}\text{Ni}_{12.6}\text{Nb}_5$  (0.214) under free corrosion and initial anodic polarization conditions. The transpassive regime resulted in sharp breakdown of the passive state due to valve metal oxidation, Cu and Ni dissolution, and water decomposition. Electrolyte flow and rotation velocity affected the breakdown potential. At transpassive potential (3 V vs. SCE), current density levels  $> 1 \text{ A/cm}^2$  led to severe alloy dissolution. The degradation patterns after transpassive treatment showed random microroughness, preserving the glassy surface state. Additionally, Guo et al. [167] reported similar polarization behavior and transpassivation ability during ECMM of four types of Zr-based BMGs in  $\text{NaNO}_3$ -ethylene glycol electrolyte, making them suitable for ECMM with high machining localization. A higher scan rate improved the repassivation ability. Cu and Ni demonstrated high electrochemical activity in the  $\text{NaNO}_3$ -EG electrolyte, despite Cu having a higher  $E_{\text{corr}}$ . Furthermore, applying the pulse voltage over the inter-electrode gap caused pitting, oxidation, and the formation of a supersaturated film, leading to the uniform dissolution of Zr-based BMGs. Higher current density and a smaller inter-electrode gap accelerated the generation of a smooth surface.

Wire electrochemical micromachining (Wire ECMM) is a particular type of ECMM which has recently attracted attentions for micromachining of BMG. Wire ECMM is a promising method for micromachining of metallic material due to its agility and numerous advantages over wire EDM [163]. In wire ECMM (Fig. 10c), a wire acts as the tool, connected to the negative terminal (cathode) of a DC power source, while the workpiece is connected to the positive terminal (anode). An electrically conducting fluid (electrolyte) is supplied between the electrodes, and a desired shape is machined by the wire. If the wire material is chemically stable with the

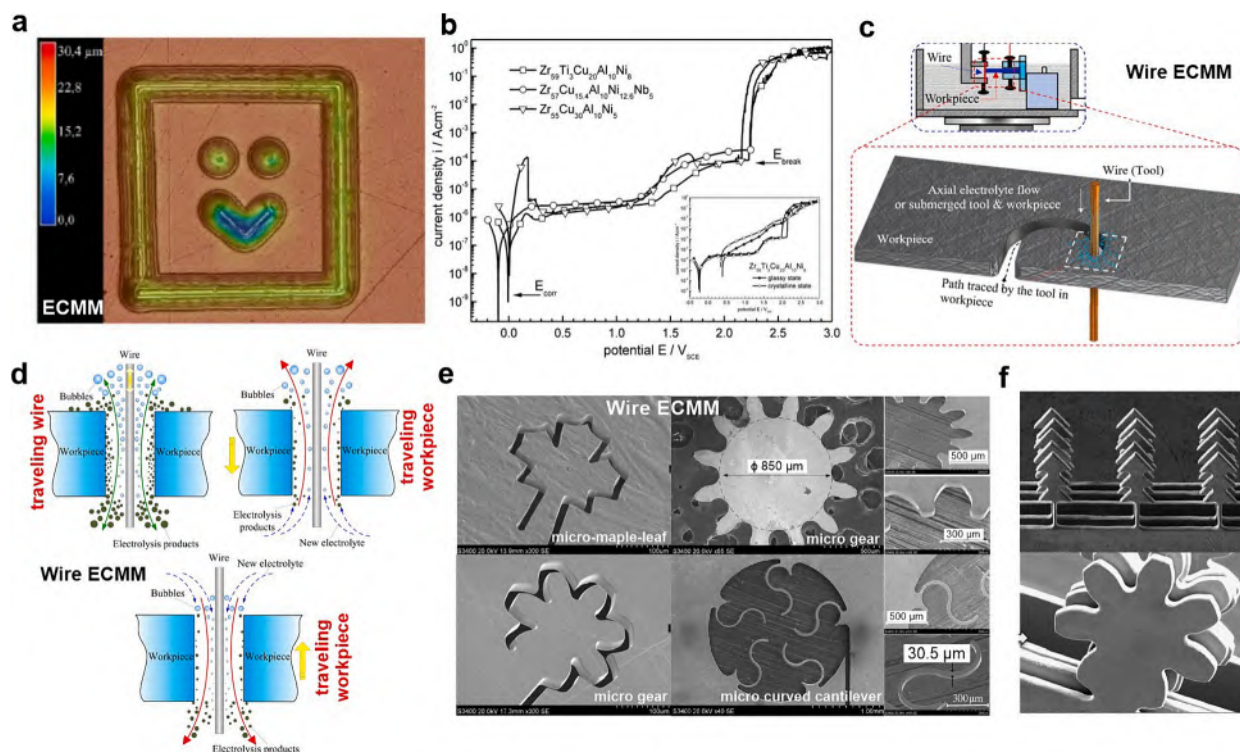


**Fig. 10.** (a) SEM image showing of a smiley lateral microstructure (Adapted from [161]). (b) Polarization curves of Zr-based BMGs recorded at 1 mV/sec in 250 g/L  $\text{NaNO}_3$  solution (Adapted from [162]). (c) Schematic of the wire ECMM process (Adapted from [163]). (d) Schematic diagrams of mass transport in wire ECMM with a traveling wire (top right), a downward-traveling workpiece (top left), and an upward-traveling workpiece (bottom). Adapted from [164]. (e) SEM images of complex microstructures and surface topographies fabricating under optimal machining conditions. Adapted from [165,166]. (f) SEM images of multilayered microstructures fabricated on Ni-based MG by wire ECMM (adapted from [164]).

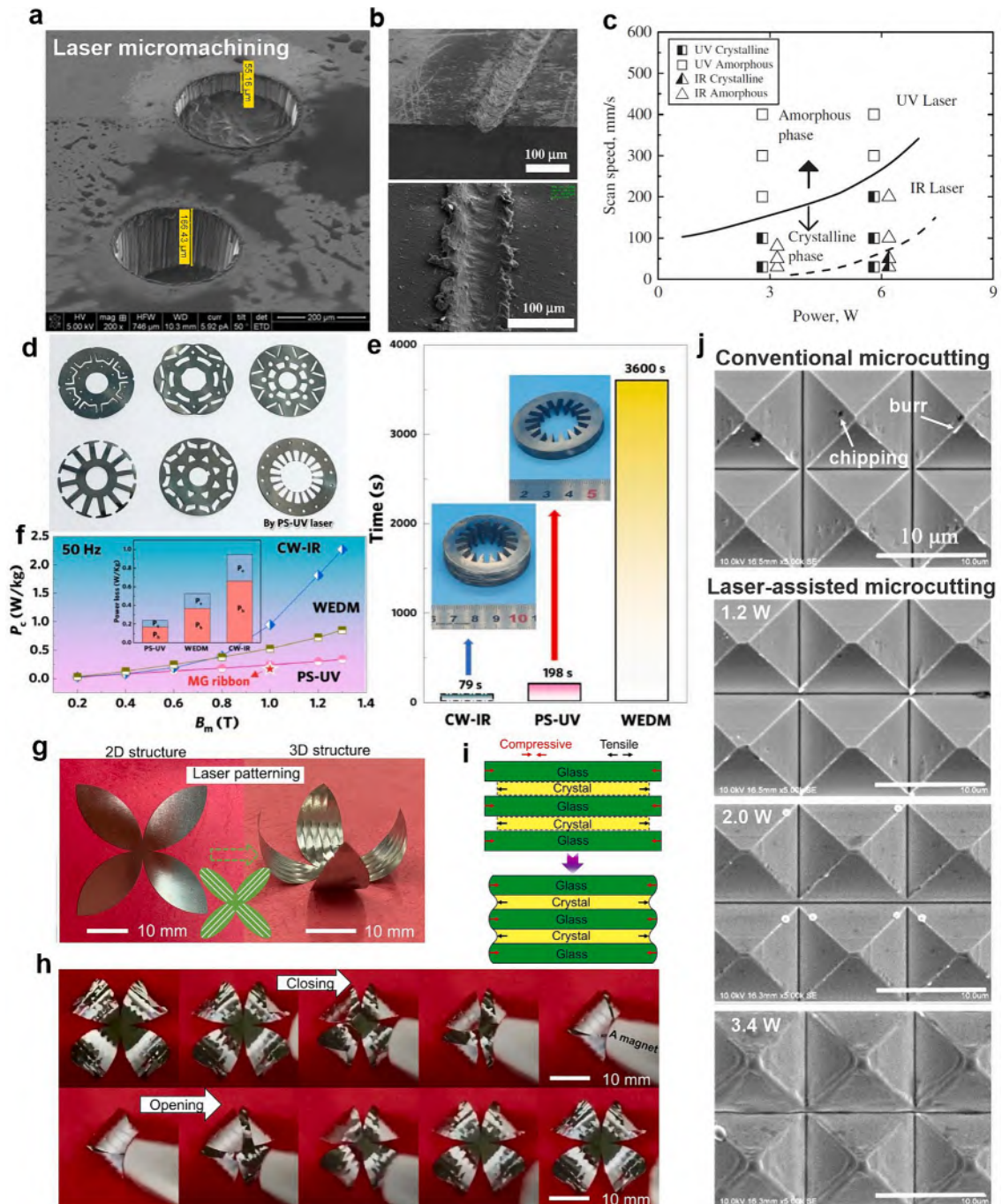


**Fig. 11.** (a) SEM image of laser-machined holes in  $Zr_{47}Cu_{45}Al_8$  BMG. The holes are filled partially with carbon adhesive for imaging. Adapted from [173] (b) Top view and cross-sectional view of Mg-based BMG after laser micro-machining with a UV laser. (c) Phase transformation summary of Mg-based BMG after laser scanning at various processing parameters (Adapted from [176]). (d) Optical images showing core shapes cut from amorphous ribbons using the PS-UV laser. (e) Efficiency in processing compared between laser cutting and wire-EDM (WEDM) method. (f) Stator core losses measured at frequency of 50 Hz for cores fabricated using different methods. The inset displays different core losses at 1 T. Adapted from [178]. (g) Fabrication of MG composite leaves via ps-pulsed laser cutting and ns-pulsed laser patterning. (h) Snapshots of the closing and opening of the leaves in the magnetic field. (i) The periodic structure of the glass matrix and crystallized regions. Adapted from [179]. (j) Morphology of the micro-pyramids fabricated by conventional micro-cutting and laser-assisted micro-cutting at different laser powers (Adapted from [180]).

electrolyte, no material is dissolved, allowing the wire to be reused. This process is unaffected by the mechanical properties (hardness, toughness) of the workpiece, ensuring accuracy, efficiency, and surface quality. However, the feed rates in wire ECMM of MGs are typically lower than  $2 \mu\text{m/s}$ , significantly lower than those achievable in micro-EDM. This limitation confines wire ECMM mainly to 2D MG ribbons with micro-sized thicknesses [168–170].

Mass transport significantly influences the anodic material dissolution process in wire ECMM. It affects the current density distribution in the machining gap and plays a crucial role in shaping accuracy and the microscopic surface topography resulting from dissolution. An innovative technique has been recently developed by employing a travelling anodic MG workpiece to improve mass transport during wire ECMM (Fig. 10d) [164,165,170]. Unlike the traditional method using a travelling wire, the anodic Ni-based MG workpiece with upward-traveling or downward-travelling motions facilitates enhanced electrolyte refreshment in the machining gap, leading to improved performance. Hence, efficient mass transport with the traveling workpiece method leads to a favorable surface quality, reflecting the even electrochemical removal of material through nonselective dissolution. However, the travelling wire method has a limited effect on electrolyte refreshment near the machining surface of the workpiece. Additionally, solid electrolysis products, such as hydroxides and other non-metallic particles, tend to accumulate near the anodic dissolution surface, thus deteriorating mass transport.

Among machining parameters such as the the working electrode, feed rate, pulse duration and applied voltage [164,166,168,170], the electrolyte type and concentration play a crucial role in determining the machined surface quality. Hang et al. [166] found that MG exhibited higher corrosion resistance in salt solutions compared to acidic solutions during the fabrication of micro-slits. Additionally, the passivation film of MG in HCl was easily broken, affecting the surface quality.  $\text{H}_2\text{SO}_4$  solution exhibited a faster corrosion rate, allowing for a higher feed rate. On the other hand, tungsten wire electrode corroded in  $\text{NaNO}_3$  solution, affecting processing efficiency. Hence,  $\text{H}_2\text{SO}_4$  solution is considered the optimal choice for the electrolyte in wire ECMM of Ni-based MGs. Additionally, at solution concentrations equal to or lower than 0.2 M, the wire electrode experienced deposition of insoluble products, causing a disorderly local electric field and flow field. Consequently, the micro-slits exhibited poor quality with increased width, negatively impacting the cutting effectiveness and resulting in an abnormal appearance. However, as the solution concentration increased to values larger than 0.2 M, the product deposition started to decrease.

Suitable wire ECMM parameters enable the fabrication of intricate microstructures in MGs with minimum surface roughness. Fig. 10e illustrates various microstructures of Ni-based MGs achieved through different machining parameters and mass transport methods [165,166]. Moreover, stacking multiple workpieces enables a significant increase in machining efficiency. For instance, Fig. 10f displays five-layered complex microstructures of pointers (top) and spur gears (bottom), each with a height of  $500 \mu\text{m}$  and width of  $100\text{--}200 \mu\text{m}$ , achieving average surface roughnesses  $R_a = 0.018 \mu\text{m}$  and maximum roughness depth  $R_{\text{max}} = 0.225 \mu\text{m}$  [164].

#### 4.2.3. Laser micromachining

Laser micromachining is a non-contact, precise manufacturing process that utilizes the energy from a focused laser beam to remove material from a workpiece. The energy is absorbed by the material, leading to localized heating and subsequent vaporization, melting, or ablation, depending on the laser parameters and material properties. The versatility of laser micromachining enables it to be utilized across various materials, including MGs [171].

Laser machining has demonstrated potential in fabricating microstructures such as micro holes, channels, and trenches on Zr-based [172–174], Cu-Zr based [173,175], and Mg-based [176] MGs. As an example, Fig. 11a and b illustrate laser-machined micro holes in  $\text{Cu}_{45}\text{Zr}_{47}\text{Al}_8$  [173] and a micro groove in  $\text{Mg}_{65}\text{Cu}_{25}\text{Gd}_{10}$  [176] BMGs. Regarding exploring the laser micromachining parameters, Jia et al. [177] investigated the impact of femtosecond laser ablation at fluences of  $3.18 \text{ J/cm}^2$  and  $6.36 \text{ J/cm}^2$  on the surface and sub-surface microstructure of Fe-Cu-Nb-Si-B MG ribbons. Ripples were observed in both weakly and strongly ablated zones. Further, XRD analysis confirmed the unchanged amorphous phase in the damaged area, with minimal crystallization observed in the ablation zone. Using the same technique, Wang et al. [172] successfully machined  $\text{Zr}_{65}\text{Cu}_{17.5}\text{Ni}_{10}\text{Al}_{7.5}$  MG foils and fabricated micrometer-sized holes and trenches without inducing crystallization by selecting fluences ranging from 5 to  $25 \text{ J/cm}^2$ . Additionally, Lin et al. [176] machined surface of Mg-based BMG specimens with different laser sources, energies, and scan speeds and achieved cutting depths ranging from 0.1 to  $80 \mu\text{m}$ . Using an ultraviolet (UV) laser with fluence of  $12 \text{ J/cm}^2$  and scan speed of  $30 \text{ mm/s}$  resulted in grooves with small ridges and re-deposited materials between them, indicating plasma cloud effects. Slow scan speeds induced plastic wrinkles in the HAZ, while faster scan speeds ( $200 \text{ mm/s}$  or above) reduced HAZ size and wrinkles. The infrared (IR) laser with larger fluence of  $19 \text{ J/cm}^2$  caused surface heating and viscous flow, but no grooves were formed on the Mg-based BMG specimens.

Fig. 11c summarizes the phase transformation behavior of  $\text{Mg}_{65}\text{Cu}_{25}\text{Gd}_{10}$  BMG after laser cutting using different wavelengths and powers [176]. Amorphous and crystalline phases were identified, with the amorphous phase retained at low laser power and high scan speed, while crystallization occurred at high power and low scan speed. Shorter laser wavelengths promoted crystallization, with  $355 \text{ nm}$  demonstrating higher energy absorption and cutting capability than  $1064 \text{ nm}$ .

It should be noted that the surface quality in laser-machined BMG microstructures, as depicted in Fig. 11a and b, often falls short of expectations. The local melting of BMGs during laser micromachining leads to the formation of craters and significant surface roughness. Additionally, re-solidification and material deposition from the generated craters create ridges and cross around the machined surface, along with the spray-out of BMG particles [174,176]. These challenges can be attributed to the coupling effect between BMGs' inherently low melt temperatures and their relatively small thermal conductivity, favoring confined volumetric heating [181]. As a result, the achievement of satisfactory surface quality in laser-machined BMGs remains a critical area of research and improvement.

In addition to fabricating microstructures, laser micromachining can be utilized as a technique for surface finishing of as-cast BMGs. Li et al. [182] employed femtosecond laser double-pulse ablation for surface smoothing of a Zr-based MG. The critical point for the

smoothing effect was a double-pulse energy ratio of approximately 40 %, achieving minimal ablation efficiency. This method resulted in smooth surfaces with roughness reduced to nearly 100 nm, without laser-induced periodic surface structures. The smoothing effect was attributed to molten material flow, driven by surface tension and gravity, flattening surface undulations.

In a recent study, Zhang et al. [178] introduced an innovative method for the precise cutting of  $\text{Fe}_{78}\text{Si}_9\text{B}_{13}$  (at.%) amorphous ribbons to create electromagnetic cores for electric motor applications. Using two types of lasers, namely the picosecond pulse UV (PS-UV) laser and the continuous-wave IR (CW-IR) laser, the research revealed that the PS-UV laser minimized heat diffusion into adjacent materials, thereby preserving the amorphous nature of the alloy. In contrast, the use of CW-IR led to severe crinkling, cack formation, and crystallization of the  $\alpha$ -Fe phase at the cut-edge produced by the CW-IR laser. The PS-UV laser facilitates fabricating intricate and precise core shapes (Fig. 11d), leading to the creation of stators with elevated stacking coefficients (0.88), which is approximately 1.8 times higher than that achieved with the CW-IR laser. Further, the processing efficiency of the PS-UV laser is impressive. As Fig. 11e shows, a layered amorphous stator core, composed of 200 layers of amorphous ribbons, is crafted in just 198 s, a sharp contrast to the 3600 s required by the wire-EDM technique (Fig. 11e). These stators show reduced iron loss (Fig. 11f), making PS-UV preferable for electric motor applications, with nearly 70 % of the power loss attributed to minimized hysteresis loss ( $P_h$ ) and eddy current loss ( $P_e$ ), as shown in the inset of Fig. 11f.

Laser cutting and patterning also allows for the fabrication of functionally structured MG components. In an interesting study, Li et al. [179] designed and manufactured 3D biomimetic metallic buckling structures with shape-changing abilities using ns-pulsed laser patterning of  $\text{Fe}_{78}\text{Si}_9\text{B}_{13}$  MG and writing an array of laser-crystallized lines in MG ribbons (Fig. 11g). The 2D leaf-like geometry was transformed into 3D buckling structures, enabling controllable shape changes with a magnet bar (Fig. 11h). The key mechanisms underlying buckling involve size mismatch and elastic deformability of composite materials, resulting in distortion energy and internal stress (Fig. 11i).

Laser can also be utilized as an assistive tool in the process known as laser-assisted micro-cutting. This hybrid approach combines the cutting action of traditional mechanical tools, such as micro-milling tools, with the assistance of a laser. The laser is directed at the cutting zone to locally heat the material, reducing its strength and facilitating the removal of material by the mechanical tool. By implementing a low power laser, reduced cutting forces and improved surface finish were achieved during micro-cutting of Zr-based [183] and amorphous Ni-P alloy [184]. In addition, Qui et al. [180] found that laser-assisted micro-cutting at suitable temperatures (near  $T_g$ ) significantly reduces the accumulation of elastic potential energy and the deformation zone, effectively suppressing the generation of in-plane chipping and edge chipping. Fig. 11j displays the micropyramid morphologies achieved through conventional micro-cutting and laser-assisted micro-cutting of Ni-P amorphous alloy at different laser powers. In conventional approach and also laser-assisted approach when the laser power is 1.2 W, chipping exceeding 1  $\mu\text{m}$  is observed at the exit edge. Further, burrs appear in almost every tool exit of conventionally micro-grooved surface, though they decrease when using laser-assisted micro-cutting. As

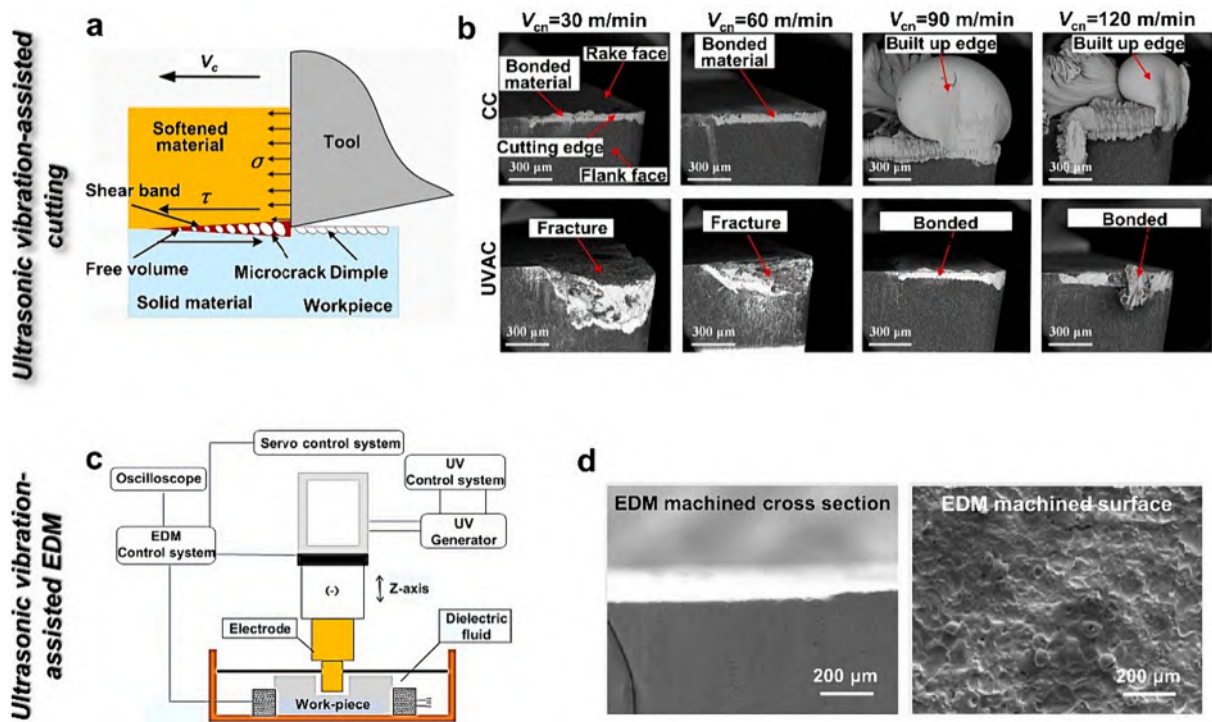


Fig. 12. Different complex joining types under liquids. (a) Schematic diagram of ultrasonic vibration-assisted cutting (UVAC). (b) Comparison of the SEM morphology of tools between UVAC and conventional cutting (CC). Adapted from [189]. (c) Schematic diagram of ultrasonic vibration-assisted EDM (UV-assisted EDM). (d) SEM image of the UV-assisted EDM machined surface and its cross section. Adapted from [190].

higher powers are applied during laser-assisted micro-cutting, chipping nearly disappears from the microgroove surface. However, at power of 3.4 W, thermal distortion results in reduced sharpness of edges and vertices in the microarray.

#### 4.2.4. Ultrasonic-vibration-assisted machining (UVAM)

Ultrasonic vibration-assisted machining (UVAM) is a non-traditional processing technology that uses a transducer (made by piezoelectric ceramics) to convert high-frequency electrical energy into high-frequency mechanical vibration energy, and then achieve material removal through mechanical effects and cavitation. In the 1960 s, UVAM was adopted as a completely new processing method, extending into the 1980 s and 1990 s with improved materials and methods [185,186]. In recent years, advances in technologies such as ultrasonic generators, ultrasonic transducers, and ultrasonic booster have caused the rapid development of UVAM. With this trend, multiple novel designs and concepts for UVAM have emerged [186]. Compared to conventional machining (CM), the material removal mechanism of UVAM is fundamentally changed. Conventional machining processes (turning, milling, grinding, etc.) exist with various drawbacks such as excessive cutting forces, high cutting temperatures, severe tool wear, and poor surface quality [186–188], especially for the machining of advanced materials (e.g., titanium alloys, carbon fiber materials, ceramics, semiconductor materials, etc.). The development of UVAM has overcome such issues, improving the accuracy and efficiency of machining workpiece materials [186]. However, although UVAM can be applied to an extensive range of materials, UVAM technologies that can be used to machining MGs is extremely rare due to MG's characteristics such as high strength, high hardness, and easy crystallization at high temperatures [52].

Chen et al. [189] reported that ultrasonic vibration-assisted cutting (UVAC) is an effective technique to improve the cutting performance of BMGs. The motion of the UVAC tool consists of cyclic vibration and nominal cutting motion, as shown in Fig. 12a. In the cutting cycle, the tool starts to move at  $t_1$ , reaches the maximum speed at  $t_2$ , cuts into the workpiece at  $t_3$ , starts to move away from the chip after reaching the maximum cutting distance at the  $t_4$ , and ends the cutting cycle at  $t_5$ ; then, the next cutting cycle starts. In conventional cutting, the BMG surface roughness increases with cutting speed and leads to the appearance of built-up edge due to the softening or even melting of the BMG, which caused by the temperature rise (Fig. 12b). In contrast, UVAC causes tool breakage at slower cutting speeds, yet inhibits built-up edge formation at higher cutting speeds (Fig. 12b). Therefore, UVAC has lower surface roughness than conventional cutting, with a maximum difference of 36.7 %. In addition, due to the room temperature non-uniform deformation of BMG, the faster the cutting speed leads to the higher strain rate and cutting temperature as a result. Excessive temperature softens the material will cause a shear band layer formed at the solid–liquid interface. As the tool cuts in, dimples form on the newly generated surface within the shear band thus affecting the quality of the conventional cutting. Therefore, the temperature can be reduced by optimizing the cutting parameters (nominal cutting speed, ultrasonic amplitude, etc.) during UVAC, which further improve the surface quality of machined BMG.

Ultrasonic vibration-assisted EDM (UV-assisted EDM) has also been reported to be used for the drilling of Fe-based MG. Compared to conventional machining, the performance of EDM not only not affected by the mechanical properties of the material (e.g., hardness, strength, and stiffness), but also easy to operate, efficient, and cost effective [191]. However, EDM also presents numerous troubles: poor surface roughness, porosity and microcrack formation [192,193]. The most fatal is the difficulty to remove electrode and discharge debris, which will significantly affect the machining accuracy. Tsui et al. introduced two assisted techniques into EDM [190]: ultrasonic vibration and adding conductive powder, the schematic is shown in Fig. 12c. The introduce of UV can causes stirring effect and cloud cavitation effect, which will beneficial to the cleaning of debris. Meanwhile, the addition of conductive Al powder in the dielectric fluid can disperse the discharge energy to avoid the crystallization. Under the influence of these two assisted techniques, the surface quality after machining was improved compared to conventional EDM. The morphology of the UV-assisted EDM machined hole surface and cross-section is shown in Fig. 12d.

#### 4.2.5. Other non-traditional methods

Some other non-traditional methods have been also developed for subtractive manufacturing of MGs. Abrasive water jet (AWJ) has been used to polish and machine Zr-based BMGs. The process involves mixing water with abrasive materials (usually garnet granules of 1–2  $\mu\text{m}$  diameter) and ejecting the mixture through a focusing nozzle under high pressure to create a cutting jet. Surface roughness in AWJ polishing is influenced by factors such as abrasive material, concentration, impact angle, standoff distance, pressure, and polishing time. For ( $\text{Zr}_{53}\text{Cu}_{30}\text{Ni}_9\text{Al}_8$ ) $_{99}\text{Si}_1$  Zr-based BMG, optimal parameters include using SiC particles (6.7  $\mu\text{m}$  diameter), 1:5 abrasive concentration, 30° impact angle, 15 mm standoff distance, 2  $\text{kg}/\text{cm}^2$  hydraulic pressure, and 60 min polishing time, resulting in a remarkable 97 % improvement in mean surface roughness (from 0.685  $\mu\text{m}$  to 0.016  $\mu\text{m}$ ) after AWJ polishing [194].

AWJ machining has the potential to rapidly fabricate complex parts without causing destructive damage to the original materials, outperforming other techniques such as milling, laser cutting, and wire-EDM [195]. The XRD studies have shown that after AWJ processing, the machined workpiece retains its original amorphous structure.

Focused Ion Beam (FIB) machining is another approach for micromachining of MGs. FIB enables precise features to be created on the surface of MGs and has been frequently used to fabricate micropillar specimens for micro-compression mechanical testing on MGs [196,197]. By directing a beam of gallium ions at the materials surface, material can be milled away with high beam current, allowing for features ranging from micrometers to nanometers. The drawback is the time required to mill a given area, making it impractical for machining mm-scale areas. Nevertheless, FIB machining can add submicron features to grossly machined tools, providing value. Unlike crystalline metals, BMGs exhibit sharp patterns when machined with FIB at submicron length scales [173,198].

### 4.3. Shear punching

As a common plastic forming technique, shear punching is known for its high production output, high efficiency, and low cost. Its products are utilized in various industries including communication, electronics, aerospace, and biomedical fields [199]. MGs are considered as a new generation of structural materials due to their exceptional physical, chemical, and mechanical properties [200]. However, their limited plastic forming capacity at room temperature hinders their widespread use in industry. When stress exceeds their yield strength, the rapid expansion of shear bands can result in failure [201]. Despite these challenges, efforts have been made to apply shear punching to MGs and some progress has been made in this area.

#### 4.3.1. Traditional shear punching

The traditional shear punching process for MGs can be categorized into two types: soft punching [202–204] and rigid punching [205–209]. Huang et al. [210] studied the rigid punching of  $\text{Ti}_{40}\text{Zr}_{25}\text{Ni}_3\text{Cu}_{12}\text{Be}_{20}$  BMG plate. The typical rigid punching setup, as shown in Fig. 13a, consists of a punch, die, and a sensor (LVDT). The results show that the relative clearance, defined as the ratio of clearance to plate thickness, significantly impacts the fracture surface. And similar to the punching process of crystalline materials, the deformation of MGs can be divided into three stages: contact engagement, penetration, and final fracture (see Fig. 13b). The results in Fig. 13c show a disk with a diameter of 10 mm punched out from the BMG plate. The fractured surface, as shown in Fig. 13d, can be divided into three regions with distinct characteristics along the shear loading direction: (I) deformation band, (II) fracture zone, and (III) burr. With an increase in relative clearance, the fracture surface changes from vein-like to river-like, and more plastic deformation and shear zones are generated at the edges of the hole.

Moreover, soft punching has also proven to be effective. Cui et al. [204] adopted a flexible film as a micro punch and successfully punched gear holes with a thickness of 30  $\mu\text{m}$  under dynamic laser loading (shown in Fig. 13e and f). The results demonstrate that, in comparison with crystalline materials with good plasticity, MGs do not produce significant rollover or burr during punching. As shown in Fig. 13g, the fracture surface produced by soft punching mainly consists of smooth and vein zones. Two fracture modes exist: brittle

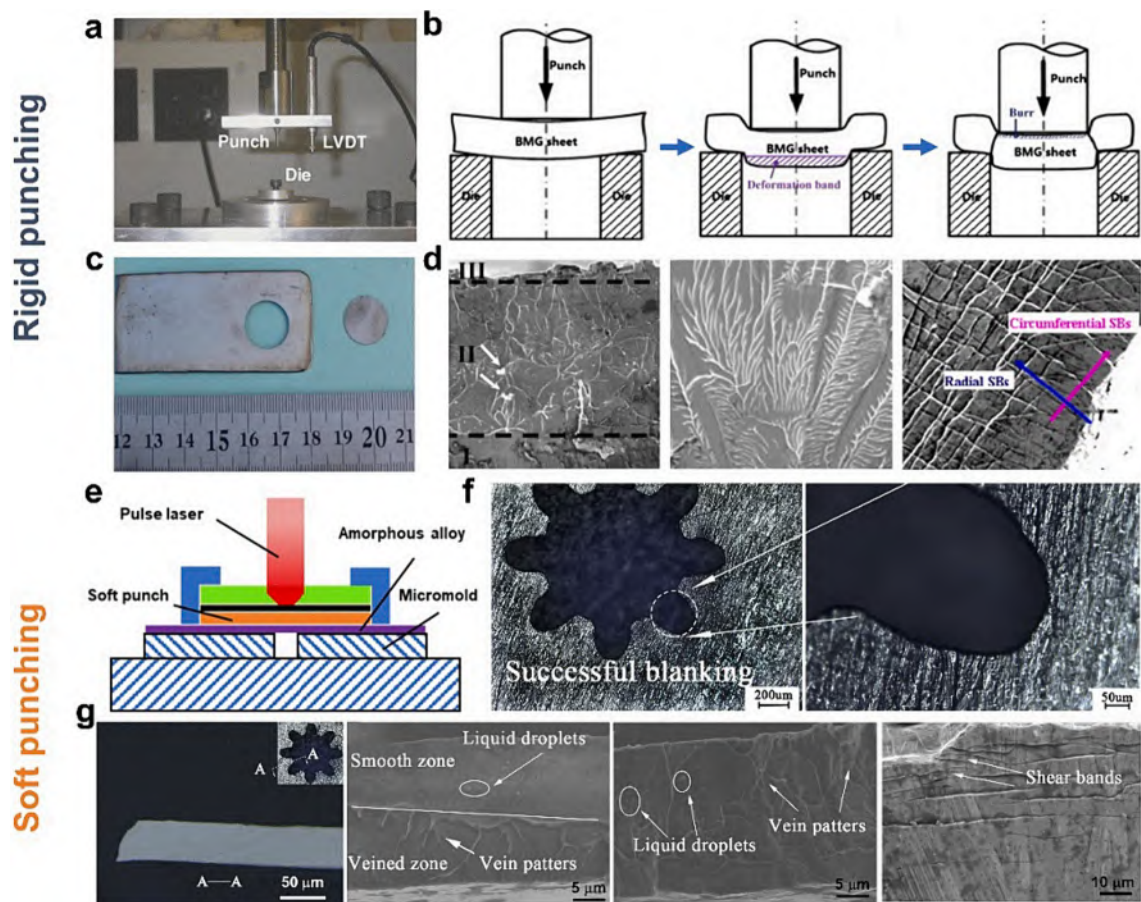


**Fig. 13.** (a) Schematic of a typical rigid punching. (b) Deformation process of BMG punching. (c) A successful punching product for rigid punching. (d) Typical cross-sectional morphology of rigid punching. Adapted from [210] (e) Schematic of a typical soft punching. (f) A successful punching product for soft punching. (g) Typical cross-sectional morphology of soft punching. Adapted from [204].

fracture and plastic fracture. And from the top to the bottom of the workpiece, there is a gradual transition from brittle fracture to plastic fracture. It is worth mentioning that during the fracture process, adiabatic heating occurs within the material and a large number of molten droplets are present on the fracture surface. Furthermore, due to the high-speed, high-pressure, and short time nature of laser loading, the shear bands rapidly extend and interlace with each other in a very short time, resulting in a large number of shear bands appearing at the edge of the workpiece.

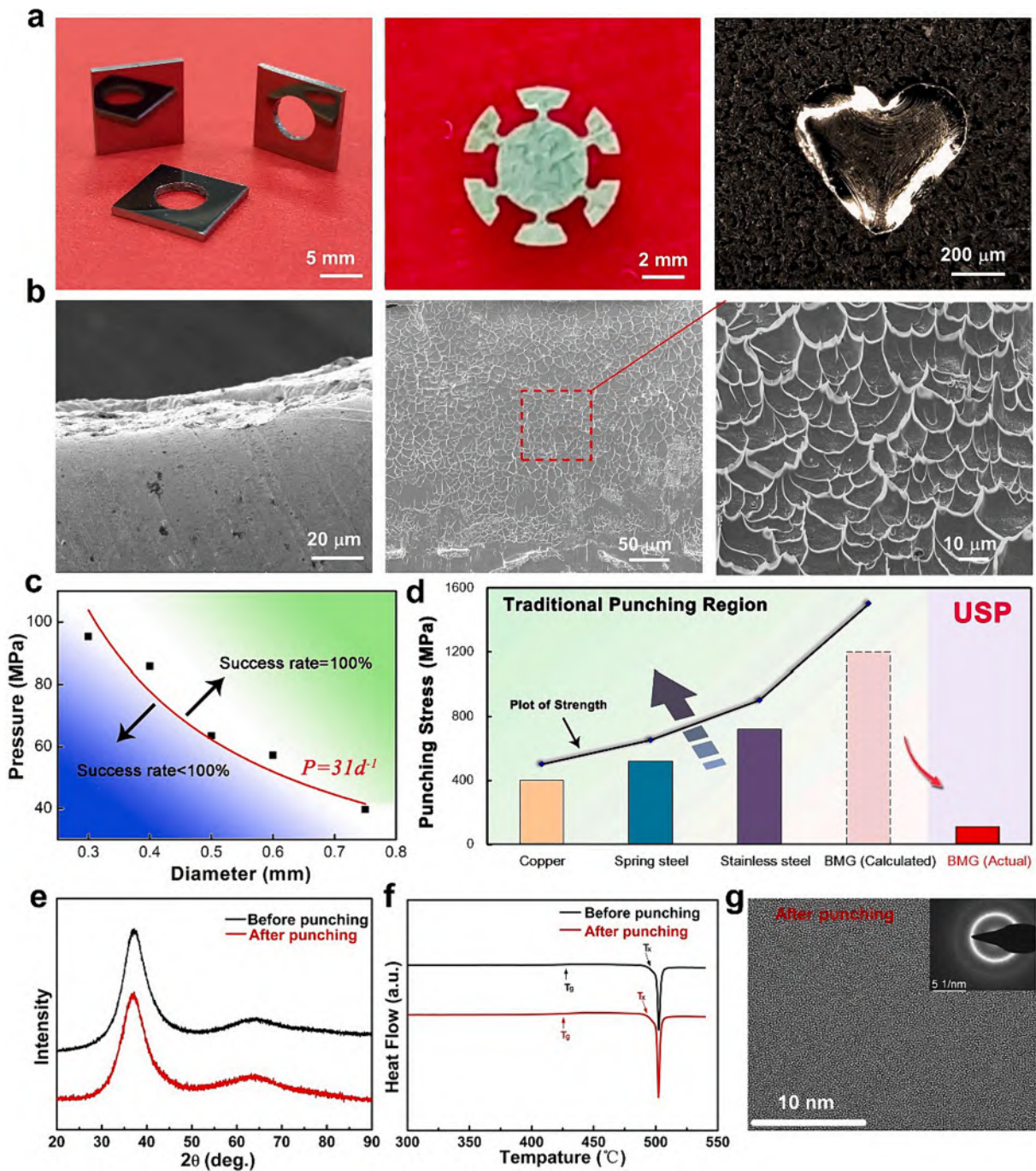


**Fig. 14.** (a) Punching products fabricated by USP (b) SEM morphology of edges and cross-sections. (c) The punching pressure with a success rate of 100% versus hole diameter. (d) Comparison of theoretical punching stress and actual stress of the MG plate during the USP. (e) Comparison of XRD results before and after the USP. (f) Comparison of DSC results before and after the USP. (g) HRTEM micrographs and diffraction patterns of deformed regions. .

Adapted from [211,214,215]

#### 4.3.2. Ultrasonic-vibration-assisted shear punching

The ultra-high strength and brittle nature of MGs make them challenging to work with using traditional shear punching methods. As a result, there is a pressing need for the development of a more efficient and cost-effective punching technology for these materials. Benefiting the ultrasonic-vibration induced plasticity of MGs [211–213] developed by Ma's group at Shenzhen University, China (see Section 5.2), the novel technique of ultrasonic-vibration-assisted shear punching (USP) [214–216], which combines ultrasonic vibration with conventional shear punching, is proved to be advantageous. By using USP, a circular hole with a diameter of 5 mm and some complex shapes were successfully obtained in 50 ms (shown in Fig. 14a). The results of the experiments indicate that the USP technique has improved punching efficiency and reduced costs compared to traditional punching methods. This is due to the unique ultrasonic softening mechanism of MGs that supports the USP process, leading to significant plastic deformation characteristics. As shown in Fig. 14b, the shear band cannot be found in the edge after USP, which is distinctly different from the hole edge produced by the conventional technique. In addition, it can be seen that the dimples with wire-like margin appearance is formed and distributed evenly throughout the section. The wire-like margin appearance means that a Newtonian-flow behavior occurred during the torn apart process of MG. The MG softening induced by ultrasonic vibrations enables the stress required to complete the shear punching to be much lower than with conventional techniques. Therefore, another feature of USP is that the stress required to complete shear punching is much lower than that of conventional methods. For crystalline materials, the pressure required to complete shear punching is expressed by the following equation:

$$P = \frac{4T\sigma}{d} \quad (1)$$

where  $P$ ,  $T$ ,  $\sigma$  and  $d$  are the required punching pressure, workpiece thickness, tensile strength of workpiece material and diameter of die, respectively. For USP, the punching pressure with a success rate of 100 % versus diameter was plotted in Fig. 14c [214]. Using the nonlinear fitting, the data points in Fig. 14c can be fitted by the following power equation:  $P = 31d^{-1}$ . It can be seen that the actual punching pressure is much lower than the calculated values. In another study, Sun et al. [215] designed comparative experiments to further demonstrate the low stress characteristics of USP. As presented in Fig. 14d, the pressure required to complete MG punching (calculated by Eq. (1) is 1200 MPa. However, the actual applied pressure is only 110 MPa, which is less than one tenth of the theoretical calculated pressure, and even lower than the low strength crystalline alloy.

The microstructure and properties of BMG samples were investigated before and after USP [215]. As depicted in Fig. 14e, the XRD spectra of the BMG samples post-USP exhibited consistent amorphous peaks without alteration. The differential scanning calorimetry (DSC) curves in Fig. 14f further substantiate the amorphous nature post-shear punching, with minimal change in the enthalpy of crystallization. High-resolution electron micrographs and diffraction patterns of the deformed regions are presented in Fig. 14g, revealing the persistence of the amorphous structure and a distinct halo ring. This observation suggests that the selected region retains its amorphous nature.

## 5. Formative manufacturing of MG components

Formative manufacturing of MGs is a critical research area, encompassing diverse approaches to shape MG feedstocks into intricate structures through different deformation or consolidation techniques. This section explores various formative techniques and structure and properties of manufactured components, starting with the thermoplastic forming of MGs, including compression molding, blow molding, and more. It then delves into plasticity induced by ultrasonic vibrations and powder consolidation methods, including hot pressing and spark plasma sintering. The section concludes with an examination of MGs as metallic glue, a novel approach for bonding and influencing material properties. Each subsection contributes to a comprehensive understanding of MG component manufacturing through formative techniques.

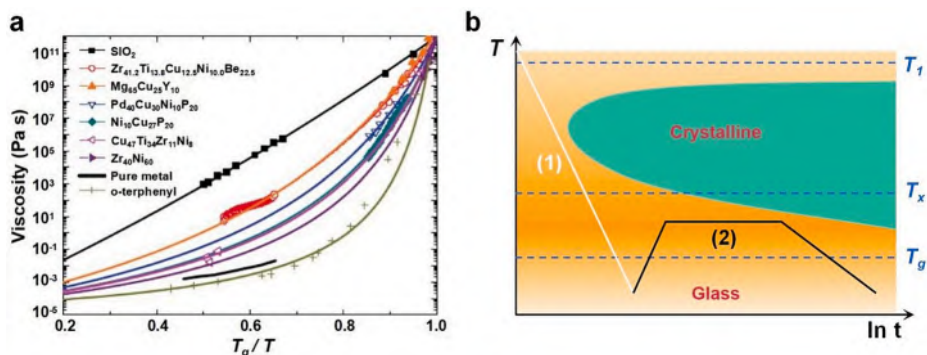


Fig. 15. (a) Variation of the viscosity of different materials with temperature (Adapted from [219]). (b) A typical TTT curve of MGs (Adapted from [23]).

### 5.1. Thermoplastic forming of MGs

The emergence of thermoplastic properties, one of the most distinctive properties of MGs, has greatly expanded MGs processing options [24,217,218]. The thermoplastic properties of MGs, as opposed to the other excellent properties of MGs at room temperature, refer to the fact that as the overall temperature of the MGs increases when heated, it will gradually soften in a certain temperature range, which is often referred to as the SLR.  $T_g$  and  $T_x$  are temperatures where the SLR begins and ends.

The majority of thermoplastic materials, including polymers and MGs, clearly depend on temperature and viscosity when being heated [219,220]. In contrast,  $\text{SiO}_2$  obeys the Arrhenius law, which states that temperature and viscosity have a linear relationship. Most polymers and MGs exhibit anti-Arrhenius law behavior [24,221]. For MG systems, as the temperature rises, the viscosity of MGs gradually decreases in the SLR. This behavior can be quantified by the VFT equation.

$$\eta = \eta_0 \times \exp[D^* \times T_0 / (T - T_0)] \quad (2)$$

where  $\eta_0$  is the viscosity at infinite temperature,  $\eta$  is the viscosity,  $D^*$  a measure of the kinetic fragility of the liquid,  $T_0$  is a temperature, at which the flow barriers would reach infinite [219].

The considerable decrease in viscosity of MGs brought on by the temperature increase would drastically shorten the time required to process MGs (Fig. 15a) [23,47,219]. Additionally, MGs can be processed to the micron [222–224], nano [225–227], or even atomic-level structures [228–230] with higher dimensional accuracy than other metallic materials since they lack grain and grain boundaries. Due to these benefits, thermoplastic forming (TPF) is among the most effective processes for processing MGs.

However, maintaining the intrinsic amorphous character of the MGs themselves before or after processing, i.e. to avoid crystallization, remains a crucial factor when processing MGs utilizing TPF. When processing MGs in the SLR, the temperature–time–transformation (TTT) curves (Fig. 15b) [23,24,231], can be utilized to observe the fluctuation in the connection between processing time and temperature and its crystallization. When the cooling rate is too low during the manufacturing of MG, curve (1) crosses the crystalline region, and the manufactured MGs will crystallize. The processing time will have the most impact on the crystallization behavior of the glass in the SLR when processing the manufactured MGs by TPF. In contrast to the rigorous cooling rate necessary for casting, the final cooling rate will not directly impact the internal atomic disorder.

#### 5.1.1. Thermoplastic formability of MGs

More than 1000 compositions of MGs, including Fe [232,233], Zr [234,235], Pt [236,237], Ce [238,239], Mg-based [240,241], and many others, have been discovered. The thermoplastic formability (TPFA) of various MG systems varies significantly, and the development of a set of parameters to estimate TPFA will impact the prospects for using these MGs in this performance. One of the most straightforward methods to estimate TPFA is to calculate the width of the SLR [233,242]. Although it is widely acknowledged that a broad SLR allows MGs to be operated for longer periods and also increases the filling time for MGs by TPF, this indicator is not absolute.  $\text{Zr}_{44}\text{Ti}_{11}\text{Cu}_{10}\text{Ni}_{10}\text{Be}_{25}$ , for example, has a larger SLR than  $\text{Au}_{49}\text{Ag}_{5.5}\text{Pd}_{2.3}\text{Cu}_{26.9}\text{Si}_{16.3}$ , but its TPFA is inferior [243].  $S = (T_x - T_g) / (T_l - T_g)$  is a broader model, where  $T_l$  denotes the liquidus temperature. The model has been normalized and can be used to compare the TPFA of different MG systems as well as to describe the differences between the TPFA of the same MG system [231].

Aside from the above-mentioned qualitative comparison of the TPFA, it can also be visually characterized. The standard for this TPFA was proposed by Schroers (Fig. 16) [243]. Different MG systems were treated into  $0.1 \text{ cm}^3$  blocks and then heated in their SLR at

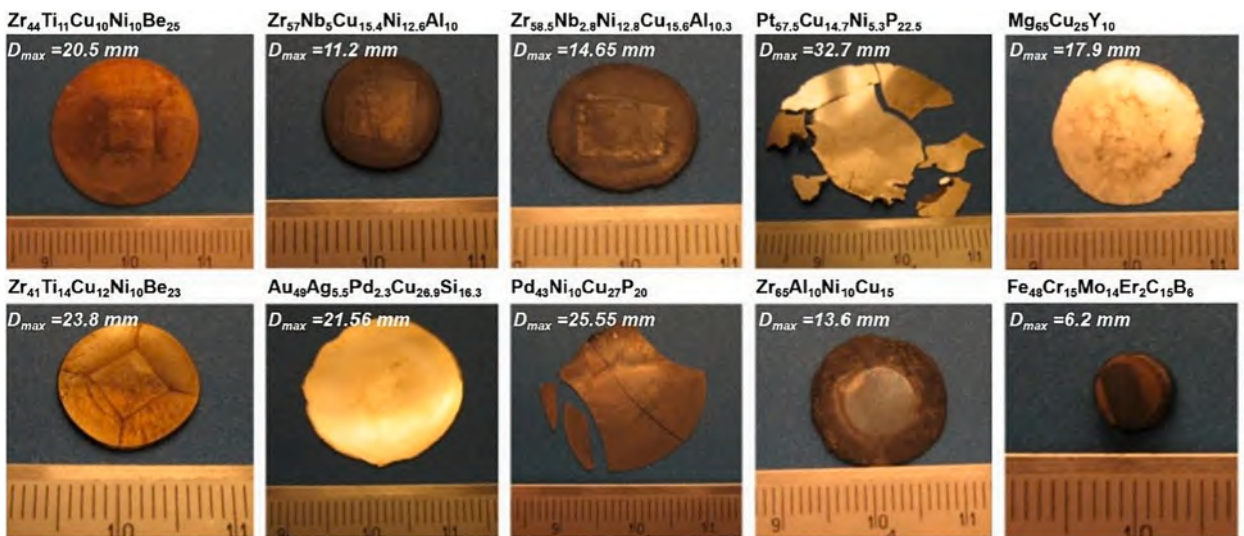


Fig. 16. Physical images of different MGs after TPF under the same conditions. . Adapted from [243]

a constant rate of temperature rise while applying a load of 4500 N to the MGs. After TPF, the final diameter of the flattened MGs was measured. The accuracy of this diameter in describing the TPF was then determined by examining the correlation between the maximum diameter of the spread and the previous TPF parameters.

The above-mentioned spread diameters have proven to be useful in describing the TPF. In other words, the TPF is closely related to the maximum deformation of MGs in the SLR. On this basis Schroers et al. [243] also used equation (2) to quantitatively describe TPF by the maximum strain achievable under isothermal conditions ( $\epsilon_{max}$ ):

$$\epsilon_{max} = \frac{\sigma^* t_{crystallization}}{3\eta} \tag{3}$$

A straightforward solution to the preceding equation yields a  $F_{TPFA}$  for quantitatively describing the TPF.

$$F_{TPFA} = \frac{t_{crystallization}}{3\eta} \tag{4}$$

where  $t_{crystallization}$  indicates the time at which crystallization of the MGs begins to occur in the TTT curve in Fig. 15b,  $\eta$  indicates the viscosity at that temperature point. It is worth noting that the maximum deformation of MGs at a constant temperature point is not absolute and that external conditions such as ultrasonic vibration can increase the TPF in the SLR [244,245].

The assessment of TPF is primarily for the aim of promoting the development of MGs family. This ability currently enables high-throughput searching of BMG components [246]. However, the TPF has broken the dilemma that MGs are difficult to process and difficult to regulate in terms of composition, driving the development of MGs into the field of micro and nano forming and functional applications [26].

In the subsequent section about the TPF of MGs, we will focus on a review of the manufacturing and application of MGs by TPF in the above-mentioned areas in recent years.

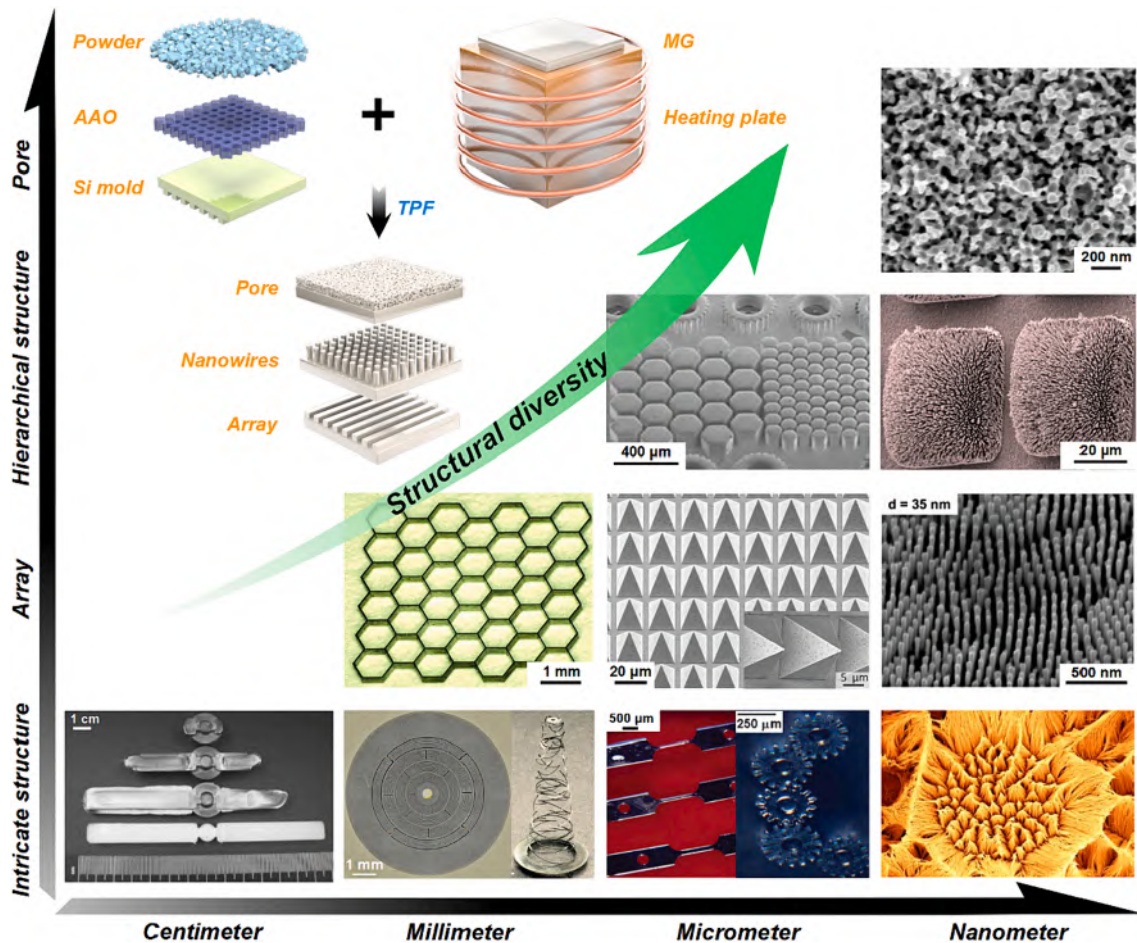


Fig. 17. Some structures of MGs using compression molding by TPF. . Adapted from [225,251–254,257–260]

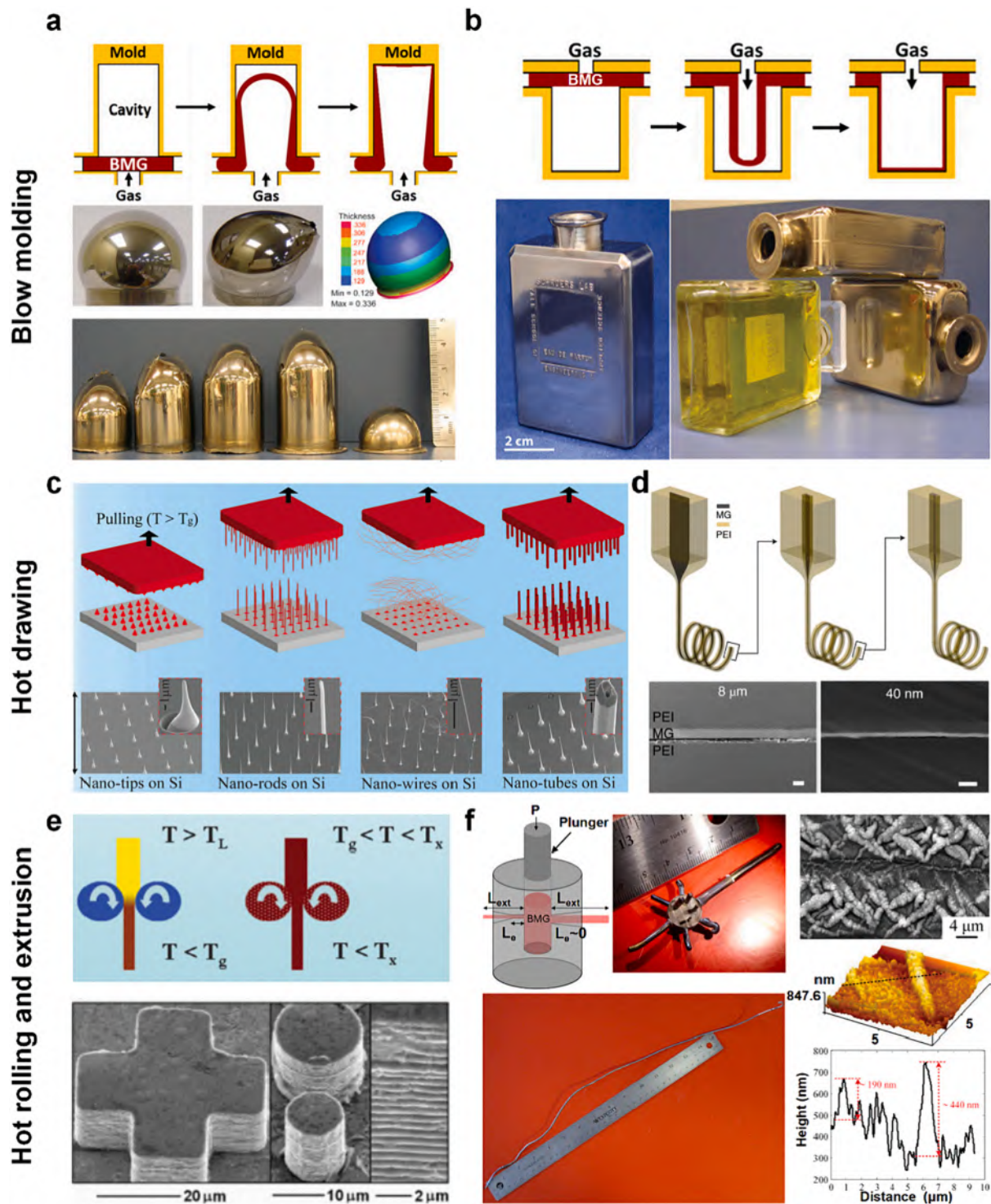


Fig. 18. Other processes developed based on the thermoplastic properties of MGs. (a) Direct blow molding. Adapted from [270]. (b) Blow molding from parison. Adapted from [217]. (c) and (d) Hot drawing. The scale bars in d are 10  $\mu\text{m}$  (left) and 200 nm (right). Adapted from [247,248]. (e) Hot rolling. Adapted from [273]. (f) Hot extrusion. Adapted from [274,275].

### 5.1.2. TPF-based manufacturing methods

**5.1.2.1. Compression molding.** Compression molding [24,225], thermal drawing [247,248], and thermal blow [217,249] are currently well-known techniques based on the thermoplastic characteristics of MGs. Among them, the easiest and most effective technique for processing MGs is compression molding. In a nutshell, the process of compression molding involves applying pressure to the flowing MGs in SLR to press it into the template, then removing the template to receive the corresponding structure [222]. The schematic diagram in the top left corner of Fig. 17 depicts the processing principle of compression molding and highlights some of the common mold materials such as NaCl, AAO and silicon molds. Besides these molds, MGs [225], polymers [250], BaTiO<sub>3</sub> [251], and mica [228] are also used as molds for compression molding. Various kinds of cross-scale and cross-morphological structural patterns have been achieved on MGs by this principle. The lower right corner of Fig. 17 shows some structural designs after compression molding from both dimensions of scale and morphology. Multi-scale structural designs with dimensions ranging from centimeters to millimeters, microns to nanometers have now been achieved. These include injection molding of centimeter-sized MGs by Wiest et al. [252], millimeter-scale 3D MG structures preparation using a mechanically guided manufacturing method accomplished by Wu et al. [253], and microdevices as well as nanowire structures successfully created by Kumar et al. [225]. It is pertinent to note that although the atomic-scale structures created on MG are not represented in this Fig. 17 because there lack specific atomic-scale molds, the atomic-scale replication accuracy of MG has been demonstrated [228–230]. The structural diversity of MGs morphologies is mainly determined by the molds used in compression molding. Regular array structures require simpler molds, and precision CNC milling, photolithography, and anodic oxidation are common means of preparing such molds. Sarac et al. [254] prepared the pyramid structure, grating structure prepared by Ma et al [224], photonic crystals prepared by Liu et al [255], and Li et al prepared the micro-channel [256], etc. are all realized by such molds.

For complicated structures such as hierarchical structures, secondary compression molding, as used by Ma et al. [261] and Hasan et al. [259], offers a route for the production of hierarchical structures. A small feature size template such as AAO with nanopores is used to prepare a feature structure of that size on a MG surface, and the surface with the nanostructure is then compression molded secondarily to create a number of microstructures, thus achieving a hierarchical structure on the MG surface. Apart from secondary compression molding, hierarchical structures can also be prepared through the use of microstructures prepared by this method as precursors and then modifying the structures on the surface [262,263]; however, this method can destroy the intrinsic amorphous properties of MGs. Due to molds for porous structures are challenging to design and prepare using traditional processing methods, foaming [264], pitting [265], and de-alloying methods [266,267], among others, are frequently explored for the preparation of porous MGs. Recently, Ma et al. have ingeniously used some water-soluble salt particles as templates for compression molding [268,269], and successfully prepared porous structures with regulated pore size on the MGs surface, which provides a new perspective for preparing porous MGs.

Some progress has been made in the multi-dimensional production of MG by compression molding; however, the most important aspect of this method is the use of molds, and the present single molds has severely restricted the application of this manufacturing method. On this basis, breakthroughs in this type of processing can be made in mold design, the development and design of atomic-level mold structures, the introduction of polymorphic molds to reduce the number of process steps, and the optimization of mold materials to improve environmental friendliness when dissolving or removing molds.

**5.1.2.2. Blow molding.** Based on its thermoplastic properties, blow molding is another method for manufacturing MGs. The development of this technology is primarily aimed at producing thin-walled MG devices with complicated forms [270–272]. However, there is a limit to the total strain that can be exhibited while manufacturing MGs utilizing direct blow molding. Zr<sub>44</sub>Ti<sub>11</sub>Cu<sub>10</sub>Ni<sub>10</sub>Be<sub>25</sub> can only attain a total strain of 400 % at a certain temperature, pressure, and material thickness, and when this threshold is surpassed, the generated thin-walled structure ruptures [270]. The total strain is caused by an unequal distribution of stresses during the forming process, which allows the device to break at particular spots during processing, as proven by finite element analysis [217]. On this basis, increasing the thickness of the raw material at vulnerable locations is the simplest way to increase the total strain that can be breached by direct blow molding, and the increase in total strain threshold that can be achieved in this way has been demonstrated; however, this strategy only increases the previous total strain by a factor of 0.5, which is insufficient when molding more complex thin-walled deformed parts [217]. Fig. 18a depicts some classic examples of direct blow molding development. Following this, Schroers et al. [217] employed a method involving controlled temperature gradients and preforming, enabling the fabrication of more intricate thin-walled devices. Preforming techniques can greatly minimize the total strain required for final molding, and temperature gradient management can lessen the influence of temperature on MGs viscosity sensitivity during blow molding. Some of the more complex perfume bottles can be easily forming (Fig. 18b) [23,217].

Recently, a way of introducing stretch blow molding has integrated the two steps of preforming and blow molding into one continuous step. The integrated process allows blow molding of up to 2000 % of the total strain in a much shorter period of time [249]. However, the multi-step process will still cause the risk of crystallization of the MG itself, in addition to the short processing time required for blow molding, and the uniform change in temperature gradient over a short period of time is a major challenge, some rapid heating methods try to tackle this challenge such as infrared heating [276].

**5.1.2.3. Hot drawing.** Compression molding is a method that can only produce microstructures with restricted aspect ratios due to the limitations of the molding pressure, which makes it difficult to produce structures with very high aspect ratios [225,277]. The development of the hot drawing process has improved this to some extent.

Fig. 18c shows the hot drawing process for preparing microstructures with very high aspect ratios, in which one end of the SLR MGs are molded into template and the MGs are then pulled away from the surface of the template at different speeds, with the MGs at the middle end becoming thinner as the distance between the two ends increases, eventually breaking to form microstructures with very high aspect ratios [218,247].

The tensile speed and processing temperature will mainly influence the final shape of the microstructure at both ends. At low strain rates, the no-slip boundary condition prevents the MGs from being completely demolded, thus allowing the MGs in the SLR to undergo both necking and stretching [247].

During the low-speed stage, the MGs in the middle stretching zone will neck and then split into two sharp conical structures, when the MGs are in Newtonian fluid flow. In the medium speed phase, the flow behavior changes from Newtonian to non-Newtonian fluid flow, with the intermediate MGs in the stretching phase resulting in the formation of fibers of relatively uniform diameter with very high aspect ratios. The process temperature influences the flow stresses in the SLR of the MGs, mainly through viscosity, thus delineating the stages through which the MGs undergo hot drawing, which also involves the three stages of necking, stretching and demolding described above [278]. These stages can be clearly delineated by comparing the flow stress of the MGs with the strength of the bond between it and the mold. The following equation describes the relationship between flow stress versus viscosity and strain rate for MGs in the SLR [23]:

$$\sigma_{flow} = 3\eta\dot{\epsilon} \quad (5)$$

where  $\sigma_{flow}$  is flow stress,  $\eta$  is viscosity,  $\dot{\epsilon}$  is strain rate.

It is evident that to obtain microstructures with very high aspect ratios, MGs need to exhibit very low flow stresses in the SLR, which means that higher temperatures or lower stretching speeds are required, and this also carries the risk of crystallization.

A new hot drawing process has recently achieved controllable feature sizes from several microns to several dozen nanometers with aspect ratios greater than 1010. The process consists of wrapping the MGs with a polymer that matches the rheological properties of

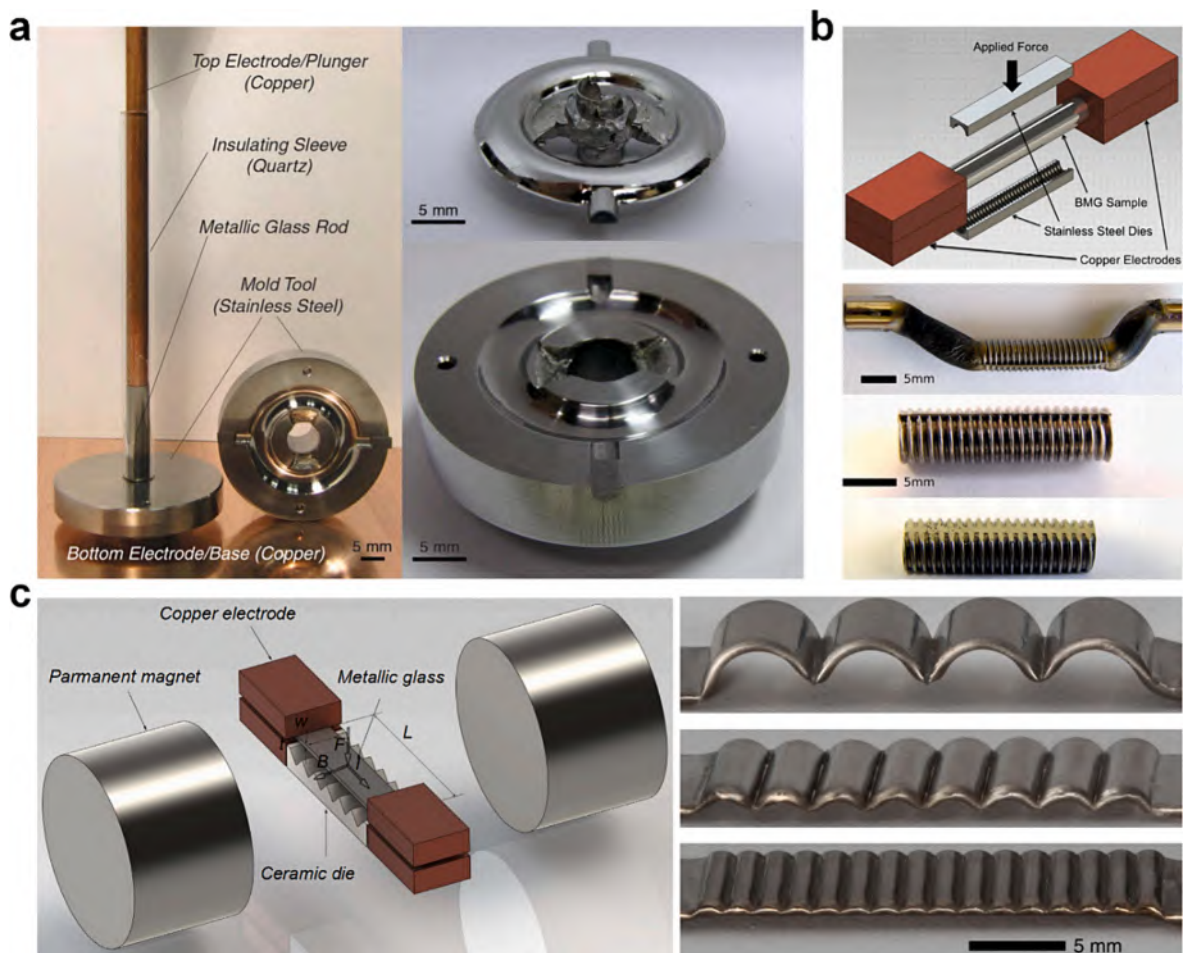


Fig. 19. Advanced forming methods based on thermoplastic properties. (a) and (b) Capacitive discharge heating. Adapted from [282,283]. (c) electromagnetic pulsing. Adapted from [284].

**Table 2**  
Processes developed via TPF properties of MGs.

Process	Composition	Template	$T_{formed}$	Structure	$D_{formed}$	Ref.
Compression molding	La <sub>62</sub> Al <sub>14</sub> Cu <sub>12</sub> Ni <sub>12</sub>	Si dies	155 °C	Patterned	100 μm	[286]
Compression molding	Pd <sub>40</sub> Cu <sub>30</sub> P <sub>20</sub> Ni <sub>10</sub>	Si dies	347 °C	Grating	2.1 μm	[224]
Compression molding	Pd <sub>40</sub> Cu <sub>30</sub> P <sub>20</sub> Ni <sub>10</sub>	Si dies	347 °C	Hole, Grating	~3 μm	[287]
Compression molding	Pd <sub>40</sub> Cu <sub>30</sub> P <sub>20</sub> Ni <sub>10</sub>	AAO	347 °C	Micro-nano hierarchical shell	80 nm	[261]
Compression molding	Pd <sub>40</sub> Cu <sub>30</sub> P <sub>20</sub> Ni <sub>10</sub>	AAO		Nanowires	300 nm	[17]
Compression molding	La <sub>55</sub> Al <sub>25</sub> Ni <sub>5</sub> Cu <sub>10</sub> Co <sub>5</sub>	AAO	200–205 °C	Nanowires	170 nm	[277]
Compression molding	Pt <sub>57.5</sub> Cu <sub>14.7</sub> Ni <sub>5.3</sub> P <sub>22.5</sub>	NaCl	267 °C	Hierarchical porous, Patterned	~3 μm	[268]
Compression molding	Mg <sub>65</sub> Cu <sub>25</sub> Y <sub>10</sub>	AAO	200 °C	Nanowires	169 nm	[288]
Compression molding	Zr <sub>35</sub> Ti <sub>30</sub> Cu <sub>8.25</sub> Be <sub>26.75</sub>	Zn Si die	370 °C	Patterned	/	[235]
Blow molding	Zr <sub>44</sub> Ti <sub>11</sub> Cu <sub>10</sub> Ni <sub>10</sub> Be <sub>25</sub>		450–477 °C	Hemispherical shell	~400 μm	[272]
Blow molding	Zr <sub>62</sub> Cu <sub>17</sub> Ni <sub>13</sub> Al <sub>8</sub>		520 °C	Part	/	[276]
Compression molding	(Co <sub>0.5</sub> Fe <sub>0.5</sub> ) <sub>62</sub> Nb <sub>6</sub> Dy <sub>2</sub> B <sub>30</sub>	dime coin	680 °C	Patterned	/	[289]
Compression molding	Zr <sub>55</sub> Cu <sub>30</sub> Ni <sub>5</sub> Al <sub>10</sub>	AAO Si dies	450 °C	Patterned, Grating	300 nm	[290]
Compression molding	Zr <sub>35</sub> Ti <sub>30</sub> Cu <sub>8.25</sub> Be <sub>26.75</sub>	Carbide balls	350 °C	Patterned	867.2 μm	[291]
Compression molding	Au <sub>49</sub> Ag <sub>5.5</sub> Pd <sub>2.3</sub> Cu <sub>26.9</sub> Si <sub>16.3</sub>	Ni dies	160 °C	Patterned		[225]
Compression molding	Pt <sub>57.5</sub> Cu <sub>14.7</sub> Ni <sub>5.3</sub> P <sub>22.5</sub>	AAO Si dies Ni dies	270 °C	Patterned, Nanowires	53 nm	[225]
Compression molding	Pd <sub>43</sub> Ni <sub>10</sub> Cu <sub>27</sub> P <sub>20</sub>	AAO		Nanowires	20 nm	[292]
Compression molding	Pt <sub>57.5</sub> Cu <sub>14.7</sub> Ni <sub>5.3</sub> P <sub>22.5</sub>	AAO Si pillars	270 °C	Patterned, Nanowires	250 nm	[293]
Compression molding	Pt <sub>48.75</sub> Pc <sub>9.75</sub> Cu <sub>19.5</sub> P <sub>22</sub>	Si dies	277 °C	Patterned	0.1 μm	[237]
Compression molding	(Zr <sub>0.507</sub> Cu <sub>0.28</sub> Ni <sub>0.9</sub> Al <sub>0.123</sub> ) <sub>98.5</sub> Y <sub>1.5</sub> (ZrY <sub>1.5</sub> )	AAO		Nanowires	300 nm	[294]
Compression molding	Ti <sub>41</sub> Zr <sub>25</sub> Be <sub>28</sub> Fe <sub>6</sub>	AAO	415 °C	Nanowires	400 nm	[295]
Compression molding	Pt <sub>57.5</sub> Cu <sub>14.7</sub> Ni <sub>5.3</sub> P <sub>22.5</sub>	Si dies	250 °C	Nanowires	300 nm	[296]
Compression molding	(Zr <sub>65</sub> Cu <sub>17.5</sub> Ni <sub>10</sub> Al <sub>7.5</sub> ) <sub>98</sub> Er <sub>2</sub>			Gear wheel		[297]
Compression molding with vibration	Ti <sub>16.7</sub> Zr <sub>16.7</sub> Hf <sub>16.7</sub> Cu <sub>16.7</sub> Ni <sub>16.7</sub> Be <sub>16.7</sub>	Si dies	450 °C	Patterned	~100 μm	[298]
Compression molding	Pt <sub>57.5</sub> Cu <sub>14.7</sub> Ni <sub>5.3</sub> P <sub>22.5</sub>			Patterned, Nanowires	~200 nm	[259]
Compression molding	Pd <sub>40</sub> Ni <sub>40</sub> Si <sub>4</sub> P <sub>16</sub>	AAO	370 °C	Patterned, Nanowires	100 nm	[260]
Compression molding	Pd <sub>40.5</sub> Ni <sub>40.5</sub> Si <sub>4.5</sub> P <sub>14.5</sub>	AAO	350 °C	Nanowires	200 nm	[299]
Compression molding	Ti <sub>45</sub> Zr <sub>20</sub> Be <sub>30</sub> Fe <sub>5</sub>	AAO	421 °C	Nanowires	400 nm	[300]
Compression molding	Pt <sub>57.5</sub> Cu <sub>14.7</sub> Ni <sub>5.3</sub> P <sub>22.5</sub>	AAO		Nanowires	100 nm	[301,302]
Compression molding	Pd <sub>42.5</sub> Ni <sub>7.5</sub> Cu <sub>30</sub> P <sub>20</sub>	Si dies	330 °C	Grating	8 μm	[303]
Compression molding	Pd <sub>40.5</sub> Ni <sub>40.5</sub> Si <sub>4.5</sub> P <sub>14.5</sub>	Si dies	370 °C	Patterned	311 nm	[255]
Compression molding	Zr <sub>41.2</sub> Ti <sub>13.8</sub> Cu <sub>12.5</sub> Ni <sub>10</sub> Be <sub>22.5</sub>			Patterned	~100 μm	[304]
Compression molding	Ce <sub>65</sub> Al <sub>10</sub> Cu <sub>20</sub> Co <sub>5</sub>	Si dies	110–130 °C	Patterned	9 μm	[262]
Compression molding	Au <sub>49</sub> Ag <sub>5.5</sub> Pd <sub>2.3</sub> Cu <sub>26.9</sub> Si <sub>16.3</sub>	Si dies	157 °C	Patterned	156 nm	[305]
Compression molding	Pd <sub>43</sub> Ni <sub>10</sub> Cu <sub>27</sub> P <sub>20</sub>	AAO		Nanowires		[306]
Compression molding	Pt <sub>57.5</sub> Cu <sub>14.7</sub> Ni <sub>5.3</sub> P <sub>22.5</sub>	AAO		Nanowires	~200 nm	[307]
Compression molding	Pt <sub>57.5</sub> Cu <sub>14.7</sub> Ni <sub>5.3</sub> P <sub>22.5</sub>	AAO		Nanowires	200 nm	[308]
Compression molding	Pt <sub>57.5</sub> Cu <sub>14.7</sub> Ni <sub>5.3</sub> P <sub>22.5</sub>	AAO	242 °C	Nanowires	200 nm	[227]
Micro injection molding	Zr <sub>47</sub> Cu <sub>45</sub> Al <sub>8</sub>			Patterned	1.91 μm	[309]
Compression molding	Pd <sub>40</sub> Cu <sub>30</sub> Ni <sub>10</sub> P <sub>20</sub>	Si dies	330 °C	Patterned	35.5 μm	[310]
Compression molding	Zr <sub>35</sub> Ti <sub>30</sub> Cu <sub>8.25</sub> Be <sub>26.75</sub>			Patterned	35.5 μm	[311]
Compression molding	Pd <sub>40</sub> Ni <sub>40</sub> P <sub>20</sub>	Si dies AAO	352 °C	Patterned	~10 μm	[312]
Compression molding	Pd <sub>40.5</sub> Ni <sub>40.5</sub> P <sub>19</sub>	AAO	360, 370 °C	Nanowires	50.5 nm	[226]
Compression molding	Mg <sub>65</sub> Cu <sub>25</sub> Y <sub>10</sub>	AAO	175 °C	Nanowires	200 nm	[313]
Compression molding	Zr <sub>35</sub> Ti <sub>30</sub> Cu <sub>8.25</sub> Be <sub>26.75</sub>	AAO	435 °C	Nanowires	200 nm	[313]
Compression molding	Zr <sub>44</sub> Ti <sub>11</sub> Cu <sub>10</sub> Ni <sub>10</sub> Be <sub>25</sub>	AAO	435 °C	Nanowires	200 nm	[313]

(continued on next page)

Table 2 (continued)

Process	Composition	Template	$T_{formed}$	Structure	$D_{formed}$	Ref.
Compression molding	Pt <sub>57.5</sub> Cu <sub>14.7</sub> Ni <sub>5.3</sub> P <sub>22.5</sub>	AAO	260 °C	Nanowires	35 nm	[314]
Hot-pulling	Pt <sub>57.5</sub> Cu <sub>14.7</sub> Ni <sub>5.3</sub> P <sub>22.5</sub>	AAO	270 °C	Nanowires	50 nm	[315]
Compression molding	Pt <sub>57.5</sub> Cu <sub>14.7</sub> Ni <sub>5.3</sub> P <sub>22.5</sub>	AAO		Nanowires	55 nm	[316]
Compression molding	Pt <sub>57.5</sub> Cu <sub>14.7</sub> Ni <sub>5.3</sub> P <sub>22.5</sub>	AAO	267 °C	Nanowires	55 nm	[317]
Compression molding	Pt <sub>57.5</sub> Cu <sub>14.7</sub> Ni <sub>5.3</sub> P <sub>22.5</sub>	AAO		Nanowires	13 nm	[257]
Blow molding	Zr <sub>44</sub> Ti <sub>11</sub> Cu <sub>10</sub> Ni <sub>10</sub> Be <sub>25</sub>		460 °C	Spherical shell		[217]
Compression molding	Pd <sub>40</sub> Ni <sub>10</sub> Cu <sub>30</sub> P <sub>20</sub>		320 °C			[318]
Hot drawing	Pt <sub>57.5</sub> Cu <sub>14.7</sub> Ni <sub>5.3</sub> P <sub>22.5</sub>	Al Si dies Steel Quartz	265 °C	Nanowires	~300 nm	[247]
Hot drawing	Pd <sub>43</sub> Cu <sub>27</sub> Ni <sub>10</sub> P <sub>20</sub>	Si dies	360 °C	Nanowires	~300 nm	[247]
Hot drawing	Ni <sub>60</sub> Pd <sub>20</sub> P <sub>17</sub> B <sub>3</sub>	Si dies	380 °C	Nanowires	~300 nm	[247]
Hot drawing	Zr <sub>35</sub> Ti <sub>30</sub> Cu <sub>8.25</sub> Be <sub>26.75</sub>	Si dies	395 °C	Nanowires	~300 nm	[247]
Hot drawing	Pt <sub>57.5</sub> Cu <sub>14.7</sub> Ni <sub>5.3</sub> P <sub>22.5</sub>	Si dies	260 °C	Nanowires	~150 nm	[278]
Compression molding	Pd <sub>40</sub> Ni <sub>40</sub> P <sub>20</sub>	Si dies	370 °C	Patterned	90 nm	[319]
Compression molding	Au <sub>49</sub> Ag <sub>5.5</sub> Pd <sub>2.3</sub> Cu <sub>26.9</sub> Si <sub>16.3</sub>	Pd BMG	157 °C	Patterned	213.9 nm	[319]
Compression molding	Pt <sub>57.5</sub> Cu <sub>14.7</sub> Ni <sub>5.3</sub> P <sub>22.5</sub>	AAO Si dies	260 °C	Nanowires, Patterned	25 µm	[320]
Compression molding	Zr <sub>58.5</sub> Cu <sub>15.6</sub> Ni <sub>12.8</sub> Al <sub>10.3</sub> Nb <sub>2.8</sub>	WC-Co	450–496 °C	Patterned	60 µm	[321]
Compression molding	Zr <sub>48</sub> Cu <sub>36</sub> Al <sub>8</sub> Ag <sub>8</sub>	Si dies	475 °C	Patterned	16.5 µm	[322]
Compression molding	Ti <sub>40</sub> Zr <sub>10</sub> Cu <sub>34</sub> Pd <sub>14</sub> Ga <sub>2</sub>	Si dies	420 °C	Patterned	16.5 µm	[322]
Compression molding	Pd <sub>40</sub> Cu <sub>30</sub> Ni <sub>10</sub> P <sub>20</sub>	Si dies	347 °C	Patterned	20 µm	[323]
Compression molding	Mg <sub>68</sub> Cu <sub>22</sub> Y <sub>10</sub>	Si dies	150 °C	Patterned	~500 µm	[246]
Compression molding	Zr <sub>35</sub> Ti <sub>30</sub> Cu <sub>7.5</sub> Be <sub>27.5</sub>	Si dies	277 °C	Patterned	~100 µm	[324]
Compression molding	Zr <sub>47.3</sub> Cu <sub>32</sub> Al <sub>8</sub> Ag <sub>8</sub> Ta <sub>4</sub> Si <sub>0.7</sub>		491 °C	Grating	~0.6 µm	[325]
Compression molding	Ni <sub>60</sub> Pd <sub>20</sub> P <sub>17</sub> B <sub>3</sub>	AAO	390 °C	Patterned, Nanowires	200 nm	[326]
Compression molding	Pt <sub>57.3</sub> Cu <sub>14.6</sub> Ni <sub>5.3</sub> P <sub>22.8</sub>	Si dies	270 °C	Patterned	~25 µm	[327]
Compression molding	Ni <sub>62</sub> Pd <sub>19</sub> Si <sub>2</sub> P <sub>17</sub>	Si dies	360 °C	Patterned	20 µm	[328]
Compression molding	Pt <sub>57.5</sub> Cu <sub>14.7</sub> Ni <sub>5.3</sub> P <sub>22.5</sub>	AAO	270 °C	Nanowires	200 nm	[329]
Electro-aided compression molding	Mg <sub>94.8</sub> Al <sub>3.5</sub> Zn <sub>1.2</sub> Mn <sub>0.5</sub>	Si dies	<200 °C	Patterned, Grating	~2 µm	[330]
Compression molding	Pd <sub>40</sub> Ni <sub>10</sub> Cu <sub>30</sub> P <sub>20</sub>	Si dies	347 °C	Patterned	19.23 µm	[331]
Compression molding	Zr <sub>35</sub> Ti <sub>30</sub> Be <sub>26.75</sub> Cu <sub>8.25</sub>	Si dies	370 °C	Patterned	50 µm	[256]
Compression molding	Zr <sub>65</sub> Cu <sub>17.5</sub> Ni <sub>10</sub> Al <sub>7.5</sub>	Si dies	410 °C	Gear wheel	300 µm	[332]
Compression molding	Zr <sub>35</sub> Ti <sub>30</sub> Cu <sub>7.5</sub> Be <sub>27.5</sub>	Si dies	425 °C	Patterned	10 µm	[258]
Compression molding	Pt <sub>57.5</sub> Cu <sub>14.7</sub> Ni <sub>5.3</sub> P <sub>22.5</sub>	Si dies	275 °C	Patterned	10 µm	[258]
Compression molding	Pt <sub>57.5</sub> Cu <sub>14.7</sub> Ni <sub>5.3</sub> P <sub>22.5</sub>	Si dies	420 °C	Patterned	50 µm	[253]
Compression molding	Zr <sub>35</sub> Ti <sub>30</sub> Cu <sub>7.5</sub> Be <sub>27.5</sub>	Si dies	270 °C	Patterned	50 µm	[253]
Compression molding	Zr <sub>44</sub> Cu <sub>40</sub> Al <sub>8</sub> Ag <sub>8</sub>	Si dies	472 °C	Patterned	50 µm	[333]
Thermal drawing	Pt <sub>57.5</sub> Cu <sub>14.7</sub> Ni <sub>5.3</sub> P <sub>22.5</sub>		270 °C	Nanoribbons	40 nm	[248]
Compression molding	(Fe, Ni, Co, Mo) <sub>75</sub> P <sub>10</sub> C <sub>10</sub> B <sub>5</sub>	Si dies	450 °C	Patterned	150 nm	[334]
Compression molding	Fe <sub>40</sub> Co <sub>35</sub> P <sub>10</sub> C <sub>10</sub> B <sub>5</sub>	Si dies	440 °C	Patterned	~5 µm	[335]
Compression molding	Fe <sub>40</sub> Co <sub>35</sub> P <sub>10</sub> C <sub>10</sub> B <sub>5</sub>	Si dies	440 °C	Patterned	100 nm	[336]
Electromagnetic pulsing	Zr <sub>35</sub> Ti <sub>30</sub> Cu <sub>7.5</sub> Be <sub>27.5</sub>			Semicircular corrugations	~1 mm	[284]
Compression molding	Mg <sub>58</sub> Cu <sub>31</sub> Y <sub>11</sub>	Si dies	150 °C	Patterned	330 µm	[337]
Compression molding	Pt <sub>57.5</sub> Cu <sub>14.7</sub> Ni <sub>5.3</sub> P <sub>22.5</sub>	AAO	<300 °C	Nanowires	54 nm	[338]
Compression molding	Zr <sub>35</sub> Ti <sub>30</sub> Cu <sub>8.5</sub> Be <sub>26.5</sub>	Si dies	370 °C	Patterned	50 µm	[339]
Thermoplastic drawing	Pt <sub>57.5</sub> Cu <sub>14.7</sub> Ni <sub>5.3</sub> P <sub>22.5</sub>		270 °C	Nanowires	~200 µm	[340]
Pulsated orifice ejection method	[(Fe <sub>0.5</sub> Co <sub>0.5</sub> ) <sub>0.75</sub> Si <sub>0.05</sub> B <sub>0.2</sub> ] <sub>96</sub> Nb <sub>4</sub>		563 °C	Gear	~200 µm	[341]
Compression molding	Pt <sub>57.5</sub> Cu <sub>14.7</sub> Ni <sub>5.3</sub> P <sub>22.5</sub>			Atomically smooth surfaces		[228]
Compression molding	Zr <sub>44</sub> Ti <sub>11</sub> Cu <sub>10</sub> Ni <sub>10</sub> Be <sub>25</sub>			Atomically smooth surfaces		[228]

(continued on next page)

Table 2 (continued)

Process	Composition	Template	$T_{formed}$	Structure	$D_{formed}$	Ref.
Compression molding	Pt <sub>57.5</sub> Cu <sub>14.7</sub> Ni <sub>5.3</sub> P <sub>22.5</sub>	Strontium titanate	270 °C	Atomically surfaces	0.37 nm	[229]
Compression molding	Pt <sub>57.5</sub> Cu <sub>14.7</sub> Ni <sub>5.3</sub> P <sub>22.5</sub>	LaAlO <sub>3</sub>	360 °C	Atomically surfaces	0.22 nm	[230]
Compression molding	Pd <sub>40.5</sub> Ni <sub>40.5</sub> P <sub>19</sub>	AAO		Nanowires	55 nm	[342]
Capacitive- discharge forging	Zr <sub>35</sub> Ti <sub>30</sub> Cu <sub>7.5</sub> Be <sub>26.5</sub>			Screw part	~200 µm	[283]
Resistance welding	Zr <sub>35</sub> Ti <sub>30</sub> Cu <sub>7.5</sub> Be <sub>26.5</sub>			Part	165 µm	[285]
Hot rolling	Zr <sub>44</sub> Ti <sub>11</sub> Cu <sub>10</sub> Ni <sub>10</sub> Be <sub>25</sub>	Si		Pattern	300 nm	[273]
Hot extrusion	Zr <sub>44</sub> Ti <sub>11</sub> Cu <sub>10</sub> Ni <sub>10</sub> Be <sub>25</sub>	Tool steel		Filament	~2 mm	[274]
Compression molding	Pd <sub>43</sub> Cu <sub>27</sub> Ni <sub>10</sub> P <sub>20</sub>		447 °C	part		[282]

Temperature for TPF ( $T_{formed}$ ).

Minimum forming size ( $D_{formed}$ ).

the glass and then hot drawing it (Fig. 18d). MGs with complex structures can also be realized in this process by means of different wrapping patterns. However, the structures produced by this process are susceptible to mechanical breakage after a certain limit of size has been breached due to faster crystallization kinetics [248].

**5.1.2.4. Hot rolling and extrusion.** The TPF properties of MGs can also be applied in hot roll and extrusion processes. In terms of hot rolling, this process is mainly used for manufacturing MG sheets. The process can be divided into three categories depending on the temperature during processing. In one category, the MGs are heated above its  $T_x$  for processing, similar to the stripping process (Fig. 18e) [279], in the second category it is rolled mainly in the SLR (Fig. 18e), and in the last category the MGs are cold rolled at room temperature [141,280]. The deformation induced by hot rolling below the  $T_g$  is mainly caused by shear locational strengthening [281], while MGs in the SLR are allowed to undergo hot rolling with greater strain as the temperature increases due to the sharp drop in viscosity [219]. Martinez et al. [273] showed the Zr<sub>44</sub>Ti<sub>11</sub>Cu<sub>10</sub>Ni<sub>10</sub>Be<sub>25</sub> was rolled within the SLR, with strains of up to 1400 % achieved at a strain rate of 70 s<sup>-1</sup>. It is worth mentioning that MGs still show excellent structural reproduction properties during hot rolling and can reproduce features as small as 300 nm.

MG filaments are frequently manufactured by using the hot extrusion method, which is shown in Fig. 18f. This method is merely a variation of the compression molding method used to create individual micro pillars, except that the diameter of the generated size is altered from microns to millimeters. Through a mold with a 2 mm opening diameter, Zr<sub>44</sub>Ti<sub>11</sub>Cu<sub>10</sub>Ni<sub>10</sub>Be<sub>25</sub> with a disc diameter of 11 mm and a height of 15 mm may be manufactured into a 2 mm diameter filament with a diameter ratio of more than 250 [274]. Furthermore, other processes can also induce the hot extrusion process. For example, the strong energy will heat the MG during laser processing, and the thermal stress brought on by thermal expansion will cause the MG to be thermoplastic extrusion. The minimum feature size of the process is close to 6 µm [275].

**5.1.2.5. Advanced forming methods based on thermoplastic properties.** Recently, a variety of forming methods for quickly heating MGs to the SLR have demonstrated certain special benefits. Capacitive discharge heating is a forming technology that heats MGs to the SLR at a rate of 10<sup>6</sup> °C/s, overcoming thermal relaxation during processing and forming in milliseconds [282]. Furthermore, this process not only swiftly heats the metal glass, but also keeps its overall temperature uniform during processing. Fig. 19a depicts a physical diagram of the equipment utilized for method, as well as the mold and MGs after forming. Some 3D parts with duplication and practical uses, such as the MG screw part illustrated in Fig. 19b, may also be manufactured using this technology [283]. It is worth noting that even with a short processing window, this type of processing approach may still accomplish successful processing for different MGs, and the formed MGs does not crystallize.

Electric current and magnetic field electromagnetic coupling may be applied to TPF MGs without the need of a standard heating source or mechanical force. This type of processing method has the same formation duration as the capacitive discharge heating method, which can make MG in milliseconds [284]. Fig. 19c depicts a schematic illustration of this process, in which an electric pulse heats the glass to the SLR while a magnetic field induces a big enough magnetic force to form MGs to the mold shape. This type of processing may manufacture semi-circular wavy MG. Additionally, Ma et al. [285] developed a resistance welding forming process for fast manufacturing of MG in 150 ms, which may be utilized to create macroscopically to microscopically scaled components and structures.

Based on the thermoplastic properties of MG, numerous methods to manufacture different kinds of MG have been developed. Table 2 summarizes the components of MGs, process temperatures, and the manufactured structures employed in these techniques. Although the processing technology created based on the thermoplastic characteristics of MG displays considerable benefits over conventional manufacturing techniques, it is nevertheless necessary to bring out the drawbacks of these procedures at this time. Firstly, these processes still require templates, which results in high costs and expenses during the process. Second, despite the established property of MGs to replicate at the atomic level, the characteristic size of manufactured structure has not made a bigger stride forward. Moreover, to accomplish the necessary structural form and prevent crystallization throughout the manufacturing process, considerable thought must be given to how to optimize these process parameters.

The introduction of the TPF technique has brought a significant shift to the challenges faced by MGs. However, it is crucial to recognize that the intrinsic properties of MGs fabricated through this process undergo alterations [24]. Assessing the impact of this

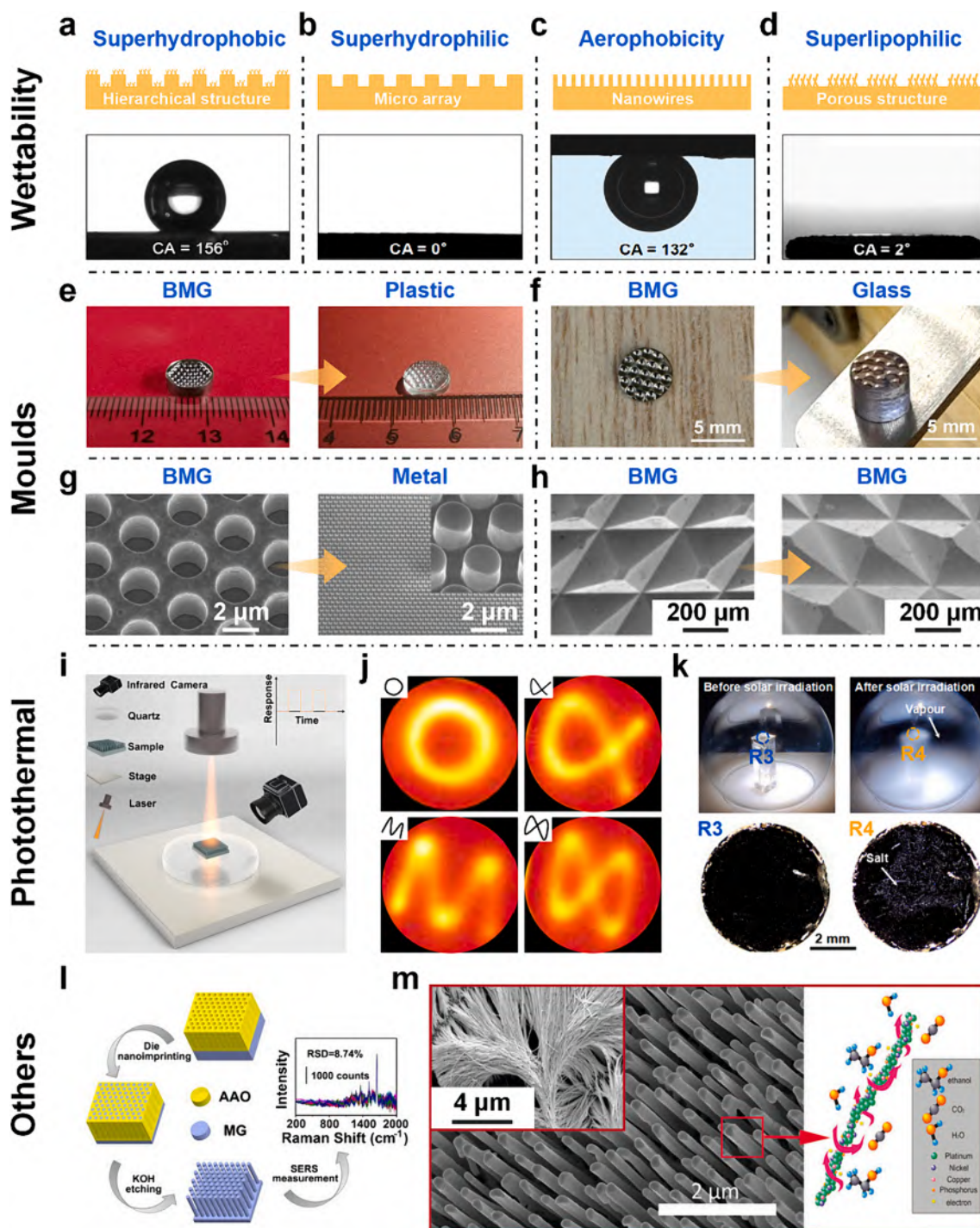


**Fig. 20.** Functional application of MG formed by TPF. (a) Superhydrophobic MG. Adapted from [261]. (b) Superhydrophilic MG. Adapted from [262]. (c) Aerophobic MG. Adapted from [17]. (d) Superlipophilic MG. Adapted from [268]. (e) MG mold for forming plastic. Adapted from [328]. (f) MG mold for forming glass. Adapted from [290]. (g) MG mold for forming metal. Adapted from [296]. (h) MG mold for forming MG. Adapted from [225]. (i) Schematic diagram of MGs used for photothermal properties testing. Adapted from [227]. (j) MG for photothermal imaging. Adapted from [301]. (k) MG for seawater desalination. Adapted from [251]. (l) MG for enhanced surface Raman scattering. Adapted from [352]. (m) MG for catalytic reactions. Adapted from [257].

technique on the mechanical properties of MGs is paramount, given the critical role these properties play in determining the material's suitability for specific applications and its overall service life.

Under appropriate temperature and applied load conditions, MGs produced through TPF can maintain their internal atomic disorder, retaining an amorphous state. However, these disordered atomic structures may undergo structural relaxation, affecting mechanical properties such as bending strength and hardness [321,343,344]. Enthalpy changes serve as a valuable metric for gauging the extent of atomic structure relaxation in MGs both before and after TPF, as highlighted in various studies [211,321]. TPF samples, in comparison to their as-cast counterparts, exhibit lower crystallization enthalpy, indicating an evolution from a disordered to a more ordered state in the internal structure of TPF-based MGs [343]. The enthalpy of relaxation becomes instrumental in evaluating the state of relaxation in the internal atomic structure of MGs post-TPF, while preventing crystallization. Although mechanical properties of TPF-treated samples may experience degradation, various reprocessing techniques have been developed to counteract these effects, including post-elastostatic loading [343], high-pressure torsion [345], and innovative methods like ultrasonic vibration, demonstrated to mitigate changes in the mechanical properties of annealed and cast MGs [211,346,347].

### 5.1.3. The functional applications of TPFed structures

Based on the TPF properties of MGs, several multiscaled structures have been manufactured. These structures enable MGs to be employed in a greater range of applications, including wettability [261,262], manufacturing [225,328], photothermal [227,302,348], and electrocatalytic [257,349] fields.

MGs typically have a lower surface free energy than conventional metallic materials resulting in wettability that is hydrophobic at room temperature [310], however, some oxidation-prone MG systems, such as  $\text{La}_{55}\text{Al}_{25}\text{Ni}_5\text{Cu}_{10}\text{Co}_5$  [277] and  $\text{Ce}_{65}\text{Al}_{10}\text{Cu}_{20}\text{Co}_5$  [262], often exhibit hydrophilic properties due to the formation of metallic oxides on their surfaces. Despite the fact that MG wettability can be regulated by selecting different MG systems for hydrophilic and hydrophobic properties, the wettability of this structureless surface is still far from superhydrophilic or superhydrophobic, and it is difficult to find suitable functional applications for direct utilization [350,351]. The preparation of structures on MG surfaces is a straightforward way to modify the wettability of its surface. Currently structures based on the TPF properties of MG have been designed to achieve superhydrophobic [261], superhydrophilic [262], aerophobic [17] and superlipophilic properties [268] on MG surfaces (Fig. 20a-d). Aside from the building structure, which directly effects the wettability of the surface, the generated structure can also be employed as a precursor for further alteration of the contact angle by other procedures. For instance, the honeycomb surface is further chemically etched to transform the hydrophobic properties of the surface into superhydrophobic properties [263], further chemical deposition on regular arrays achieves a dramatic transition from superhydrophilic to superhydrophobic [262].

The high strength of MG at room temperature [18,353] and the high reproduction accuracy exhibited in TPF allow the formed surface to be used as a mold for mirroring structures on other materials. MG molds can be used to form structures on plastics with  $T_g$ . This forming process necessitates that the SLR of the plastics to be processed does not cross the SLR of the molds and that the  $T_g$  of the material to be processed is lower than the  $T_g$  of the molds, as in the case of patterning on polycarbonate (PC), polypropylene (PP), cycloolefin copolymer (COC), and polyethylene (PE) with Pd-based MG molds [287] and 3D microlens array forming on polymethyl methacrylate (PMMA) with Zr-based MG molds [354] (Fig. 20e). For materials with high  $T_g$ , such as glass, further crystallization of the MG mold is possible. The strength of the crystallized MGs itself is reduced, but it is no longer limited by its own SLR. In this way the molds have proven to be able to form structures on the surface of the glass [290] (Fig. 20f) and can be used to form structures on the surface of the same material [225] (Fig. 20h). However, the release of residual stresses during the crystallization process affects the accuracy of the formed structure, a point that has rarely been investigated. Apart from thermoplastic materials, MG molds can also be used as molds for the forming of elastomeric metallic materials such as Al [296] (Fig. 20g) and AZ31 magnesium alloy [330], which can be achieved at room temperature.

The unique atomic structure of MGs gives them optical properties that are different from those of their crystalline material [355,356], which has led to numerous studies on MGs focusing on the design of their optical properties on the surface. In previous studies, colourful effects [224] and homogeneous structure colors [255] could be achieved on their surfaces by the rational design of the shape and size of their micron structures. Nanostructured surfaces with excellent light absorption properties have been noted in a number of works [58,227], and the main structures that have been reported to lead to MG surfaces with excellent light absorption are hierarchical porous structures [251] and nanowire structures [301], which have demonstrated strong advantages for photothermal applications. Fig. 20i shows a schematic diagram for testing the photothermal properties of MGs with nanostructured surfaces. The laser is directed at MGs with nanostructure and the temperature change is recorded with the corresponding sensing device. In terms of photothermal properties of nanowires, the nanostructures on the surface reduces the thermal conductivity of its surface [357], which promotes less heat conduction, resulting in a large convergence of heat on the surface and excellent photothermal properties on its surface. Additionally, the aspect ratio of the structure will affect the temperature variation at its surface, with nanowires with high aspect ratios having stronger absorption compared to those with lower aspect ratios, resulting in a bigger temperature rise for the same laser power irradiation [302]. Due to the customizable nature of the templates, macroscopic structures consisting of a large number of nanostructures stitched together on the MG surface may be easily created for photothermal imaging applications using laser light [288,301] (Fig. 20j). Recently, Ma et al. [251] have designed a hierarchical porous structure with excellent light absorption and photothermal properties, which, by combining the hydrophilic properties of its surface, enables its functional use in seawater desalination and wastewater treatment (Fig. 20k).

Apart from the above-mentioned applications, MGs are also promising in other fields. Nanowires formed on  $\text{Pd}_{40.5}\text{Ni}_{40.5}\text{P}_{19}$  MG surfaces for enhanced surface Raman scattering [352] (Fig. 20l). By constructing surface nanostructures a significant increase in specific surface area is achieved for specific catalytic reactions such as hydrogen evolution reaction (HER) [17], oxygen reduction

reaction (ORR) [349], ethanol and methanol oxidation of carbon monoxide [257] (Fig. 20m). Furthermore, based on a TPF process of MG, Sekol et al. [293] have assembled for the first time a functional proton exchange membrane micro fuel cell with catalytic and gas flow field components made of MG, Liu et al. [253] design 3D MG structure to enable use in force sensors. Additionally, Sorin et al. [248] used a hot drawing process to construct surface micro-nanostructures and implanted MGs electrodes and fine fiber probes into rats by a to achieve real time neuronal monitoring in rats. In terms of drug delivery, Kumar et al. [340] have made some progress with solid and hollow microneedle structures prepared using this process.

In conclusion, the functional applications that can be developed using the thermoplastic properties of MG have already been explored in a number of areas, and many more will be explored over time. The design of specific structures according to the required properties is a priority in this process, and further consideration of the relevance of the elemental composition of the material to the application will allow MG to be used in more applications.

### 5.2. Ultrasonic vibration-induced plasticity (UVIP)

One of the main challenges in using MGs as structural materials is their susceptibility to shear-banding-induced softening behavior, which can cause catastrophic failure during deformation [358]. Due to the lack of long-range order, the plasticity mechanism of MGs differs significantly from that of their crystalline counterparts. At low temperatures, plastic flow in a shear band of MGs involves a significant rearrangement of local atoms and a considerable increase in free volume [56,359]. Shear banding in MGs is often accompanied by dilatation and temperature rise, resulting in shear-induced softening and the rapid propagation of a mature and detrimental shear band under unconstrained loading conditions [360–362]. The plasticity of MGs is inherently linked to “defects”, which can manifest as structural heterogeneity, it can be considered as free volume [363], STZs [364,365], and flow units [366]. It is

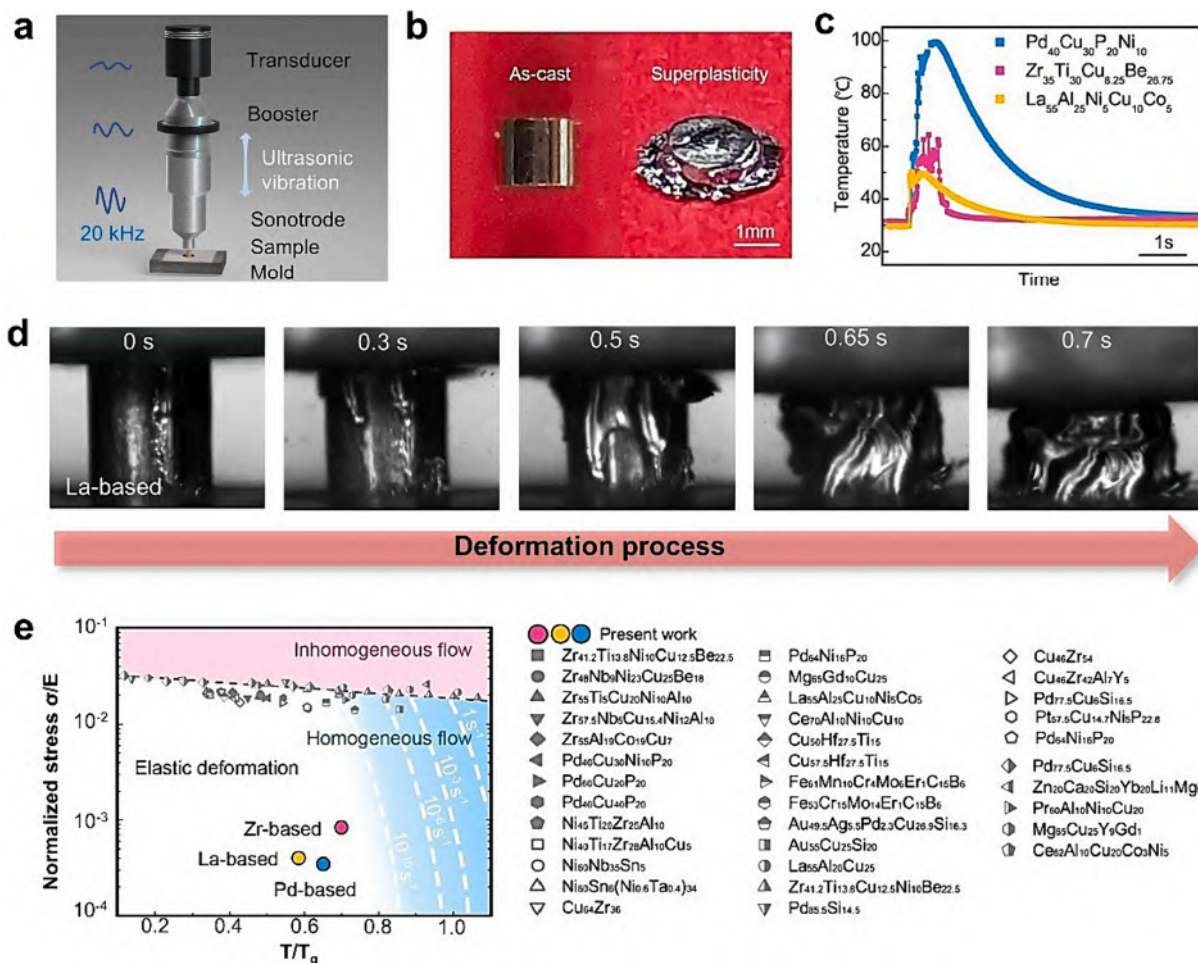


Fig. 21. (a) Schematic diagram of the ultrasonic plastic set-up. (b) The comparison of BMGs before and after ultrasonic plasticity. (c) Temperature change during the ultrasonic plasticity of different BMGs. (d) The images of the BMG during the ultrasonic vibrations by high-speed camera. (e) Deformation map for MGs in stress-temperature axes. . Adapted from [211]

believed that modifying the microstructural heterogeneity is an effective approach to improve the plasticity of MGs.

The ultrasonic waves can induce mechanical vibration in the MG material, which can lead to a reduction in its viscosity and an increase in its fluidity. Additionally, ultrasonic technology can also enhance the heterogeneity of the MGs by promoting the mixing of its constituents. Therefore, ultrasonic technology has been applied to the plastic processing of MG, and has a significant effect [211,367,368]. The device used in ultrasonic plasticity technology typically consists of several components, As shown in Fig. 21a, including transducer, booster, and sonotrode. Transducer convert high-frequency AC signals into mechanical vibrations, while booster amplify the amplitude of these vibrations. The sonotrode, which is typically the working tool, then amplifies the amplitude further and concentrates the vibration energy on the contact surface. In Fig. 21b, the image on the left portrays an original as-cast MGs, while the image on the right shows the same sample after ultrasonic processing. Notably, the processed sample exhibits substantial plastic deformation compared to the original one, with the plastic flow occurring uniformly. As shown in Fig. 21c, the experimental temperature peaked at about 0.5 s, and the peak temperatures were all less than 100 °C, which is much lower than the  $T_g$  temperature of MGs. At the same time, the author also used an infrared camera to collect temperature data and compared it with thermocouple data. The results show that the ultrasonic processing of MG will not crystallize due to excessive temperature.

Fig. 21d provides a detailed illustration of the deformation process undergone by the MG during ultrasonic processing. This figure, captured by a high-speed camera, shows that the top of the MGs undergoes flow deformation first, followed by a fresh top exhibiting similar behavior, culminating in plastic deformation of the entire sample. Therefore, ultrasonic vibration can induce the softening of MGs, and this behavior is known as UVIP. According to the results of quasi-static compression tests conducted at the peak temperature measured, it can be concluded that UVIP is not induced by temperature but by the special processing method of ultrasonic vibration, which leads to significant plastic deformation.

Moreover, ultrasonic technology offers a versatile approach to the forming process of MGs. As depicted in Fig. 22a, various ultrasonic forming samples of MGs are represented in different dimensions, encompassing macroscopic samples, microscale cylindrical arrays, and nanoscale nanowire structures [369]. Fig. 22b further exemplifies three distinct forming processes: extrusion molding, riveting molding, and injection molding [211,370]. This demonstrates the exceptional scale adaptability of the ultrasonic forming process for MGs, and its capability to seamlessly integrate with existing multiple forming techniques, expanding the possibilities for shaping MG components.

### 5.2.1. Mechanism of ultrasonic plasticity

The deformation map in Fig. 21e suggests that BMGs should display elastic deformation under low stress, low homologous temperature, and high strain rate conditions which is like UVIP. However, UVIP exhibits substantial plastic deformation in MGs, indicating revealing an underlying flow behavior that is not yet fully understood. The researchers employed machine learning techniques to gain

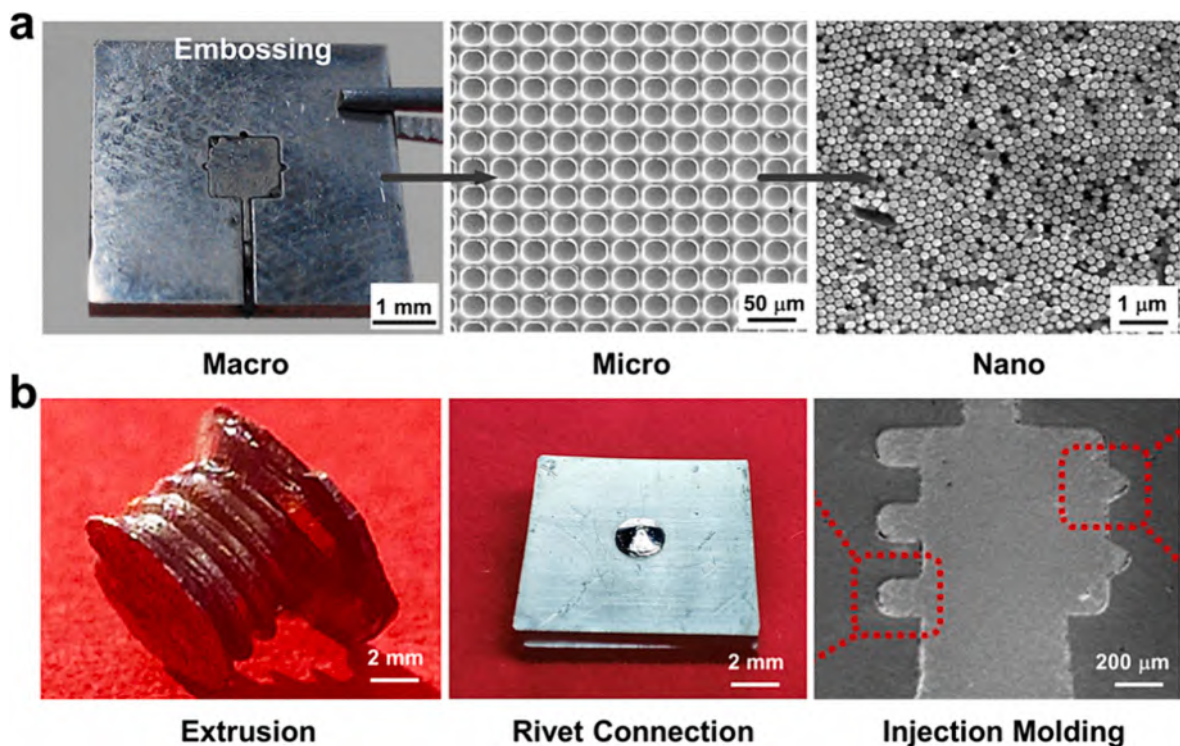
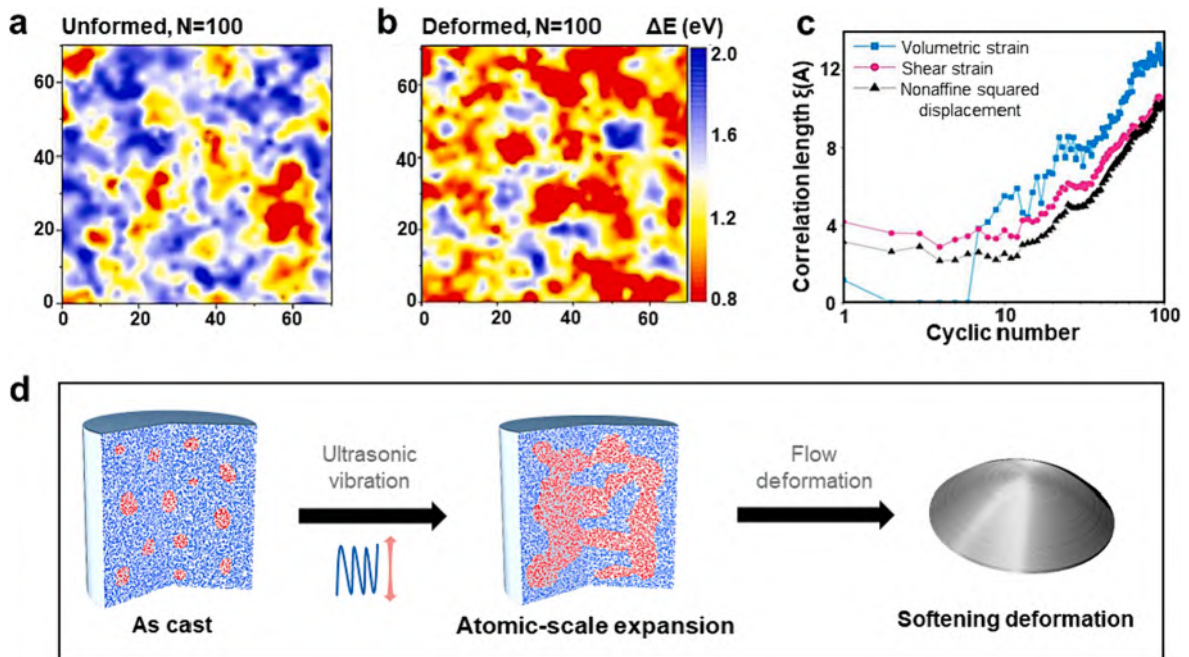


Fig. 22. (a) Typical macrostructure, microstructure, nanostructure prepared by UVIP (Adapted from [369]). (b) Extrusion, rivet connection, injection molding of MGs by ultrasonic vibration (Adapted from [211,370]).



**Fig. 23.** (a) Contour plots of the activation energies explored in the initial and (b) cyclically deformed samples. (c) Variation of the correlation lengths as a function of cyclic number. (d) mechanism illustration of ultrasonic plasticity. . Adapted from [211]

insights into plastic flow, locate atoms in the liquid-like zone, and uncover the source of ultrasonically induced plasticity in MGs [371]. They investigated the structural rearrangement and mechanical response mechanisms underlying ultrasonic-induced plasticity, and their findings indicate that this approach can significantly enhance the activation energy of atomic diffusion [213]. DSC data indicate that MGs exhibit rejuvenation after UVIP, which is further supported by the reduction in hardness and modulus measured in nano-indentation. Additionally, TEM shows an increase in diffraction ring radii after UVIP, indicating a higher degree of atomic packing and a smaller interatomic spacing. These results suggest that the amorphous structure becomes more loosely packed and rejuvenated after UVIP, consistent with a process of rejuvenation. However, after thermal annealing, the structure becomes more densely packed and relaxed, consistent with a process of relaxation.

Why do MGs exhibit rejuvenation by UVIP? Researchers have proposed using molecular dynamics (MD) simulations [211], as shown in Fig. 23a-b, to understand the mechanical, thermodynamic, kinetic, and structural evolution of UVIP. And in Fig. 23c,  $\text{Cu}_{50}\text{Zr}_{50}$  has been used as a model system and applied 100 cycles of symmetric strain with a strain rate of  $10^{-9}$ . The results showed that as the number of cycles increased, the modulus and stress of the material decreased, while the potential energy increased. These results correspond to structural and thermodynamic rejuvenation, and the authors also presented a distribution of activation energy under cyclic loading. Comparison of Fig. 23a and b plot revealed a significant increase in the low activation energy state distribution after cycling, indicating a significant increase in the activated volume fraction of the STZ. All of the results consistently indicate a state of restored activity, with more potential shear transition zones after cycling.

Under the action of UVIP, as-cast MGs experience an increase in their soft regions, that is free volume as shown in Fig. 23d, leading to the phenomenon of rejuvenation and softening of the sample and ultimately resulting in overall rheological behavior [211]. The increase in free volume is mainly attributed to the dynamic heterogeneity of MGs and the atomic-scale expansion induced by long-term cycling. However, it should be noted that the application of ultrasonic technology to MGs processing is still in its early stages and further research is needed to fully understand its potential and limitations.

### 5.2.2. Design and modulation of properties

MGs are novel metallic materials with a wide range of promising applications in many fields. To obtain MGs with particular property enhancement, various methods have been used to tuning the energy state, such as high pressure [372,373], physical vapor deposition techniques [374,375], annealing [376], elastic loading [377], ion radiation [378], thermal cycling [134], and plastic deformation [379]. However, these methods present several limitations: unidirectional modification of energy state, time-consuming, unstable and complex operation.

In contrast, UV technology is a simple and effective means to rapidly design and modulate the performance of MGs in multiple energy directions. Extensive research summarizes that the potential energy state of MG exhibits a diverse trend when dealing with different materials or using different UV parameters. The potential energy landscape (PEL) diagram is generally used to describe the energy state of the glassy material, as shown in Fig. 24a, which summarizes the structural evolution of MG during UV treatment in

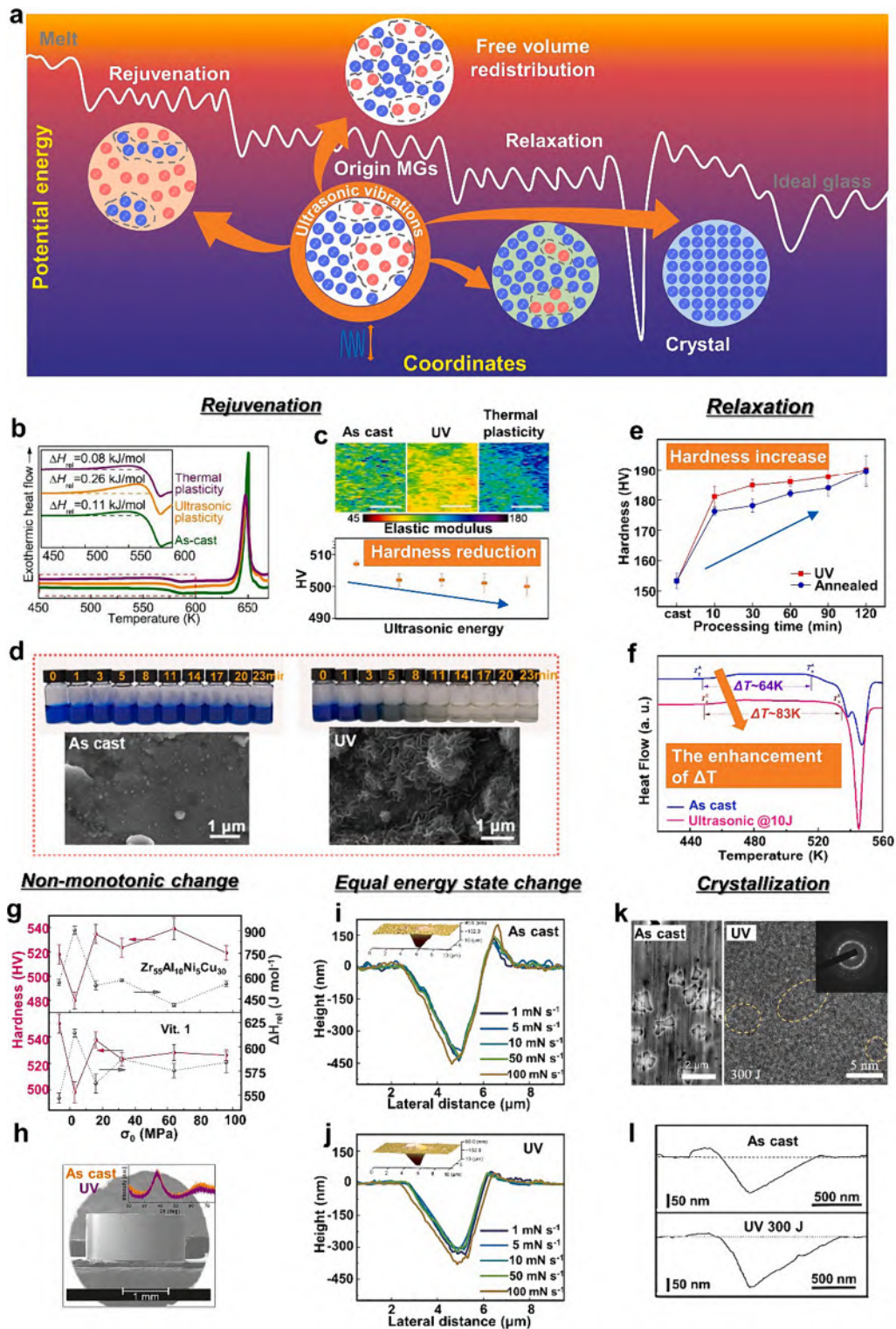


**Fig. 24.** Design and modulation of properties. (a) The PEL diagram of structural evolution in MG during UV treatment. (b-c) The DSC curve and mechanical properties after rejuvenation of BMG. (d) Improved catalytic degradation performance of the Fe-based MG after rejuvenation. (e) Hardness changes after ultrasonic vibration induced relaxation of MG. (f) The DSC curve show  $\Delta T$  of MG can be significantly widened from 64 K to 83 K. (g-h) The effect of different ultrasonic stress on hardness and  $\Delta H_{rel}$  in  $Zr_{55}Al_{10}Ni_5Cu_{30}$  and Vit.1 MGs. (i-j) The cross profile of the indents after nanoindentation for the as-cast and ultrasonic-vibrated samples. (k) The TEM images of tunable crystallization after ultrasonic vibration treatment.

(l) The comparison of nanoindentation between as-cast MG and MGC. .

Adapted from [139,346,384,385]

reported studies. One can see that UV can basically actuate energy state transitions in almost all directions: structural relaxation [380], structural rejuvenation [211,381,382], crystallization behavior [383], and even free volume changes in homoenergetic state [213,384]. Through these structural tuning, MGs will achieve the anticipated mechanical properties, degradation properties, catalytic properties, etc. that without composition change. This demonstrated that UV technology can manipulate the energy state of the MG over a wide range, thus enabling the design and tuning of performance.

Due to the dynamic heterogeneity and cyclic induced atomic-scale dilations over a longer period of time during the UV treatment, resulting in significant rejuvenation of bulk MG (Fig. 24b and c) [211]. This rejuvenation has brought about the expected change in MG performance. For example, after rejuvenation the modulus of amorphous was raised as well as the hardness was reduced (Fig. 24c), MG fracture was dominated by ductile fracture and shear deformation was occurred [381]. Therefore, UV provides a convenient and rapid route to reduce the room temperature brittleness and improve the plasticity of BMGs. Furthermore, the rejuvenated MGs still has more functional applications. The activation site of the Fe-based MG was greatly enhanced by the modulation to the revertant state, thus improving the catalytic degradation performance of the material and optimizing the morphology after degradation [347] (Fig. 24c). Although a large number of methods exist for rejuvenation, but inevitably a relaxation effect is produced and the rejuvenation effect is diminished.

UV treatment can also effectively activate relaxation, allowing sufficient atomic rearrangement occurs in the anelastic region of the MG flow units to bring the MG to a more stable state. The atomic arrangement of these anelastic regions is enhanced by UV treatment, so that the high-energy sub-stable structures with relatively low activation energies will disappear [346]. Such denser stacking can create super-stable glasses with a broadening  $\Delta T_x$  ( $\Delta T_x = T_x - T_g$ , where  $\Delta T_x$  is the width of SLR), which can obtain a maximum enhancement of  $\Delta T_x$  of nearly 19 K, approximately equal to an increment of about 30 % (Fig. 24e). Moreover, it was proved that UV would obviously accelerate the aging (relaxation) process during annealing and save a lot of processing time (Fig. 24f). The research also achieved hardness modulation by UV, i.e. the more significant the aging, the higher the hardness improvement [385].

Under different parameters of UV processing, the intrinsic structural competition between damage and repair promoted by increased atomic mobility can also induce oscillatory changes in energy (Fig. 24g-h) [139]. Consistent with the structural oscillations, the mechanical properties also exhibit oscillatory changes. The discovery of this behavior forced a new understanding of the effect of UV action on MG, demonstrating that UV can enable energy state modulation.

The literature suggests that MGs may exist without a discernible alteration in the energy landscape following UV treatment [213]. However, it is important to note that this absence of change in energy landscape does not necessarily imply an unchanged internal structure. Investigations have revealed significant alterations in the atomic arrangement within the MG structure, particularly among atoms at the same energy level. The activation of mechanical softening and the induction of flow defects by UV contribute to the

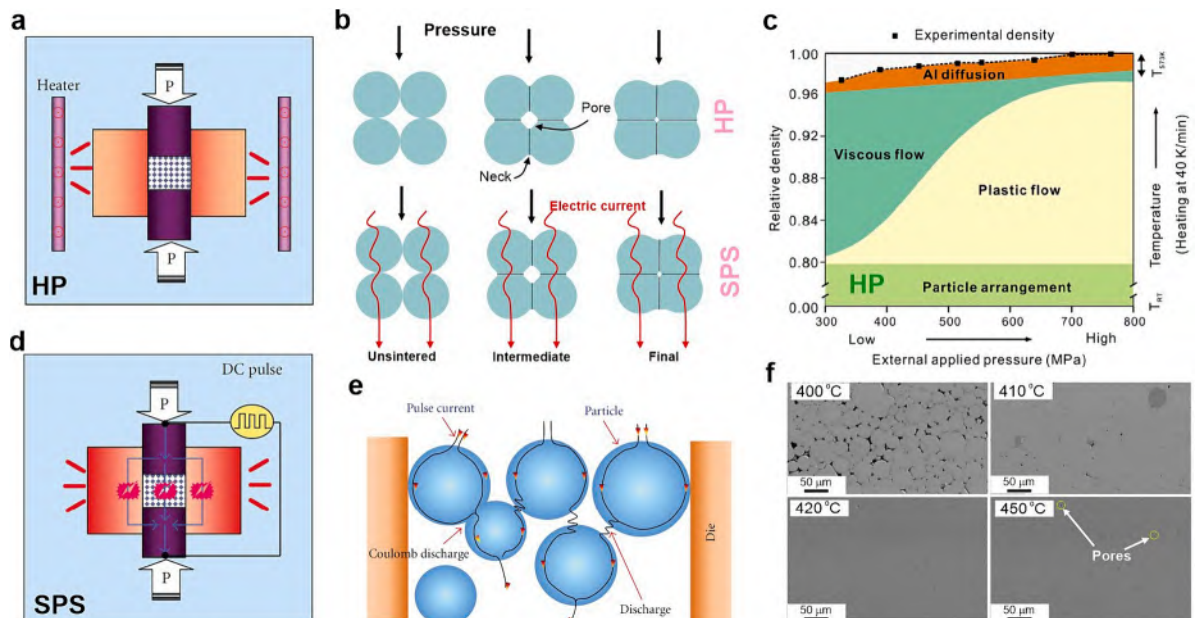


**Fig. 25.** (a) Schematic of HP method (Adapted from [395]). (b) Schematic representation of different sintering stages during HP and SPS. (c) Densification map illustrating the densification mechanisms during HP of an Al-based MG powder (Adapted from [389]). (d) Schematic of SPS method. (e) DC pulse current passing through the particles during SPS (Adapted from [395]). (f) Microstructure of CuZrAl BMG SPSed at different temperatures (Adapted from [396]).

evolution of the free volume distribution within the MG, leading to a more homogeneous state. Remarkably, this state exhibits minimal impact on mechanical properties such as hardness, elastic modulus, and brittleness parameters. It also effectively reduces the loading rate sensitivity of the stress exponent during creep deformation and the activation energy for the crystal nucleation ( $E_x$ ) (about 10 %), thus exhibiting a more uniform creep behavior than the original sample [213]. This homogeneous creep behavior was considered to be the key to determine the excellent micro-forming properties of MG, which would greatly enhance the MG plasticity at room temperature.

If extremely high ultrasonic vibration energy was applied to the MG, it would lead to another structural change—crystallization [383]. However, unlike the normal annealing treatment that makes MGs crystallization, the UV crystallization treatment will be easier to tuning. Due to the extremely short processing window, it has been a challenge for the heat treatment method to introduce nanocrystals of suitable size or quantity. The UV method is enabled to introduce the expected nanocrystals in the MG substrate, and the grain size or number of nanocrystals are fully controllable. Such embedded grains will greatly enhance the plasticity of the material and still maintain the high strength of MG.

### 5.3. Powder consolidation

Powder consolidation is an alternative method employed to overcome size limitation of BMGs. This process primarily relies on thermal sintering, where pressure and heat are applied to the powder particles. By doing so, the particles undergo rearrangement, leading to enhanced contact and interparticle bonding while reducing the presence of void spaces. Consequently, the powder particles adhere to one another, resulting in the formation of a densified structure.

Hot-pressing and spark plasma sintering are the main powder metallurgy routes to consolidate MG powders by thermal sintering. Both methods rely on densification of powders at temperatures within SLR where the viscosity of MG powder is significantly reduced [386,387] and powders can be thermoplastically deformed.

#### 5.3.1. Hot-pressing (HP)

The HP process is the conventional approach to consolidate MG powders. During HP (Fig. 25a), the die with the MG powder is placed in a hot-pressing machine or furnace and heated to a temperature within the SLR. Once the desired temperature is reached, pressure is applied to the material within the die using a mechanical press or hydraulic system and hold for a preset time, followed by cooling to room temperature. Alternatively, pressure can be also applied gradually during heating [388]. During pressure-assisted sintering of MG powders, densification mechanism has three main stages (Fig. 25b): particle rearrangement, viscous (liquid-like) flow, and diffusion. The initial stage (unsintered) involves particle rearrangement, while the intermediate stage exhibits neck growth (plastic flow) and high shrinkage rates due to viscous flow. The final stage is characterized by steady-state elemental diffusion and further densification and elimination of voids or porosity [389]. BMG components of different alloy systems have been manufactured by the HP, including Ni-based [390], Si-based [388], Ti-based [391], Fe-based [392] BMGs. The HP process takes place in a vacuum [392,393] or inert gas environment [391,394].

The main processing parameters during HP of MG powders are pressure, temperature and time. A combination of set values for these parameters determines the extent of relative density and degree of amorphicity in the sintered BMGs. Generally, higher temperatures and larger pressures are beneficial for reducing viscosity of MG powders and achieving larger densification. For instance, HP of the  $Zr_{48}Cu_{36}Al_8Ag_8$  MG powders is more effective at 753 K compared to at 743 K, which is attributed to the lower viscosity at 753 K ( $4.3 \times 10^6$  Pa s) compared to 743 K ( $4.8 \times 10^6$ ) which facilitates particle deformation [397]. However, it should be noted that rising temperature to the upper extreme of SLR (i.e., values close to  $T_x$ ) may cause precipitation of brittle intermetallic compounds, thus exacerbating the intrinsic brittleness in MGs. So, MG alloy systems with high stability against crystallization (i.e., wide SLR) are more favorable for consolidating through the HP. As a rule of thumb, fully amorphous BMGs are inaccessible via the HP of those MG powders having  $\Delta T_x < 50$  K, including some Mg-based [398–400] and Al-based [389,393] MG alloy systems. In addition, the sintering time during HP should not exceed incubation time which is needed to start crystallization at a given temperature. The common sintering time used during HP of MG powders is ~ 15–30 min, but shorter times (~5 min) are used for marginal glass formers such as Fe-based [401] MG alloys to minimize crystallization.

During HP of  $Si_{15}Al_{20}Fe_{10}Ni_5Cr_5$  MG powders, increasing temperature led to higher relative density, reaching a maximum of 98.3 % at 687 K and applied pressure of 1.5 GPa [388]. Further, hot-pressing  $Ti_{60}Al_{15}Cu_{10}W_{10}Ni_5$  glassy powders within their SLR at a consolidation pressure of 936 MPa produced fully dense (~99.85 %) BMG alloys [391]. And the  $Co_{71}Ti_{24}B_5$  MG powders hot-pressed at 835 K by applying pressure of 780 MPa reached a fully density of ~ 99.5 % [394]. Regarding lower applied pressures, uniaxial hot pressing of the  $Al_{85}Ni_9Nd_4Co_2$  MG powder at 513 K and ~700 MPa for less than 15 min produced bulk samples with a decreased density of ~ 94 %. Additionally, consolidating the  $Al_{85}Y_8Ni_5Co_2$  MG powder at various temperatures below  $T_x$  using low pressures of 150 to 340 MPa resulted in compacts with relative densities as small as ~ 80 % [402].

Pressure has a substantial influence on the densification mechanisms during the HP process, specially at the intermediate stage of sintering [389]. Fig. 25c illustrates densification map of  $Al_{84}Gd_7Ni_6Co_3$  MG powder and the corresponding mechanisms at different external pressures and temperatures. At temperatures far below  $T_g$ , particle arrangement plays a crucial role, facilitating particle contact and pore closure. At higher temperatures within SLR, the main densification mechanism changes from viscous flow (liquid-like) to plastic flow with increasing the pressure. During this intermediate stage, pores change from a connected network to isolated entities, and necks form and grow. In the final stage when the temperature is quite high, Al diffusion becomes the primary densification mechanism, essential for achieving higher density and lower porosity with increasing the external pressure.

### 5.3.2. Spark plasma sintering (SPS)

SPS, or Field-Assisted Sintering Technology (FAST), consolidates powder materials using pulsed DC and mechanical pressure [403]. The application of electrical current leads to rapid and uniform heating, promoting atomic bonding and sintering. SPS involves four main stages (Fig. 25d): gas removal, pressure application, rapid heating through DC pulse, and cooling. The localized high temperatures generated by spark discharge facilitate oxide surface evaporation, thermoplastic deformation, and neck formation between particles (Fig. 25b and e) [395,404]. Compared to conventional HP method, SPS offers higher heating rates and shorter sintering time. Replacing HP processes with SPS enables cost savings, increased production volume, and reduced energy expenses, making it a cost-effective solution for manufacturing materials with superior properties [404].

SPS utilizes the viscous flow behavior of MG powders in the SLR, enabling the production of BMGs with adjustable sintering parameters [28]. Compared to the HP process, SPS of MG powders requires lower pressures (~300 MPa [20, 21]) and shorter sintering times (~5 min [396,405]) to achieve fully amorphous BMGs with high relative densities, reducing the risk of devitrification.

SPS enabled the production of fully amorphous Zr-based AMZ4 BMGs with ~100 % relative density when sintered at 693 K/480 s and 713 K/60 s [406]. Following the optimization of the processing parameters during SPS of  $\text{Cu}_{50}\text{Zr}_{45}\text{Al}_5$  MG powder (693 K, 90 MPa, 30 min), both dense and amorphous specimens were successfully fabricated, with a diameter of up to 30 mm and thickness of 4 mm [396]. The fabrication of large-size  $\text{Ni}_{52.5}\text{Nb}_{10}\text{Zr}_{15}\text{Ti}_{15}\text{Pt}_{7.5}$  BMGs with nearly 100 % relative density was accomplished through SPS at a temperature of 773 K under a loading pressure of 600 MPa [407]. These examples represent a wide range of studies on developing BMGs of various alloy systems using SPS, including Fe-based, Al-based, Ti-based, and Zr-based MG powders [408].

Similar to HP process, increasing the pressure improves the densification of MG powders during SPS [409,410]. The application of larger pressures during SPS facilitates atomic diffusion and enhances powder densification by increasing the diffusion flux between particles [409]. However, reaching maximum density is also dependent on optimizing other parameters such as sintering temperature. For instance, sintering the  $\text{Al}_{82}\text{La}_{10}\text{Fe}_4\text{Ni}_4$  MG powder at 400 MPa yielded low relative density ( $\approx 80$  %) with free-standing particles. Increasing the pressure to 600 MPa improved relative density ( $\approx 96$  %), but visible pores remained, possibly due to low viscosity at the sintering temperature and carbon impurities hindering the sintering process [411].

The sintering temperature is another parameter influencing the density of BMGs prepared by SPS. By increasing the sintering temperature, the relative density of the specimens also increases until reaching a nearly full density at a given temperature, while higher temperatures yield devitrification in the sintered samples [396,407,412–414]. As shown in Fig. 25f, pores can be seen in the solidified  $\text{Cu}_{50}\text{Zr}_{45}\text{Al}_5$  BMG compacts that were sintered at 400 °C and 410 °C, indicating that complete consolidation did not occur at these temperatures. The porosity decreased as the temperature rises, and effective consolidation was achieved when the temperature exceeded 420 °C. Larger temperature (450 °C) did not affect density but induced crystallization [396].

Powder characteristics such as size and shape of MG powders also affect densification process during SPS. For example, the SPSed pellets fabricated from Hf-based powder particles larger than 75  $\mu\text{m}$  and smaller than 25  $\mu\text{m}$  exhibit a relative densification of approximately 96–98 %. However, by combining powder particles of both size ranges, a higher densification of 99.8 % has been attained [405]. In another study, Li et al. [415] investigated shrinkage behavior, densification mechanism, and atomic diffusivity of gas-atomized and milled  $\text{Ti}_{40.6}\text{Zr}_{9.4}\text{Cu}_{37.5}\text{Ni}_{9.4}\text{Sn}_{3.1}$  MG powders during SPS. Mechanical milling alters the powder shape, increasing contact area and enhancing mass transfer kinetics. The milled powders exhibit additional sintering stages and higher densification compared to atomized powders during SPS. This is attributed to the higher defect concentration induced by high-energy mechanical milling, which lowers the activation energy of atomic diffusion and accelerates powder densification.

Another processing parameter influencing relative density of BMGs during SPS is heating rate (pulse power input). As the heating rate increases, the activation energy for the viscous flow of the MG decreases, promoting the densification process of the MG powder [416]. Further, a higher heating rate lowers the optimal temperature for maximum densification. The maximum densification rate of the milled  $\text{Ti}_{40.6}\text{Zr}_{9.4}\text{Cu}_{37.5}\text{Ni}_{9.4}\text{Sn}_{3.1}$  MG compact is observed at 689 K if the heating rate is 120 K/min. In comparison, at the heating rate of 30 K/min, the maximum densification rate is achieved at 719 K [415]. The common heating rates used during SPS of MG powders is 50 K/min or higher [407,410,414,417]. Nonetheless, the use of pulsed current input may not be the most suitable method for sintering MG powders. In the early stages of sintering, when the necks between particles are small, the pulsed current input can cause excessive overheating ( $>T_x$ ) in the vicinity of the necks, leading to partial devitrification. However, when the necks become larger, further current input can promote complete densification of the material [418,419].

The SPS process is also effectively employed to fabricate BMGs with controlled porosity. One approach to obtain porous BMGs is sintering at temperatures below  $T_g$  to restrict the densification of the alloy. Additionally, the compacting pressure is minimized to prevent viscous deformation of the MG powders during sintering [408]. The porosity of  $\text{Zr}_{55}\text{Cu}_{30}\text{Al}_{10}\text{Ni}_5$  BMG compacts can be adjusted by varying the sintering temperature and loading pressure during the SPS process [420]. Further, the porosity of Ti-Fe-Si BMG has been controlled to ~ 30 % by adjusting the loading pressure [421]. At different sintering pressures (15 MPa, 50 MPa, and 80 MPa), the pores between  $\text{Ti}_{45}\text{Zr}_{10}\text{Cu}_{31}\text{Pd}_{10}\text{Sn}_4$  MG powders exhibit irregular, multi-angular, and three-dimensional characteristics. As the loading pressure increases, the pores transition from through-holes to closed cavities, eventually closing completely at 150 MPa [422].

A different method to fabricate porous BMGs through SPS involves combining MG powders with solid salt (NaCl) powder, followed by leaching treatment to remove the salt phase. This approach was effectively used to produce porous Ti-based BMG samples with diameters larger than 15 mm using the spacer technique with SPS. By adjusting the volume fraction of the salt phase, controlled porosity of up to 60 % was achieved [423,424].

A new strategy to enhance densification and reduce the sintering temperature during SPS of MG powder is two-step SPS process [417]. The process included a lower-temperature pretreatment followed by high-temperature sintering. The pretreatment improves powder billet density and distribution, ensuring a homogeneous temperature field during sintering and preventing localized crystal

phase precipitation. The reduced electrical resistivity of pretreated billets enhances current flow, promoting internal joule heat generation and particle discharge, resulting in improved densification.

### 5.3.3. Structure and properties in consolidated components

During HP and SPS of MG powders, preventing devitrification is critical to achieve fully amorphous BMG components. Nanocrystallization phases precipitated during consolidation process alters the structure in different ways. For example, the full width at half maximum (FWHM) for the halo pattern of HPed Al-based BMG in the XRD pattern gets slightly narrower than that of the milled powder, which is germane to strain relief and limited nanocrystallization during the process of consolidation [393]. Additionally, the crystallization temperature of  $\text{Ni}_{57}\text{Zr}_{20}\text{Ti}_{20}\text{Si}_3$  samples shifts towards lower values as the HP time increases, indicating a decrease in crystallization temperature due to the occurrence of nanocrystallization [390].

Sintering at high temperatures within SLR leads to the presence of nanocrystallites and increased hardness compared to fully amorphous compact. During SPS of  $\text{Hf}_{55}\text{Cu}_{28}\text{Ni}_5\text{Al}_{12}$  ( $T_g$  of 498 K), the formation of a complete amorphous phase is only observed when the compaction experiment is conducted at temperatures as low as 460 °C and 480 °C under a pressure of 800 MPa [405]. Sintered specimens of  $\text{Ni}_{52.5}\text{Nb}_{10}\text{Zr}_{15}\text{Ti}_{15}\text{Pt}_{7.5}$  below 773 K consist entirely of a glassy phase. However, increasing the sintering temperature beyond 798 K, yet lower than  $T_g$  (821 K), leads to the emergence of additional crystalline peaks [407].

Graeve et al. [425] developed a time-temperature-crystallinity (TTC) diagram to predict and guide the SPS of MG powders. Their analysis using the TTC diagram revealed that the  $\text{Fe}_{49.7}\text{Cr}_{17.7}\text{Mn}_{1.9}\text{Mo}_{7.4}\text{W}_{1.6}\text{B}_{15.2}\text{C}_{3.8}\text{Si}_{2.4}$  MG alloy exhibits accelerated devitrification compared to the  $\text{Fe}_{48}\text{Mo}_{14}\text{Cr}_{15}\text{Y}_2\text{C}_{15}\text{B}_6$  MG alloy. This difference is attributed to variations in the critical cooling rate between the two alloys rather than differences in glass transition temperature.

Pressure can also influence devitrification behavior during sintering of MG powder. Generally, pressure has three main effects on crystallization in MGs [426]. Firstly, it promotes densification, favoring the crystallization process. Secondly, it suppresses atomic mobility, limiting atomic diffusion in MGs. Lastly, pressure alters the relative Gibbs free energies of the glassy and crystalline phases, affecting sequence of the precipitated crystalline phases. The specific crystallization behavior depends on the dominant effect. For example, pressure suppresses primary  $\alpha$ -Al crystallization and promotes eutectic crystallization, likely due to its influence on atomic diffusivity [4]. During HP of  $\text{Mg}_{49}\text{Y}_{15}\text{Cu}_{36}$  [399] and  $\text{Cu}_{60}\text{Zr}_{30}\text{Ti}_{10}$  [427] MG powders, lower pressures ( $\sim 720$  MPa) promoted crystallization, but higher pressures ( $\geq 960$  MPa) hindered atomic diffusion, leading to an increased amount of residual amorphous phase in the samples. This decrease in long-range atomic diffusion was attributed to the elevated diffusion barrier resulting from the reduction in volume and elimination of excess free volume caused by high pressure.

The occurrence of devitrification is also closely associated with particle size. Specifically, smaller particle sizes and broader particle size distributions lead to a higher average number of contact points between particles, which in turn results in a greater extent of devitrification [419].

Mechanical properties of the large size BMG samples manufactured by optimized powder consolidation parameters closely resemble those of the cast alloy, including. For instance, the hot-pressed  $\text{Zr}_{48}\text{Cu}_{36}\text{Al}_8\text{Ag}_8$  BMG exhibits a fracture strength of  $1864 \pm 37$  MPa and a fracture strain of  $1.8\% \pm 0.1\%$ , which is comparable with its cast counterpart [397]. In addition, the hardness values of SPSed AMZ4 BMG samples, exceeding HV1 519, surpass those of cast materials, and their compressive strengths of 1625 MPa are comparable to commercial cast products [406]. In another investigation,  $\text{Cu}_{50}\text{Zr}_{45}\text{Al}_5$  BMGs were successfully consolidated using SPS, yielding mechanical properties (hardness, Young's modulus, density, and compressive strength) comparable to cast alloys. However, a lower toughness was observed due to weak cohesion among the powder particles, despite optimized sintering conditions. This drawback was partially addressed by applying higher pressures, up to 1 GPa, resulting in significantly improved bonding between the powder particles [396].

By adjusting the loading pressure in SPS, Young's modulus and strength of BMGs can be optimized by controlling the sintering neck size between powders. This is particularly important for developing BMG orthopedic implants with mechanical properties close to the natural bone. The Young's modulus of the sintered sample increases with higher loading pressure during SPS. Similarly, increasing the loading pressure also enhances the strength of the sintered samples [421,422]. Ti-Fe-Si BMG with a porosity of 24 % exhibited a low Young's modulus of 37 GPa and a strength of 130 MPa [421]. To ensure compatibility  $\text{Ti}_{45}\text{Zr}_{10}\text{Cu}_{31}\text{Pd}_{10}\text{Sn}_4$  BMG implant with human bones, Wu et al. [422] determined that the optimal loading pressure for porous BMG during SPS should be in the range of 50–74 MPa at a sintering temperature of 643 K with a heating rate of 50 K/min for 10 min.

On the other hand, porous BMGs display distinct corrosion behavior compared to fully dense BMGs [410]. The potentiodynamic polarization curves of porous Ti-based BMGs lacked a defined passive region and showed metastable current transitions, indicating localized pitting within the pores. This crevice corrosion was in contrast to the stable passive region observed in the BMG sample without pores. Furthermore, the porous BMGs exhibited narrower ranges between open circuit potential and transpassive potential, indicating higher sensitivity to local corrosion [424]. In another study, the corrosion behavior of Fe-based samples was found to be strongly dependent on SPS parameters, resulting in the formation of an oxide layer on the alloy surface [410]. The oxide layer, enriches in Cr and Mo under suitable conditions, induces a passive state with a steady current. Porosity, which increases with crystallinity, along with surface defects, promoted localized corrosion. Additionally, non-uniform porosity distribution affects corrosion resistance, and the presence of surface roughness and interconnected pores facilitates localized corrosion, particularly if the oxide layer lacks strength. Moreover, Li et al. [428] studied  $\text{Mg}_{66}\text{Zn}_{30}\text{Ca}_4$  BMG samples with different particle sizes (22.9, 45.4, and 62.4  $\mu\text{m}$ ) prepared by SPS. Particle size affected mechanical properties and corrosion behavior. Increasing particle size led to reduced strength and hardness, while larger particles showed improved long-term corrosion resistance [44].

Powder consolidation by HP and SPS is a suitable method for fabricating BMG composites (BMGCs) through solid-state sintering as it allows for precise control of microstructure, particle size, and volume fraction. During sintering of MG powders in the SLR, BMGCs

can be fabricated in-situ by partial devitrification of the amorphous alloy [429], or ex-situ by adding microcrystalline phase as the secondary phase into the amorphous matrix [430]. Alternatively, MG powders can be used as a reinforcement in metallic matrix composites [431].

By employing a time–temperature–crystallinity diagram, Kelly et al. [432] successfully developed BMGCs of SAM2X5 ( $\text{Fe}_{49.7}\text{Cr}_{17.1}\text{Mn}_{1.9}\text{Mo}_{7.4}\text{W}_{1.6}\text{B}_{15.2}\text{C}_{3.8}\text{Si}_{2.4}$ ) with varying degrees of devitrification. Additionally, they incorporated tungsten and tantalum particles into the composites (ex-situ) to tune the microstructure at different scales. Further, high compressive strength (780 MPa) and fracture strain (2 %) was achieved in SPSed Al- $\text{Fe}_{66}\text{Cr}_{10}\text{Nb}_5\text{B}_{19}$  MGCs, which was attributed to the reinforcing element  $\text{FeAl}_3$  formed through aluminum-MG interaction. In addition, Cu-coated Cu-Zr-Al BMGC demonstrated exceptional properties, including high strength (721 MPa), high electrical conductivity (35.02 % IACS), and significant plasticity (13.1 %) when the powder particle size of the Cu-Zr-Al BMG was below 15  $\mu\text{m}$  [433,434].

Extensive research has been conducted on the magnetic properties of Fe-based BMGs and BMGCs fabricated through thermal sintering. In this context, amorphous FINEMET ( $\text{Fe}_{73.5}\text{Si}_{13.5}\text{B}_9\text{Nb}_3\text{Cu}_1$ ) powders were successfully consolidated into a nanocrystalline BMGC using SPS, achieving a density of approximately 97 % [435]. The BMG volume consisted of Fe(Si) nanocrystals with an average size of 9 nm, comprising approximately 84 % of the material. The sintered sample displayed a magnetization of 122.9 emu/g and coercivity of 123 A/m. The consolidation mechanisms during SPS involved particle rearrangement followed by viscous flow, with an activation energy of 22.9 kJ/mol. In addition, the BMGCs comprising FeSiCrB MG ribbons (Metglas 2605SA3 alloy) and  $\text{Fe}_x\text{N}$  ( $x = 2-4$ ) powder showed improved magnetic performance and high stacking factors, approaching 100 % in amorphous ribbon/iron nitride configurations [436]. Additionally, the hot-pressed nanocrystalline/amorphous Nd-Fe-B magnets achieved a density of 7.5  $\text{g}/\text{cm}^3$  above 650  $^\circ\text{C}$ , providing optimal magnetic performance with an optimum energy product  $(BH)_{\text{max}}$  of 282.5  $\text{kJ}/\text{m}^3$  and intrinsic coercivity of  $H_{\text{cj}} = 1130.0$  kA/m. Fine platelet-like grains measuring 410–440 nm in length contributed to favorable magnetic properties between 625 and 675  $^\circ\text{C}$  [437]. Moreover,  $\text{Fe}_{84}\text{Si}_7\text{B}_5\text{C}_2\text{Cr}_2$  soft magnetic amorphous powders compacts could be smoothly prepared using SPS at temperatures above 773 K. Increasing the sintering temperature led to higher density, saturation magnetization, coercivity, and compressive strength of the compacts [414].

#### 5.3.4. Mgs as metallic glue

In contrast to previous methods of manufacturing MG matrix composites, such as process-induced second phase formation [179,383], SPS sintering [438], 3D printing [439], and others [440], some recent research has discovered that MGs have a certain adhesion in the SLR, and a number of composites have been developed to take use of this property. Ma et al. [441] used Fig. 26a to describe the preparation of composites that use the adhesive properties of MGs, with MG powder particles and additive particles uniformly mixed with different mass fractions; the composite material can be obtained by pressing and forming the mixed powder in the SLR. The breakdown of the oxide layer at the interface region during processing is believed to be the cause of the tight bonding mechanism between the MG and the composite [442]. Currently, it has been demonstrated that this type of metallic glue may be utilized for bonding a variety of materials, including metal to non-metal and conductor to insulator. A variety of materials are bonded together with metallic adhesive in Fig. 26b [200,441,443].

The mentioned composite materials also have some potential applications in some different fields. MGs have limited uses since they are not deformable at room temperature. The composites developed by Ma et al. [441] were shown to be plastic and to retain their corresponding strength, and the gradient of strength and plasticity was created by artificially adjusting the MG and the powder of admixture (Fig. 27a). The composites were created by bonding MGs to other materials with excellent room temperature plasticity.

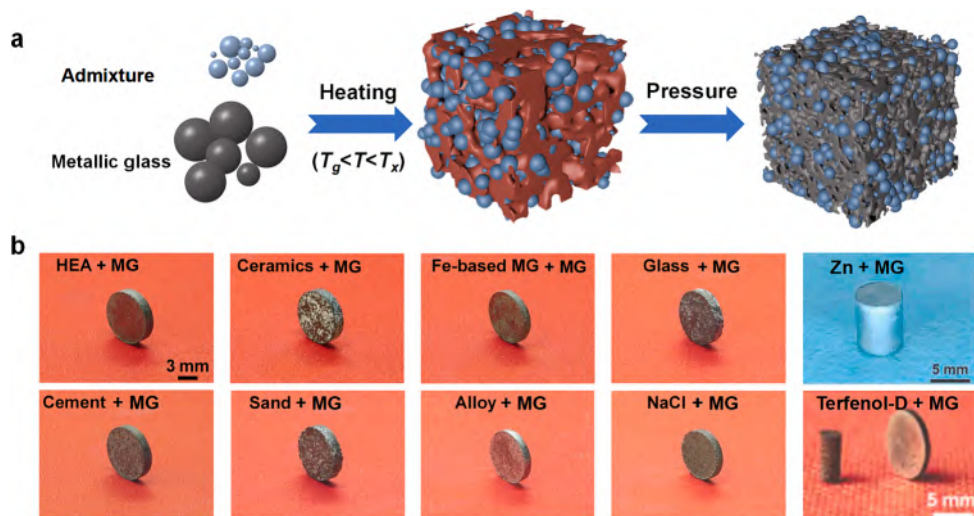


**Fig. 26.** (a) Schematic diagram of metallic glue used for bonding admixture, (b) Composite materials obtained by metallic glue. . Adapted from [200,441,443]

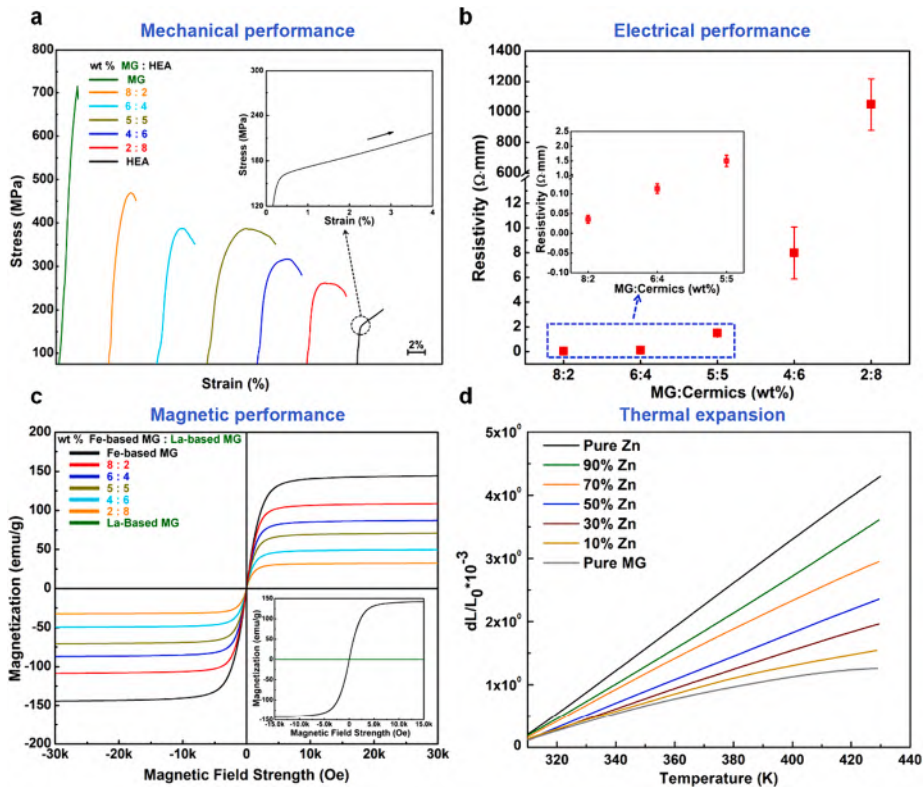


Fig. 27. (a) Regulation of mechanical performance. Adapted from [441]. (b) Regulation of electrical performance. Adapted from [441]. (c) Regulation of magnetic performance. Adapted from [441]. (d) Regulation of thermal expansion. Adapted from [443].

Additionally, control is also gained over other conventional electrical (Fig. 27b), magnetic (Fig. 27c), thermal expansion (Fig. 27d), and magnetostrictive [200,443,444].

The advantages of structural adjustment are included in these strategies in addition to performance adjustment. The application of this method to structural regulation is illustrated in Fig. 28a [441]. Metallic glue was utilized for bonding water-soluble components, such as NaCl, and water was then used to dissolve the composite to create the desired porosity structure. Porous MGs will maintain the intrinsic structure of the amorphous state (Fig. 28b). The size of the particles introduced to the composite can affect how porous the structure is. Fig. 28c–e illustrates the porous structures made from NaCl with various particle sizes.

## 6. Joining and welding of MG components

The welding and joining techniques have emerged as vital approach in the fabrication and assembly of MG components. Welding and joining strategy can enable the integration of MG components into complex structures, facilitate repairs, and enable the combination of MGs with dissimilar metals and alloys. With their exceptional mechanical properties and unique characteristics, MGs offer immense potential for a wide range of applications. By understanding and utilizing the diverse welding and joining techniques available, researchers and engineers can unlock the full potential of MGs and pave the way for the development of innovative and high-performance material systems.

This section provides a comprehensive review of welding and joining methods for MGs and their resulting joint structure and properties. The techniques are classified into three categories: fusion welding, supercooled liquid state welding, and solid-state welding. Fusion welding involves melting the base MGs to create a joint, while supercooled liquid state welding and solid-state welding achieve joining without melting by applying pressure and/or heat. Supercooled liquid state welding specifically utilizes the SLR of the MGs to form the bond, while solid-state welding achieves coalescence at lower temperatures. Both supercooled liquid state welding and solid-state welding may involve some localized melting at the joint interface, but the extent and characteristics of this melting differ from those in fusion welding.

### 6.1. Fusion welding

#### 6.1.1. Laser welding

Laser welding has emerged as a highly efficient and precise technique for joining metals. By harnessing the power of laser beams, this process offers several advantages such as narrow and well-defined weld seams, minimal HAZs, reduced risk of distortion, and fast

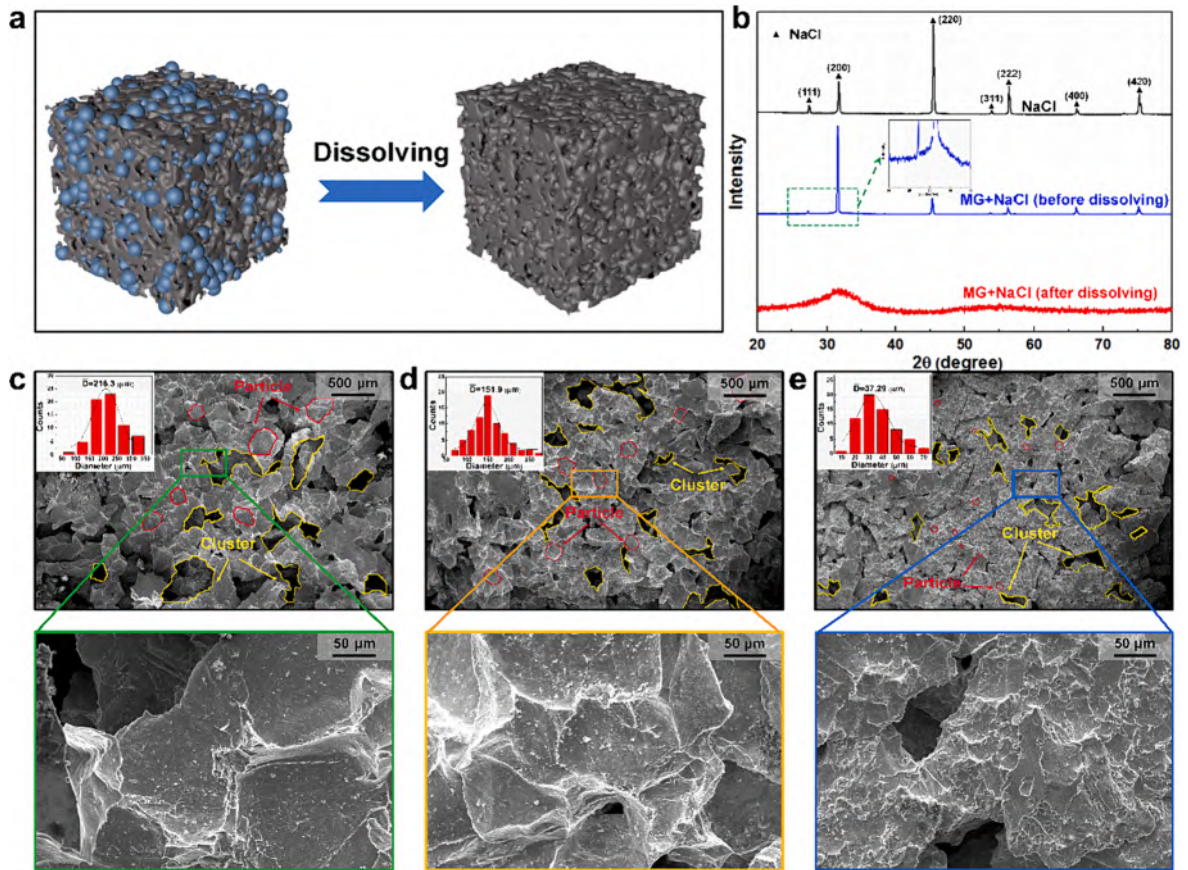


**Fig. 28.** (a) Schematic diagram of porous structure formed by dissolving water-soluble components, (b) Internal structure analysis by X-ray diffraction, (c)–(e) Porous structures with different pore sizes. . Adapted from [441]

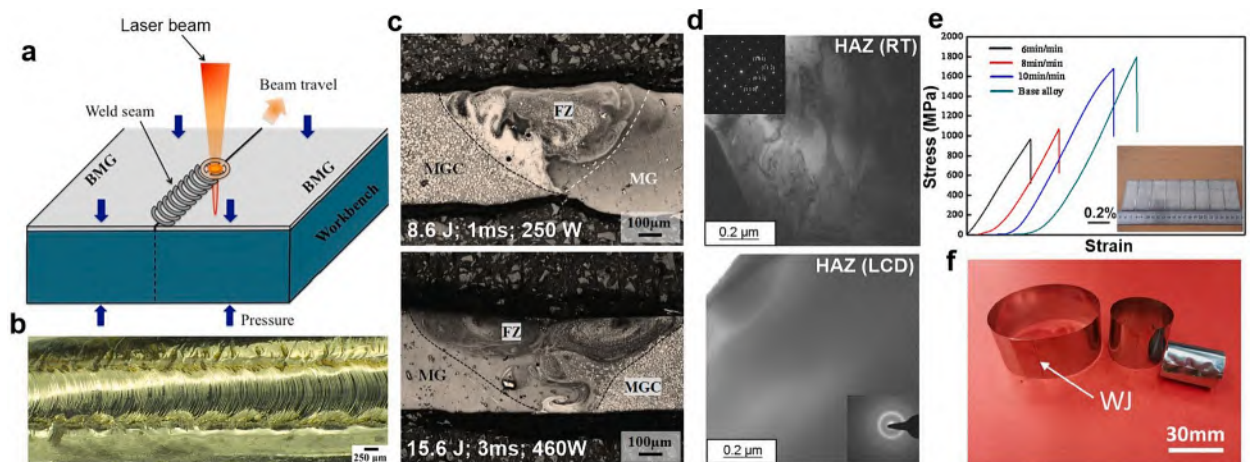


**Fig. 29.** (a) Schematic of the pulsed laser butt welding. (b) Morphology of bead-on-plate of Pd<sub>43</sub>Cu<sub>27</sub>Ni<sub>10</sub>P<sub>20</sub> BMG obtained by laser welding. Adapted from [451]. (c) Microstructures of the welded joints (Adapted from [453]) (d) TEM analysis HAZ area welded in room temperature and with a working liquid cooling device (LCD). Adapted from [459]. (e) Tensile stress–strain curves obtained from base alloy and welded samples with the inset showing a BMG plate welded at 10 m/min welding speed (Adapted from [452]). (f) Welded bracelets with different diameters (WJ: welding joint). Adapted from [447].

heating and cooling rates. Laser welding proves to be highly advantageous when it comes to BMGs. The reason behind this is the size limitations inherent in manufacturing BMG components, making it crucial to establish an effective joining method in order to expand the scope of engineering applications for BMGs [171].

In 2006, Li et al. [445] successfully joined  $Zr_{45}Cu_{48}Al_7$  BMGs without crystallization using laser welding for the first time. At a scanning speed of 8 m/min and laser power of 1200 W, no visible cracks or crystallization were observed in the weld bead and heated-affected zone. Rapid cooling below 430 °C prevented crystallization in the HAZ and facilitated glass formation in the bead. Since then, several pieces of work have reported laser welding of MG parts with different compositions, including Zr-based [446–449], Fe-based [447], Cu-based [450], Pd-based [451], and Ti-based [452,453] MGs. Dissimilar joining of Zr-based BMGs to crystalline metals and alloys such as Zr [454] has been also accomplished by laser welding. Additionally, weldability of in-situ [455,456] and ex-situ [457,458] BMGCs using laser welding has been also taken into consideration.

In the laser welding process of BMGs (as illustrated in Fig. 29a), two BMG sheets are placed on a workbench and pressed together to ensure tight contact between the alloy and the workbench, as well as between the alloy plates themselves. A laser beam is then applied to the joint, moving in the direction indicated by the orange arrow. This results in the formation of a weld seam at the joint of the specimen [451]. Fig. 29b shows a porosity-free weld seam of  $Pd_{43}Cu_{27}Ni_{10}P_{20}$  BMG after bead-on-plate experiments in air, showing no visible oxidation. During laser welding process, the BMG parts are usually protected by argon atmosphere to avoid oxidation.

During laser welding, the microstructures within the fusion zones (FZs) of the welded joint can differ from the base materials produced through casting, leading to alterations in mechanical properties. Consequently, it is crucial to comprehend the effects of laser welding parameters (i.e., laser power, welding speed, and pulse duration) on material solidification, particularly the evolution of phases and microstructures within the FZ and the corresponding welding quality.

Wang et al. [460] laser welded two different types of Ni-free Zr-Cu-Ag-Al and Zr-Cu-Ni-Al BMGs using three energy inputs of 6.2 J, 8.0 J, and high 9.2 J. The Zr-Cu-Ni-Al BMG weld crystallized at the lowest energy input, while the Zr-Cu-Ag-Al BMG welds remained crystallization-free in the HAZ and weld FZs. This preserved the GFA and microhardness of the Zr-Cu-Ag-Al BMGs, unaffected compared to the unwelded plates. Further, using a wide range of laser power (750–1124 W) during pulsed laser welding of  $Pd_{43}Cu_{27}Ni_{10}P_{20}$  BMG resulted in weld seams without crystallization [451]. In another study, Chen et al. [453] investigated laser welding of dissimilar Ti-based BMGs, focusing on laser energy and pulse duration effects. Crack-free, inclusion-free welded joints between Ti-based MG and Ti-based MGC were observed (Fig. 29c). Metallurgical bonding showed a smooth FZ-to-base metal (BM) transition. Laser pulse width influenced FZ size, while welding speed had minimal impact. Non-uniform microstructures, similar to other dissimilar laser-welded joints, in the FZ suggested incomplete mixing of molten BMs. In addition, increased laser pulse energy and duration resulted in  $\beta$ -Ti grain growth from spherical to dendritic shape, with maximum size around 1  $\mu$ m. Grain refinement due to rapid cooling resulted in microhardness of ~ 470–525 HV and average tensile strength of ~ 1510 MPa in welded joints.

Welding initial temperature can also significantly influence the microstructure and mechanical properties in welded BMGs. Wang et al. [461] studied the effects of initial welding temperature and parameters on crystallization in laser spot welded ( $Zr_{53}Cu_{30}Ni_9Al_8$ )  $Si_{0.5}$  BMG. Crystallization-free HAZ was achieved through welding with lower energy input and initial temperature. They also developed a liquid cooling device (LCD) for lower welding temperatures, preventing crystallization in Zr-Cu-Ni-Al-Si [459] and Zr-Al-Co-Ta [448] BMGs. The selection of a suitable initial temperature emerges as a critical criterion for weldability, specifically denoting the cooling temperature maintained under the LCD. A lower initial temperature implies a faster cooling rate, resulting in a shorter retention time ( $R_{T_m/T_g}$ ) between the onset of melting ( $T_m$ ) and  $T_x$  during the welding process. This significantly mitigates the risk of crystallization. For instance, considering Zr-Al-Co MGs as an exemplar, at an initial temperature of 0 °C, the  $R_{T_m/T_g}$  is 55.58 ms, whereas at room temperature, the  $R_{T_m/T_g}$  is 61.92 ms.

TEM images and SAED patterns (Fig. 29d) showed crystallization in the HAZ of the room temperature sample but not in the LCD sample [459]. Hardness decreased in the crystallization area in the sample welded at room temperature but remained unaffected in the crystallization-free HAZ compared to the as-cast plate.

Another processing parameter affecting structure/properties in welded samples is welding speed. Kim et al. [450] studied  $Cu_{54}Ni_6Zr_{22}Ti_{18}$  BMG welding speeds using a pulsed Nd:YAG laser. At 60 mm/min, no crystallization occurred in the weldment and HAZ, while at 20 mm/min, band-shaped crystallized areas were observed. Kawahito et al. [446] explored ultra-high-speed welding of  $Zr_{55}Al_{10}Ni_5Cu_{30}$  BMG at 48 and 72 m/min. At 48 m/min, wide weld beads with crystalline peaks were observed, while at 72 m/min, no crystallization was found. Wang et al. [452] examined  $Ti_{40}Zr_{25}Ni_3Cu_{12}Be_{20}$  BMG welding at different speeds of 6 m/min, 8 m/min, and 10 m/min and constant laser power of 3.5 kW. While lower welding speeds yielded crystallization in the welded area, welding at 10 m/min resulted in amorphous FZ and HAZ without defects. The tensile stress–strain curves of  $Ti_{40}Zr_{25}Ni_3Cu_{12}Be_{20}$  joint and base alloy exhibited characteristic behavior of brittle fracture without yielding (Fig. 29e). The welded samples at 6 m/min and 8 m/min speeds had fracture strengths of 950 MPa and 1100 MPa, respectively. Notably, the sample welded at 10 m/min showed a tensile strength of 1650 MPa, 93 % of the parent BMG sample. A photograph in the inset of Fig. 29e showcases a sample welded from eight BMG plates using optimal laser welding parameters: a welding speed of 10 m/min and a laser power of 3.5 kW.

The microstructural evolution and welding quality during laser welding of BMGs depend not only on the processing parameters but also on the microstructure of the as-cast BMG. In a study conducted by Chen et al. [462], different welding speeds and annealing conditions influenced the microstructure and welding quality during laser butt welding of  $Zr_{55}Cu_{30}Ni_5Al_{10}$  BMG sheets. Annealing at 415 °C for 10 min resulted in an amorphous structure with few nanoparticles. The annealed joint exhibited higher hardness and strength, but excessive annealing was detrimental to the BMGs. Furthermore, Shao et al. [449] found that pre-existing nuclei affects the crystallization behavior of Zr-based BMGs during laser welding. Higher nucleus density increased the likelihood of crystallization under the same welding conditions. Laser welding resulted in an amorphous FZ and a crystallized HAZ due to nucleus accumulation. The TTT curve for BMGs with nuclei showed an unusual  $\varepsilon$  shape instead of the typical C shape, revealing differences in heating and

cooling processes.

Compared to continuous lasers, pulsed lasers have demonstrated potential as a heat source for welding due to their small duty cycle and extremely high pulse power, enabling amorphous alloys to cool at a faster rate during the welding process [450,451,453]. While ms-pulsed lasers are mainly used for welding BMG parts, ns-pulsed lasers with shorter durations and lower power densities are better suited for MG ribbon welding. Recently, ns-pulsed laser welding was studied on  $\text{Fe}_{78}\text{Si}_9\text{B}_{13}$ ,  $\text{Zr}_{65}\text{Cu}_{15}\text{Ni}_{10}\text{Al}_{10}$ ,  $\text{La}_{55}\text{Ni}_{20}\text{Al}_{25}$ , and  $\text{Ce}_{65}\text{Al}_{10}\text{Cu}_{20}\text{Co}_5$  MG ribbons [447]. Successful welding without crystallization was achieved by adjusting the laser parameters. Fig. 29f represents welded bracelets with different diameters made of  $\text{Fe}_{78}\text{Si}_9\text{B}_{13}$  MG ribbons.

### 6.1.2. Electron beam welding

Electron beam welding (EBW) is a versatile joining technique that has gained significant attention in recent years due to its capability to weld a wide range of materials, including BMGs. The application of EBW in welding BMGs offers numerous advantages, including high precision, minimal distortion, rapid cooling rates, and the ability to achieve strong and defect-free welds. EBW provides concentrated welding energy and offers advantages such as lower heat input, deep and narrow welds, minimal heat affected zones, and rapid cooling rates. To ensure optimal results, EBW requires a vacuum environment to control contamination, prevent oxidation, and avoid gas bubble formation.

Liquidmetal Technologies [463] has successfully employed the EBW method for post-processing cast BMGs and fabricating larger structures. Fig. 30a illustrates a butt-joint of 9.6 mm wide plates, showcasing a flawless and void-free joint with minimal crystallization. Interestingly, the weld exhibited a beaded appearance in the 3.6 mm wide specimen, while appearing nearly flush with the two parent plates of 9.6 mm width. This observation suggests the precise control achieved during the welding process. Moreover, the Vickers microhardness values across the joint interface are found to remain constant, indicating a highly uniform and featureless joint.

The EBW has been successful in welding Ti-based [464] and Zr-based [467] BMG sheets and dissimilar welding of Zr-based BMGs to Zr [468,469], Ti [470,471], Ni [465], and stainless steel [466]. For instance, Kawamura et al. [469] achieved successful EBW of 3.5 mm thick Zr-based BMG plates for the first time by using 60 kV electron beam acceleration voltage, 15–20 mA beam currents, and a scanning speed of 33 mm/s. The welded  $\text{Zr}_{41}\text{Be}_{23}\text{Ti}_{14}\text{Cu}_{12}\text{Ni}_{10}$  BMG plates showed no crystallization in the bead and HAZ, with no visible defects or cracks. The tensile strength of the welded BMG matched that of the original BMG. However, EBW of  $\text{Zr}_{55}\text{Cu}_{30}\text{Al}_{10}\text{Ni}_5$  BMG plates under the same conditions resulted in crystallization in the bead and HAZ [467]. Furthermore, attempts to weld the  $\text{Zr}_{41}\text{Be}_{23}\text{Ti}_{14}\text{Cu}_{12}\text{Ni}_{10}$  BMG plate to Ti metal failed due to the formation of brittle intermetallic compounds. In contrast, successful welding to Zr

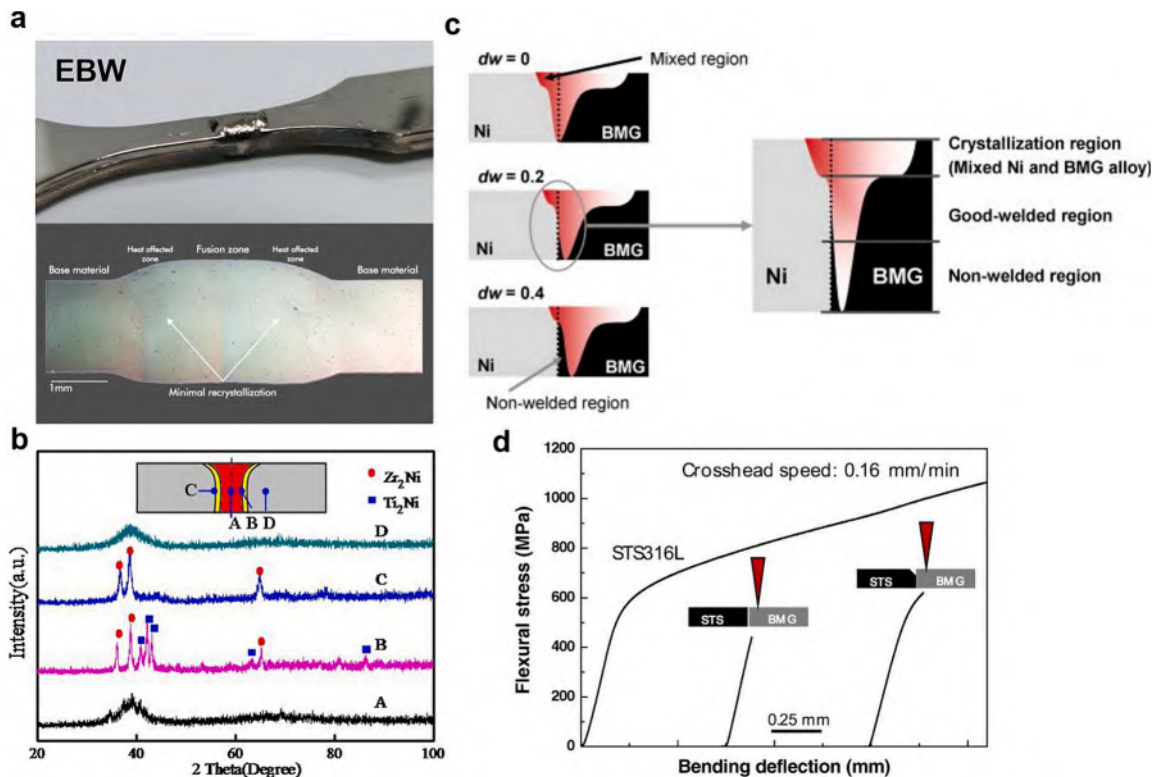


**Fig. 30.** (a) Electron beam welded butt-joint of BMG plates and the corresponding joint optical micrograph (Adapted from [463]). (b) Micro-XRD patterns of welded Ti-based joint at different zones (Adapted from [464]). (c) Schematic diagrams for shape of melting region according to different electron beam irradiation positions (dw) (Adapted from [465]). (d) Flexural stress–deflection curves of the STS316L steel and welded samples with varying STS316L weld design (Adapted from [466]).

metal produced a ductile interface.

Furthermore, the degree of crystallization can vary among different regions of the joint. An example is seen in the micro-focused XRD patterns obtained from various regions across the joint interface of an EBWed Ti-based BMG joint, as depicted in Fig. 30b [464]. In region A, faint diffraction peaks suggest the presence of a nanocrystalline phase. Region B exhibits clear diffraction peaks, indicating a mixture of  $Zr_2Ni$  and  $Ti_2Ni$  phases. Meanwhile, distinct diffraction peaks of  $Zr_2Ni$  phases are observed in region C. Finally, region D shows a broad halo pattern, signifying the presence of the glassy phase in the bead material. These variations in the microstructure within different regions of the joint illustrate the complexity of the welding process and its impact on the resulting joint properties.

Another parameter influencing microstructure and mechanical properties of joint is electron beam irradiation position [465]. The schematic diagram in Fig. 30c illustrates the melting regions resulting from electron beam welding of a Zr-based BMG to Ni metal at different beam irradiation positions. The higher thermal conductivity and melting temperature of Ni make achieving the melting temperature challenging. Increasing the distance of the beam irradiation position from the interface reduces the melting region of the Ni metal. This melting process can alter the chemical composition of the weld by mixing BMG and Ni metal. The welding process is highly dependent on the distance, and deviations can impact critical cooling rate and properties of the joint. The shape of the melting region can be controlled by adjusting welding parameters, such as beam current and welding speed.

Kim and Kawamura [466] recommended a specific specimen design to control the melting of STS316L steel during EBW of BMG to stainless steel, resulting in flawless joints and minimized steel deformation. The designed STS316L steel sample exhibited a maximum flexural stress of 642 MPa (Fig. 30d), surpassing the yield strength of STS316L steel, indicating strong joint strength for industrial applications.

### 6.1.3. Reactive foil joining

Freestanding reactive foils consist of alternating layers of materials with a negative heat of mixing. When activated by an external source, such as a spark or flame, the layers undergo intermixing, initiating a self-propagating reaction. This reaction travels along the foil at velocities of 1 to 30 m/s, reaching temperatures of 1000 to 3000 °C [472].

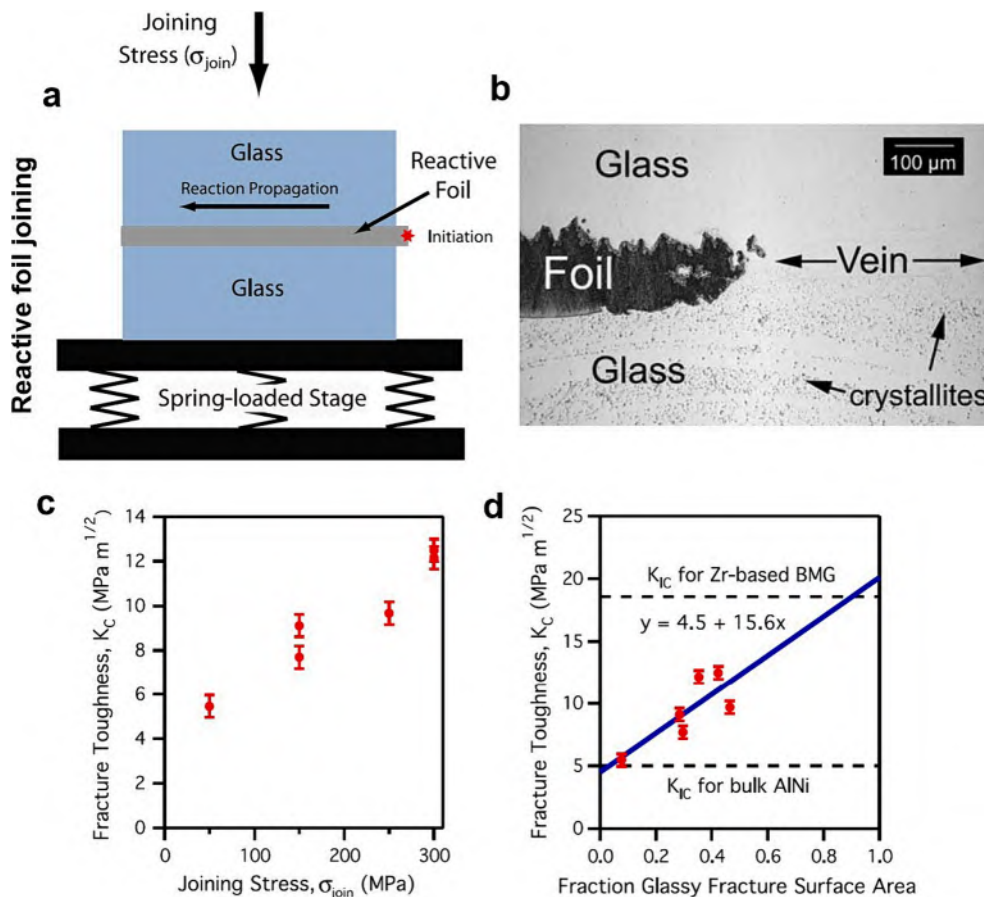


**Fig. 31.** (a) Schematic of the joining process using a spring-loaded stage. Adapted from [474]. (b) Optical micrograph of an etched foil-glass interface. The dark structure on the left is the reacted foil, and the solid region on the right is a metallic vein. Adapted from [473]. (c) Fracture toughness as a function of joining stress. (d) Fracture toughness as a function of joint that is glassy, the solid line is a linear fit to the data. Adapted from [474].

Reactive multilayers can be used as controlled heat sources for welding applications. According to numerical simulations [473], the  $Zr_{57}Ti_5Cu_{20}Ni_8Al_{10}$  MG in the vicinity of the interface between the glass and foil undergoes rapid heating at a rate of  $10^7$  K/s, reaching temperatures of approximately 1350 K, which surpasses the  $T_1$  the amorphous alloy (1115 K). Subsequently, rapid cooling occurs at a rate of  $10^5$  K/s once the reaction front has advanced.

Schematic of reactive foil joining process is shown in Fig. 31a. A reactive foil is inserted between MG segments and pressure is applied using a load frame and foil reaction is initiated by a spark [474]. Fig. 31(b) shows an etched foil-glass interface. The lower component contains dispersed crystallites, while the upper component shows no discernible crystals near the interface or within the bulk region [473]. Rapid heating and cooling during reactive joining minimize crystallization in MGs, as supported by simulations and experiments.

Increasing the applied joining stress positively influences the fracture toughness of a Zr-based BMG (Fig. 31c). At 300 MPa, the fracture toughness exceeds half of the mode I fracture toughness of fatigue-precracked Zr-based BMG. Fig. 31d reveals a correlation between fracture toughness and the fraction of MG ligaments on fracture surfaces, following a rule of mixtures. Joints with higher glassy ligament content approach the mode I fracture toughness of fatigue-precracked Zr-based BMGs. Joints lacking glassy ligaments, consisting of glass/AlNi interfaces and partially devitrified glass, exhibit fracture toughness similar to crystalline AlNi. Interfacial toughness between glass and AlNi is primarily governed by AlNi plasticity, with minimal contribution from BMG plasticity [474].

## 6.2. Supercooled liquid state welding

### 6.2.1. Friction welding techniques

Friction welding involves generating heat at the interface between two materials through controlled frictional rubbing. Notably,

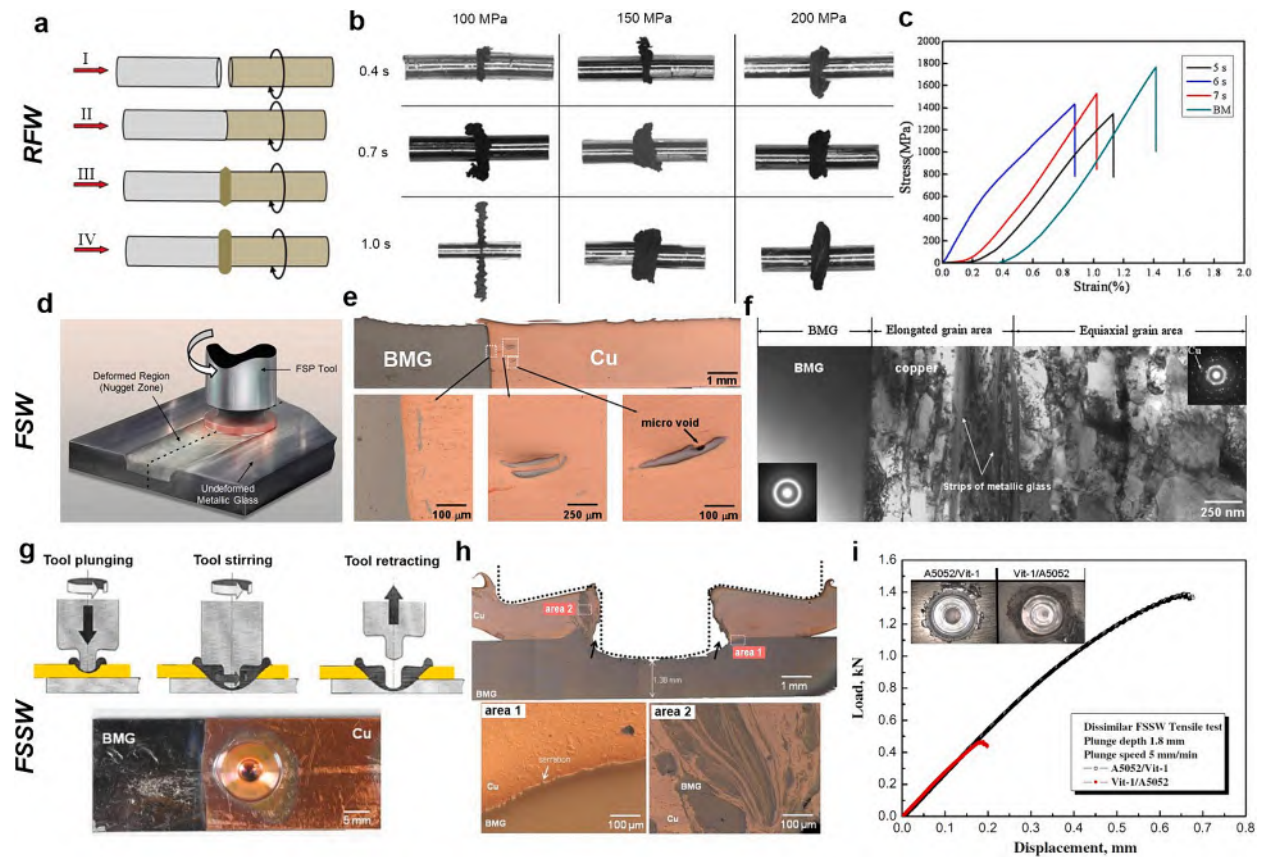


**Fig. 32.** (a) Basic steps in rotary friction welding (Adapted from [476]). (b) Appearance of friction welded  $Zr_{55}Al_{10}Ni_5Cu_{30}$  BMG specimens fabricated under different pressures and times (Adapted from [480]). (c) Nominal tensile stress–strain curves obtained from the welded samples at different processing times (Adapted from [485]). (d) Schematic of friction stir processing. Adapted from [486]. (e) Optical microscopy images showing the cross-sectional macrostructure of the stir zone perpendicular to the welding direction (Adapted from [487]). (f) TEM image showing the microstructural transition across the BMG/Cu interface (Adapted from [487]). (g) Schematic diagram showing the principle of the friction stir spot welding technique and appearance of the spot FSW processed Cu/BMG joint (Adapted from [488]). (h) Cross-sectional microstructure of the friction stir spot welded BMG to copper and enlarged optical microscopy image of area 1 and area 2 (Adapted from [488]). (i) Load-displacement curves obtained after tensile-shear tests for dissimilar FSSW between BMG and crystalline metals, inset shows appearances of surface views at stirred part for each material configuration (Adapted from [489]).

friction welding does not require the use of filler metal, flux, or shielding gas [475]. Friction welding encompasses several distinct techniques, each offering unique advantages and applications [476].

Friction welding operates without melting BMG plates, preserving its amorphous structure and unique properties. The absence of a liquid phase eliminates concerns about solidification defects and composition changes. BMG compositions with wide SLR and large GFA are required to establish metallurgical bonding of BMG using frictional welding [477]. The  $Zr_{55}Cu_{30}Ni_5Al_{10}$  BMG, exhibiting excellent GFA with a wide SLR [478], has been extensively used in friction welding studies.

Rotary friction welding (RFW) is a solid-state (non-fusion) joining technique that achieves material coalescence through the application of compressive force while the workpieces rotate or move relative to each other. The fundamental steps of RFW are illustrated in Fig. 32a [476]. In the initial stage (I), one of the workpieces is set in rotation while the other remains stationary. Once the desired rotational speed is achieved, the two workpieces are brought into contact, and an axial force is applied (II). The friction generated at the interface leads to localized heating, initiating the process of upsetting (III). Finally, the rotation of the workpiece is halted, completing the upsetting process (IV). The resulting friction weld exhibits distinct characteristics, including a narrow HAZ, thermoplastically deformed material surrounding the weld (flash), and the absence of FZ. RFW has been successfully used in joining Pd-based [477,479] and Zr-based [480–482] BMGs as well as dissimilar joining of Zr-based/Pd-based [483,484] BMGs and Zr-based BMG/Al [484].

The RFWed BMG rods show protrusions at the interface [480,482,485], varying in shape and volume based on friction pressure and time (Fig. 32b) [480]. These protrusions result from outward displacement and thermoplastic deformation of the material under axial friction pressure. Elevated temperatures facilitate their formation by exceeding the glass transition temperature ( $T_g$ ). Expulsion of the oxide film establishes metallurgical bonding [484]. Tensile tests on welded samples (Fig. 32c), compared to base materials (BM), exhibit elastic deformation followed by brittle fracture. Ultimate strength can reach up to 1540 MPa, with the 7 s friction time achieving 90 % of the base BMG strength (1710 MPa), indicating excellent metallurgical bonding.

Another friction welding technique is friction stir welding (FSW). FSW involves a rotating tool with a specially designed pin that is inserted between the components to be joined (Fig. 32d). As the tool moves along the joint line, it generates friction and heat. The softened material undergoes thermoplastic deformation and mixing, resulting in a metallurgical bonding upon cooling. The nugget zone represents the region with extensive plastic deformation [486].

$Zr_{55}Cu_{30}Ni_5Al_{10}$  BMG plate was successfully FSWed without crystallization using optimized welding conditions [490,491]. Flash formation was minimized with a 25 mm shoulder diameter and a 3-degree recessed angle on the shoulder surface, preserving the amorphous structure and mechanical properties of the MG. Moreover, Vitreloy 106a was friction stir welded without altering its amorphous state. Optimal FSW conditions (400 rev/min rotational speed, 25.4 mm/min traveling speed) produced defect-free welds with increased amorphicity and reduced short range order domain size [492]. Atomic-scale structural evolution was observed through decreased nearest atom distances at all locations after FSW.

Regarding dissimilar FSW of BMG components with crystalline metals and alloys, defect-free joints between  $Zr_{55}Cu_{30}Ni_5Al_{10}$  BMG and 7075-T651 alloy were achieved by offsetting the pin to the aluminum side [493]. The nugget zone consisted of fine recrystallized aluminum grains with some BMG particles. No crystallization or reaction layer was detected, and the joint strength reached 74 % of the 7075 alloy. Failure occurred in the nugget zone on the aluminum side, indicating good bonding but slight reduction in strength due to large BMG particles. Similar behaviors was observed during FSW of  $Zr_{46}Cu_{46}Al_8$  BMG plate with pure Al plate [494].

The FSW of BMG/pure Cu yields a clear BMG-Cu interface (Fig. 32e), indicating successful defect-free welding [487]. Unlike previous joints, no mixed area is observed due to minimal tool-BMG contact. However, irregularly shaped BMG fragments dispersed in the copper side are present, some with micro-voids suggesting incomplete filling. The interface microstructure (Fig. 32f) shows the maintained amorphous structure on the BMG side and transitional microstructure with elongated copper grains as a result of extrusion between the rotating probe and the hard BMG plate.

Friction stir spot welding (FSSW) is another type of friction welding technique which is used to create spot welds between two overlapping metal sheets (Fig. 32g). It is a variation of FSW that is specifically designed for spot welding applications. FSSW involves inserting a rotating tool into the upper plate while applying a fixed load, stirring the material for complete mixing and bonding. The tool is then retracted to conclude the welding process.

Jamili-Shirvan et al. [495] studied a FSSWed joint of  $(Ti_{41}Zr_{25}Be_{28}Fe_6)_{93}Cu_7$  BMG. Different regions were identified in the weld spot, including the BM, shoulder stir zone (SSZ), tip stir zone (TSZ), and thermo-mechanically affected zone (TMAZ) between BM and SSZ. Vickers micro hardness testing revealed distinct hardness and elastic modulus characteristics among the regions. Pop-in marks on the nanoindentation load–displacement curves indicated tensile stress in TSZ, excess free volume in TMAZ, and nanocrystal formation in SSZ during welding.

Sun and Fujii [488] joined  $Zr_{55}Cu_{30}Ni_5Al_{10}$  to pure Cu by FSSW using a rotation speed of 400 rpm, an applied load of 1000 kg, and a dwell time of 2 s. The welded Cu/BMG joint (Fig. 32g, lower part) showed no cracks or fractures on the BMG plate despite its inherent brittleness. Further, the presence of a keyhole at the center of the joints, typical for spot welds, was observed (Fig. 32h). In addition, two welding zones, labeled as area 1 and area 2, were observed. In area 1, the interface between the Cu and BMG plates appears clean without defects, but small serrations suggest deformation or wear on the BMG plate. Area 2 displays a microstructure with a high density of BMG fragments embedded in the Cu plate, showing significant plastic deformation.

In another study, Shin and Jung [489] discovered that the configuration of the specimens during dissimilar FSSW affects the fracture load (Fig. 32i), with higher loads observed when the crystalline metal was positioned on the upper side. This was attributed to the effective stirring of the BMG alloy, which led to the penetration of BMG particles into the Al alloy side, resulting in a strong joint. This is similar to FSSW of BMG to Cu [488], where only BMG fragments mix into crystalline materials, and no crystalline materials mix into the BMG plates. Later, they investigated the characteristic features of applying FSSW to Zr-based BMG sheets and discussed the

effects of plunge depth and plunge speed of the probe tool [496]. They showed that vertical load dropped when the temperature around the tool pin entered the SLR, while the weld interface temperature remained constant. The fracture load after FSSW increased with plunge depth but was unaffected by speed. Successful joining and high fracture load occurred with a well-formed stir zone in the supercooled liquid region.

6.2.2. Diffusion bonding

To prevent crystallization in BMGs during fusion-based welding, extremely high welding speeds are needed to achieve rapid solidification of the melt pool beyond the critical cooling rate. On the other hand, friction welding techniques facilitate bond formation in the supercooled liquid state below  $T_x$  of BMGs through enhanced elemental inter-diffusion and mechanical interlocking. Nevertheless, it is important to avoid excessive frictional heating above  $T_x$ . Further, structural relaxation can occur in the HAZ of a welded BMG.

Diffusion bonding is a non-fusion joining process that involves the use of heat and pressure to create a bond between two solid materials. The initiation of the diffusion bonding process involves the plastic deformation of surface ridges in the weldments caused by the applied load [497]. As a result of this deformation, the fragile surface oxide layer fractures, and metal without oxide is extruded through the broken oxides, leading to the connection and bonding of the metal surfaces [498].

Diffusion bonding of BMGs shows great potential for joining large areas with controlled temperatures, offering an alternative to fusion-based and friction-based methods while helping suppress crystallization in BMGs. However, diffusion bonding poses challenges due to restricted atomic diffusion and the presence of a stable oxide layer on BMG surfaces [499]. Additionally, the high melting temperature of certain BMGs can impede elemental diffusion.

Temperature, pressure, and time are found to be crucial for successful bonding during diffusion bonding of BMGs within the SLR [500]. While diffusion bonding parameters shrink nano-voids and facilitate metallurgical bonding, they may not enhance material performance. Diffusion can cause structural relaxation and bulk embrittlement. Balancing these aspects is key for successful bonding and material utility. The optimal joining time for diffusion bonding is typically between 30 and 60 min, while the recommended pressure ranges from 50 to 150 MPa [499,501].

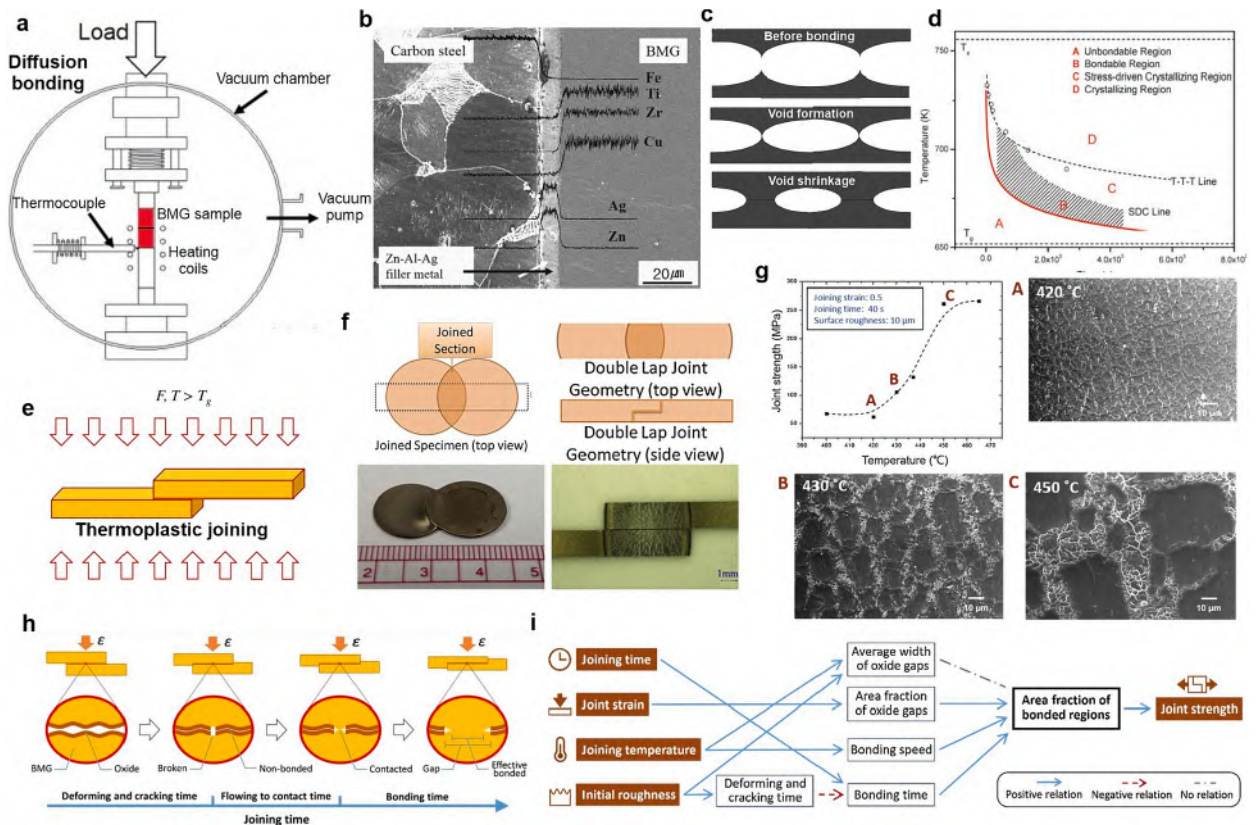


Fig. 33. (a) Schematic diagram of diffusion bonding (Adapted from [502]). (b) Electron probe microanalysis (EPMA) profile of the joint interface between  $Cu_{54}Ni_6Zr_{22}Ti_{18}$  BMG and SS400 carbon steel when using the Zn–Ag–Al filler metal (Adapted from [502]). (c) Schematic of diffusion bonding mechanism of BMGs (Adapted from [503]). (d) Prediction map showing relationship between temperature and time for high quality diffusion bonding (Adapted from [504]). (e) Schematic of thermoplastic joining of BMGs at the SLR. (f) Preparation of the lap shear test samples. Adapted from [505]. (g) Measured joint strength for various joining temperatures. The dotted line is guide for the eye. (h) Schematic of the mechanism of joining BMGs in the SLR (i) The influence of the joining conditions on the joint strength. Adapted from [506].

Kim et al. [502] examined the effects of interlayers using zinc-based fillers in dissimilar diffusion bonding/brazing of  $\text{Cu}_{54}\text{Ni}_6\text{Zr}_{22}\text{Ti}_{18}$  BMG and carbon steel (Fig. 33a). The soldering process at 713 K and 15 MPa for 3 min using Zn-Ag-Al filler resulted in a sound joint with an excellent bonding strength of 45 MPa, compared to 9 MPa for the sample joined with pure Zn filler. Significant changes in elemental profiles at the SS400-filler and BMG-filler interfaces were observed (Fig. 33b), indicating the absence of detrimental phase formation and diffusion. Enhanced wettability, surface-active elements, and suppressed intermetallic compound formation contributed to the improved bonding properties.

Additionally, Hongchao et al. [498] investigated the bonding of Zr-based BMG to crystalline Cu with and without a Ni-foil interlayer, observing the formation of a thin diffusion layer at the interface in both cases. However, the use of a nickel interlayer led to crystallization at the interface due to the higher bonding temperature required. As the order–disorder effect at the bonding interface hinders crystallinity matching in BMG/crystalline dissimilar couples, Wen et al. [22] employed copper and aluminum interlayers as transition materials for diffusion bonding of Zr-based BMGs. This strategy aims for a similarity in volume ratios between the interlayers and the BMG composition to promote elemental inter-diffusion and solid-state bonding in the SLR. MD simulations were also utilized to model the diffusion bonding interaction between oxidized BMG interfaces and crystalline alloys, providing insights into atomic interaction energies [504,507].

The diffusion bonding process can be divided into void formation and void shrinkage stages (Fig. 33c) [503]. The void formation stage occurs instantaneously and is not time-dependent. When pressure is applied, the contact area of the interface expands rapidly until it can withstand the applied pressure. Subsequently, the void shrinkage stage takes place, where high-quality diffusion bonding is achieved through plastic deformation and atomic diffusion as the bonding time increases.

In another study, Lin et al. [504] proposed a diffusion bonding for BMGs, considering the superplastic deformation behavior and Pilling's model [508]. The model identified two stages in the diffusion bonding process: plastic deformation and void shrinkage. The developed model accurately predicted bonding time for a Zr-based MG and presented a map for achieving high-quality bonding with optimal temperature and time (Fig. 33d). The map included regions for unbondable, bondable, stress-driven crystallizing (SDC), and crystallizing states. Perfect bonding without crystallization could be achieved within the shaded area below the TTT or SDC lines and above the predicted bonding time line (Region B).

Most studies in diffusion bonding of BMGs focused on preventing crystallization and surface oxide layer removal to facilitate solid-state bonding. Kuo et al. [501] characterized the joining behavior of similar and dissimilar BMGs, emphasizing the importance of GFA parameters such as  $\gamma$  ( $T_x/(T_g + T_l)$ ) and  $\Phi$  ( $T_{rg}(\Delta T_x/T_g)$ , where  $T_{rg} = T_g/T_l$  is the reduced glass transition temperature) in amorphous bonding quality. In addition, Xu et al. [509] developed a novel method for joining Zr-based BMG through high-speed heating, enabling rapid inter-diffusion and strong metallurgical bonding. By deforming Zr-based BMG and reducing viscosity in the supercooled liquid region, cavities were filled and crystallization was avoided. This approach achieved bonding timescales of microseconds with bonded strength comparable to the strength of BMG.

Further, Saadati et al. [510,511] studied diffusion bonding between a Cu-based BMG and pure aluminum at different temperatures and holding times. While BMGs undergo diffusion bonding within the temperature range of  $T_g$  and  $T_x$ , an optimal bonding temperature was determined to be 10 K below  $T_g$ . Various holding times were tested, and it was found that the diffusion couple could be effectively

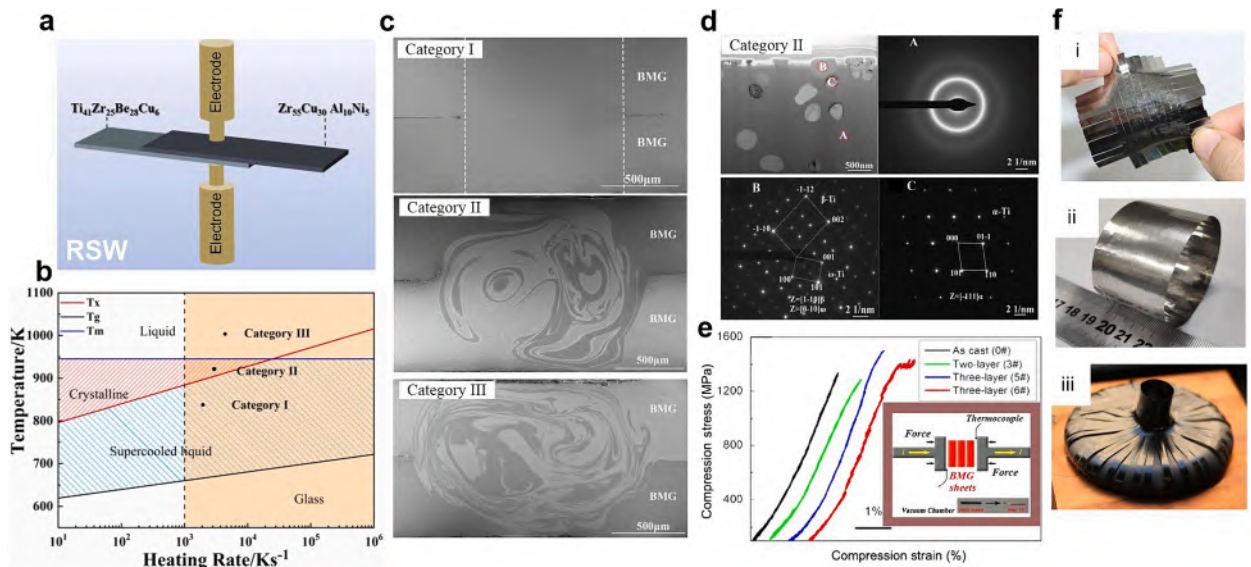


**Fig. 34.** (a) Schematic illustration of RSW (electro-pulse joining) of dissimilar BMG laminates (Adapted from [522]). (b) The SLR diagram of  $\text{Zr}_{35}\text{Ti}_{30}\text{Cu}_{7.5}\text{Be}_{27.5}$  at different heating rates. (c) Representative cross-sectional SEM images of the three categories joints. (d) TEM images of the category II joint (Adapted from [520]). (e) Compression stress–strain curves of the as cast, two-layer (3#) and three-layer (5# and 6#) BMGs. The inset shows schematic drawing of the process (Adapted from [318]). (f) i: Electromagnetic foils; ii: Thin-walled hollow cylinders; iii: Special-shaped part (Adapted from [526]).

bonded without crystallization occurring in the BMG side. A 1–2  $\mu\text{m}$  reaction layer formed at the interface, primarily on the BMG side, indicating oxygen accumulation and intermetallic compound formation through elemental diffusion.

Regarding surface oxide layer removal and improvements in the bonding quality during diffusion bonding, different methods have been explored including ion irradiation [503,512,513] and pre-friction assisted diffusion bonding [514,515]. Notably, these studies demonstrated that removing oxide films increased interfacial diffusion and enhanced bonding quality.

### 6.2.3. Thermoplastic joining

Diffusion bonding, which relies on long-range diffusion, typically requires joining times of  $\sim 30$ – $60$  min, similar to the timescales for crystallization within the SLR. However, the diffusion coefficient limitations and the absence of grain boundaries in BMGs pose challenges for achieving high diffusion rates during the bonding process. Further, the presence of stable oxide layers on BMG surfaces complicates the quality of diffusion bonding.

In 2014, Chen et al. [505] introduced a thermoplastic joining method for BMGs in ambient air based on the process of breaking the oxide film and refilling it with pristine MG. The process (Fig. 33e) involved heating BMG strips to the SLR, applying thermoplastic compression, and maintaining joint strain and time. Surface oxide fracture allowed pristine BMGs to flow through the cracks and establish metallic bonds, eliminating the need for controlled atmosphere or vacuum. In addition, within a typical timeframe of milliseconds to seconds for thermoplastic joining, the occurrence of crystallization can be effectively prevented.

A lap shear joint specimen was fabricated (Fig. 33f), and the shear strength increased with higher joining temperatures (Fig. 33g). Fracture morphologies (Fig. 33g) revealed that the width of the bonded regions increases with the joining temperature: approximately 1  $\mu\text{m}$  at 420  $^{\circ}\text{C}$ , 5  $\mu\text{m}$  at 430  $^{\circ}\text{C}$ , and 15  $\mu\text{m}$  at 450  $^{\circ}\text{C}$ . In addition, the constant surface roughness suggested that joint strength is influenced by the joining process, including temperature and processing time [505].

Later, Liao et al. utilized this technique for joining La-based and Zr-based MG ribbons [516]. The welded samples, featuring sandwiched structures of La- and Zr-based ribbons, demonstrated improved fracture strength and enhanced tensile strain compared to solely La-based welded samples, attributed to the strengthening effect of the second phase. The findings highlighted the potential of MG as an excellent material choice for in-space manufacturing, as it can be successfully processed in a non-melting state while maintaining favorable mechanical properties.

During thermoplastic joining, the joining mechanism involves three stages (Fig. 33h): deformation and cracking, flowing to contact, and bonding [506]. Deformation and cracking occur when surface oxide deforms and fractures due to shear stress. Pristine MGs then flow into the gap through cracked oxide, followed by the formation of metallic bonds during the bonding stage. The bonding time is crucial for effective bonding as it allows more MGs to join and increase the bonding area. Understanding this mechanism, Peng et al. [506] established a correlation between joining conditions and joint performance, specifically joint strength (Fig. 33i). The joint strength is primarily influenced by the area fraction of bonded regions, which can be controlled by adjusting joining conditions such as temperature, pressure, and bonding time.

### 6.2.4. Resistance spot welding (RSW)

RSW uses the application of pressure and electric current through two opposing electrodes to create heat and join the materials at specific points of contact between two metal sheets or parts, known as weld spots (Fig. 34a). The rapid and localized heating during RSW is advantageous to join BMGs as joining time is short enough to prevent crystallization and minimize structural relaxation within the SLR. RSW has been successfully used to join Zr-based [29,517–520], Ti-based [521], and Pd-based [318] BMGs and dissimilar joining of Zr-based/Pd-based [522] and Zr-based [523] BMGs.

Yang et al. [522] explored supercooled liquid state joining of dissimilar BMGs with non-common supercooled liquid regions using RSW. The  $\text{Zr}_{55}\text{Cu}_{30}\text{Al}_{10}\text{Ni}_5$  and  $\text{Ti}_{41}\text{Zr}_{25}\text{Be}_{28}\text{Cu}_6$  BMG sheets were successfully joined, achieving a remarkable tensile shear strength of  $\sim 1.7$  GPa. The Lasocka equation [524], which relates heating rate and characteristic temperature, guided the joining process. High heating rates allowed for the overlap of supercooled liquid regions and reduced the viscosities of dissimilar BMGs, which exhibited significant differences at low heating rates.

The RSW method, despite being classified as a fusion welding method [525], exhibits different joining modes in BMGs depending on the energy density. By applying different discharge voltages, Yang et al. [520] identified three modes of joining during RSW of  $\text{Zr}_{35}\text{Ti}_{30}\text{Cu}_{7.5}\text{Be}_{27.5}$  BMG sheets (Fig. 34b): supercooled liquid state joining (Category I; 220–268 V), crystalline phase joining (Category II; 278–286 V), and liquid phase joining (Category III; 288–350 V). The crystalline phase joining demonstrates the highest strength, while the liquid phase joining surpasses the supercooled liquid phase joining. Increasing energy density leads to larger joint areas (Fig. 34c), with distinct blending patterns emerging at higher densities, indicating flow and the formation of a strong metallic bond. TEM analysis (Fig. 34d) reveals an intermixed microstructure with amorphous matrix and small nanocrystalline particles for crystalline phase binding. The presence of Ti solid solutions explains the enhanced shear strength in the crystallized samples compared to the uncrystallized ones.

Fujiwara et al. [518] successfully joined  $\text{Zr}_{50}\text{Cu}_{30}\text{Al}_{10}\text{Ni}_{10}$  BMG sheets using small- RSW, preserving the amorphous structure and ensuring sufficient joint strength. Metal expulsion during welding led to the drainage of supercooled liquid and the formation of small liquid droplets. The estimated cooling rate exceeded  $10^2$  K/s, preventing crystallization. Moreover, increasing the welding current resulted in larger weld nuggets and a transition from shear to nugget pull-out or tear failure due to increased tensile load. The shear strength of the joints reached approximately 730 MPa, representing 75 % of the base alloy strength.

RSW has been also utilized to manufacture sandwich-laminated BMG plates. Ma et al. [318] developed multi-layer laminated Pd-based BMGs using an electric current induced heating process. By stacking and heating the multilayer BMG sheets in a vacuum environment, followed by compression and holding, the bonded BMG samples exhibited improved plasticity compared to the brittle

fracture behavior of the as-cast specimen (Fig. 34e). The two-layer BMG sample had slight improvement, while the three-layer BMG samples demonstrated significant enhancement. The bonding interface in the multi-layer BMGs played a vital role in enhancing mechanical properties by extending cell patterns. Additionally, Guo et al. [523] joined dissimilar Zr-based BMGs, fabricating amorphous sandwich-laminated plates without crystallization. The joints showed uniform elemental distribution, indicating a strong metallurgical bond. The welded laminate had comparable tensile strength to the original glasses. Fracture analysis revealed multiple failure planes, suggesting crack branching across the joint interface, resulting in enhanced strain energy absorption compared to monolithic BMGs.

RSW has been recently used for joining Fe-based MG ribbons and making 3D structures [526]. The integration of pulse power supply, multi-dimensional platform, and multi-head delivery mechanism enables continuous heating and pressing of MG ribbons, facilitating the manufacturing of diverse 3D geometries [526]. This method has been successfully applied in fabricating various MG components, as shown in Fig. 34f.

Spark welding is another welding method relying on a high-energy electrical discharge to create the necessary heat. Kawamura and Ohno [527] could join  $Zr_{55}Al_{10}Ni_5Cu_{30}$  BMGs by spark welding under pressure, resulting in no crystallization, visible interface, and maintaining the original tensile strength of 1540 MPa. Metallurgical bonding was achieved through interface local melting without crystallization in the HAZ.

### 6.3. Solid-state welding

#### 6.3.1. Impact welding techniques

Impact welding techniques use high-energy collisions to create a bond between two materials. The main impact welding techniques used for joining BMGs are magnetic pulse welding and explosive welding.

Magnetic pulse welding is a solid-state joining method that utilizes powerful electromagnetic forces to achieve high-speed welding. By employing pulse currents to generate repelling magnetic fields, the impulsive Lorenz force is harnessed to accelerate the joining materials, leading to a high-velocity collision and the formation of welded joints.

Watanabe et al. [528,529] joined pure aluminum plate with micrometer-sized Zr-based MG foils by magnetic pulse welding, resulting in a wavy interface in both similar-metal and dissimilar-metal joints. An intermediate layer formed along the wavy interface, comprising ultrafine aluminum solid solution grains and multiple thin layers of amorphous phase with a different composition from the MG matrix.

The discharge voltage, gap, inductance, and capacitance are key factors that determine the welding quality during magnetic pulse welding. The discharge voltage controls the output energy and velocity, while the gap between sheets affects the collision velocity of the flyer sheet. Inductance and capacitance typically remain constant with specific welding equipment. By exploring weldability window under various discharge voltages and gaps, Wang et al. [530] could join Zr-based BMG sheets of 1 mm thickness to 1060 Al sheet using the typical magnetic welding process shown in Fig. 35a. A current pulse in the coil created a high-density magnetic flux, inducing an eddy current on the flyer Al plate. The interaction of these opposing magnetic fields generated a repulsive force, welding

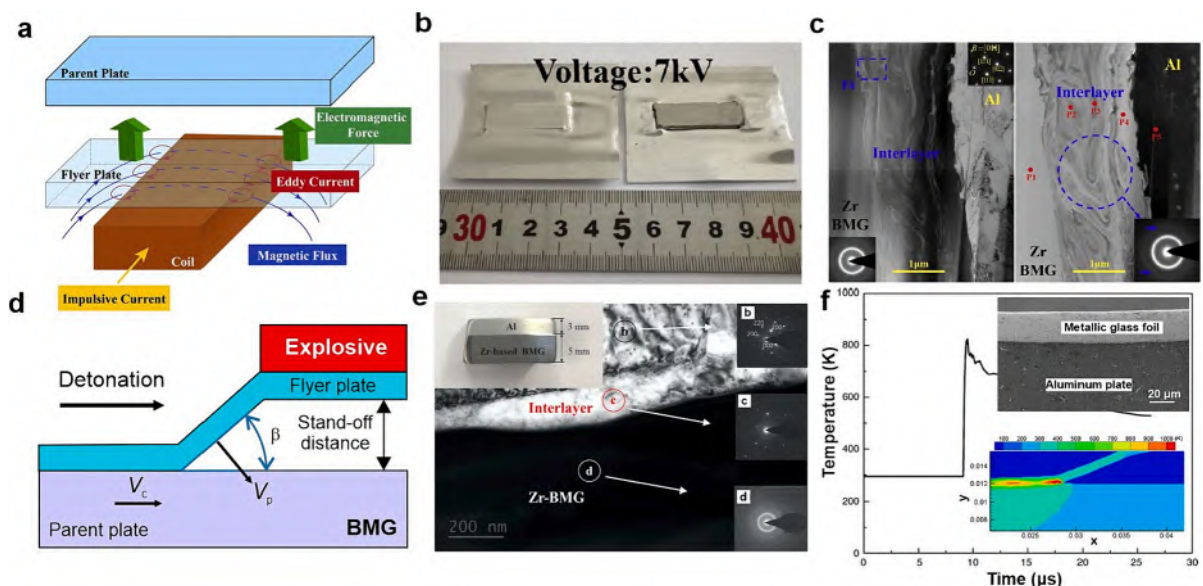


**Fig. 35.** (a) The schematic of magnetic pulse welding. (b) Macroscopic appearance of Al/Zr-BMG lap joints. (c) TEM analysis of the interface. Adapted from [530]. (e) Schematic of explosive welding. (f) TEM characterization of joint interface. The inset in the top left corner shows the joint composite (Adapted from [531]). (g) Calculated temperature history curve of the MG foil near a typical collision point. The insets show SEM image of the weldment and temperature contours of the weldment at  $t = 10 \mu s$  (Adapted from [532]).

the Al plate to the Zr-based BMG (Fig. 35b). A thin interlayer ( $\sim 2.5 \mu\text{m}$ ) composed of amorphous phase and Al nano-particles formed at the welding interface, displaying vortex-like structures (Fig. 35c). Further, the Zr-based BMG maintains its amorphous structure after magnetic pulse welding, confirmed by diffraction patterns. Chemical analysis of interlayer regions (labeled P1-P5) reveals Al-Zr atomic

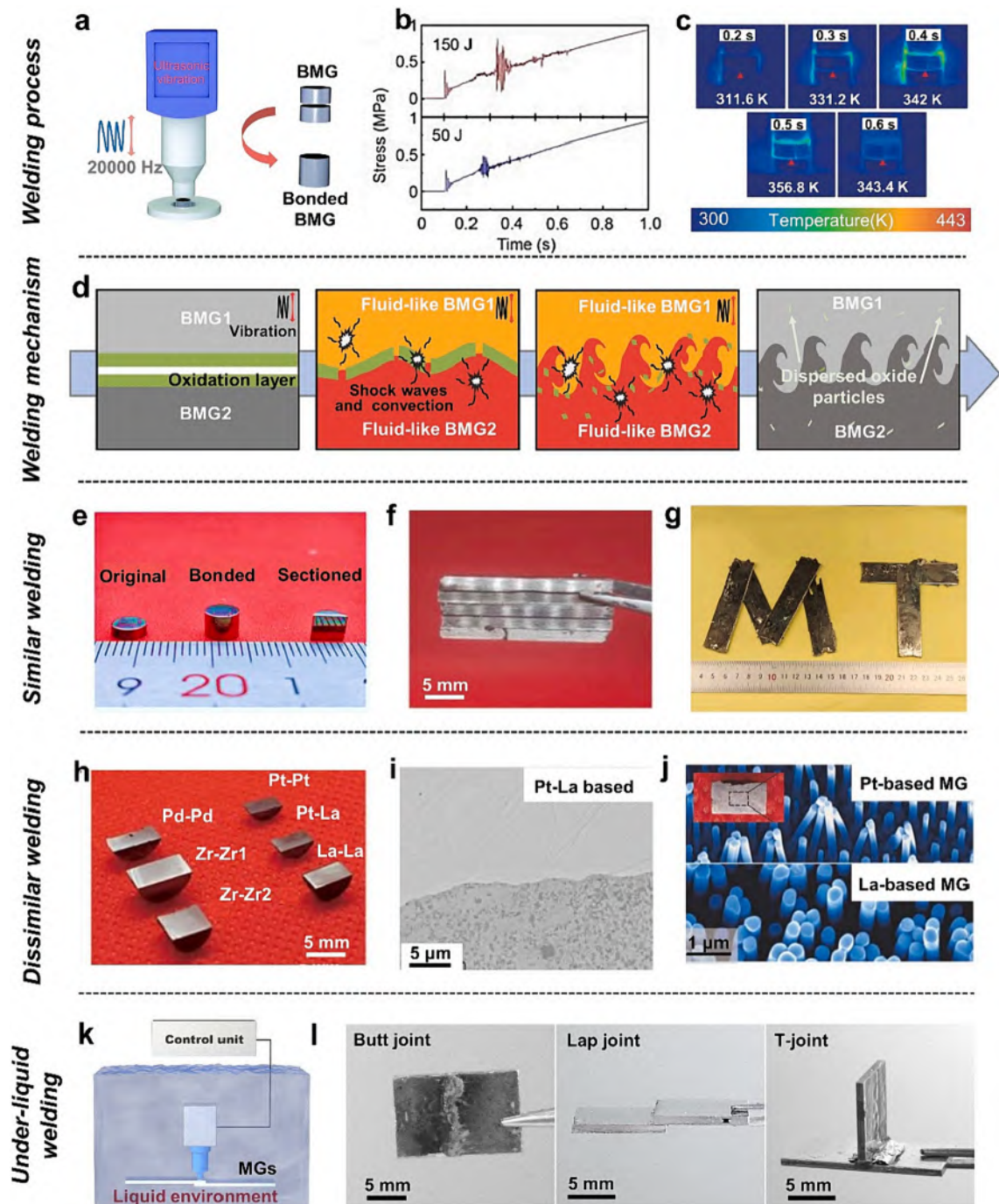


**Fig. 36.** (a) Schematic diagram of the ultrasonic welding set-up under vertical vibration. (b) Stress–time curves of Ultrasonic welding under 150 J and 50 J. (c) Thermal imaging temperature acquisition during ultrasonic welding process (Adapted from [552]). (d) Schematic diagram illustrating the mechanism of interfacial bonding of MGs, adapted from [553]. (e) Original sample, bonded sample, and sectioned welded sample images (adapted from [544]). (f) MGs overlaid by ultrasonic welding (adapted from [552]). (g) “M” and “T” symbol MGs prepared by ultrasonic welding. (h) heterogeneous MGs prepared by ultrasonic welding. (i) SEM image of Pt-based and La-based MGs welding seam. (j) Pt-based and La-based MG nanowire of heterogeneous welding samples. Adapted from [552]. (k) Schematic diagram of the ultrasonic welding under liquid set-up. (l) Three different joint prepared by ultrasonic welding: butt-joint, lap joint, and T-joint.

mixing in regions P2 (64.2/35.8 at.%) and P3 (80.3/19.7 at.%), respectively. Region P4 exhibits a similar Al/Zr atom ratio (13.8/86.2 at.%) to the Zr-BMG matrix (P1, 13.2/86.8 at.%). The presence of a long strip in the interlayer originating from the Zr-BMG matrix indicates substantial material movement and mixing during the welding process. Theoretical analysis suggested that vortices were initiated by local metal melting and fusion joining mode driven by stress waves from high-velocity impact.

Recently, Lazurenko et al. [533] successfully joined Ti foils and Ti-based MG ribbons by magnetic pulse welded to form three-layer composites. Mixing zones with increased titanium content were observed at the severe welding interface. The Ti foil exhibited fine-grained structure and grain twinning due to high-strain-rate deformation. The amorphous structure of the Ti-based MG was preserved, with nanosized  $\alpha$ -Ti precipitates found in the mixing zones. A face-centered phase and the formation of titanium oxides and nitrides were also observed at the interface.

Another impact welding technique is explosive welding. Explosive welding is a solid-state joining method that utilizes controlled explosive detonation on metal surfaces. The detonation generates an extremely high-pressure shockwave that propels the flyer plate onto the base plate, resulting in a high-speed collision at the interface (Fig. 35d). During this collision, the materials experience severe plastic deformation and local melting, leading to the formation of metallurgical bonds. The main processing parameters during explosive welding include collision point velocity  $V_c$ , collision angle  $\beta$ , and the velocity of flyer plate  $V_p$ . Explosive welding enables joining of both similar and dissimilar materials [534]. Explosive welding and magnetic pulse welding exhibit similar structure formation, including waves, mixing zones, amorphization, metastable phases, and nanosized particle precipitation. This similarity arises from their shared principle of high-velocity collision.

Explosive welding has been used for dissimilar joining MGs (Zr-, Ni-, Ti-, and Fe-based) to Al [531,532,535,536], Ti [29,537], stainless steel [537,538], brass [539], and Cu [540]. Jiang et al. [539] introduced a thick-walled cylinder explosion method for joining a Zr-based BMG (Vit. 1) and brass. The study demonstrated the successful formation of a robust metallurgical bond, attributed to extensive atomic diffusion at the welding interface and the propagation of shock waves within the weldment. In addition, Liu et al. [535] utilized parallel plate explosive welding technique to join a crystalline aluminum and a  $\text{Ti}_{40}\text{Zr}_{25}\text{Cu}_{12}\text{Ni}_3\text{Be}_{20}$  BMG. Experimental and numerical evidence confirmed atomic-scale bonding between the BMG and aluminum, preserving the amorphous state without crystallization. Nanoindentation tests showed significantly increased hardness at the explosive joint interface. In another study,  $\text{Zr}_{53}\text{Cu}_{35}\text{Al}_{12}$  BMG and crystalline Cu were explosively welded, resulting in a defect-free bond. Characterization techniques confirmed a tight connection and the formation of a thin diffusion layer at the interface. The BMG retained its amorphous state near the interface, while amorphous and partially crystallized structures were observed within the diffusion layer. The interface exhibited increased hardness compared to the surrounding matrix [540]. The observation of interfacial (melt) zones during ultrasonic welding are mainly ascribed to trapped metal jet [534].

Conventional explosive welding in open air has drawbacks like noise, air pollution, vibration, and destruction of thin foils. In contrast, underwater explosive welding minimizes pollution and vibration. Water, with its high density and incompressibility, serves as a pressure-transmitting medium, preventing high temperatures. This enables the propagation of forces for welding the flyer plate and base plate. Underwater explosive welding has potential to minimize crystallization when joining BMGs with dissimilar materials.

Hokamoto et al. [538] investigated underwater explosive welding to join a thin Ni-based MG foil to a 304 stainless steel base plate. A varied-thickness explosive assembly ensured uniform pressurizing conditions along the 50 mm welded length, resulting in clear waves at the interface. Microscopic analysis revealed excessive melting due to metal jet confinement. Numerical analysis considered the importance of parameters like dynamic bending angle and horizontal collision point velocity. More recently, Liang et al. [531,536] joined Zr-based BMG sheet to aluminum 1060 plates without any noticeable cracks on the surface (inset in Fig. 35e) using the same technique. Fig. 35e showcases a well-bonded interface with a coating thickness of  $\sim 25 \mu\text{m}$ , matching the original foil thickness. The MG foil exhibited no visible defects like gaps or inclusions. Electron diffraction characterizations conducted on three positions within the interlayer (Fig. 35e insets): The inset (b) exhibited a crystalline lattice structure, indicating the presence of the Al phase. The inset (c) showed a mixed phase with lattice structures and an indistinct halo ring, suggesting crystallization and nanocrystals. The inset (d) displayed patterns with only a halo ring, confirming the amorphous structure of the Zr-based BMG after explosive welding [531].

Fig. 35f shows temperature changes during and after explosive welding of  $\text{Fe}_{40}\text{Ni}_{40}\text{P}_{14}\text{B}_6$  MG foil with aluminum plate from numerical simulation [532]. The insets display SEM micrograph of the weldment and temperature contours near the interface at  $t = 10$  ms. High temperatures are observed near the collision points. The average temperature in the collision zone after impact is approximately 850 K, below the melt temperature (1150 K) but above the  $T_g$  (660 K). The temperature rises rapidly during welding ( $10^9$  K/s) and decreases rapidly afterwards ( $10^7$  K/s), exceeding the critical cooling rate ( $10^6$  K/s) to preserve the amorphous state. A thin, high-temperature region near the collision zone contributes to these high cooling rates, as supported by experimental and theoretical findings.

### 6.3.2. Ultrasonic welding

The ultrasonic welding of MGs involves placing two MG components in contact and subjecting them to high-frequency ultrasonic vibrations. During ultrasonic welding of MGs, vibrations can be transmitted to the mating surfaces in either vertical (normal) direction or the parallel direction. While the latter mainly generates localized frictional heating to the SLR at the interface between the foils [541–543], the softening mechanism in the former is based on vibration-induced enhancement of atomic diffusion and formation of a strong bond between the two pieces [544] at temperatures well below  $T_g$  (Fig. 36a). This method has unparalleled advantages in the welding of both similar and dissimilar metals compared to other welding methods [545,546]. In addition to the welding of MGs-MGs, ultrasonic vibration has also enabled the joining of amorphous-crystalline metals by introducing low melting point solders or external heating source [547–550].

Ultrasonic welding in vertical direction does not require flux or external heat sources, does not deform due to heating, and has no

residual stress. It also has low requirements for pre-weld surface treatment. It can not only weld similar metals but also meet high welding requirements for dissimilar metals. Additionally, it can weld thick plates [551]. Ultrasonic welding in vertical direction boasts numerous advantages including fast operation, energy efficiency, high joint strength, good conductivity, spark-free process, and solid-state processing.

Based on the information provided in Fig. 36b, it seems that the entire welding process lasted less than 1 s, which indicates that it was a relatively quick process. Additionally, the welding stress was lower than 1 MPa, which suggests that the stress levels experienced by the material were relatively low [552]. Meanwhile, researchers also used an infrared camera to record the temperature changes during the ultrasonic process in vertical direction, as shown in Fig. 36c. The results showed that the highest temperature reached was only 356.8 K, which is much lower than the  $T_g$  temperature of the material. This characteristic sets it apart from other special processes and becomes a distinct advantage, as it effectively preserves the disordered structure of MGs, thereby harnessing their high strength and other inherent benefits. The unique mechanism of welding under vertical ultrasonic vibration is not based on thermal effects; instead, it relies on UVIP, which is discussed in detail in Section 5.2.

The dynamic heterogeneity of MGs, coupled with the expansion of the liquid-like region induced by vertical ultrasonic vibration, contributes to the creation of a fluidic state across the entire interface [211]. Consequently, the vertical ultrasonic vibration triggers cavitation and acoustic streaming effects in the softened MGs, leading to strong convection and turbulence. These effects, in turn,

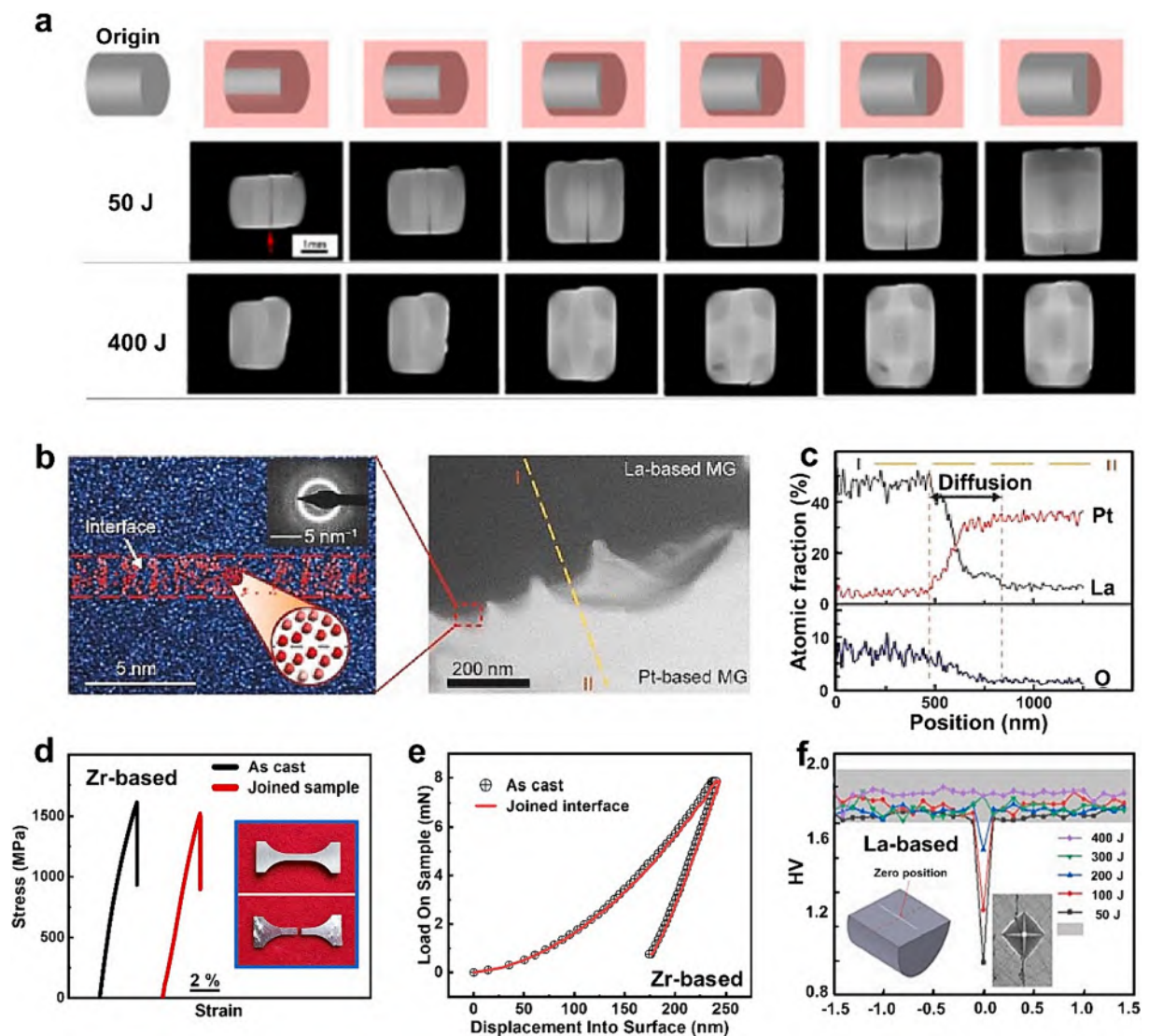


Fig. 37. The properties of the MG joints obtained by ultrasonic welding. (a) CT images of welding samples under different energies (Adapted from [544]). (b) TEM images of the Pt-La-based MG. (c) Distribution of the linear elements perpendicular to the welding surface. Adapted from [552]. (d) Compressive stress–strain curves of as-cast and joined sample. (e) Load depth curves of as-cast and joined sample by nanoindentation [13]. (f) Hardness distribution of dots across welding seam under different energies, adapted from [544].

**Table 3**

Hardness values of PMs, hardness at the joint interface, and joint strength data obtained through various techniques of welding and joining of MGs.

Welding/joining method	Parent metals (PMs)	Hardness of PMs (HV)	Hardness @ joint interface (HV)	Joint strength (MPa)	Ref
<i>Fusing welding</i>					
Laser Welding	Zr <sub>41</sub> Ti <sub>14</sub> Cu <sub>12</sub> Ni <sub>10</sub> Be <sub>23</sub>	BMG:510–550/ Zr:90–133	500–550		[454]
	Zirconium	620	660		[448]
	(Zr <sub>53</sub> Al <sub>17</sub> Co <sub>29</sub> ) <sub>99</sub> Ta <sub>1</sub>	585	589		[459]
	(Zr <sub>53</sub> Cu <sub>30</sub> Ni <sub>9</sub> Al <sub>8</sub> )Si <sub>0.5</sub>	520–530	510–560	2667/2568 (flexural strength)	[462]
	Zr <sub>55</sub> Cu <sub>30</sub> Ni <sub>5</sub> Al <sub>10</sub>				[446]
	Zr <sub>55</sub> Cu <sub>30</sub> Ni <sub>5</sub> Al <sub>10</sub>				[460]
	(Zr <sub>48</sub> Cu <sub>36</sub> Ag <sub>8</sub> Al <sub>8</sub> )Si <sub>0.75</sub>	527–535	514–535		[452]
	Ti <sub>40</sub> Zr <sub>25</sub> Ni <sub>3</sub> Cu <sub>12</sub> Be <sub>20</sub>			1650 (tensile)	[447]
	Ce <sub>65</sub> Al <sub>10</sub> Cu <sub>20</sub> Co <sub>5</sub>			243/308 (tensile)	[451]
	Pd <sub>43</sub> Cu <sub>27</sub> Ni <sub>10</sub> P <sub>20</sub>	714	714		[465]
Electron beam welding	Zr <sub>41</sub> Be <sub>23</sub> Ti <sub>14</sub> Cu <sub>12</sub> Ni <sub>10</sub>			415 (flexural strength)	
	Ni				
	Zr <sub>62</sub> Al <sub>13</sub> Ni <sub>7</sub> Cu <sub>18</sub>	BMG:360/Ti:175	375		[471]
	Ti				
	Zr <sub>41</sub> Be <sub>23</sub> Ti <sub>14</sub> Cu <sub>12</sub> Ni <sub>10</sub>			642 (flexural strength)	[466]
	stainless steel				
	Zr <sub>41</sub> Be <sub>23</sub> Ti <sub>14</sub> Cu <sub>12</sub> Ni <sub>10</sub>			1840 (tensile)	[467]
	Zr metal				
	Zr <sub>41</sub> Be <sub>23</sub> Ti <sub>14</sub> Cu <sub>12</sub> Ni <sub>10</sub>			850 (flexural strength)	[470]
	Ti metal				
reactive foil joining	Zr <sub>57</sub> Ti <sub>5</sub> Ni <sub>8</sub> Cu <sub>20</sub> Al <sub>10</sub>			150 (shear)	[474]
	Zr <sub>58.5</sub> Cu <sub>15.6</sub> Ni <sub>12.8</sub> Al <sub>10.3</sub> Nb <sub>2.8</sub>	BMG:456/Cu:95	200–375		[558]
	Cu metal				
	Zr <sub>57</sub> Ti <sub>5</sub> Cu <sub>20</sub> Ni <sub>8</sub> Al <sub>10</sub>			480 (shear)	[472]
<i>Supercooled liquid state welding</i>					
RFW	Zr <sub>55</sub> Al <sub>10</sub> Ni <sub>5</sub> Cu <sub>30</sub>	545–560	550		[480]
	Ti <sub>40</sub> Zr <sub>25</sub> Ni <sub>3</sub> Cu <sub>12</sub> Be <sub>20</sub>			1540 (tensile)	[485]
	Zr <sub>41</sub> Ti <sub>14</sub> Cu <sub>12.5</sub> Ni <sub>10</sub> Be <sub>22.5</sub>	655	650		[481]
	Zr <sub>55</sub> Al <sub>10</sub> Ni <sub>5</sub> Cu <sub>30</sub>	545–560	550		[482]
	Zr <sub>55</sub> Cu <sub>30</sub> Al <sub>10</sub> Ni <sub>5</sub>	525–530	525		[490]
FSW	Zr <sub>55</sub> Cu <sub>30</sub> Al <sub>10</sub> Ni <sub>5</sub>			432 (tensile)	[493]
	Al–Zn–Mg–Cu alloy				
	Zr <sub>55</sub> Cu <sub>30</sub> Al <sub>10</sub> Ni <sub>5</sub>	BMG:542/Cu:70	80	253 (tensile)	[487]
	pure copper				
	Zr <sub>58</sub> Al <sub>12</sub> Ni <sub>10</sub> Cu <sub>20</sub> Ti <sub>5</sub>	480–500	480–500	1491 (tensile)	[491]
	Zr <sub>55</sub> Al <sub>10</sub> Ni <sub>5</sub> Cu <sub>30</sub>				
	Zr <sub>46</sub> Cu <sub>46</sub> Al <sub>8</sub>	BMG:545/Al:50	150	190 (tensile)	[494]
FSSW	pure aluminum				
	(Ti <sub>41</sub> Zr <sub>25</sub> Be <sub>28</sub> Fe <sub>6</sub> ) <sub>93</sub> Cu <sub>7</sub>	475	440–590		[495]
	Zr <sub>41.5</sub> Ti <sub>13.8</sub> Cu <sub>12.5</sub> Ni <sub>10</sub> Be <sub>22.5</sub>			260 (shear)	[489]
	Mg alloy (AZ31B) and Al alloy (A5052-H32)				
	Zr <sub>55</sub> Cu <sub>30</sub> Al <sub>10</sub> Ni <sub>5</sub>	BMG:673.7 /Cu:67.8		shear tensile load of 2300 N	[488]
Diffusion bonding	pure copper				
	Zr <sub>55</sub> Cu <sub>30</sub> Al <sub>10</sub> Ni <sub>5</sub>			194.38 (shear)	[514]
	Cu <sub>54</sub> Ni <sub>6</sub> Zr <sub>22</sub> Ti <sub>18</sub>	BMG: 675		45 (shear)	[502]
	carbon steel				
	Cu <sub>50</sub> Zr <sub>43</sub> Al <sub>7</sub>	BMG:300–400/Al: 30	~200	~11/~17 (compressive shear)	[510]
	aluminum (AA1050) alloy				
	Zr <sub>55</sub> Cu <sub>30</sub> Al <sub>10</sub> Ni <sub>5</sub>	508		138–155 (shear)	[559]
	Al alloy				
	Zr <sub>55</sub> Cu <sub>30</sub> Al <sub>10</sub> Ni <sub>5</sub>			58.42 (tensile)	[515]
	Al-5Fe alloy				
	Zr <sub>52.5</sub> Al <sub>10</sub> Cu <sub>15</sub> Ni <sub>10</sub> Be <sub>12.5</sub>			1510–3350 (flexural strength)	[500]
	Zr <sub>65</sub> Al <sub>10</sub> Ni <sub>10</sub> Cu <sub>15</sub>			138–155 (shear)	[499]
Zr <sub>55</sub> Cu <sub>30</sub> Al <sub>10</sub> Ni <sub>5</sub>	BMG:816–1428/ Al:51–76.5		90/105/110 (tensile)	[512]	
Thermoplastic joining	aluminum alloy				
	Zr <sub>41.2</sub> Ti <sub>13.8</sub> Cu <sub>12.5</sub> Ni <sub>10</sub> Be <sub>22.5</sub>	587–612	587		[509]
	Zr <sub>35</sub> Ti <sub>30</sub> Cu <sub>7.5</sub> Be <sub>27.5</sub>	775–877	816	72/179 (shear)	[505]
	La <sub>60</sub> Ni <sub>15</sub> Al <sub>25</sub>			327 (tensile)	[516]
RSW	Zr <sub>64.13</sub> Cu <sub>15.75</sub> Ni <sub>10.12</sub> Al <sub>10</sub>				
	Zr <sub>55</sub> Cu <sub>30</sub> Al <sub>10</sub> Ni <sub>5</sub>	673–694	673–693	1700 (shear)	[522]
	Ti <sub>41</sub> Zr <sub>25</sub> Be <sub>28</sub> Cu <sub>6</sub>				

(continued on next page)

Table 3 (continued)

Welding/joining method	Parent metals (PMs)	Hardness of PMs (HV)	Hardness @ joint interface (HV)	Joint strength (MPa)	Ref
Spark welding	Zr <sub>35</sub> Ti <sub>30</sub> Cu <sub>7.5</sub> Be <sub>27.5</sub>			837–1467 (shear)	[520]
	Zr <sub>50</sub> Cu <sub>30</sub> Al <sub>10</sub> Ni <sub>10</sub>			730 (shear)	[518]
	Zr <sub>55</sub> Cu <sub>30</sub> Ni <sub>5</sub> Al <sub>10</sub>			1540 (tensile)	[527]
Solid-state welding					
Magnetic pulse welding	Ti <sub>55.6</sub> Ni <sub>10.5</sub> Zr <sub>6.8</sub> Cu <sub>17.8</sub> Be <sub>8.6</sub> V <sub>0.8</sub> pure Ti foils	MG: 600/Ti foils:195	670		[533]
Explosive Welding	Zr <sub>41.2</sub> Ti <sub>13.8</sub> Cu <sub>10</sub> Ni <sub>12.5</sub> Be <sub>22.5</sub> pure Ti and SUS304 plates			Zr/Ti: 300–400 (tensile) Zr/SUS: 400–500 (shear)	[537]
Ultrasonic welding	Ti <sub>40</sub> Zr <sub>25</sub> Cu <sub>12</sub> Ni <sub>3</sub> Be <sub>20</sub> crystalline aluminum	BMG:714–867/ Al:51–102	1275		[535]
	Zr <sub>60</sub> Ti <sub>17</sub> Cu <sub>12</sub> Ni <sub>11</sub> 1060 Al	BMG:1000–1200/ Al:100	180		[531]
	Fe <sub>40</sub> Ni <sub>40</sub> P <sub>14</sub> B <sub>6</sub> aluminum plate 1060	BMG:714/Al:51			[532]
	Zr <sub>53</sub> Cu <sub>35</sub> Al <sub>12</sub> Crystalline Copper	BMG:765/Cu:204	867		[540]
	Zr <sub>62</sub> Cu <sub>33</sub> Al <sub>4</sub> Ti <sub>1</sub> 1060-Al alloy			68 (shear)	[548]
	Zr-14Cu-10Ti-8Ni Ti-6Al-4 V alloy			20–50 (shear)	[550]
	La <sub>55</sub> Al <sub>25</sub> Ni <sub>5</sub> Cu <sub>10</sub> Co <sub>5</sub>	220.5–251.21	220.5–251.2		[544]

thoroughly break the oxide layer and facilitate the mixing of fresh softened MGs. As shown in Fig. 36d, this dynamic process results in the formation of a tighter bond between the MGs, ensuring a robust and well-connected joint.

La-based BMG had been demonstrated to be welded using ultrasonic technology into larger blocks of MG, as shown in Fig. 36e [544]. The interface of the welding joint had no gaps, and the sample remained intact with no damage or defects in the weld [544]. As shown in Fig. 36f, Zr-based MG multilayer stacking samples were also prepared using ultrasonic welding, suggesting that the additive manufacturing of BMGs can also be achieved using ultrasonic technology [552]. Finally, as shown in Fig. 36g, BMG plates were welded into “M” and “T” shapes. Subsequently, in 2021, the research team optimized the welding process and successfully welded La-, Pd-, and Zr-based BMGs (Fig. 36h-i) [552]. After welding, different substrate MGs can be thermoplastically formed into nanowire structures (Fig. 36j), resulting in a dual-phase amorphous alloy nanowire structure.

Conventional ultrasonic welding processes are typically completed at atmospheric pressure, and have not been used in low-temperature and atmospheric-isolated environments such as the ocean or space. Some researchers have proposed ultrasonic welding of MGs in various complex environments, such as liquid water, seawater, alcohol, and liquid nitrogen. Fig. 36k shows a schematic of ultrasonic welding of MGs in various complex environments, where the punch and welding parts are placed in a liquid environment to complete the welding. Fig. 36l shows the samples after welding, including butt joints, lap joints, and T-joints, indicating that ultrasonic welding can be used to weld MGs in the aforementioned complex environments. Therefore, ultrasonic welding of MGs has great potential and can be adapted to various complex environments [553].

What are the properties of the amorphous alloy joints obtained by ultrasonic welding method? First, as shown in Fig. 37a, computed tomography (CT) scanning technology is used to characterize the alloy structure [544]. If there are gaps or welding defects in the structure, they will be marked in black in the figure. It can be easily seen from the figure that when the welding energy is increased to 400 J, the welding gaps and defects have completely disappeared. Therefore, it can be concluded that ultrasonic welding of MGs can completely bond the MG samples into a whole without any defects or gaps.

The TEM analysis (Fig. 37b) reveals a disordered atomic arrangement, as shown in the magnified image, with a diffraction halo-like pattern indicating complete glassiness. After bonded the MGs shows a gap-free welding interface between the La-Pt-based MGs, with the white and black regions indicating the Pt-based and La-based MGs, respectively. Elemental distribution analysis across the interface confirms no significant increase in oxygen content (Fig. 37c). Therefore, the formation of a metallic bond at the MGs interface clearly indicates that any surface oxide layer, if present, would have been broken down into fragments under ultrasonic vibration [552].

Regarding the performance of the welding joints, the tensile performance curve of the welded samples is shown in Fig. 37d, and the fracture strength performance of the welded samples is not significantly different from that of the cast samples. The nanoindentation data in Fig. 37e also show that the micro-properties of the samples before and after welding has not changed significantly [553]. The hardness of the welding seam area under different welding energies in Fig. 37f also shows that the strength of the MGs can be restored using appropriate ultrasonic welding energy [544]. The above data fully demonstrate that ultrasonic processing of MGs has the advantages of tight bonding and no impact on the performance of the joints, which can achieve the large-scale production of BMGs and promote their wide application.

The weldability criteria for ultrasonic vibration welding are commonly associated with welding energy (or time): insufficient energy results in poor welding effects, while excessive energy can trigger crystallization phenomena [383]. Therefore, appropriate values must be selected based on the specific materials involved. According to the findings by Li et al. [544], the optimal energy for La-

based materials is below 300 J, while for Zr-based materials, it is around 500 J [553]. In liquid environments, this value needs to be higher due to energy dissipation.

Other parameters influencing weldability include welding pressure, amplitude, and frequency, with the frequency of ultrasonic vibration having the most significant impact. Both simulations and micro-zone experiments have illustrated that higher vibration frequencies accentuate the softening phenomenon in MGs [211], thereby facilitating the welding process [553]. For instance, at 72,000 Hz, the average viscosity of Zr-based MGs has decreased by three orders of magnitude compared to the viscosity at 200 Hz [553,554]. Although existing literature on ultrasonic welding has primarily explored frequencies up to 20,000 Hz, achieving metal bonding in various MGs, experimenting with welding equipment featuring even higher frequencies could represent a breakthrough in MG welding technology.

Table 3 offers a comprehensive dataset, presenting hardness values of parent metals (PMs), hardness at the joint interface, and joint strength for various welding and joining methods in MGs. The data provide valuable insights into the mechanical properties and performance of the joints achieved through each method.

During the welding of BMG components, the hardness values of the parent BMG and the joint interface are typically comparable. However, some welding techniques have shown larger joint hardness values than their parent BMG counterparts. For instance, FSSW welding of a Ti-based BMG [495] and laser welding of Zr-based BMGs [448,462] have reported higher joint hardness. In dissimilar welding, the hardness value at the joint interface usually falls between the hardness of the PMs. Nevertheless, in certain dissimilar welding cases, a remarkable increase in hardness at the joint interface has been observed. Examples of such cases include magnetic pulse welding of a Ti-based BMG to pure Ti foils [533], EBW of a Zr-based BMG to Ti [471], and explosive welding of a Ti-based BMG to crystalline aluminum [535] and a Zr-based BMG to crystalline copper [540]. The increase in hardness at the joint interface is generally an indication of induced nanocrystallization or minute diffusion of elements from the crystalline PM to the weld-affected zone.

Joint strength is a critical parameter in engineering applications. The values of joint strength in Table 3 exhibit significant variation, mainly attributed to the test method used and the inherent strength of the PMs. In a given row, the range of joint strength values highlights the dependence on welding parameters. Based on reported data, diffusion bonding of  $Zr_{52.5}Al_{10}Cu_{15}Ni_{10}Be_{12.5}$  BMG achieves the highest flexural strength of  $\sim 3$  GPa [500], followed by laser welding of  $Zr_{55}Cu_{30}Ni_5Al_{10}$  BMG with  $\sim 2.5$  GPa [462]. On the other hand, the lowest strengths have been observed in shear strengths of joints made by diffusion bonding a Cu-Zr-Al BMG to

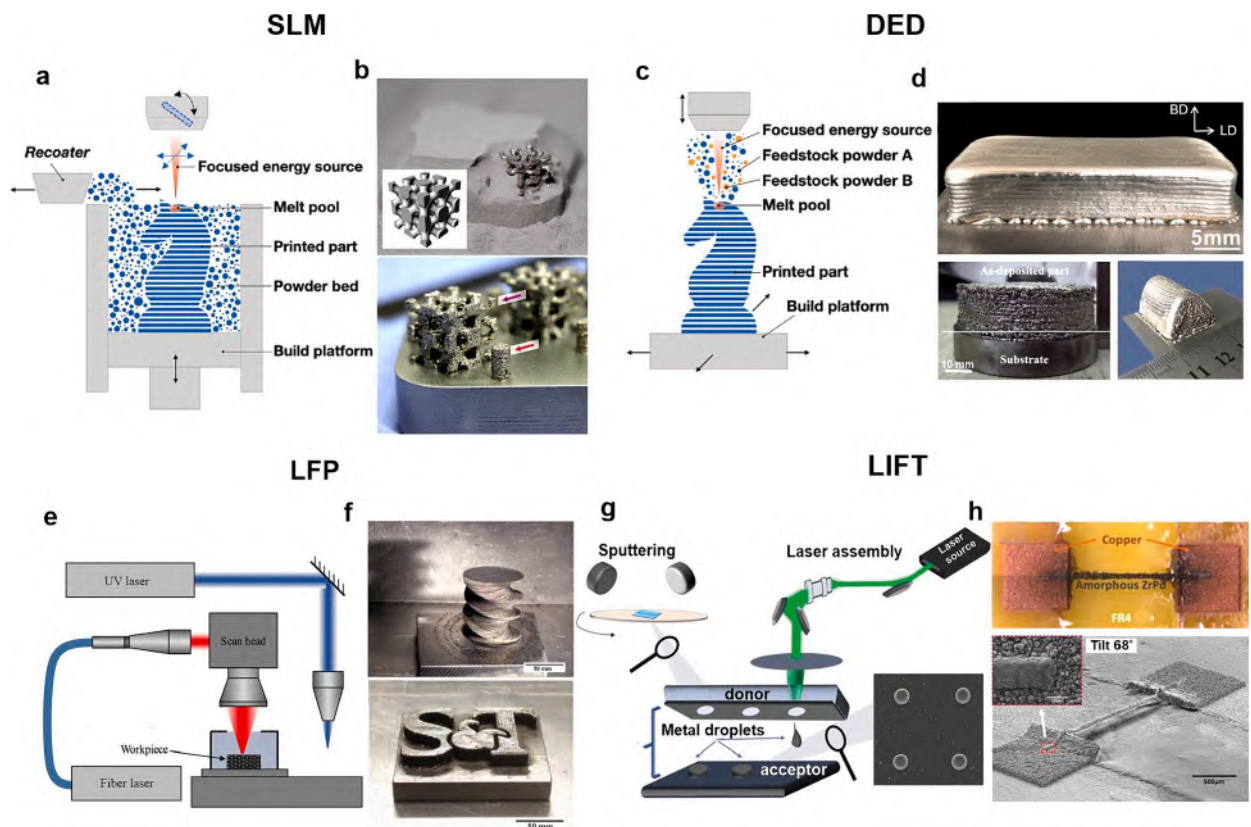


**Fig. 38.** Laser-based AM techniques. (a) Schematic of SLM process (Adapted from [562]). (b) Fe-based 3D printed MG scaffold structure on top of 316L steel base plate (Adapted from [563]). (c) Schematic of DED process (Adapted from [562]). (e) Schematic illustration of LFP method (Adapted from [564]). (f) As-fabricated amorphous 3D parts by LFP (Adapted from [565]). (g) Schematic illustration of LIFT 3D printing. (f) Optical (top) and SEM (bottom) images of LIFT-printed MG microbridge hanging 100  $\mu$ m above surface. Adapted from [566].

aluminum alloy (~11–17 MPa) [510], and ultrasonic welding of Zr-based BMGs to 1060 Al alloy (68 MPa) [548] and Ti-6Al-4 V alloy (20–50 MPa) [550].

The matter of fracture toughness warrants attention, as there is limited literature addressing the fracture toughness of welded samples. In the case of reactive joints in  $Zr_{57}Ti_5Ni_8Cu_{20}Al_{10}$  BMG, formed using Al/Ni reactive multilayer foils, the fracture toughness increases with compressive loading, reaching a peak value of  $12 \text{ MPa m}^{1/2}$ . This value is approximately two-thirds of the fracture toughness observed in the as-cast MG [555]. Additionally, La-based materials welded under ultrasonic vibration exhibit a fracture toughness of  $4.56 \text{ MPa m}^{1/2}$ , as estimated using the indentation method [544,556]. Notably, this value closely aligns with the fracture toughness of cast samples, which is recorded at  $5 \text{ MPa m}^{1/2}$  [557].

## 7. Additive manufacturing (AM) of MG components

This section delves into the fascinating world of AM of MGs, exploring its principles and the process-structure-property relationships in MG parts fabricated by AM strategy.

According to the standard terminology for AM technologies (ASTM F2792–12A [560]), metal AM techniques are divided into four main categories: powder bed fusion, directed energy deposition, binder jetting, and sheet lamination. These techniques are further subcategorized based on the specific attributes of the high-energy heat source and the form of the feedstock used. While AM techniques to fabricate MG components are not well classified, or only classified according to the type of feedstock material (powder/non-powder) [34], this review classifies various AM techniques based on the underlying manufacturing principles.

### 7.1. Laser-based AM techniques

Laser-based AM, involves layer-by-layer deposition of metallic materials by melting and solidification of MG feedstock using a high-power laser beam [561]. The high cooling rates achieved during the process enable the formation of large-sized BMGs. Furthermore, laser-based AM has outstanding ability to fabricate multi-material structures with complex geometries, offering opportunities for creating functionally gradient materials with tailored properties. However, challenges such as control over the cooling rates and solidification defects still need to be addressed to achieve optimal results.

#### 7.1.1. Selective laser melting (SLM)

SLM is a powder bed fusion process for creating complex 3D structures using a high-energy laser beam. It involves selectively melting and fusing metallic powders layer by layer based on computer-aided design (CAD) models. SLM is also referred to as laser powder bed fusion (LPBF). The process (Fig. 38a) includes preparing a metallic substrate as the build platform, spreading metal powder uniformly, scanning the powder with a high-energy laser beam (e.g. fiber laser with micrometer-sized spot), and gradually building up the component layer by layer. To ensure quality, parameters such as laser power, scanning speed, hatch spacing, and layer thickness are carefully controlled. A protective environment with gases like nitrogen, argon, or helium is used to prevent contamination and oxidation [561].

The SLM process offers high cooling rates at a local level, reaching approximately  $\sim 10^5 \text{ K/s}$  [567], allowing for the synthesis of BMG components in a layer-by-layer approach. Interestingly, SLM enables the production of BMG parts with larger dimensions compared to cast counterparts. Pauly et al. [563] made the first attempt to fabricate a complex lattice structure using SLM  $Fe_{74}Mo_4P_{10}C_{7.5}B_{2.5}Si_2$  powders (Fig. 38b), showing no increase in crystalline volume fraction. Later, Mahbooba et al. [568] reported fabrication of large size FeCrMoCB BMG with thicknesses  $\sim 15$  times larger than the thicknesses achieved by conventional casting ( $<2\text{mm}$ ). Other studies have successfully fabricated BMG structures using various systems such as Zr-based [569–576], Al-based [577,578], Fe-based [563,579–581], and Ti-based [582,583] alloys. SLM is the most extensively studied AM technique for BMG structures [35].

#### 7.1.2. Laser-based directed energy deposition (DED)

DED, also known as laser engineered net shaping (LENS), direct metal deposition (DMD), and laser solid forming (LSF), utilizes powder or wire feedstock material [562]. The process involves injecting the feedstock into the deposition zone and using a high-power laser to melt and depositing the material in a layer-by-layer fashion (Fig. 38c). DED offers advantages such as higher deposition rates, the ability to work with multiple powder compositions, adaptability for coatings and repairs, and processing of large part volumes. While DED may result in lower dimensional accuracy and larger surface roughness compared to SLM, its benefits make it a preferred choice for coatings/cladding and repair, and processing of large part volumes [562].

DED technique offers the advantage of achieving high and localized cooling rates at each deposition point, thanks to the small size of the melt pool and efficient thermal energy conduction into the substrate. This enables the processing of net-shaped MG components through careful control of cooling conditions. Initial attempts at 3D printing MGs with DED focused on simple shapes using gas-atomized  $Fe_{58}Cr_{15}Mn_2B_{16}C_4Mo_2Si_1W_1Zr_1$  (at.%) powder [584], but resulted in partially crystalline structures. Since then, several works have reported partially crystalline Zr-based [585–587] BMGs built by DED process with sizes larger than the critical diameters by casting. Fig. 38d shows 3D BMG structures built by the DED process. Due to the difficulties in achieving fully amorphous BMG parts by DED process, the process has been mainly used in fabricating Zr-based [588–591], CuZr-based [592], and Fe-based [593] BMGCs, some of which contain controlled gradient structure [588,590]. Further, DED has also enabled fabrication of Nb-reinforced [594] and Ta-reinforced [595] ex-situ BMGCs.

### 7.1.3. Laser foil printing (LFP)

In contrast to conventional laser-based AM techniques using metal powders, LFP utilizes metal foils as the feedstock material. The LFP process (Fig. 38e) involves laser welding to join the foils and laser cutting to shape the desired regions [564]. Each layer is constructed by securely positioning a foil on a substrate, welding it, and cutting off the excess. This iterative process continues until the 3D part is fully formed. While LFP is cost-effective and straightforward [565], it generates higher material waste compared to SLM, where unused powders can be reused.

During LFP of BMGs, amorphous foils ( $\sim 100 \mu\text{m}$  thick) are laser-welded layer by layer, forming 3D amorphous structures. Critical parameters include laser power, pulse duration, and spot spacing. With proper parameter selection (i.e., laser power, laser pulse duration, and spot interspacing [596]), LFP achieves equal or improved amorphization compared to as-cast foils [565,596]. Unlike processes involving powder spreading and fusion dynamics, LFP enables layer-by-layer fabrication through selective laser welding of metal foils, yielding low-porosity 3D printed BMG parts. LFP has successfully produced Zr-based BMG parts with gradient/laminated structures and enhanced mechanical properties [565,596–598]. Fig. 38f illustrates 3D parts created using LFP with of  $\text{Zr}_{52.5}\text{Ti}_{15}\text{Al}_{10}\text{Ni}_{14.6}\text{Cu}_{17.9}$  amorphous foils. Laser foil printing holds promise for AM of MG components, with untapped potential for further exploration.

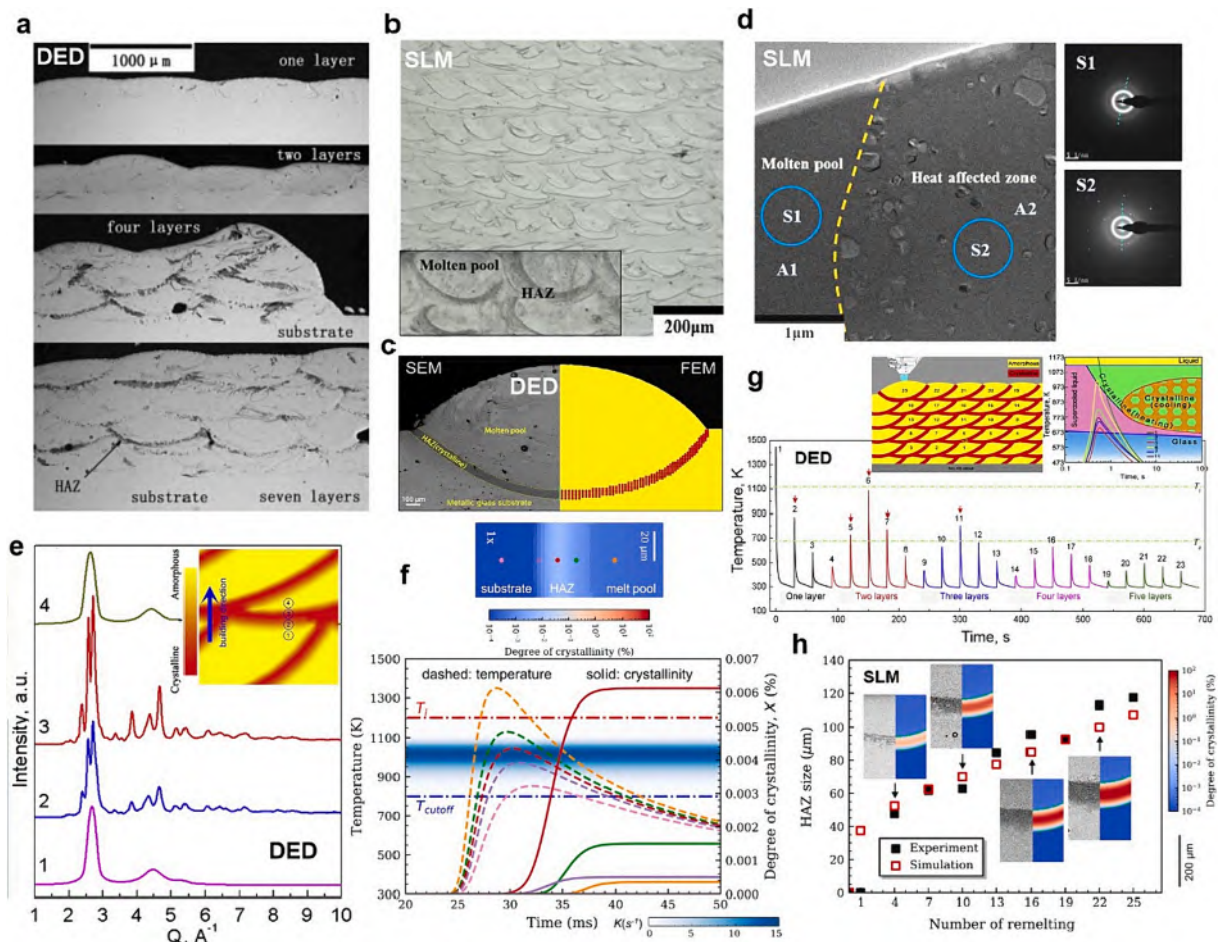


**Fig. 39.** Microstructural characterization in additively manufactured (AMed) BMGs processed with laser-based techniques. (a) Microstructures of the deposits with one, two, four and seven layers. Adapted from [585]. (b) SEM image of the 3D printed Zr-based BMG by SLM (Adapted from [601]). The inset shows the scanning track including molten pool and HAZ. (Adapted from [602]). (c) Left: SEM image showing the microstructure in the cross section of the single-track deposited BMG; Right: spatial distribution of crystallization obtained from the FEM analysis. (d) TEM bright-field image from the boundary of molten pool and HAZ and corresponding electron diffraction patterns in the SLMed BMG (Adapted from [601]). (e) The scattering intensity  $I(Q)$  versus scattering vector  $Q$  obtained from high-energy XRD (HE-XRD) analysis. The inset shows schematic illustration of four relative positions 1–4 where HE-XRD experiments are conducted. Adapted from [604]. (f) Temperature history and crystallinity simulations at five different positions during SLM process of BMG (Reproduced from [605]). (g) Simulated thermal history during layer-by-layer DED process. The inset curves show schematic cross section of five deposited layers and thermal cycle curves after some typical tracks and the TTT diagram of  $\text{Zr}_{50}\text{Ti}_{15}\text{Cu}_{27}\text{Ni}_{10}\text{Al}_8$  BMG (Adapted from [604]). (h) The simulated predicted values and experimentally measured values of the size of HAZ at different remelting times (Adapted from [605]).

### 7.1.4. Laser-induced forward transfer (LIFT) printing

LIFT is a novel technique for micro-3D printing of metallic components [599]. It involves heating a thin film on a transparent substrate with a laser pulse, propelling micro-droplets onto a receiver substrate (Fig. 38g). This enables the digital printing of intricate 3D structures with high accuracy. However, LIFT-printed metal structures often have voids, resulting in inferior mechanical, electrical, and thermal properties compared to bulk metal counterparts [600].

The high cooling rates during LIFT printing, ranging from  $10^8$  to  $10^{11}$  K/s, enable the digital fabrication of BMGs. Successful printing of ZrPd-based MG structures has been demonstrated under normal atmospheric conditions (Fig. 38h) [566,600]. The printed structures exhibit dense and compact structures with minimal voids, indicating high quality. However, there is limited literature available on micro-3D printing of MGs using the LIFT technique.

## 7.2. Solidification in laser AM of BMGs

Laser-based AM techniques involve the localized melting of feedstock metal to form the desired BMG components. The repetitive cycles of heating and rapid cooling during the printing process play a crucial role in solidification and formation of amorphous and partially crystalline microstructures in BMGs.

### 7.2.1. Microstructure evolution

The microstructures of 3D printed BMGs often exhibit inhomogeneities at different length scales, primarily due to repeated laser scanning. At the microscale, the microstructures of BMGs deposited by SLM [601–603], DED [585,587], and LFP [564] consist of featureless amorphous molten pools (MPs) surrounded by crystalline HAZs with sporadic micropores. For example, the microstructures of  $Zr_{55}Cu_{30}Al_{10}Ni_5$  BMG deposited by DED show distinct crystalline bands separating amorphous deposited zones (Fig. 39a) [585]. While there is no apparent distinction in the microstructure between one and two deposited layers, distinctive crystalline bands are observed when four layers are deposited separating featureless white deposited zones. These crystalline bands result from crystallization within the HAZ of the pre-deposited layer during the laser deposition of the adjacent layer. The featureless white deposited zones are amorphous in nature. Similar microstructures are observed in the same BMG composition produced by SLM [601], with MPs and HAZ regions present in the layered structure (Fig. 39b).

The microstructure of a single-track deposition by DED process is shown in Fig. 39c. This deposition consists of  $Zr_{50}Ti_5Cu_{27}Ni_{10}Al_8$  (Zr50) powder on an as-cast substrate with the same composition. The microstructure can be divided into three distinct regions: the light grey molten pool in the upper side, characterized by a light grey appearance; the dark grey crystalline HAZ in the middle part, surrounded by a dark grey region; the light grey amorphous HAZ in the lower side. By combining thermal cycle curves obtained from finite-element method (FEM) analysis and the time–temperature–transformation (TTT), Lu et al. [588,604,606] have successfully predicted crystallization in the single-track DED process of Zr50 BMG. As shown in right panel of Fig. 39c, the distribution of crystalline positions (red dots) calculated through FEM aligns closely with the experimental observations [604].

At the nanoscale, the microstructural heterogeneities become more complex. TEM characterizations of an SLMed Zr-based BMG are shown in Fig. 39d. The MP exhibits a maze-like structure, indicating a fully amorphous state, which is confirmed by the diffused halo ring in the electron diffraction pattern. In contrast, the HAZ shows partial crystallization, with nanocrystals dispersed within the amorphous matrix. A comparison of electron diffraction patterns between the MP and HAZ reveals a larger diffraction ring for the HAZ (Fig. 39d), indicating a relatively shorter average atomic distance within this region [601,602]. The molten pools and HAZs exhibit different characteristics in terms of composition and crystallization kinetics.

In laser DED processing of  $Zr_{58.5}Cu_{15.6}Ni_{12.8}Al_{10.3}Nb_{2.8}$  BMG, rapid heating forms micro-scale spherulites instead of nanocrystallization [607]. The spherulites grow from pre-existing nuclei, while phase separation and nucleation are suppressed. The composition is similar to the amorphous matrix, but a secondary Zr-Nb solid solution phase forms at elevated temperatures. A numerical model predicted complete crystallization prior to melting at heating rates up to 3350 K/s.

Other nanoscale microstructural features reported during laser-based 3D printing of BMG parts include composition segregation [577,590] and intricate microstructure between adjacent deposited layers [608].

The atomic-scale structural analysis of laser-based AM of BMG components has been conducted using high-energy X-ray diffraction (HE-XRD). Lu et al. [604] examined the graded microstructure of DED processed Zr50 BMG by performing HE-XRD experiments across a thin crystalline band. Fig. 39e shows the scattering intensity  $I(Q)$  patterns measured at four different positions. Positions 1 and 4 exhibit fully amorphous nature without sharp diffraction peaks. Position 1 shows a higher  $Q$  value compared to position 4, indicating a shrinkage in interatomic distance in the lower section of the deposited sample. This is attributed to more thermal cycles undergone by the lower parts, leading to excess free volume annihilation and densification of the glassy atomic structure. Positions 2 and 3 show sharp Bragg peaks corresponding to crystalline phases. The intensities of these peaks increase from position 2 to position 3, indicating an increase and subsequent decrease in crystalline content across the thin crystalline band.

Best et al. [609] used synchrotron X-ray microdiffraction to analyze structural heterogeneity in SLMed Zr-based BMG. Periodic variations on a small scale of 40–80  $\mu$ m were detected due to solidification of the melt-pool, resulting in a localized strain variation of  $\pm 0.1$  %. Later, they observed hardness and atomic-scale structure variations along the build height during SLM [610]. The bottom region showed larger medium-range order clusters and was softer, attributed to differences in heat dissipation. Faster cooling rates at the bottom and less reheating led to a less relaxed state in the top region.

### 7.2.2. Crystallization

In traditional casting of BMGs, the cooling rate during a single cooling process determines the material's resistance to

crystallization. However, in laser-based 3D printing, the cyclic process of cooling and heating during layer-by-layer manufacturing affects the formation of BMGs [611]. The amorphous phase formation in the 3D printed alloy is influenced by both cooling and subsequent heating processes.

In laser-based additive manufacturing, high cooling rates prevent crystallization. However, cyclic reheating during layer-by-layer deposition and heat accumulation can cause partial crystallization of the previously formed amorphous HAZ as the temperature exceeds  $T_x$  [601]. Thus, effective crystallization mainly occurs within the HAZ due to thermal gradients. As the process of remelting is repeated, the HAZ gradually increases in crystallinity but does not become fully crystalline [575,603].

A recent study has revealed an inverse transition from crystalline phase to amorphous structure in the HAZ during SLM of TiZr-base BMG composite, where the  $(\text{Ti,Zr})_2\text{Cu}$  intermetallic compound transforms into MG in the HAZs [612]. This solid-state amorphization is driven by thermodynamic factors, as revealed by the molar Gibbs free energy-component diagram. The heterogeneous nature of the transformation is evident from the well-defined interface between the MG and the intermetallic compound.

Yang et al. [605] simulated temperature profiles and crystallization behaviors during laser-metal interaction at different positions of a deposited track (Fig. 39f). Crystallization varied across regions, with the red point spending more time in the effective crystallization region (ECR) and exhibiting higher crystallinity. The substrate point had a temperature too low for observable crystallization, while the melt pool point experienced crystallization during solidification but lost it during melting.

Lu et al. [604] simulated the thermal cycle curves during DED process of a 5-layer  $\text{Zr}_{50}\text{Ti}_5\text{Cu}_{27}\text{Ni}_{10}\text{Al}_8$  BMG (Fig. 39g). The initial track rapidly cools without crystallization. Subsequent tracks cause structural relaxation, leading to regions with higher crystallinity. A physics model [585] and also MD simulations [613] support crystallization due to buildup of structural relaxation in the HAZ during laser-based AM. Subsequent layer deposition imposes thermal cycles on the first track, but only track 6 causes devitrification of the amorphous phase. This is due to a significant increase in temperature exceeding the crystalline curve (Fig. 39g). The heat effects extend up to the third layer before falling below the glass transition temperature ( $T_g$ ).

It should be noted that the HAZ thickness is not uniform throughout the build formation and changes continuously with increasing remelting cycles ( $N_{\text{remelt}}$ ). Yang et al. [575] observed that the thickness of the HAZ in SLMed  $\text{Zr}_{59.3}\text{Cu}_{28.8}\text{Al}_{10.4}\text{Nb}_{1.5}$  (AMZ4) BMG increases rapidly at first and then slows down. Experimental and simulated HAZ sizes (Fig. 39h) showed good agreement, indicating significant crystallization within the HAZ [605]. At  $N_{\text{remelt}} = 13$ , the simulated HAZ size of  $77.5 \mu\text{m}$  closely matched the experimental value of  $84.6 \mu\text{m}$ .

The cooling rate decrease with increasing layer deposition enables the tuning of crystallization in BMG materials. Utilizing this

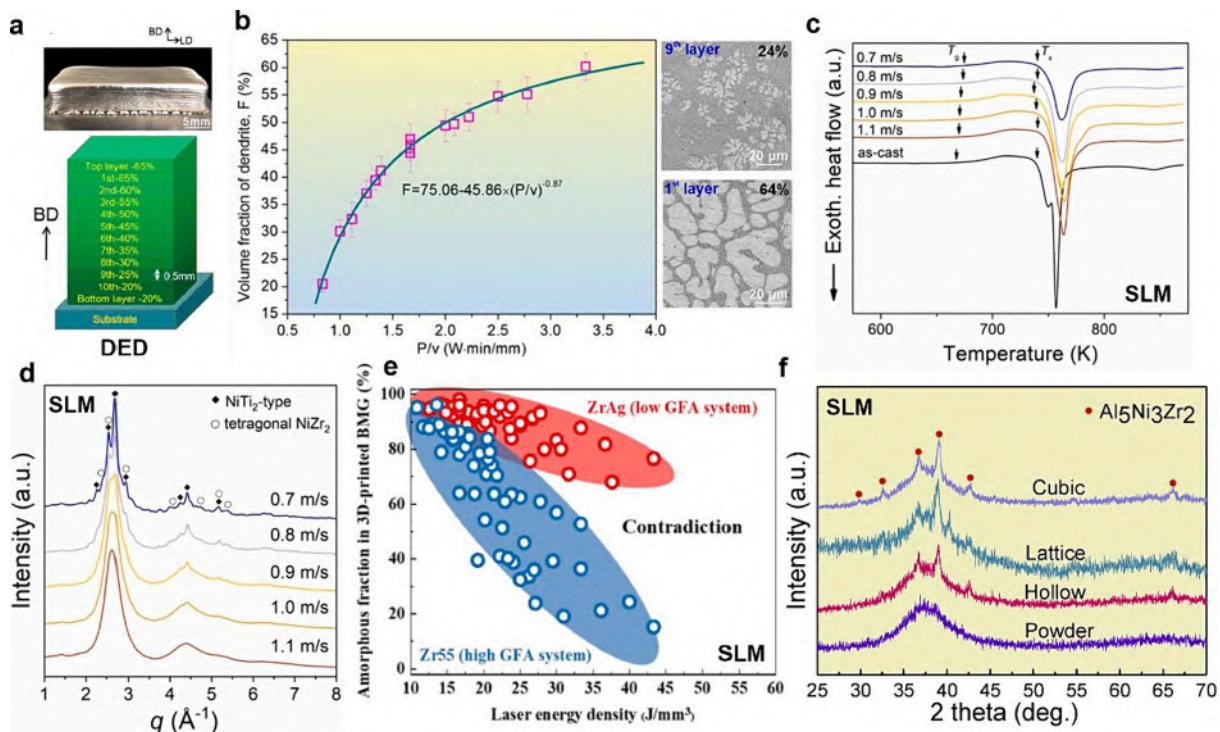


**Fig. 40.** (a) The as-deposited 10-layered gradient BMGC by DED process. The schematic illustration of 10-layer lamellated structure with a gradient transition in volume fraction of the crystalline dendrites is also shown (Adapted form [590]). (b) Dendrite volume fraction as a function of  $P/v$ . The SEM images show microstructural morphologies of the first and ninth deposited layer (Adapted form [590]). (c) DSC traces of as-cast and as-built BMGs fabricated by SLM process at different varying scanning velocity ( $v$ ) and constant  $P = 110 \text{ W}$  and  $h = 180 \mu\text{m}$  (Adapted form [567]). (d) HE-XRD patterns corresponding to the SLMed Zr-based BMG specimens in (c). (e) Variations of amorphous content with laser energy density for two different BMG systems (Adapted from [83]). (f) The XRD pattern for as-deposited Zr-based BMGs with different geometries (Adapted from [614]).

phenomenon, it may be possible to design functionally graded materials (FGM) with distinct characteristics by leveraging inherent sensitivity of BMGs to cooling rate. Lu et al. [590] fabricated a gradient Zr-based BMGC by controlling the heat input and cooling rate during DED. The composite exhibited varying volume fractions of crystalline dendrites, with microstructural differences observed between layers (Fig. 40a-b). The fabrication of the gradient BMGC was achieved by controlling the heat input and cooling rate using the linear energy density ( $P/v$ ) along the build direction (Fig. 40b). This had a direct influence on the microstructure and composition of the composite. The SEM images in Fig. 40b revealed that the size and spacing of crystalline dendrites varied between layers, with the first layer having larger dendrites (64 % volume fraction) compared to the ninth layer (20 % volume fraction). Chemical partitioning was observed between the amorphous matrix and crystalline phases, with enrichment of specific elements in each phase. Further, Laser processing parameters had consistent effects within each layer, ensuring uniformity.

The crystallization in laser-based additively manufactured BMG components is strongly influenced by process parameters [615,616], including laser power, scanning speed, and laser spot size. These parameters dictate the energy input, heat dissipation, and cooling rates experienced by the molten material. For instance, MD simulations have shown that increased laser energy density, achieved by higher power and lower scanning speed, promotes crystallization in Fe50Ni50 due to higher fractions of bcc bond pairs (1661 and 1441) and corresponding Voronoi polyhedrons ( $\langle 0,6,0,8 \rangle$  and  $\langle 0,5,2,6 \rangle$ ) [617]. Thus, optimizing processing parameters is crucial to control the cooling rate and tailor the resulting microstructure.

DSC traces of SLM-processed  $Zr_{52.5}Cu_{17.9}Ni_{14.6}Al_{10}Ti_5$  BMGs at different scanning speeds ( $v$ ) [567] are shown in Fig. 40c. As-deposited samples exhibit a sharp glass transition similar to the as-cast specimen, but with larger enthalpy of crystallization ( $\Delta H_x$ ) at faster scanning speeds. The as-cast specimen shows a different crystallization sequence with overlapping peaks, attributed to high oxygen content influencing the formation of metastable phases. Despite these differences,  $\Delta H_x$  values of as-cast and SLM-fabricated samples at  $v = 1.1$  m/s are nearly identical, suggesting they are fully amorphous. The HE-XRD patterns in Fig. 40d reveal broad glassy maxima for the fastest scanning speed, while lower speeds exhibit sharper reflections corresponding to the NiTi<sub>2</sub>-type “big cube phase”, indicating increased concentration with higher oxygen content. This is consistent with the crystallization behavior observed in the DSC signals.

Composition-dependent crystallization behavior is crucial in amorphous-to-crystalline transformation during laser-based AM of BMG parts. It is well known that even minor changes in chemical composition can significantly alter devitrification kinetics and physical properties in BMGs [126,618–620]. So, the amorphous content in 3D printed BMGs depends on the composition-dependent difficulty of crystallization in the previously formed amorphous phases in the HAZ. Regarding this, Ouyang et al. [83] compared crystallization behavior in two different glass formers low GFA (Zr60.14Cu22.31Fe4.85Al9.7Ag3; ZrAg) and high (Zr55Cu30Ni5Al10; Zr55) GFA and found that the ZrAg BMG consistently had a higher amorphous content than the Zr55 BMG, regardless of laser energy inputs (Fig. 40e). Crystal growth rate plays a critical role in determining the resistance of 3D printed BMGs to amorphous-to-crystalline transformation. Despite lower glass-forming ability, ZrAg BMG exhibited a slower crystal growth rate compared to Zr55 BMG due to

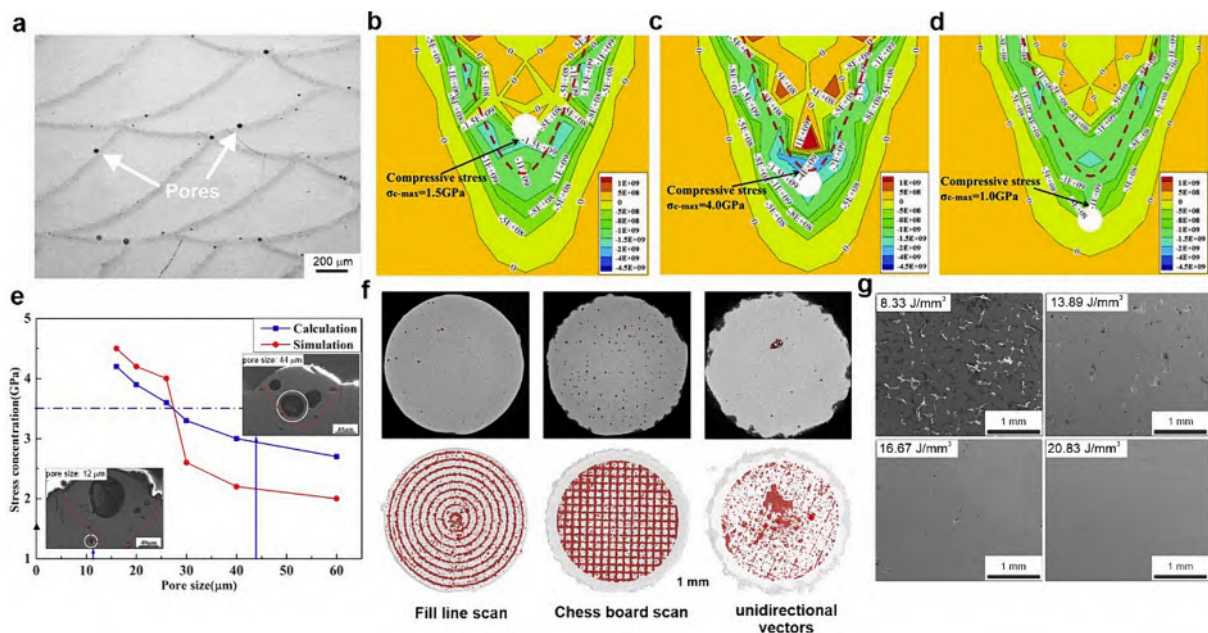


**Fig. 41.** (a) SEM image illustrating a typical microstructure of the 10-mm-thick  $Zr_{50}Ti_5Cu_{27}Ni_{10}Al_8$  BMG deposited by DED process (Adapted from [588]). (b-d) Thermal stress distributions around molten pools ( $E_{line} = 625$  J/m) containing micropores located at different positions: (b) inside, (c) at the edge, and (d) outside the molten pool (Reproduced from [629]). (e) The stress concentration around micropores of varying sizes located at the edge of molten pools. The inset images depict the micropores with sizes of 12  $\mu m$  and 44  $\mu m$  (Adapted from [629]). (f)  $\mu$ -CT images under different scanning strategies. The upper row displays a representative cross-section, while the lower row illustrates a projection of all pores onto the cross-section (Adapted from [574]). (g) SEM cross-sectional morphologies of 3D printed Zr-based BMG samples at different energy densities [630].

their different crystallization mechanisms: primary-type for ZrAg and polymorphous-type for Zr55 [83].

Recently, Sohrabi et al. [621] conducted calorimetric investigations on industrial-grade AMZ4 ( $Zr_{59.3}Cu_{28.8}Al_{10.4}Nb_{1.5}$ ) BMG using flash DSC. The alloy's critical cooling rate was found to be 2500 K/s, while the critical heating rate was determined as 45,000 K/s. This significant difference suggested the formation of a self-doped glass with quenched-in nuclei during the cooling process. In contrast, chemically homogeneous glasses [622] do not contain quenched-in nuclei. Therefore, in AM processes, it is preferable to use materials that can form chemically homogeneous glasses.

Geometrical complexity also influences crystallization. XRD patterns of 3D printed  $Zr_{55}Cu_{30}Ni_5Al_{10}$  parts with different geometries show varying extents of partial crystallization (Fig. 40f) [614]. Calorimetric measurements indicated higher amorphous phase content in hollow and lattice specimens (90 % and 81 %, respectively) compared to cubic specimens (74 %). Larger molten pool size in complex geometries promotes amorphous structure preservation.

### 7.2.3. Solidification defects

Laser-based AM techniques have shown great potential for the fabrication of BMG components, offering the possibility of producing complex geometries and tailored properties. However, during the solidification process of MGs using laser-based AM methods such as SLM and DED, various solidification defects can arise, affecting the quality and properties of the final components.

**7.2.3.1. Pore formation.** One common solidification defect observed during laser-based AM of BMGs is the formation of porosity. A typical microstructure of 3D printed BMGs contains is shown in Fig. 41a. There are several types of pores formed during laser-based AM, namely interlayer pores, open pores, and metallurgical pores. The main mechanisms of pore formation during laser-based 3D printing includes gas entrapment [623], insufficient remelting [624], powder denudation around the molten pools [625], and evaporation of volatile (high vapor pressure) elements [626]. Porosity not only compromises the mechanical integrity of the

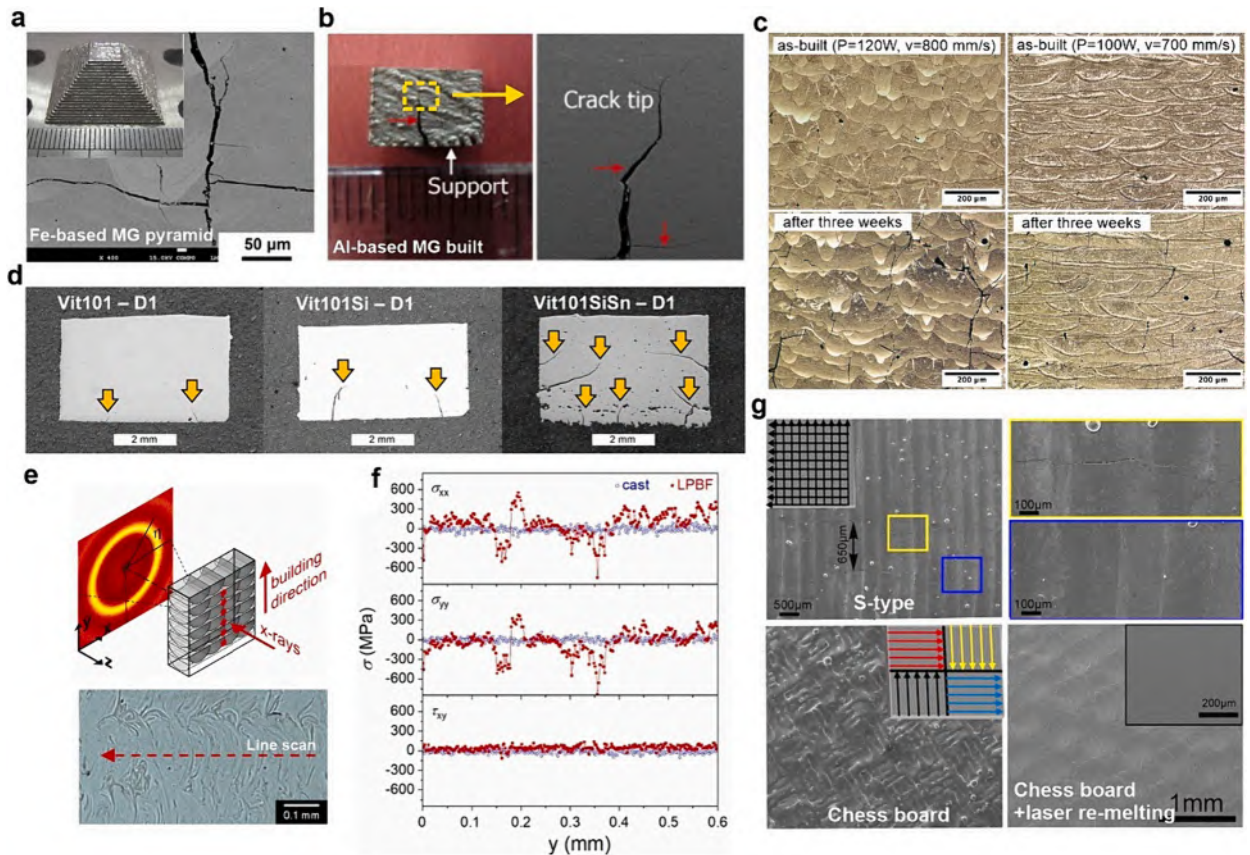


**Fig. 42.** (a) SEM image of microcracks in an Fe-based pyramid fabricated by SLM. The inset shows the Fe-based BMG pyramid (Adapted from [580]). (b) Obvious macrocracking in as-built Al-based BMG processed by SLM (Adapted from [578]). (c) The microstructure of as-built Fe-based samples (top) produced by SLM at different processing parameters. The bottom shows the microstructure three weeks after the process (Adapted from [632]). (d) Optical micrographs of cuboid samples of different compositions (Adapted from [633]). (e) Top: Schematic of the setup of the HE-XRD used for the measurement of residual stress. Bottom: optical micrograph of the SLMed specimen showing the line scan direction (parallel to the building direction). (f) Position-resolved components of residual stress tensor determined by HE-XRD. Adapted from [567]. (g) SEM morphology of fresh surfaces of Fe-based SLM-fabricated samples with s-type and chess board scanning strategies. (Adapted from [634]).

component but also degrades its functional properties such as fatigue performance [627]. Strategies to mitigate porosity include optimizing process parameters, such as laser power, scanning speed, and scanning strategy, to ensure adequate powder melting and fusion during solidification [628].

Micropore location and size significantly affect micro-crack formation. FEM simulations (Fig. 41b-d) show that the highest thermal stress occurs at the molten pool-HAZ interface [629], reaching compressive stresses up to 4.0 GPa, much higher than stresses within or outside the molten pool. Additionally, smaller pore sizes lead to increased thermal stress concentration (Fig. 41e). A microcrack initiates at a 12 μm pore (Fig. 41e inset), while no crack forms at a larger 44 μm pore in the same location. This is because thermal stress exceeds the fracture stress of the Fe-based BMG when pore size is below 30 μm.

Pauly et al. [574] studied the impact of different scanning strategies on pore formation in SLM of a Zr-based BMG. Fig. 41f shows micro-computed tomography (μ-CT) images of three samples with comparable energy densities and different scanning strategies. The fill line strategy minimizes surface roughness, aligning pores along concentric circles. The chessboard strategy produces a grid pattern without affecting pore distribution significantly, which concentrates at the edges or center of each melt track. The unidirectional vectors strategy, despite similar energy density, exhibits the lowest porosity and a more random pore distribution.

Xing et al. [630] investigated defect evolution in Zr60.14Cu22.31Fe4.85Al9.7Ag3 BMG during SLM using experimental analysis and computational fluid dynamics (CFD) simulations. Fig. 41g shows surface morphologies of four samples with different energy densities. Increasing energy density reduced porosity significantly. At the lowest energy density (8.33 J/mm<sup>3</sup>), porosity exceeded 25 %, while at 20.83 J/mm<sup>3</sup>, it dropped to less than 1 %. At 13.89 J/mm<sup>3</sup>, large pores diminished but irregular pores appeared. Pore size and number were greatly reduced at 16.67 J/mm<sup>3</sup>. At 20.83 J/mm<sup>3</sup>, the SLMed BMG samples exhibited high densification with small pores at high magnifications. Different defects were observed in 3D printed BMGs, influenced by laser energy inputs. Low energy densities caused balling, moderate energy densities led to interlayer and open pores, and high energy densities resulted in fine metallurgical pores on the upper surface due to gas escaping during rapid solidification.

**7.2.3.2. Crack formation.** Cracks are a common defect in laser-based AM of BMGs. Fig. 42a illustrates microcracks in an Fe-based MG pyramid printed by SLM [580]. In Fig. 42b, a macrocrack is seen in an Al-based MG built by SLM [578]. Al-based and Fe-based BMGs, being intrinsically brittle, are prone to microcracking during 3D printing, and even process optimization struggles to eliminate it completely [580,631].

Microcracks in BMGs are primarily caused by thermal stresses resulting from rapid cooling rates and thermal gradients during solidification [611]. Changes in local free volume may also contribute to the development of internal stresses [575]. Therefore, a

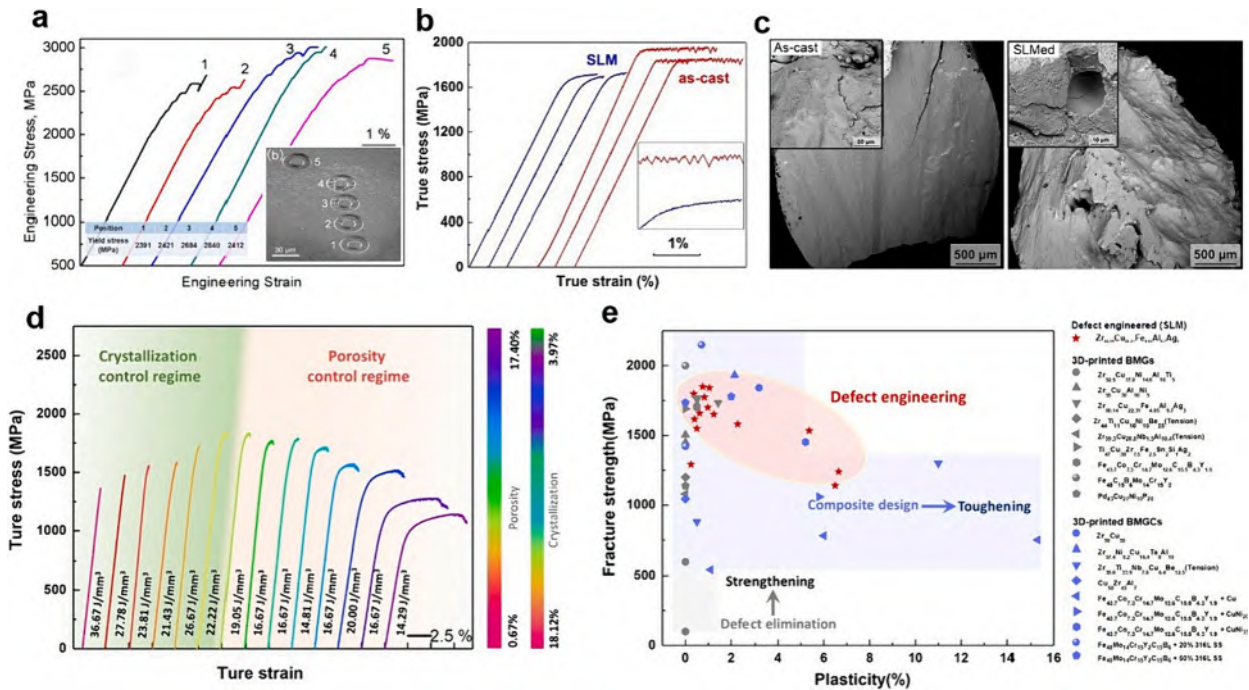


**Fig. 43.** (a) The stress–strain curves taken from micro-compression test. Position 1 is inside molten pool, but the positions 2–5 corresponds to the regions across a single HAZ, as shown in the inset figure. Adapted from [588]. (b) True stress–strain curves of Zr-based samples prepared by casting and SLM. Inset is enlarged view of serrated region. Three curves for each sample shows the reproducibility of results. Adapted from [572]. (c) The fracture surface of as-cast and SLM process Zr-based compression test specimen (Adapted from [574]). (d) Compressive stress–strain curves Zr-based BMG samples with different porosity and crystallization fractions. (e) Fracture strength versus plasticity for 3D printed BMGs and BMG composites. Adapted from [573].

combination of internal stresses from phase transitions and thermal stresses from thermal gradients leads to the formation of microcracks.

In a recent study by Szczepański et al. [632], microcracking in 3D printed BMGs was found to be more complex than previously thought. Microcracks in an SLMed Fe-based BMG were observed several days after the completion of the SLM process (Fig. 42c). Although the as-built samples appeared crack-free, re-observation three weeks later revealed numerous previously unnoticed microcracks, primarily originating from the fusion line and propagating perpendicular to it.

Micropores in as-built BMGs are preferred regions for the initiation of microcracks. As it was discussed in the previous section, FEM simulations and experimental observations by Xing et al. [629] revealed that a critical pore dimension of 30  $\mu\text{m}$  is necessary to trigger the formation of micro-cracks in 3D printed components made of Fe-based BMGs. In another simulation study, Li et al. [580] reported that stress concentration near micro-pores at the boundary of a spherical pore can reach  $\sim 4.1$  GPa. This value exceeds the fractural strength ( $\sim 3.5$  GPa) of the studied Fe-based BMG, leading to the initiation of microcracks.

The intrinsic brittleness of the feedstock MG affects the resilience of built parts against crack propagation. Frey et al. [633] investigated three CuTi-based BMG formers, Vit101 ( $\text{Cu}_{47}\text{Ti}_{34}\text{Zr}_{11}\text{Ni}_8$ ), Vit101Si ( $\text{Cu}_{47}\text{Ti}_{33}\text{Zr}_{11}\text{Ni}_8\text{Si}_1$ ), and Vit101SiSn ( $\text{Cu}_{47}\text{Ti}_{33}\text{Zr}_{11}\text{Ni}_6\text{Si}_1\text{Sn}_2$ ), for SLM 3D printing. Minor additions of Si and Sn to Vit101 enhances GFA and thermal stability but increased brittleness [635]. Higher microalloying levels resulted in increased defect formation, including pores and cracks [633]. Fig. 42d shows Vit101 had the lowest crack content, while Si and Si-Sn additions increased susceptibility to thermally induced cracks and process instability. Cracks in SLM-printed Vit101SiSn indicate residual stresses exceeded its strength, whereas Vit101 and Vit101Si showed resistance to in-plane stresses.

Kosiba et al. [567] used HE-XRD analysis to determine residual stress tensor in as-cast and SLMed  $\text{Zr}_{52.5}\text{Cu}_{17.9}\text{Ni}_{14.6}\text{Al}_{10}\text{Ti}_5$  BMG. Fig. 42e-f show significant residual stresses in the as-built specimen compared to the cast material, with local variations exceeding  $\pm 500$  MPa. Shear stress is negligible in both specimens. This finding demonstrates the influence of localized thermal gradients on stresses detectable by HEXRD.

Microcracks can propagate and deteriorate the structural integrity and mechanical performance of the AMed components. Employing post-processing treatments such as re-scanning [578] and introducing a second crystalline phase [580] can help reduce the formation of microcracks in AMed BMGs.

Zou et al. [634] discovered a scanning strategy that eliminates microcracks in 3D printing of BMG components. Fig. 42g shows surface characteristics of samples fabricated using the s-type and chessboard scanning strategies. The s-type strategy results in a smooth surface with a ripple-like pattern, but cracks appear when the single-track length exceeds 650  $\mu\text{m}$ . In contrast, the novel chessboard strategy, which changes the track direction beyond the critical length, allows for strong metallurgical bonding without cracks. Laser re-melting treatment using this strategy enables crack-free Fe-based BMGs with smooth surfaces.

### 7.3. Mechanical properties in 3D printed BMG(C) components

Developing BMG components as structural materials requires exhibiting good mechanical performance. While 3D printed BMG parts offer advantages in terms of design flexibility and complex geometries, they often exhibit comparable but inferior mechanical properties compared to their conventionally cast counterparts. Several factors contribute to these limitations, including the inherent challenges associated with the AM process and the unique characteristics of BMGs.

The microstructure of 3D printed BMGs causes gradual variations in mechanical properties. In a Zr-based BMG fabricated using the DED process, hardness gradually increases towards the center of the HAZs and decreases towards the molten pools due to partial crystallization in the HAZ [604]. Similarly, in the SLM of  $\text{Al}_{86}\text{Ni}_6\text{Y}_{4.5}\text{Co}_2\text{La}_{1.5}$  MG, non-monotonic changes in hardness were observed across different regions of the scan track [577]. The cooling rate within the solidified scan track decreases from the center to the edge influenced by the laser's Gaussian distribution, resulting in higher hardness at the edge due to reduced free volume content.

Lu et al. [588] conducted micro-compression tests on DED-processed Zr-based BMG, specifically within the HAZ (Fig. 43a). While the elastic behavior of partially crystallized samples resembles that of fully amorphous sample, the yield stresses vary at different testing positions. As the volume fraction of precipitated crystals increases, the yield stresses gradually increase. For example, the heavily crystallized sample at position 4 experiences a stress level of 2840 MPa, 18 % higher than the amorphous sample at position 1 (molten pool). This increase in yield stress can be attributed to dispersion strengthening caused by the dispersion of crystals in the amorphous matrix. Additionally, localized deformation through shear banding is observed through "pop-in" events. The strengthening of the annealed MG in the HAZ is due to the higher hardness of the crystals compared to the glassy matrix.

The most common approach in evaluating mechanical properties of 3D printed parts is simple compression. During compression tests, the 3D printed BMGs often show deteriorated plasticity and slightly decreased yield stresses and fracture strengths compared to the as-cast counterparts. As reported for various SLM-processed Zr-based [570,574,602,636], Cu-based [637], and Ti-based BMGs [582], the compressive fracture strength ranges between 600 and 1800 MPa, while the plasticity varies from 0 % to 1.5 %. Presence of microcrack can even reduce fracture stresses in an Fe-based BMG fabricated by SLM to values as small as 100 MPa [580].

Fig. 43b compares the plastic deformation behavior in as-cast and SLMed Zr-based BMGs [572]. The true stress-strain curves in Fig. 43b show that SLMed samples have lower yield and fracture stresses and a smaller plastic strain compared to as-cast samples. The stress drops during serrated flow are more uniform and smaller in SLMed samples, attributed to shear band-pore interactions. It was further analyzed that pores influence shear band behavior by either being cut through or generating multiple shear bands around them. Even in the absence of nearby shear bands, pores act as initiation sites. The presence of pores leads to a higher density of shear bands with smaller offsets, resulting in enhanced shear band stability and smaller stress drops in SLMed samples.

Fig. 43c illustrates typical fracture surface of an as-cast and a SLMed Zr-based rod, displaying a smooth surface with a fracture angle

of approximately 45° and characteristic vein-like and river-like patterns in the as-cast sample. In contrast, the fracture surface of SLM samples appears much rougher, lacking a single fracture plane. Instead, two intersecting fracture planes resembling a roof structure are observed. At higher magnifications (insets), larger defects ranging from 10 to 50 μm become apparent, some of which contain unmelted powder. Localized patterns emerge, combining characteristics of both dimples and vein-like patterns. The presence of residual porosity alters the stress state in SLM samples during compression, resulting in a corrugated fracture surface with multiple cracks [574].

Regarding mechanical properties in 3D printed BMGs fabricated using LFP, Bordeenithikasem et al. [596] showed that LFPed  $Zr_{65}Cu_{17.5}Ni_{10}Al_{7.5}$  BMGs exhibit exceptional strength and plastic deformation during bending, surpassing the properties of cast beams manufactured from the same remelted feedstock sheet metal. Moreover, Li et al. [638] reported that LFP enables production of fully amorphous BMG parts with high density (~99.9 %). The fully amorphous sample exhibits superior micro-hardness ( $551 \pm 18$  HV), ultimate tensile strength ( $1796 \pm 60$  MPa), and maximum flexural strength ( $2186 \pm 109$  MPa) compared to the cast sample. Partially crystallized LFP parts still demonstrated comparable or higher strengths than the cast parts.

In 3D printed porous MG parts, lattice structures can also impact mechanical performance. Wu et al. [639] recently studied the effects of lattice structures on the mechanical properties of SLMed MG ZrCuAl scaffolds. The inclusion of curved struts resulted in a substantial increase in compressive ductility (122 %) and improved energy absorption (106 %) compared to straight struts. These curved struts effectively prevent shear fracture and delay fracture by reducing strain concentrations.

Laser-based AM of BMGs can introduce secondary phases or defects due to the inherent challenges associated with achieving complete melting and solidification. These secondary phases, such as crystalline particles or residual stresses, can be detrimental to the mechanical properties and structural integrity of the BMG component.

3D printed BMGs have higher oxygen contamination compared to the cast BMGs. The elevated oxygen content in 3D printed samples originates from the large surface area of the powdered MG precursor which can absorb oxygen from the surrounding environment during 3D printing. The oxygen content in 3D printed BMGs prepared by laser-based AM can significantly impact their mechanical properties. Elevated levels of oxygen can lead to various effects, including reduced plasticity, decreased fracture toughness, and increased brittleness [640,641].

The lower fracture toughness in SLM-processed BMG compared to casting is attributed to increased oxygen content, resulting in a

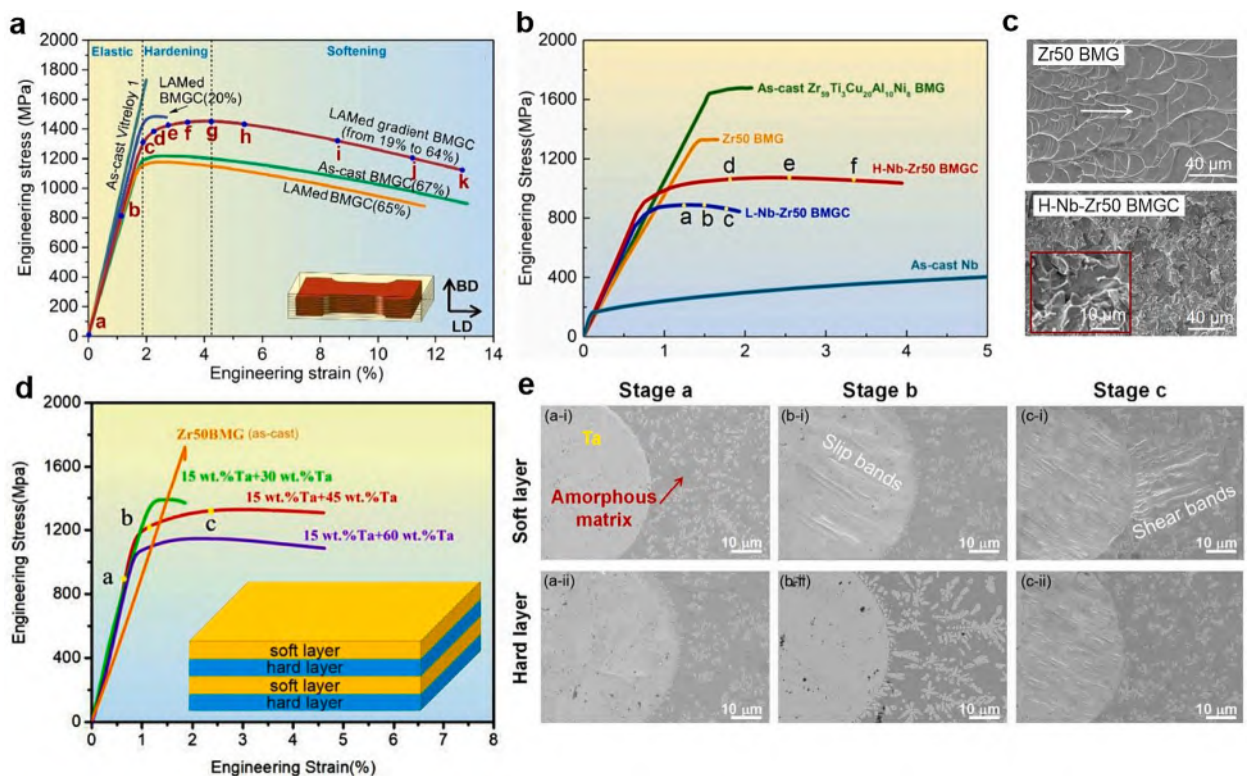


**Fig. 44.** (a) Stress–strain curves of the gradient Zr-based BMGC under tensile testing, accompanied by an inset depicting the sampling location of the tensile specimen (Adapted from [590]). (b) Compressive stress–strain curves of DED manufactured Zr-based BMGs and BMGCs (adapted from [594]). (c) SEM images of the fracture surfaces of compression tested (d) Zr50 BMG and Nb-reinforced BMGC DED processed at high laser power (H-Nb-Zr50 BMGC). Adapted from [594]. (d) Compressive engineering stress–strain curves of DED-manufactured Zr50-Ta BMGCs and as-cast Zr50 BMG. (e) Microstructural evolution of the 15 wt% (hard) + 45 wt% (soft) lamellated BMGC during the deformation process. The deformation stages correspond to the labels indicated on the stress–strain curve presented in (d). Adapted from [595].

higher shear transformation barrier [640]. Load drop behavior during micro-pillar compression differed between the two processes, with as-cast samples (containing 168  $\mu\text{g/g}$  oxygen) showing pre-yield drops and SLM samples showing none, linked to higher oxygen content in SLM BMG (1271  $\mu\text{g/g}$ ) [86]. Additionally, SLMed AMZ4 BMG exhibited fracture toughness of 24–29  $\text{MPa}\cdot\text{m}^{1/2}$ , much lower than 97–138  $\text{MPa}\cdot\text{m}^{1/2}$  ( $K_{\text{IC}}$ ) and 158–253  $\text{MPa}\cdot\text{m}^{1/2}$  ( $K_{\text{JIC}}$ ) in the cast alloy with the same composition [641]. Further, experiments on fatigue crack growth indicated relatively low values for the fatigue threshold,  $\Delta K_{\text{th}}$ , of  $\sim 1.33 \text{ MPa}\cdot\text{m}^{1/2}$ , and the Paris law exponent,  $m = 1.14$ . These inferior mechanical properties were attributed to approximately 7.5 times higher dissolved oxygen concentration compared to the cast alloy. In another work, a threshold of approximately 1600  $\mu\text{g/g}$  oxygen in the starting material was identified to prevent strength loss from nano-crystallization in SLM Zr-based BMGs [81]. In addition, Cu-Ti-based BMGs printed by SLM showed minimal impact on thermal stability with varying oxygen concentration [76]. The HRTEM analysis confirmed fully amorphous phase in commercial purity powders and SLM samples, ruling out oxygen-induced nucleation. These findings highlight successful AM of Cu-Ti-based BMGs in their amorphous state, using commercial purity feedstocks and accounting for potential oxygen uptake during production.

Porosity is another crucial factor that limits the mechanical properties of 3D printed BMGs compared to their cast counterparts. Porosity in 3D printed BMGs causes decreased plasticity in compression [570,574,637] and brittle fractures with minimal ductility in tension [642]. Ultimate Tensile Strength decreases linearly with porosity, and Young's modulus is insensitive at low porosity ( $<2\%$ ) but decreases significantly at high porosity. FEM simulations reveal different deformation mechanisms: pore-free BMGs form shear bands uniformly, while BMGs with pores experience plastic deformation around the pores with STZs. Increasing load connects STZs, resulting in localized shear bands and fracture. Fracture orientation in 3D printed BMGs differs from as-cast Zr-based BMGs due to pore structures [642]. While large irregular pores decrease toughness as stress concentrator [574], small spherical pores enhance shear banding in MGs (see discussion on Fig. 43b) [572].

Crystallinity in AMed BMGs is another factor influencing their mechanical properties. Increased crystallinity and the formation of brittle crystalline phases disrupt the amorphous structure, resulting in lower strength, toughness, and ductility [571,602]. For example, Lin et al. [586] have argued that the brittleness of DED processed  $\text{Zr}_{55}\text{Cu}_{30}\text{Al}_{10}\text{Ni}_5$  BMGs is due to excessive intermetallic precipitation ( $\text{NiZr}_2$ ,  $\text{CuZr}_2$ ,  $\text{Al}_5\text{Ni}_3\text{Zr}_2$ ) and defects in the deposit. Although maintaining a high degree of amorphicity is vital to preserve the desirable mechanical properties of 3D printed BMGs, later it will be discussed that partial devitrification in 3D printed BMGs and developing BMGCs by dispersing ductile precipitates in the glassy matrix is an effective strategy to enhance the plasticity and toughness of AMed BMG components.

Laser-based AM not only enables the production of large BMG samples with complex geometries but also allows enhancing mechanical properties of 3D printed Zr-based BMGs through synergistic defects engineering [573]. Precise control of porosity and crystallization optimizes the trade-off between fracture strength and plasticity. As can be observed from Fig. 43d, increasing porosity from 2.87 % to 17.4 % boosts plastic strain from 1.05 % to 6.6 %, while maintaining a strength of 1100 MPa even at 17.4 % porosity.

A comparison of different strategies for tuning fracture strength and plasticity of 3D printed BMGs is shown in Fig. 43e [573]. The conventional approach of defect elimination strengthens BMGs but lacks plasticity, while composite design compromises strength for toughness. In contrast, defect engineering combines porosity and crystallization to achieve a favorable balance of strength and plasticity. However, achieving simultaneous strength, plasticity, and fracture toughness remains a challenge, particularly for brittle BMG materials.

As mentioned before, laser-based 3D-printing also enables the tailoring of mechanical properties in BMGCs through the incorporation of reinforcement phases. There are two main approaches for making BMGCs [643]. The first approach is in-situ, where the reinforcement is precipitated within the BMG during solidification. The second approach is ex-situ, where solid reinforcements are added to the BMG melt and then cooled. While in-situ precipitate reinforced BMGCs are commonly used, they have limitations in terms of available compositions. On the other hand, ex-situ precipitate reinforced BMGCs offer more flexibility in terms of composition but suffer from microstructural and mechanical heterogeneity due to segregation.

The SLM and DED techniques are well-suited for manufacturing BMGC structures due to their ability to control the microstructures and compositions during the layer-by-layer shaping and consolidation process using laser powder feed deposition [578,580,590,593–595,644–646].

Lu et al. [590] fabricated gradient Zr-based BMGC using laser-based DED technique. The gradient BMGC displayed exceptional properties (Fig. 44a), with a yield strength exceeding 1.3 GPa and a tensile ductility of  $\sim 13\%$ . The synergistic strengthening effect between adjacent layers and the heterogeneous microstructure contributed to the outstanding combination of strength and ductility.

Moreover, Luo et al. [644] manufactured Cu-containing Fe-Co-B-Si-Nb BMGCs using SLM with varying laser power and scanning speed. Dense  $\text{FeCoBSiNb-Cu}$  BMGCs fabricated at 1.39  $\text{J}/\text{mm}^2$  exhibited high fracture strength ( $900 \pm 18 \text{ MPa}$ ) and large fracture strain ( $10.7 \pm 2.1\%$ ) due to the composite effect of a hard Fe(Co)-rich amorphous phase and a ductile Cu-rich phase. On the other hand, SLM-produced porous BMGCs at 0.69  $\text{J}/\text{mm}^2$  had lower fracture strength ( $722 \pm 2 \text{ MPa}$ ) but increased fracture strain ( $16.3 \pm 2.7\%$ ) due to the presence of lack-of-fusion pores.

Further, Zhang et al. [647] and Gao et al. [648] 3D printed a CuZr-based BMGCs with in situ-formed B2 CuZr phase using SLM. The B2 phase transformation to B19' martensite during deformation improved ductility through transformation-induced plasticity (TRIP) [647,649]. The combination of B2 phase in HAZs and amorphous phase created a "brick-and-mortar" structure, effectively blocking crack propagation and improving fracture toughness [647]. More recently, the TRIP effect and precipitation of B2 phase was also observed during 3D printing of  $\text{Zr}_{48}\text{Cu}_{46.5}\text{Al}_4\text{Nb}_{1.5}$  BMGC by DED process [591]. Regarding exploring TRIP effect to improve plasticity and toughness in BMGCs, Yu et al. [592] have recently introduced a novel high-throughput strategy to accelerate the exploration of TRIP BMGCs in Zr-Cu-Al system by using DED technique.

Li et al. [580] employed high toughness Cu and Cu-Ni alloys to manufacture crack-free Fe-based BMGCs. The findings indicated

that the presence of high-density dislocations in the second phases during SLM effectively mitigated thermal stress by dissipating strain energy, thereby suppressing micro-crack formation. Further, the incorporation of the second phase significantly enhanced the fracture toughness of Fe-based BMGs to  $47 \text{ MPa}\cdot\text{m}^{1/2}$ , a value approximately 20 times greater than that of the Fe-based BMG ( $2.2 \text{ MPa}\cdot\text{m}^{1/2}$ ). Recently, it was reported that the addition of 316L stainless steel powder with “fishbone” shaped phases to the brittle Fe-based amorphous powder during DED process can also effectively suppress micro-crack propagation, resulting in a Fe-based BMGC with a plastic strain of  $\sim 17\%$  and a strength of 2355 MPa, the highest plasticity among BMGCs with dimensions larger than 1 mm [593].

Gao et al. [650,651] fabricated Ti/Zr-based BMGCs with in-situ  $\beta$  phase reinforcement using SLM, where increasing Cu content (5%, 10%, 15% at.) improved hardness but decreased plasticity, causing cracks in high Cu-containing samples. However, sample with 5 at.% Cu showed a comparable yield strength of  $1386 \pm 64 \text{ MPa}$ , attributed to finer microstructure and twinning/martensitic transformation. In their further research, Gao et al. [646] investigated the effects of Al addition on SLMed Ti/Zr-based BMGCs,  $(\text{Ti}_{0.65}\text{Zr}_{0.35})_{100-x-y}\text{Cu}_x\text{Al}_y$  ( $x = 5, 10; y = 1, 3 \text{ at.}\%$ ). While Al had a lesser influence on microstructure compared to Cu, increasing Al content enhanced amorphous phase formation and suppressed  $(\text{Ti}, \text{Zr})_2\text{Cu}$  precipitation, improving the  $\alpha$  phase. The  $\beta$  phase experienced  $\alpha'$  and  $\alpha''$  martensitic phase precipitation during SLM. Compression tests on Cu5Al1 and Cu5Al3 manufactured parts revealed reduced yield strength, increased plastic strain, and improved strain hardening with higher Al content. However, Cu10Al3 deposit showed decreased plastic deformation due to numerous  $\alpha'$  martensitic phases and crack formation.

Several studies have explored developing ex-situ BMGCs by laser-based AM techniques. Zhang et al. [652] achieved high amorphous phase fraction ( $>90\%$ ) in in-situ Zr-based BMGCs with Ta precipitates using optimized SLM technique. The printed composites exhibited remarkable properties: fracture strength of 1.9 GPa, plastic strain of 2.15%, and notched fracture toughness of  $60 \text{ MPa}\cdot\text{m}^{1/2}$ , similar to the as-cast sample. These properties were attributed to the abundant amorphous phase and ductile Ta precipitates, promoting shear bands and hindering crack propagation, enhancing plasticity and toughness.

Hu et al. [594] investigated laser-based DED-manufactured  $\text{Zr}_{50}\text{Ti}_5\text{Cu}_{27}\text{Ni}_{10}\text{Al}_8$  (Zr50) BMGCs reinforced with 50 wt% Nb. The Nb-reinforced BMGCs showed improved plasticity compared to monolithic BMGs (Fig. 44b). The presence of Nb restricted structural relaxation, reduced brittle phase formation, and resulted in ductile fracture behavior. SEM images (Fig. 44c) revealed flat fracture surfaces with vein-like patterns in the monolithic BMG, while the Nb-reinforced sample exhibited undulations and fine dimples indicative of ductile fracture. The improved plasticity was attributed to Nb's higher thermal diffusivity and its role in delaying shear band propagation and transforming them into cracks. Laser power optimization was necessary to balance load transfer and nanocrystal volume fraction. Most recently, Wang et al. [653] manufactured  $\text{Cu}_{47}\text{Zr}_{47}\text{Al}_6$  BMGCs with Mo microparticle reinforcement using SLM. Enhanced mechanical properties resulted from high glassy phase content, ductile Mo particles, reduced porosity, and absence of thermal cracks. Mo particles minimized cracks and pores, promoted shear bands, and impeded crack propagation, improving composite properties.

While incorporating ductile crystalline dendrites into a glassy matrix enhances the ductility of BMGCs, this can lead to a strength decrease and a tradeoff between strength and ductility. Cui et al. [595] employed a flexible laser-based DED approach to produce a lamellated Zr-based BMGC with a notable combination of yield strength ( $\sim 1.2 \text{ GPa}$ ) and ductility ( $\sim 5\%$ ) (Fig. 44d). The design involves alternating soft and hard layers, utilizing asynchronous deformation at different scales. The incorporation of dual-scale Ta particles uniformly distributed in the amorphous matrix further enhances the mechanical properties, achieving a remarkable balance between strength and ductility. The microstructural analysis (Fig. 44e) reveals elastic deformation in stage a, slip bands in the soft layers Ta particles during stage b, and slip band accumulation at interfaces during stage c, leading to plastic deformation in both the Ta particles and amorphous matrix. The dispersed Ta dendrites restrict shear banding and promote plastic deformation across the soft and hard layers.

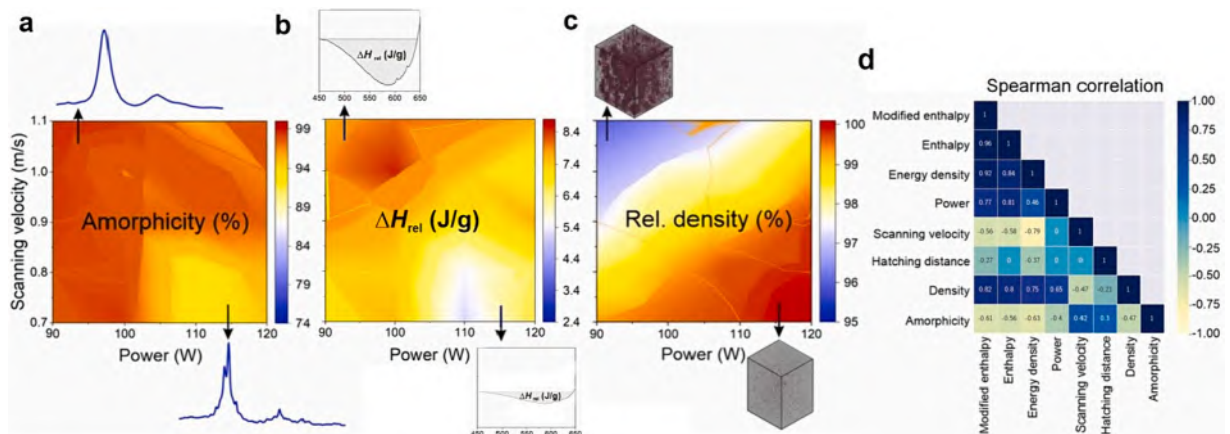


**Fig. 45.** Optimizing process parameters during SLM of a Zr-based BMG. Amorphicity (a), relaxation enthalpy (b), and relative density (c) a function of scanning velocity (v), laser power (P) at a hatching distance (h) of 200  $\mu\text{m}$  and layer thickness ( $l_p$ ) of 40  $\mu\text{m}$ . (d) Spearman's rank correlation coefficients and correlation matrix for various processing parameters. .

Adapted from [567]

#### 7.4. Optimizing processing parameters during laser-based AM

Optimizing the processing parameters during laser-based AM of BMGs is crucial to achieve desired microstructures and properties, minimize solidification defects, and enhance the overall performance of the fabricated parts. Controlling laser power, scanning speed, layer thickness, hatching distance (i.e., overlapping between adjacent melt tracks), and implementing preheating or pre-alloying strategies can help regulate the thermal gradients, enhance inter-layer bonding, and minimize defects.

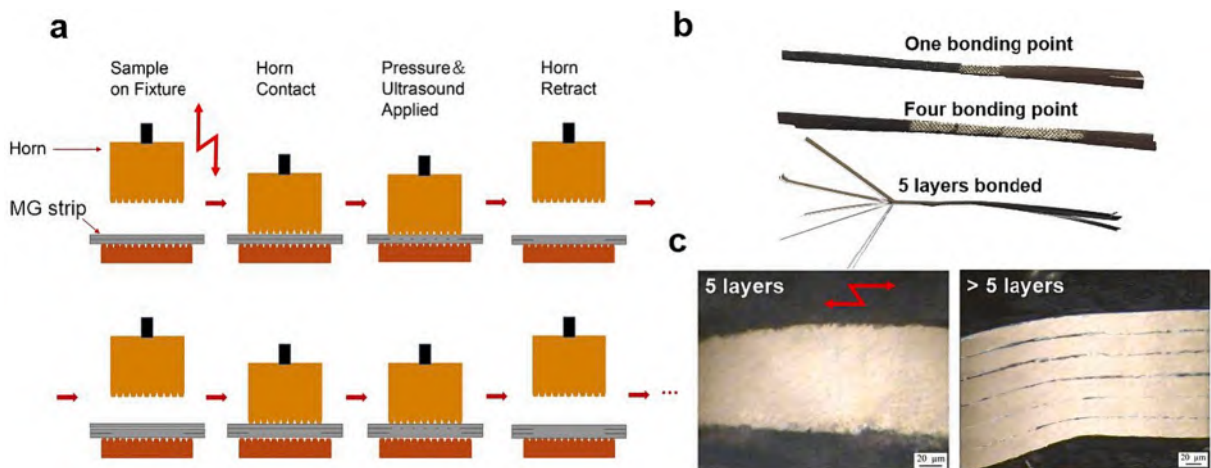
According to previous studies on Fe- [579] and Zr-based [574] BMGs during SLM process, there is a general indication that lower laser powers ( $P$ ), higher scanning speeds ( $v$ ), and large hatching distances ( $h$ ) favor amorphicity and suppression of crystallization. At high  $P$  values, the dominant convection heat transfer mechanism influences the chemical homogeneity of the liquid through oscillation or capillary effects. This can reduce GFA and increase the chances of oxidation, leading to the formation of oxide compounds which serve as sites for the heterogeneous nucleation of crystallites [568]. On the other hand, high  $P$  generally favors a high relative density. In the case of scanning speed ( $v$ ), high  $v$  will cause partial melting of MG feedstock due to inadequate energy input. Although low  $v$  is beneficial for densification, it would accumulate heat and lead to decreased cooling rates and pronounced crystallization during SLM process [574]. Further, smaller  $h$  leads to lower cooling rates and induces crystallization [571], whereas higher  $h$  increases the spacing between adjacent melt tracks and reduces their overlap and re-melting, ultimately leading to insufficient fusion and decreased relative density [574].

The scanning strategy is another adjustable parameter during SLM. As discussed in previous section, using chess board strategy followed by laser rem-melting minimizes micro-cracks and improves densification during SLM of Fe-based BMG [634]. Further, Li et al. [571] have reported that performing multiple scans leads to the averaging of the melt pool and more homogenous distribution of the constituent elements, which ultimately promotes the formation of the amorphous phase.

Kosiba et al. [567] conducted a comprehensive study on SLM fabrication of  $Zr_{52.5}Cu_{17.9}Ni_{14.6}Al_{10}Ti_5$  BMGs under various processing conditions. Processing maps were created to optimize porosity, structural relaxation, and crystallization. Fig. 45a-c demonstrate the trade-off between amorphicity, relaxation enthalpy ( $\Delta H_{rel}$ ), and relative density. Lowering power ( $P$ ) and increasing scanning speed ( $v$ ) result in higher amorphicity and  $\Delta H_{rel}$  but lower density due to the formation of irregular lack-of-fusion pores. On the other hand, higher hatch distance ( $h$ ) and lower  $v$  improve density but decrease amorphicity and  $\Delta H_{rel}$ . In addition, residual stresses generated during the SLM process (see Fig. 42) were contributed to the increased  $\Delta H_{rel}$ . By overlaying processing maps, optimal conditions for high density (99.65 %) and amorphicity (98.55 %) were identified as  $P = 100$  W,  $h = 200$   $\mu$ m, and  $v = 0.9$  m/s.

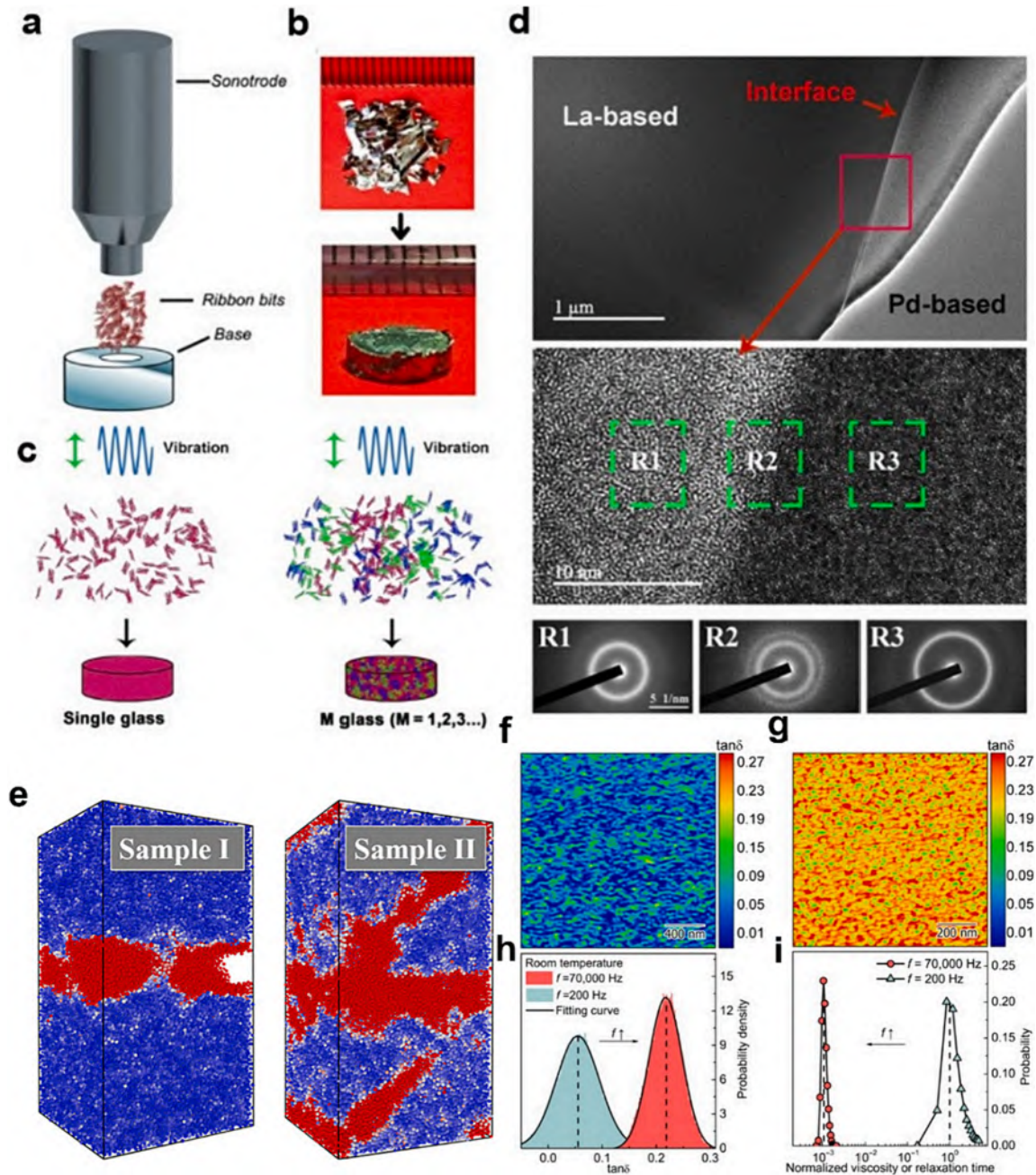
The volumetric energy density,  $E_d$ , is a commonly employed criterion for optimizing the influential SLM processing parameters to achieve high-density specimens [561,574]. By combining the processing parameters,  $E_d$  is formulated as  $E_d = \frac{P}{vhl}$ , where  $l_t$  is the thickness of deposited layer. To ensure the fabrication of dense BMG components using SLM, it is crucial to utilize high  $E_d$  to prevent the formation of elongated pores. Pauly et al. [574] found a critical  $E_d$  value of 15 J/mm<sup>3</sup> below which the Zr-based powders undergo re vitrification during SLM. In addition, Kosiba et al. [567] have shown that density variations with respect to  $E_d$  in an SLMed Zr-based BMG exhibit a strong and consistent correlation. In contrast, the relationship between amorphicity and  $E_d$  demonstrates a decreasing trend.

Fig. 45d presents the correlation matrix and Spearman's correlation coefficients for SLMed BMG parameters [567]. The Pearson correlation coefficient ranges from -1 to 1, with 0 indicating no linear relationship. It measures the strength and direction of the linear relationship between variables. In Fig. 45d, Density shows a strong correlation with volumetric energy density and normalized enthalpy. A modified enthalpy criterion incorporating the hatching distance exhibits the strongest correlation with density. Further, amorphicity displays a moderate to strong negative correlation with all three criteria. These findings highlight the need for advanced optimization strategies and comprehensive models to enhance the printability and reliability of SLMed BMG components.



**Fig. 46.** (a) Schematic of UAM process (Adapted from [656]). (b) Three-layered MG stacks with one and four bonding points and five-layers bonded MG stacks (Adapted from [656]). (c) Cross-sectional optical micrographs from stacked MG foils (Adapted from [657]).

Considering process optimization in other laser-based AM techniques, Zhang et al. [654] have performed single-track DED experiments on a Zr-based MG using a range of laser powers and scanning speeds on low carbon steel. Cracking was predominantly observed at high powers ( $P > 200$  W) or high linear energy densities ( $P/v > 0.6$  W-min/mm), while lack-of-fusion occurred more frequently at lower powers ( $P < 150$  W) or lower linear energy densities ( $P/v < 0.2$  W-min/mm). Simulation results indicated that increasing the linear energy density input during laser DED process can decrease the cooling rate and promote crystallization.



**Fig. 47.** (a) Schematic of UAM process. (b) Image of ribbon feedstock and bulk disk manufactured. (c) A schematic illustrating fabrication of single-phase and multiphase BMGs by ultrasonic vibrations from the ribbon feedstocks. (d) Microstructure of manufactured Pd-La dual-phase BMG. (e) Snapshot of samples I and II applying the constant-strain and constant-frequency vibration methods, respectively, with atoms colored by nonaffine squared displacements at the yielding point. (f-i) Dynamic mechanical properties of the Zr50Cu50 MG surface measured at frequencies of 200 and 70,000 Hz. .

Adapted from [554]

### 7.5. Ultrasonic AM (UAM)

UAM, also known as ultrasonic consolidation, is an advanced manufacturing technique combining the principles of ultrasonic welding (see Section 6.3.2) and AM to build functional parts. UAM has been successfully used to manufacture metallic parts from a wide range of materials, including aluminum, titanium, stainless steel, and nickel-based alloys [655].

UAM of MGs utilizes ultrasonic vibrations to join layers of MG ribbons (foils) or powders together, forming a solid part. The process begins with the preparation of a stack of metal foils/powders, which are micrometer-sized. The stack is then clamped between a stationary baseplate and a vibrating sonotrode. The sonotrode applies ultrasonic vibrations to the metal foils, causing the foils to soften and bond together through a solid-state diffusion process, without the need for melting or the use of additional materials such as adhesives or solder. The bonding mechanism during UAM of MGs is quite similar to ultrasonic welding.

Wu et al. [656] successfully manufactured Ni-based MG stacks using UAM. Fig. 46a illustrates their ultrasonic spot-bonding machine. The process involved placing two layers of MG strips on a fixture and configuring the bonding parameters. The ultrasonic bonding system was then activated, and the strips were pressed against the sonotrode for bonding. The sample was further compressed by the sonotrode to prevent warping. The UAM process achieved layer-by-layer accumulation (Fig. 46b), resulting in Ni-based MG stack production. This prevented crystallization and maintained the thermal properties of the MG. The interlayer bonding exhibited excellent integrity, making separation of the layers challenging. Excessive input energy led to the formation of a nanocrystalline phase. The manufactured MG stacks displayed improved internal hardness and modulus compared to the original materials.

UAM was utilized to manufacture solid bonds in multi-layer  $\text{Fe}_{78}\text{Si}_9\text{B}_{13}$  MG foils using transverse vibrations [657]. Successful bonding was achieved under two processing conditions:  $F_N = 1144.53 \text{ N}$ ,  $t = 200 \text{ ms}$ , and  $n = 4$ ;  $F_N = 1373.44 \text{ N}$ ,  $t = 220 \text{ ms}$ , and  $n = 5$ , where  $F_N$ ,  $t$ , and  $n$  denote the bonding force, bonding time, and number of layers, respectively. No visible interface or defects were observed in the welded MG samples, as shown in Fig. 46c. However, further layer addition hindered the bonding of MG foils. The amorphous structure and thermal properties of the joined MGs remained unchanged and comparable to those of the parent MG. The formation of joined MGs can be attributed to the superplastic flow and the thermal stability of the supercooled liquid state at elevated temperatures.

In 2019, Ma et al. [554] introduced a novel UAM technique. This innovative approach (Fig. 47a) offers a facile and flexible route for consolidating MG ribbons, bypassing the need for traditional high-temperature processing. The ribbons were clamped in a cemented carbide cavity under a preload pressure of  $\sim 12 \text{ MPa}$ . A sonotrode impacted the sample at 20,000 Hz and a pressure of 30–50 MPa. A photograph of a Zr-based BMG disk (5 mm diameter, 3 mm height) produced from ribbon feedstock is shown in Fig. 47b.

High-frequency vibration enables the formation of single-phase BMGs by bonding ribbons of the same type and multiphase BMGs by combining different types of ribbons, as schematically depicted in Fig. 47c. The microstructure of the Pd-La dual-phase BMG is shown in Fig. 47d, with a clear interface separating the La-based and Pd-based regions. The HRTEM images confirm the distinct amorphous structures of the two phases. The diffraction patterns in Fig. 47d indicate the amorphous nature of the multiphase BMG [554].

The bonding mechanism involves activating MG surfaces [554]. Using MD simulations on a model Zr-based MG under uniaxial

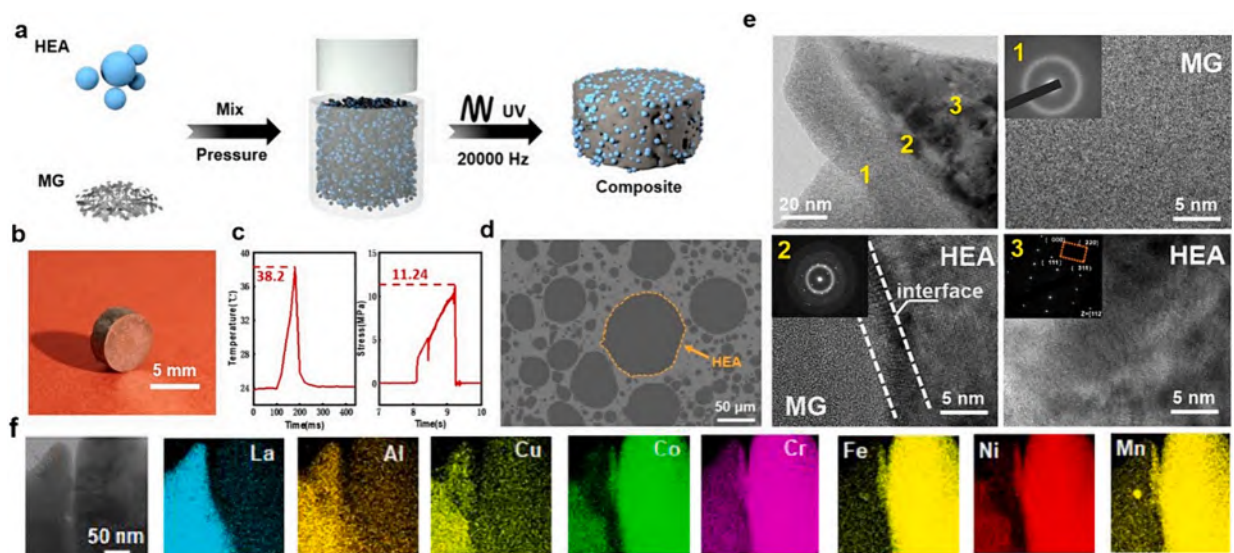


**Fig. 48.** (a) Schematic diagram for fabricating the HEA-MG BMGCs. (b) Photograph of manufactured BMGC disk. (c) Temperature and stress profiles during UAM process. (d) SEM images from BMGC with MG:HEA mass ratio of 5:5. (e) The bright-field TEM images of the bonding area in fabricated 5:5 BMGC. The corresponding diffraction pattern for three regions are shown as the insets. (f) Elemental distributions within a micro-region encompassing the interface of BMGCs. .

Adapted from [661]

compression, full contact and interface formation were achieved. Two relaxation methods were then followed: constant-strain (sample I) and constant-frequency vibration (sample II). Snapshots, applying constant-strain and constant-frequency vibration methods, are shown in Fig. 47e. Specimen I yielded from interface cracking, while sample II exhibited shear bands across the interface, associated with pronounced structural rearrangements. This indicates a notably stronger interface in sample II. Furthermore, calculated time-dependent mean square displacements near the interface surpassed those in the bulk, suggesting potential surface activation near the intrinsic relaxation frequency, strengthening surface interactions.

Viscoelastic loss tangent ( $\tan\delta$ ) maps in Fig. 47f-g show spatial heterogeneity, indicating dynamic heterogeneity within the MG. Surface atoms in localized spots exhibit high activation and energy dissipation. Mobility of active surface atoms depends on the driving frequency. Fig. 47h demonstrates an increase in  $\tan\delta$  as the driving frequency rises. Viscosity (or relaxation time) decreases by three orders of magnitude at the surface with increasing driving frequency (Fig. 47i). The observed high internal friction ( $\tan\delta = 0.2$ ) in the surface layers of the MG, activated below  $T_g$ , is similar to that observed in bulk samples around  $T_g$ . These findings support the fast mobility of surface atoms in MGs, enabling an effective fast bonding process with an appropriate high driving frequency.

In addition, the UAM strategy has been employed to fabricate amorphous-crystalline composite structures. Li et al. [658] additively manufactured Al/Ni-based and Cu/Ni-based MG composites (MGCs) using ultrasonic vibrations. The junction of the MGC samples did not exhibit the formation of intermetallic compounds, and the Ni-based MG remained amorphous. The composite specimens produced through UAM displayed hardness and modulus values that were intermediate between those of the two constituent materials, suggesting that UAM merged the mechanical properties of MG and crystalline metals together.

In another study conducted by Wang et al., [659], laminated composite structure from Fe-based amorphous strip and Al foil was built using ultrasonic consolidation. While the composite retained the properties of the amorphous state, the interface of the laminate exhibited strong bonding without visible cracks. Tensile test revealed that the bonding force exceeded the tensile strength of the aluminum layer, resulting in step-wise fracture consisting of a combination of brittle and ductile fracture. The bonding mechanism involved localized softening and partial recrystallization of the aluminum layer, along with the formation of shear bands within the amorphous alloy.

More recently, the high-entropy alloy (HEA) and MG biphasic BMGCs have been successfully manufactured by UAM [660,661]. Liang et al. [661] fabricated BMGCs using  $\text{La}_{55}\text{Al}_{25}\text{Ni}_5\text{Cu}_{10}\text{Co}_5$  MG and  $\text{Co}_{20}\text{Cr}_{20}\text{Fe}_{20}\text{Ni}_{20}\text{Mn}_{20}$  HEA. The schematic of process and a BMGC manufactured disk are shown in Fig. 48a-b, respectively. Temperature and stress profiles (Fig. 48c) demonstrate consolidation under low-temperature and low-stress conditions. By adjusting the mass ratios of the alloys, the compressive strength and plasticity of the BMGCs could be controlled. Microstructural characterizations confirmed excellent bonding quality without internal defects. SEM

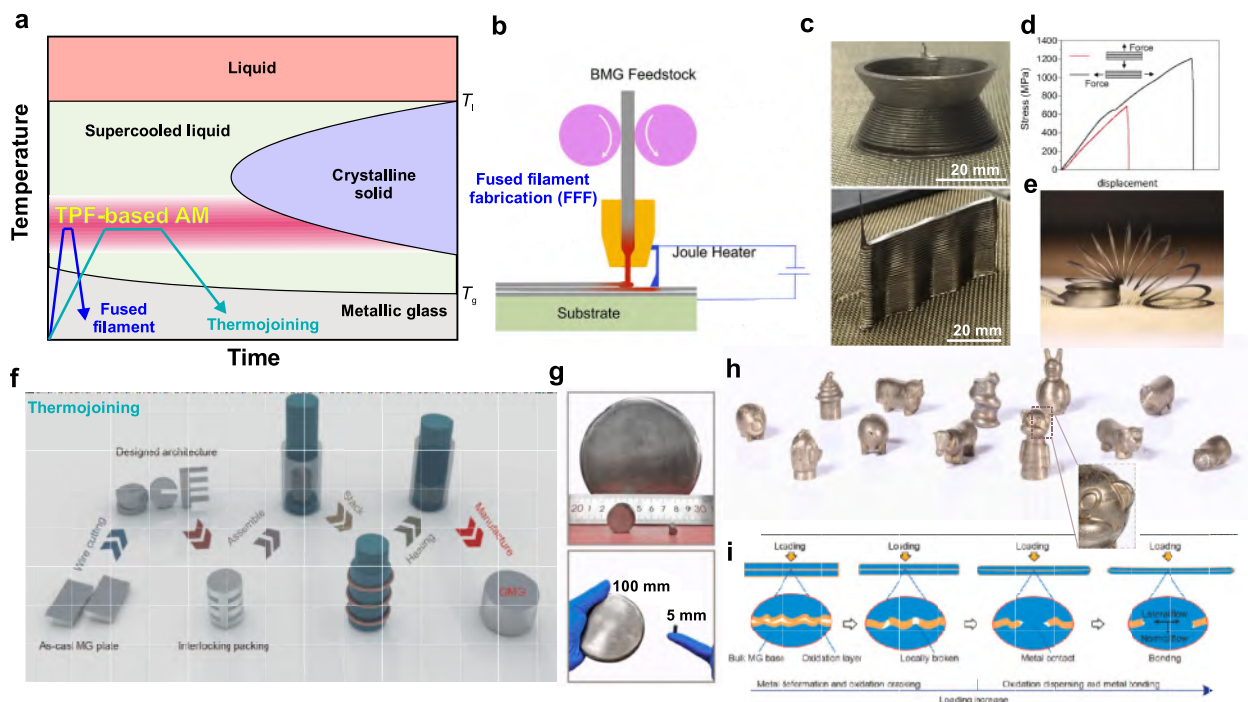


**Fig. 49.** (a) The TTT diagram illustrating processability window for TPF-based AM of BMGs in SLR. The diagram also compares FFF and thermojoining TPF-based AM techniques. (b) Schematic of FFF process. (c) BMG parts printed by the TPF-based FFF process. (d) Quasi-static tensile testing of 3D printed BMG parts parallel and perpendicular to the printing direction. Adapted from [662]. (e) Lack of metallurgical bonding due to the absence of Joule heating during printing and negligible normal strength ( $\sigma_{\perp} \sim 0$ ). (f) Schematic of thermojoining process. (g) The photographs of GMG fabricated by thermojoining AM and the as-cast rod (h) Photographs showing the traditional Chinese Zodiac, featuring twelve distinct animal symbols. (i) Schematic of the bonding mechanism during thermojoining process. Adapted from [442].

image (Fig. 48d) illustrates a BMGC with a 5:5 MG:HEA mass ratio. HRTEM images (Fig. 48e) reveal amorphous, crystalline, and interface regions. A descriptive mechanism for bonding during UAM is as follows. Ultrasonic vibration softens and deforms MG particles, filling gaps and enveloping HEA particles. High-frequency vibration breaks down MG oxide layer for element transfer. Ultrasonic vibration holds the MG and HEA together, acting as glue [441], while sonotrode compression ensures a compact composite. As shown in Fig. 48f, the La, Al, and Cu elements partially transfer from the MG side to the HEA side, while the Cr, Fe, and Mn elements partially transfer from the HEA side to the MG side. This promotes bonding between the MG and HEA, resulting in the formation of all composites with a unique sandwich-like structure.

## 7.6. Tpf-based AM

The relaxation of BMGs allows them to transition into a supercooled liquid state when heated. This unique behavior enables TPF techniques, enabling the production of metal components (see Section 5.1.2). The use of TPF-based AM involves leveraging the ability of thermoplastically formable BMGs to soften, allowing for the layer-by-layer joining of BMGs through an interlayer metallurgical bonding mechanism.

The schematic representation of TTT diagram in Fig. 49a illustrates a temperature–time processability window for TPF-based AM of BMGs. Achieving optimal behavior in TPF of BMGs requires finding the right processing temperature, which should be optimized to achieve low viscosity, as well as ensuring sufficient processing time to avoid crystallization. It is crucial to strike a balance between these factors, which can be experimentally determined to achieve the desired results in the manufactured BMG.

Gibson et al. [662] have proposed a novel approach for 3D printing MG parts using fused filament fabrication (FFF), a common technique for printing thermoplastics [663]. FFF involves heating and extruding a filament of material layer by layer. As the process schematic in Fig. 49b illustrates, the BMG feedstock is heated and dispensed through a small orifice using a high current voltage power supply and a capacitor bank. A metal brush is used to heat the previous layer, and a heated substrate stage facilitates bonding with the extruded BMG. The printing process achieves a volumetric build rate of approximately  $10 \text{ mm}^3/\text{s}$ , comparable to laser-based AM techniques. One advantage of FFF printing of BMGs is that it can be done in ambient air without significant impact on the thermal and mechanical behavior of the printed parts. Additionally, the absence of discoloration during printing indicates no oxidation.

The FFF method allows for the fabrication of fully dense BMG parts without pores. Fig. 49c illustrates exemplary 3D printed parts produced in a continuous mode, where the extrusion process remains uninterrupted throughout the entire printing process [662]. The structures of both the 3D printed and as-cast samples were analyzed using XRD and DSC. The processed sample maintained its original disordered structure, with thermal analysis results being essentially identical within experimental error. This confirmation underscores the capability of the technique to 3D-print samples without inducing structural changes.

The mechanical characterization (Fig. 49d) indicate that fracture strength of the printed BMG sample reaches up to 1220 MPa when loaded parallel to the layers ( $\sigma_{\parallel}$ ) and up to 790 MPa when loaded perpendicular to the layers ( $\sigma_{\perp}$ ). Further, the bright vein-like regions from fractured layer-layer interface insured a metallurgical bond between them. The bonding between layers depends on the temperature similarity between the extruded and previous layers to avoid a lack of metallurgical bond (Fig. 49e) and achieve sufficient bonding strength. Bonding between layers in the presence of air depends on the strain at the interface between the extruded and previous layers to break the oxide film and achieve metallurgical bonding. To ensure this bonding, it is important for the temperature of the previous layer, at the contact point with the extruded material, to match the extruded temperature.

Another TPF-based AM technique recently developed by Li et al. [442] is thermojoining. As the schematic diagram of the thermojoining process in Fig. 49f depicts, the multi-layer MG plates are stacked using an interlocking architecture design to ensure complete metallic bonding at the interfaces. Compared to FFF process, thermojoining is slower and requires longer exposures to elevated temperatures (see Fig. 49a).

The thermojoining process has proven to be a successful, straightforward, and adaptable technique for producing giant MGs (GMGs) with diameters surpassing 100 mm [442]. The joined GMG samples demonstrate virtually good performance when compared to the as-cast counterparts. Fig. 49g presents a comparison between the thermojoining GMG (100 mm in diameter) and the as-cast sample with diameters of 20 mm and 5 mm. The fabrication of the GMG involved the utilization of six layers with interlocking structures. The densities of the as-cast and manufactured GMG samples were  $6.088$  and  $6.082 \text{ g/cm}^3$ , respectively, and their compression strength reached the same value of 480 MPa. This, coupled with cross-sectional CT images at various cutting positions, ensured that GMGs exhibit fully intact bonding.

In addition, the thermojoining process enables the production of components with complex 3D shapes. While MGs, despite their excellent properties, are challenging to machine into specific shapes due to their brittle nature, thermojoining process demonstrates the simultaneous manufacturing and forming of various components, allowing for the efficient fabrication of complex structures [442]. As depicted in Fig. 49h, traditional Chinese Zodiac consisting of twelve different animal characters were successfully manufactured by thermojoining method. The figure also showcases the Monkey character, highlighting the precision and accuracy of the forming process. These intricate animal structures, exceeding the critical dimensions, feature curved profiles and sharp angles such as rat's beard, ox's horns, hare's ears, and monkey's eyes, among others. The successful fabrication of these complex structures demonstrates the scalability and simultaneous shaping capability of the thermojoining process.

The bonding mechanism in this process (Fig. 49i) is similar to thermoplastic joining (see Section 6.2.3). Stress concentration occurs at the center of the interface due to nonuniform spatial structures, breaking the oxidation layer and enabling local contact and bonding between the metal bases. As pressure and deformation increase, the locally bonded metal flows from the center to the periphery, removing fractured oxidation and improving bonding quality. Conventional bonding processes distribute stress uniformly, making it difficult to break the oxidation layer and hindering lateral metal flow, resulting in residual fractured oxidation and compromised

bonding. The interlocking structure design and loading approach used in thermojoining AM process offer advantages over conventional bonding, improving bonding quality and reducing fractured oxidation layers [442].

### 7.7. Thermal spray AM

Thermal spraying is a coating deposition approach that involves the heating of a feedstock material, typically in the form of powder, and spraying it onto a substrate surface using various techniques of high velocity oxygen fuel (HVOF) [664], high velocity air fuel spraying (HVOF) [665], plasma spray [666], and arc spray [667]. The high-velocity impact of the particles on the substrate results in the formation of a solid coating. Thermal spray techniques are well-suited for the production of amorphous coatings and surface modification due to their ability to achieve extremely rapid cooling rate [668].

In 2018, Zhang et al. [669] proposed a novel thermal spray additive manufacturing (TSAM) to fabricate large-size BMGs using HVOF system. The TSAM technique (Fig. 50a) involves injecting glassy powder into a combustion gas and oxygen mixture, depositing semi-molten particles onto a substrate at high velocities. BMG components were built layer by layer without a mold, and the process maintained the amorphous structure of the original powders. The TSAM reduces cracking issues and offers a high cooling rate, preserving the powder's properties. The technique enables flexible modification of alloy composition and structure using various powders, leading to improved BMG and BMGC components for diverse applications such as wastewater treatment, water splitting, and biodegradable implants. However, the current printing resolution of 1 mm in TSAM is larger than the resolutions achieved in SLM and laser foil printing techniques, which have beam sizes of 80  $\mu\text{m}$  [601] and 430  $\mu\text{m}$  [565], respectively. Further enhancements are needed to achieve finer resolutions.

To demonstrate the practicality of the TSAM technique, a mask mold was utilized to fabricate mechanical parts with different geometries [669]. By placing a hollow mask with between the spraying gun and substrate, different geometries including Fe-based BMGC gears were successfully produced (Fig. 50b).

The mechanical property measurements (Fig. 50c and d) demonstrate that printed  $\text{Fe}_{48}\text{Mo}_{14}\text{Cr}_{15}\text{Y}_2\text{C}_{15}\text{B}_6$  BMG sample and BMGC sample reinforced with 50 wt% stainless steel (SS) powders exhibit high fracture strength ( $\sim 2$  GPa) and excellent toughness (13–21  $\text{MPa}\cdot\text{m}^{1/2}$ ), which is 200–400 % higher compared to the toughness in the as-cast BMG of the same composition. Fig. 50e shows a HRTEM image of the interface, revealing regular lattice fringes in the SS phase and maze-like patterns in the amorphous phase. The FFT patterns confirm the unchanged crystalline and amorphous structures. The elemental mapping confirmed a compositional gradient region ( $\sim 45$  nm width), indicating atomic diffusion during TSAM.

The mechanism of enhanced toughness in BMGC parts printed by TSAM was later elaborated [670]. FEM simulation of pre-notched BMGCs (Fig. 50f) showed a stress gradient from tensile to compressive stress in monolithic BMG during bending. Increasing the SS fraction reduced stress fluctuations near the notch tip, lowering the driving force for crack propagation ( $J_{\text{tip}}$ ). The balance between intrinsic fracture resistance and  $J_{\text{tip}}$  determines the crack propagation force. In Fig. 50g,  $J_{\text{tip}}$  for crack propagation across the amorphous/SS interface was calculated. Near interface I,  $J_{\text{tip}}$  sharply increased, enabling crack penetration into the soft-SS interlayer. However, in the SS layer,  $J_{\text{tip}}$  rapidly decreased below far-field  $J$ -integral in the amorphous matrix  $J_{\text{far}}$  due to shielding, with the lowest

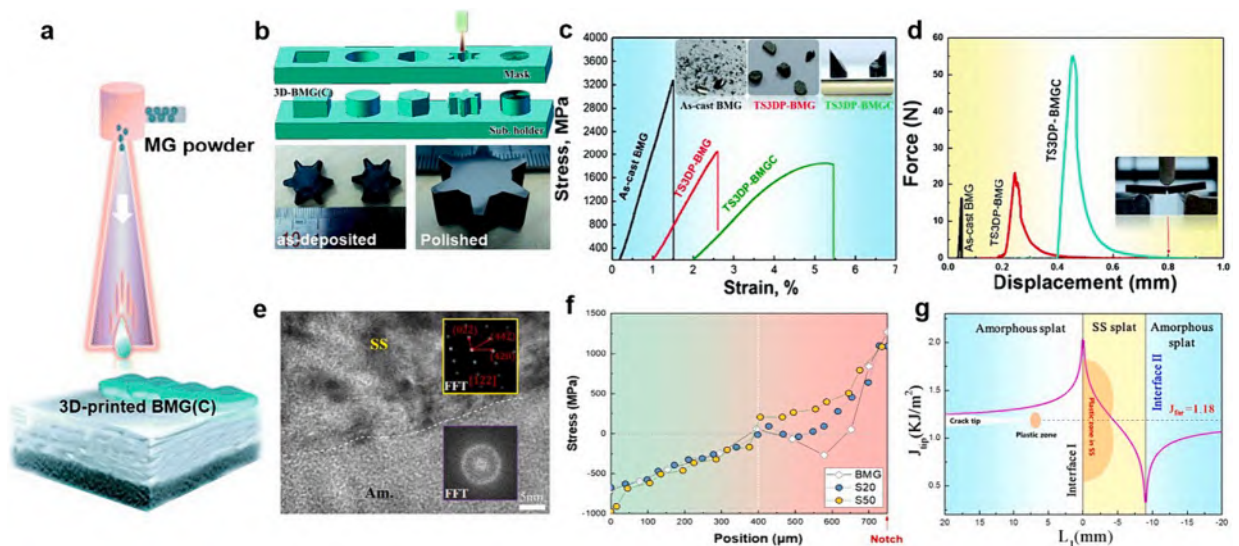


**Fig. 50.** (a) Schematic of TSAM process. (b) Schematic illustration of TSAMed BMG/BMGC parts with complex geometries and photograph of as-built Fe-based BMGC gear. (c) Compressive stress–strain curves of as-cast BMG, printed BMG and BMGC samples. (d) Load–displacement curves for notched samples under 3-point bending. Adapted from [669]. (e) HRTEM images showing the interfacial structure between MG and SS phases. (f) Simulated stress distribution values along the center line of the notch. (g) Crack driving force as a function of distance against the first interface between the SS and amorphous phase. Adapted from [670].

value at interface II. The crack tends to propagate along the intersplat region with low resistance, requiring additional energy to break the next hard-amorphous layer. This emphasizes the importance of arranging soft-to-hard materials for enhancing BMGC toughness.

### 7.8. Cold spray AM

Cold spray is an advanced material deposition technique that originated as a coating technology in the 1980 s. Unlike thermal spray methods, this process utilizes high-velocity compressed gases (such as nitrogen, air, or helium) to propel metal powders onto a substrate. The primary mechanism of deposit formation in cold spraying is the kinetic energy of the particles upon impact, rather than thermal energy. Several MG and MG composite coatings, including Fe-based [671,672], Ni-based [673], Zr-based/Cu composite [674] have been prepared by cold spray.

In a high-pressure cold spray system (Fig. 51a), compressed gas is divided into two streams. The propulsive gas is heated in a gas heater, while the carrier gas passes through a powder feeder, picking up feedstock particles. The two streams are mixed and directed into a de-Laval nozzle, creating a supersonic stream of gas and powder. The carrier gas pressure is slightly higher than the propulsive gas pressure to ensure successful powder injection. High-velocity (300–1200 m/s) particles impact the substrate, forming a coating or deposit at a temperature below their melting point [675].

Cold spray has emerged as an effective AM technique for producing standalone metal components and repairing damaged metal parts in recent years. Cold spray AM (CSAM), enabling layer-by-layer deposition of particles due to high kinetic energy, offers advantages such as shorter production times, unlimited product size, and suitability for repairing damaged components. It excels with high-reflectivity metals like copper and aluminum. However, CSAM has drawbacks like rough surface finishes and lower initial mechanical properties, requiring post-machining and heat treatments for improvement [675].

The field of CSAM for MGs is still relatively new and currently undergoing rapid development and innovation. Researchers have mainly focused on the formation mechanism of cold-sprayed MG deposits by studying the deformation behavior of individual particles upon high-velocity impact. These studies underscored the importance of impact velocity and temperature, highlighting the critical role of melting and viscous flow in particle bonding.

Observations on deposition behavior of as-atomized NiTiZrSiSn amorphous particles during kinetic spraying process revealed distinct regions in deposited MG particles, indicating strain and temperature gradients [673]. Bonding during cold spray was attributed to viscous flow and melting at the impact interface, aided by adiabatic heat generation. Melting primarily occurred at the bottom periphery of the interface. Further, switching from nitrogen to helium as the process gas significantly enhanced deposition efficiency, primarily attributed to the partial melting of the impacting MG particles. Additionally, the supplementary heating of these particles influenced their deposition behavior and contributed to the microstructure of the resulting coating.

In another investigation, List et al [677] conducted cold spraying of amorphous Cu<sub>50</sub>Zr<sub>50</sub> (at.%) at gas temperatures ( $T_{\text{gas}}$ ) of 600 °C and 800 °C, maintaining a constant gas pressure of 4 MPa. Their findings indicated that a  $T_{\text{gas}}$  of 600 °C yielded optimal results in terms of bonding and coating performance, with the possibility of further enhancement through precise adjustments of spray parameters. Notably, coatings processed at  $T_{\text{gas}} = 600$  °C were approximately four times thicker than those sprayed at  $T_{\text{gas}} = 800$  °C, reflecting variations in deposition efficiencies. Despite similarities in appearance, the coating produced with a  $T_{\text{gas}}$  of 800 °C exhibited

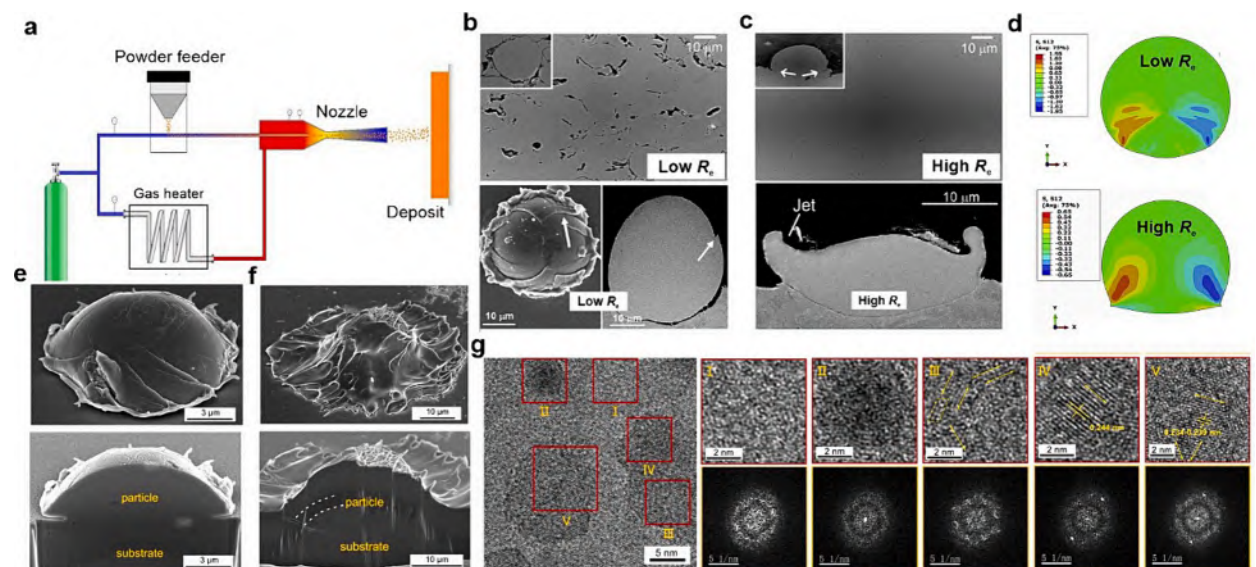


**Fig. 51.** (a) Schematic of high-pressure cold spray system (Adapted from [675]). (b-c) Microstructures of MG coatings and splats deposited at low  $R_e$  (b) and high  $R_e$  (c). (d) Simulated contours of shear stress for low  $R_e$  and high  $R_e$  conditions 10 ns after impact. Adapted from [672]. (e-f) Surface and cross-sectional morphologies for cold sprayed particles with shear localization (e) and particles with viscous flow (f). (g) HRTEM images and corresponding FFT diffraction patterns reveal the presence of localized ordered clusters near the interparticle interface. Adapted from [676].

approximately 30 % greater hardness compared to the one sprayed at 600 °C. Tensile tests on tubular coatings revealed an ultimate tensile strength of 293 MPa for the coating produced at  $T_{\text{gas}} = 600$  °C, twice as high as the coating produced at  $T_{\text{gas}} = 800$  °C, which failed at 139 MPa.

A study by Henao et al. [672] investigated the impact of Reynolds number ( $R_e$ ) on the deformation mechanism during the cold spray deposition of Fe-based MG coatings. At low  $R_e$  (Fig. 51b), minimal deformation results in a porous coating, while increasing  $R_e$  (Fig. 51c) leads to more significant deformation, resulting in compact coatings with homogeneous deformation. Shear bands are observed across the MG particle at low  $R_e$  condition originating from the contact area with the substrate. At high  $R_e$ , plastic deformation and jet formation occur at the particle edges due to low viscosity and high impact velocity. Higher  $R_e$  values improve deposition efficiency, exceeding 50 %, as MG particles flow and bond through thermal softening. These findings highlight the role of shear thinning in promoting homogeneous flow. Finite element analysis demonstrated the influence of non-Newtonian behavior and homogeneous deformation in promoting viscoplastic deformation and lateral viscous flow. Simulated shear stress contours (Fig. 51d) showed localized regions of shear stress at low  $R_e$ , corresponding to the experimental observation of shear bands. As  $R_e$  increases, the MG particle undergoes more homogeneous deformation without shear banding, as the maximum shear stress falls below the critical threshold. Severe plastic deformation primarily occurs at the edges of the contact area with the substrate, where significant shear stress is present.

In another study performed by Fan et al [676], two mechanisms for particle bonding were found to contribute to the formation of MG deposits. The first mechanism involves localized metallurgical bonding at the interface fringe caused by high-velocity impact (Fig. 51e). The observation of a nanoscale gap between the deposited particle and the substrate was attributed to the elastic forces causing springback. The second mechanism involves annular metallurgical bonding resulting from the reduction in viscosity due to high particle temperature (Fig. 51f). Additionally, the nanocrystallization process was observed in the cold-sprayed Zr-based MG deposit (Fig. 51g) which involves composition segregation and different levels of atomic ordering throughout the amorphous matrix (region I). Initially, localized interfacial regions undergo severe plastic deformation, promoting composition segregation (region II). Atomic rearrangement forms localized ordered atomic lines, leading to the appearance of 1D periodic lattice fringes (region III). These fringes evolve into higher ordered structures, eventually resulting in the formation of nanocrystals (regions IV and V).

## 7.9. Other AM techniques

### 7.9.1. Electron beam melting (EBM)

EBM is an advanced AM technology that has gained significant attention in recent years [678,679]. Selective EBM uses a high-power electron beam to selectively melt metal powder layers. In contrast to SLM, which can be used for metals, polymers and ceramics, the application field of the EBM is restricted to metallic components since electric conductivity is required. EBM offers advantages like high beam velocities and a vacuum environment, making it ideal for processing high-performance alloys. However, manufacturing under vacuum condition may come with increased costs and potential loss of low vapor pressure alloying elements.

Despite achieving success in welding (see Section 6.1.2) and surface modification [680] of MGs using electron beam, the production of BMG parts from amorphous metal powder through selective EBM has not been achieved successfully so far. Although numerous challenges were encountered during the process, appropriate parameter adjustments were made to establish a dependable sintering method for this particular alloy. Drescher and Seitz [681] conducted a study on the effects of scan speed and beam current during EBM process of  $\text{Zr}_{70}\text{Cu}_{24}\text{Al}_4\text{Nb}_2$  BMG. The range of parameter adjustments was limited by the requirement of using amorphous metal powder. In the initial sintering experiments, the impact of three key EBM parameters—beam current, focus offset, and scan speed—on the processability of the metal powder was investigated. The study unveiled a direct correlation between the strength of the beam power, scan speed, and the extent of sintering for the amorphous powder. Through iterative parameter adjustments, they were able to establish a stable sintering process, resulting in the successful creation of a sinter cake consisting of interconnected layers with a consistent thickness of 5 mm.

### 7.9.2. Direct ink writing (DIW)

DIW, also known as pneumatic-injection 3D printing, is an AM technique that involves the precise extrusion of liquid or viscous materials, often referred to as an “ink”, through a nozzle to create three-dimensional structures layer by layer [682,683]. In DIW, the ink comprises polymers, ceramics, metals, or living cells. The ink's composition is designed for specific rheological properties, enabling controlled extrusion and solidification.

Recently, a set of innovative inks fusing Fe-Si-B BMG microparticles, liquid suspension media, and polymer binders were developed [684]. During DIW process, the liquid suspension evaporated, and the BMG particles were bound together by the polymer matrix, resulting in the formation of 3D constructs made of a composite material consisting of BMG and polymer. A 50 % macroporous BMG structure exhibited exceptional strength ( $\sim 1.4$  GPa), surpassing conventional alloys of similar density. Comparable to Ti-6Al-4 V, DIWed BMG had lower density and cost. Varying filament spacing during DIW allows control over density and mechanical properties of BMG architectures. In another work, Wu et al. [685] developed a method for preparing Fe-based MG powder slurries with solid content of 50 % and uniform stability for pneumatic injection 3D printing. The influence of printing parameters on the width of deposited line was studied, and stable dispersion was achieved using spherical Fe-based MG powders with a particle size of 5–75  $\mu\text{m}$  and PAA-NH<sub>4</sub> dispersant. The deposited line width increased with pressure and decreased with platform speed. The widest line width was noted at a pressure of 3.4 bar, platform speed of 3 mm/s, and layer height of 1.2 mm. Conversely, the narrowest line width was achieved at a pressure of 2.8 bar, platform speed of 9 mm/s, and layer thickness of 0.8 mm. The nozzle speed had the most significant impact on line width, followed by injection pressure, and then layer thickness.

### 7.10. Functional properties in AMed BMGs

Functional properties in MGs refer to their unique characteristics and behaviors that make them suitable for specific applications. While MGs are primarily known for their mechanical and physical properties, they have demonstrated a variety of functional properties, namely excellent corrosion resistance [6], biocompatibility [46,686], superior wear resistance [13], and promising catalytic capabilities [17,687].

AM offers unique opportunities to improve the functionality of BMGs by enabling the fabrication of complex geometries, tailored porosity, gradient structures, and integration of multiple materials. These capabilities pave the way for the development of advanced BMG components with enhanced performance, expanded functionality, and increased application potential in various industries.

SLM-printed Zr-based samples showed similar corrosion behavior to as-cast samples in Na<sub>2</sub>SO<sub>4</sub> and NaCl electrolytes, but with reduced pitting susceptibility and improved surface healing [570]. In another study, a Ni-free and Ag-bearing Zr-based 3D printed BMG exhibited excellent corrosion resistance in a simulated body fluid solution, low corrosion rate (0.12 mm/y), and better

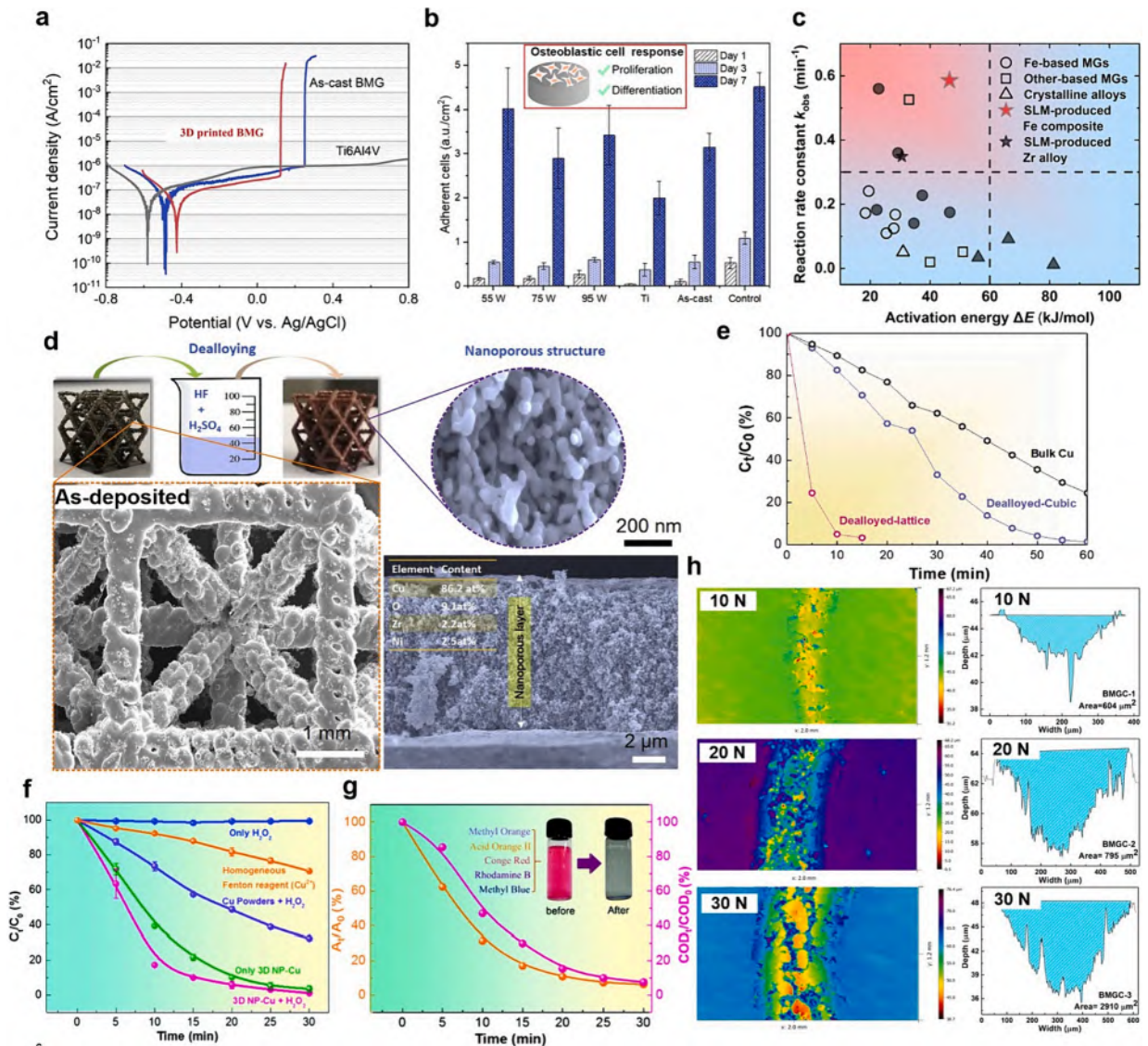


**Fig. 52.** (a) Polarization curves of 3D printed BMG sample compared to that of the as-cast BMG and Ti6Al4V alloy in the SBF solution (Adapted from [636]) (b) Cell proliferation assessed by measuring the activity of cytosolic LDH (Adapted from [688]). (c) Overall catalytic ability of different catalysts (Adapted from [439]). (d) Photographs and SEM images of as-deposited and dealloyed SLMed BMGs with lattice structure (e) Degradation rate over time in nanoporous 3D printed cubic and lattice 3D printed samples and a polycrystalline Cu. Adapted from [614]. (f) Degradation efficiency of 3D NP-Cu catalyst and other commonly used catalysts. (g) Degradation rate and COD removal of a mixture solution containing five different dyes. Adapted from [690]. (h) 3D surface topography and cross-sectional images of the wear tracks were examined at a fixed sliding speed of 250 RPM under different normal loads (Adapted from [691]).

passivation ability compared to as-cast BMG and Ti6Al4V alloy (Fig. 52a) [636]. It maintained safe metal ion release and demonstrated favorable biocompatibility, cell proliferation support, and remarkable antibacterial activity against *E. coli*.

SLMed  $Zr_{59.3}Cu_{28.8}Al_{10.4}Nb_{1.5}$  BMG (AMLOY-ZR01) was evaluated as an implant material by Larsson et al. [688]. The study showed favorable cell proliferation and differentiation of preosteoblastic cells, similar to the reference material Ti-6Al-4 V, regardless of the SLM laser energy and surface roughness of the BMG (Fig. 52b).

In another work, Liang et al. [439] 3D printed porous Fe-based MG composites with rhombic dodecahedron microstructure for catalytic degradation of BR3BA dye. Comparative studies reveal superior reusability and efficiency in sulfate radical-based reactions, with up to 45 cycles without decline. Efficiency decreases in Fenton-like processes due to surface decay. Sulfate radical-based reactions maintain surface integrity, indicating distinct catalytic mechanisms and being preferable for practical applications. Later, Liang et al. [689] incorporated Cu into an MG-based catalyst using SLM to create 3D hierarchical porous structures. These MG/Cu catalysts show exceptional efficiency in degrading RhB, surpassing commercial nano zero-valent iron and other Fenton-type catalysts. Impressively, the MG/Cu catalysts maintain high reusability, with over 100 uses without efficiency decay, setting a new longevity record.

Fig. 52c summarizes reaction rate constant ( $k_{obs}$ ) and activation energy ( $\Delta E$ ) values for Fe/Mg/Co/Al-based MGs, crystalline alloys, and 3D printed alloys [439]. MGs exhibit lower  $\Delta E$  values and higher  $k_{obs}$  compared to crystalline alloy catalysts, making them a superior alternative. The catalysts manufactured by SLM show promise with low  $\Delta E$  values and high  $k_{obs}$  values, indicating high overall catalytic ability. The SLM-produced Fe-based MG matrix composite demonstrates exceptionally high  $k_{obs}$  ( $0.586 \text{ min}^{-1}$ ) compared to the SLM-produced Zr alloy ( $0.349 \text{ min}^{-1}$ ). Despite a slightly higher  $\Delta E$  value, the Fe-based MG matrix composite still outperforms most crystalline catalysts.

The combination of 3D printing and chemical dealloying techniques presents a promising approach for fabricating intricate three-dimensional frameworks with nanoporous structures. In this regard, Yang et al [614] have investigated the catalytic performance of 3D printed Zr-based BMG with large specific surface area offered by complex geometries (Fig. 52d). By employing chemical dealloying treatment in 0.008 M HF and 1 M  $H_2SO_4$  mixture solution for 60 h, nanoporous Cu with average pore size of 60 nm and thickness of  $\sim 10 \mu\text{m}$  was obtained on the surface of the BMG, enhancing its catalytic capabilities as revealed by higher degradation efficiency of the lattice nanoporous sample decreasing methyl-orange concentration with time (Fig. 52e).

Yang et al. [690] discovered that 3D printed nanoporous Cu (3D NP-Cu) catalysts have high degradation efficiency for azo dyes (Fig. 52f), outperforming commercial  $Cu^{2+}$  catalysts and  $Cu^0$  powder. The 3D NP-Cu catalyst also demonstrates fairly good reusability and versatility, rapidly degrading complex pollutants (dyes) and reducing chemical oxygen demand (COD), as shown in Fig. 52g. The catalyst's unique 3D hierarchically porous structures, abundant active atomic steps, and Cu<sub>2</sub>O nanocrystals contribute to its exceptional performance. However, the synthesis process is complex, costly, and has limited catalyst reusability.

Regarding wear properties in 3D printed BMGs, Zou et al. [691] systematically investigated the influence of normal load and sliding speed on the microstructure, tribological properties, and wear mechanisms of ex-situ additively manufactured FeCrMoCB/Cu BMG. Increasing normal load and sliding speed led to a decrease in coefficient of friction. Fig. 52h illustrates the wear tracks at varying normal loads, showing deeper and wider grooves as the load increased at a fixed sliding speed. The wear rate decreased with increasing normal load but increased with increasing sliding speed due to the formation and stability of a tribo-layer. Wear mechanisms varied depending on the normal load and sliding speed. At 250 RPM, wear shifted from adhesive wear to oxidation wear and adhesive wear with increasing load. Under a constant load of 20 N and higher sliding speeds of 500 and 750 RPM, adhesive wear and fatigue wear were dominant.

In other studies, Bordeenithikasem et al. [569] and Deng et al., [570] assessed the wear behavior of SLMed Zr-based BMGs compared to the cast laboratory grade materials using pin-on-disk wear testing. The experimental results showed that both the laser printed samples and cast laboratory grade samples exhibited comparable wear loss, indicating similar wear behavior between the two. Furthermore, Hofmann et al. [692] additively manufactured a range of metallic alloys including AMZ4 BMG using SLM. These alloys were tested as potential excavation tools for future robotic spacecraft landing on icy planetary bodies. The performance of the cutting tools was assessed by measuring the mechanical specific energy and blade hardness while trenching through soft and hard salt, which serves as a regolith simulant for extraterrestrial ice. Notably, A2 tool steel, MS1 maraging steel, and BMG cutting tools exhibited favorable performance in the experiments.

## 8. Summary & outlooks for future research

MGs offer unique properties for various engineering applications, but their practical use is hindered by size limitation and challenges in achieving intricate geometries through conventional fabrication methods such as the commonly used casting. Alternative manufacture strategy has gained attention as a means to overcome the challenges posed by limited GFA and intrinsic brittleness in MGs. This paper provides a comprehensive review of recent advances in MG component manufacturing using various techniques. The summary and future outlooks are as follows:

- *MG feedstocks for manufacturing.*

- 1- MG powders and ribbons are widely available, cost-effective, and scalable options, particularly for AM. BMG rods and sheets, while limited in scalability, offer unique compositions but can be costlier. MG powders and ribbons are more compatible with AM and formative manufacturing, while BMG feedstocks can be used for various manufacturing techniques. Challenges include maintaining compositional diversity in powder and ribbon feedstocks.
- 2- Moving forward, the focus should be on diversifying MG powder feedstocks, reducing oxygen contamination, and improving wide ribbon production through planar flow casting of different MG alloy systems. Advancements in milling/atomization can address

powder particle size distribution challenges. Improving the GFA of feedstock materials and using MG alloys with slow crystallization kinetics can minimize nanocrystallization risks, facilitating the fabrication of fully amorphous MG components.

*- Subtractive manufacturing.*

The study of subtractive manufacturing of MGs has witnessed significant research efforts in both traditional and non-traditional machining methods, yet there remain several challenges and avenues for further exploration. Key perspectives for future research are as follows:

- 1- Understanding chip formation and cutting mechanism in traditional BMG machining is crucial due to the lack of consensus. MG machining faces challenges like crystallization, oxidation, and light emission, impacting surface quality. Exploring coolants, cooling methods, and low-temperature cutting techniques can mitigate these issues. Optimizing machining parameters like cutting speed, depth, feed rate, and spindle speed offers substantial improvements in quality, efficiency, and tool longevity.
- 2- Traditional machining of BMGs under optimized conditions does not lead to crystallization, but high temperatures during machining can induce it. Nanocrystallization and changes in interatomic distances occur due to elevated temperatures and severe plastic deformation. Further research is needed to optimize machining parameters and explore mechanical properties for potential applications.
- 3- Non-traditional methods like micro-EDM and ECMM are promising for MG micromachining. Optimizing parameters in micro-EDM reduces crystallization, and advanced materials tackle carbonization. ECMM allows precise removal but is limited to thin MG ribbons. Laser micromachining has potential for microstructures, but parameter optimization is needed. Laser can also aid surface finishing and creating functional components. Combining laser and ultrasonic-assisted machining with traditional methods can overcome challenges in machining MGs.
- 4- Shear punching is applied to MGs, but their limited plastic forming capacity at room temperature poses challenges. Ultrasonic-vibration-assisted shear punching (USP) emerges as a promising approach, utilizing ultrasonic softening mechanisms to improve efficiency and reduce costs in MG processing.

*- Formative manufacturing.*

Formative manufacturing of MG components is a promising research area with opportunities for complex-shaped structures in various length scales. Yet, some challenges and future issues require attention.

- 1- The thermoplastic properties of MGs have enabled efficient processing through thermoplastic forming methods like compression molding, blow molding, hot drawing, hot rolling, and hot extrusion, creating centimeter- to nano-scale structures with high precision. Advanced techniques like capacitive discharge heating and electromagnetic coupling offer rapid MG forming. Challenges include processing costs, limited atomic-level replication, and the need for optimal parameters to avoid oxidation and crystallization. Further research should focus on cost reduction, improved mold structures, and overcoming crystallization challenges.
- 2- Ultrasonic technology shows promise in enhancing the plasticity of MGs through UVIP. This innovative approach enables substantial plastic deformation without crystallization at room temperature and in a very short period. Further research is needed to understand the mechanism of UVIP and optimize this technique for tailored material properties in MGs. The application of ultrasonic processing to MGs is still in its early stages, presenting opportunities for advancements in processing techniques and parameters.
- 3- Powder consolidation, using thermal sintering methods like hot-pressing and SPS, is employed to overcome size limitations in BMGs. Adjusting parameters such as pressure, temperature, and particle size influences the densification and devitrification behavior of BMGs during consolidation. BMGCs with controlled microstructures and tailored properties are possible, including magnetic properties. Advancements in devitrification understanding and predictive modeling could optimize performance of consolidated BMG components.
- 4- The concept of using MGs as metallic glue has emerged as a novel method for MG matrix composites, showing promise in bonding materials, enhancing plasticity, and controlling electrical, magnetic, and magnetostrictive behavior. The technique enables structural regulation, creating porous MG structures with controlled porosity. Further research and optimization in this approach can advance MG-based composites and explore innovative engineering applications.

*- Welding and joining.*

- 1- Welding and joining of MGs are vital research areas to leverage their exceptional properties in engineering applications. However, these processes face challenges due to the inherent amorphous structure, leading to potential crystallization issues and lack of strong metallurgical bonding. Future research should delve into innovative approaches and techniques to mitigate crystallization during welding processes, ensuring the preservation of the unique properties of MGs.
- 2- Expanding the range of MG compositions that can be successfully welded is crucial. Research efforts should explore compatibility between different MG compositions and even dissimilar materials to unlock new possibilities in engineering applications. Further, expanding applications of MGs requires developing efficient and scalable methods for producing large-scale MG components through welding and joining.
- 3- Fusion welding techniques, including laser welding, is highly efficient for joining BMGs with narrow seams, minimal heat-affected zones, and rapid heating/cooling rates, but high-energy laser welding induces crystallization which deteriorates mechanical

strength of the joint. Successful laser welding of various BMG compositions has been achieved, with ongoing research to optimize parameters and improve weld quality. EBW is another versatile method, enabling strong and defect-free BMG welds, especially in dissimilar materials. The challenges inherent in EBW encompass the necessity for a stringent vacuum environment and the requirement for high surface quality. Reactive foil joining, using reactive foils, provides a controlled heat source, minimizing BMG crystallization and achieving high fracture toughness.

- 4- Supercooled liquid state welding techniques to join MG components has advanced significantly in recent years. Friction welding techniques offer a promising approach to join BMG materials by generating heat at the interface without melting the plates, preserving their unique properties. FSW technique faces challenges such as intricate process parameters, stir pin abrasion, and inevitable exit hole formation. Diffusion bonding shows potential for large BMG areas, but challenges with atomic diffusion and oxide layers require careful consideration. Thermoplastic joining eliminates the need for a controlled atmosphere, preventing crystallization within a short timeframe. RSW successfully joins various BMG compositions and dissimilar materials, preventing crystallization and ensuring strong bonds.
- 5- The outlook for supercooled liquid state welding techniques in MGs is promising, offering unique advantages in terms of structural preservation and metallurgical bonding. To advance this field, future research should focus on broadening the applications of friction welding techniques, optimizing parameters for enhanced morphology control, and exploring dissimilar joining conditions. In diffusion bonding, the exploration of alternative interlayer materials and the development of advanced simulation models are essential to overcome challenges related to structural relaxation and bulk embrittlement. Thermoplastic joining requires further optimization of conditions for increased joint strength and expanded applicability across diverse BMG compositions and geometries. For resistance spot welding, research should delve into supercooled liquid state joining of dissimilar BMGs and extend applications to manufacturing complex 3D structures.
- 6- Solid-state welding techniques, like magnetic pulse welding and explosive welding, achieve strong metallurgical bonds in MGs while preserving their unique properties. These methods successfully join various BMG compositions and dissimilar materials with minimal crystallization. Explosive welding comes with drawbacks like unfavorable working conditions and noise pollution accompanied by shock, highlighting the need for careful consideration of these factors. Ultrasonic welding, using high-frequency vibrations, offers advantages like fast operation and no impact on material performance. It has demonstrated successful BMG welding, maintaining their strength and structure. Ultrasonic welding holds potential for large-scale BMG production. Future research can optimize the process and explore its applicability in different environments.

#### - Additive manufacturing.

AM allows the creation of BMGs with intricate shapes and larger sizes than traditional casting. Techniques like SLM, DED, and LFP hold promise for BMG applications. However, achieving a fully amorphous microstructure in laser-based AM remains challenging due to temperature gradients and thermal cycles. Further research is needed to overcome these obstacles.

- 1- One primary challenge in AM of BMGs is the presence of solidification defects and thermal stress-induced cracks, which can compromise part integrity and mechanical properties. Controlling defects and crystallization is crucial for achieving fully amorphous structures in 3D printed BMGs. Understanding the processing-structure-properties relationship and optimizing process parameters are essential for enhancing performance. AI and ML methods could dynamically adjust processing parameters and engineer local microstructures to minimize crystallization [693,694]. Additionally, simulating thermal and residual stress during laser-based AM processes for BMGs requires innovative numerical strategies to address fluid flow, temperature fields, and plasma effects effectively.
- 2- AM has also enabled the development of functionally graded BMGs with enhanced plasticity and fracture toughness. Exploring combinations of BMGs with crystalline alloys or ceramics can open up new engineering applications with unique structural and functional properties.
- 3- MG components produced by laser-based AM techniques often require post-processing to achieve the desired surface finish, which adds time and cost to the manufacturing process. Developing effective post-processing techniques to achieve desired surface finishes and refine the mechanical properties of SLM-produced BMG components is an ongoing research area. While the application of thermoplastic forming to an SLMed AMZ4 ( $Zr_{59.3}Cu_{28.8}Al_{10.4}Nb_{1.5}$ ) component reduces surface roughness and create intricate surface patterns without the necessity of intricate abrasive machining processes [695], the heat treatment in the SLR of an SLMed  $Zr_{55}Cu_{30}Al_{10}Ni_5$  BMG softens HAZ regions and MPs but induces micro-cracks, deteriorating mechanical performance [696].
- 4- The TPF-based AM techniques for BMGs show great promise in advancing the field. FFF offers a rapid and cost-effective method to produce fully dense BMG parts with high mechanical performance. Efforts to minimize defects during printing by FFF in ambient air are essential. Thermojoining AM provides an adaptable approach for creating giant MGs with complex shapes. Continuous research should focus on improving efficiency, speed, and applicability to different BMG systems.
- 5- Ultrasonic AM is an advanced technique combining ultrasonic welding with AM to create functional MG components. It successfully produces parts from various materials, including MGs and MGCs. Future research aims to optimize processing parameters and expand its applications, offering high-performance components at reduced costs and production times.
- 6- Regarding 3D printing techniques, while SLM has been widely studied, new approaches like thermal spray AM and cold spray AM offer intriguing possibilities for large-scale production and efficient glass formation. Furthermore, developing new 3D printing techniques while using amorphous ribbons as feedstocks can be a novel direction for AM of BMG components.
- 7- EBM has not yet successfully produced BMG parts from amorphous metal powder, but parameter adjustments during EBM, specifically beam current and scan speed, led to a stable sintering process of MG particles. DIW, another technique, involves extrusion

of Fe-Si-B BMG microparticles with polymer binders, resulting in 3D constructs with exceptional strength and controllable properties. This offers a lower density and cost alternative to conventional alloys. Both EBM and DIW present distinctive pathways for advancing manufacturing capabilities.

In conclusion, advancing the field of the manufacture of MG components requires continued research to address the existing challenges and optimize the processing parameters. Novel techniques and strategies hold huge promise for expanding the manufacturing capabilities of MGs, leading to extensive applications in various fields.

### CRediT authorship contribution statement

**Sajad Sohrabi:** Writing – original draft, Methodology, Investigation. **Jianan Fu:** Writing – original draft, Resources, Data curation. **Luyao Li:** Writing – original draft, Data curation. **Yu Zhang:** Writing – original draft, Data curation. **Xin Li:** Writing – original draft, Data curation. **Fei Sun:** Writing – original draft, Data curation. **Jiang Ma:** Writing – review & editing, Resources, Funding acquisition, Conceptualization. **Wei Hua Wang:** Writing – review & editing, Project administration, Conceptualization.

### Declaration of competing interest

The authors declare that they have no known competing financial interests or personal relationships that could have appeared to influence the work reported in this paper.

### Data availability

Data will be made available on request.

### Acknowledgement

The work was financially supported by the Key Basic and Applied Research Program of Guangdong Province, China (Grant No. 2019B030302010), the NSF of China (Grant No. 52122105, 52271150, 52201185, 52201186, 52371160), and the Science and Technology Innovation Commission Shenzhen (Grants No. RCJC20221008092730037, 20220804091920001) and the Research Team Cultivation Program of Shenzhen University, Grant No. 2023QNT001. The authors thank Dr. Yu Chen for his assistance on the preparation of this review and the assistance on microscope observation received from the Electron Microscope Center of Shenzhen University.

### References

- [1] Greer AL. Metallic glasses. *Science* 1995;267:1947–53.
- [2] Axinte E. Metallic glasses from “alchemy” to pure science: present and future of design, processing and applications of glassy metals. *Mater Des* 2012;35: 518–56.
- [3] Wang WH. The elastic properties, elastic models and elastic perspectives of metallic glasses. *Prog Mater Sci* 2012;57:487–656.
- [4] Wang WH, Dong C, Shek CH. Bulk metallic glasses. *Mater Sci Eng R Rep* 2004;44:45–89.
- [5] Demetriou MD, Launey ME, Garrett G, Schramm JP, Hofmann DC, Johnson WL, et al. A damage-tolerant glass. *Nat Mater* 2011;10:123–8.
- [6] Jiang L, Bao M, Dong Y, Yuan Y, Zhou X, Meng X. Processing, production and anticorrosion behavior of metallic glasses: a critical review. *J Non Cryst Solids* 2023;612:122355.
- [7] Wang A, Zhao C, Men H, He A, Chang C, Wang X, et al. Fe-based amorphous alloys for wide ribbon production with high bs and outstanding amorphous forming ability. *J Alloy Compd* 2015;630:209–13.
- [8] McHenry ME, Willard MA, Laughlin DE. Amorphous and nanocrystalline materials for applications as soft magnets. *Prog Mater Sci* 1999;44:291–433.
- [9] Silveyra JM, Ferrara E, Huber DL, Monson TC. Soft magnetic materials for a sustainable and electrified world. *Science* 2018;362:eaao0195.
- [10] Li HX, Lu ZC, Wang SL, Wu Y, Lu ZP. Fe-based bulk metallic glasses: glass formation, fabrication, properties and applications. *Prog Mater Sci* 2019;103: 235–318.
- [11] Li X, Zhou J, Shen L, Sun B, Bai H, Wang W. Exceptionally high saturation magnetic flux density and ultra-low coercivity via an amorphous-nanocrystalline transitional microstructure in a FeCo-based alloy. *Adv Mater* 2022. n/a:2205863.
- [12] Ma MZ, Liu RP, Xiao Y, Lou DC, Liu L, Wang Q, et al. Wear resistance of zr-based bulk metallic glass applied in bearing rollers. *Mater Sci Eng A* 2004;386: 326–30.
- [13] Sun F, Deng S, Fu J, Zhu J, Liang D, Wang P, et al. Superior high-temperature wear resistance of an ir-ta-ni-nb bulk metallic glass. *J Mater Sci Technol* 2023; 158:121–32.
- [14] Sun C, Hu Y-C, Sun C. Functional applications of metallic glasses in electrocatalysis. *ChemCatChem* 2019.
- [15] Jiang R, Da Y, Chen Z, Cui X, Han X, Ke H, et al. Progress and perspective of metallic glasses for energy conversion and storage. *Adv Energy Mater* 2022;12: 2101092.
- [16] Wang Z-J, Li M-X, Yu J-H, Ge X-B, Liu Y-H, Wang W-H. Low-iridium-content IrNiTa metallic glass films as intrinsically active catalysts for hydrogen evolution reaction. *Adv Mater* 2020;32:1906384.
- [17] Yan Y, Wang C, Huang Z, Fu J, Lin Z, Zhang X, et al. Highly efficient and robust catalysts for the hydrogen evolution reaction by surface nano engineering of metallic glass. *J Mater Chem A* 2021.
- [18] Telford M. The case for bulk metallic glass. *Mater Today* 2004;7:36–43.
- [19] Hofmann DC, Polit-Casillas R, Roberts SN, Borgonia J-P, Dillon RP, Hilgemann E, et al. Castable bulk metallic glass strain wave Gears: Towards decreasing the cost of high-performance robotics. *Sci Rep* 2016;6:37773.
- [20] Gao K, Zhu XG, Chen L, Li WH, Xu X, Pan BT, et al. Recent development in the application of bulk metallic glasses. *J Mater Sci Technol* 2022;131:115–21.
- [21] Greer AL, Costa MB, Houghton OS. Metallic glasses. *MRS Bull* 2023;48:1054–61.
- [22] Plummer J. Is metallic glass poised to come of age? *Nature Mater* 2015;14:553–5.
- [23] Schroers J. Processing of bulk metallic glass. *Adv Mater* 2010;22:1566–97.

- [24] Sarac B, Eckert J. Thermoplasticity of metallic glasses: processing and applications. *Prog Mater Sci* 2022;127:100941.
- [25] Fu J, Ma J. Nanoengineering of metallic glasses. *Adv Eng Mater* 2023;25:2200659.
- [26] Liu Z, Liu N, Schroers J. Nanofabrication through molding. *Prog Mater Sci* 2022;125:100891.
- [27] Savaedi Z, Motallebi R, Mirzadeh H, Malekan M. Superplasticity of bulk metallic glasses (BMGs): a review. *J Non Cryst Solids* 2022;583:121503.
- [28] Graeve OA, García-Vázquez MS, Ramírez-Acosta AA, Cadieux Z. Latest advances in Manufacturing and machine Learning of bulk metallic glasses. *Adv Eng Mater* 2023. n/a:2201493.
- [29] Kawamura Y. Liquid phase and supercooled liquid phase welding of bulk metallic glasses. *Mater Sci Eng A* 2004;375–377:112–9.
- [30] Qiao J, Yu P, Wu Y, Chen T, Du Y, Yang J. A compact review of laser welding technologies for amorphous alloys. *Metals* 2020;10.
- [31] Du J, Tian B, Duan L, Ming W, Liu K, He W. Traditional and non-traditional machining technology of metallic glass. *Int J Adv Manuf Technol* 2022.
- [32] Ming W, Guo X, Xu Y, Zhang G, Jiang Z, Li Y, et al. Progress in non-traditional machining of amorphous alloys. *Ceram Int* 2022.
- [33] Zhang L, Huang H. Micro machining of bulk metallic glasses: a review. *Int J Adv Manuf Technol* 2019;100:637–61.
- [34] Zhang C, Ouyang D, Pauly S, Liu L. 3D printing of bulk metallic glasses. *Mater Sci Eng R Rep* 2021;145:100625.
- [35] Sohrabi N, Jhabvala J, Logé RE. Additive Manufacturing of bulk metallic glasses—Process. Challenges and Properties: A Review. *Metals*; 2021. p. 11.
- [36] Lashgari HR, Ferry M, Li S. Additive manufacturing of bulk metallic glasses: fundamental principle, current/future developments and applications. *J Mater Sci Technol* 2022.
- [37] Liu H, Yang D, Jiang Q, Jiang Y, Yang W, Liu L, et al. Additive manufacturing of metallic glasses and high-entropy alloys: significance, unsettled issues, and future directions. *J Mater Sci Technol* 2023;140:79–120.
- [38] Wu W, Li X, Liu Q, Hsi Fuh JY, Zheng A, Zhou Y, et al. Additive manufacturing of bulk metallic glass: principles, materials and prospects. *Materials Today Advances* 2022;16:100319.
- [39] Li X. Additive Manufacturing of advanced multi-component alloys: bulk metallic glasses and high entropy alloys. *Adv Eng Mater* 2018;20:1700874.
- [40] Heraeus AMLOY Technologies. Available at: [https://www.heraeus.com/en/landingspages/hat/home\\_hat/hat\\_home.html](https://www.heraeus.com/en/landingspages/hat/home_hat/hat_home.html). 2023.
- [41] Yihao Metal Technology. Available at: <https://www.yihaometal.com/>. 2023.
- [42] Liquidmetal Technologies. Available at: <https://liquidmetal.com/>. 2023.
- [43] Biały M, Hasiak M, Laszcz A. Review on biocompatibility and Prospect biomedical applications of novel functional metallic glasses. *Journal of Functional Biomaterials* 2022;13:245.
- [44] Li J, Shi L-l, Zhu Z-d, He Q, Ai H-j, Xu J. Zr61Ti2Cu25Al12 metallic glass for potential use in dental implants: biocompatibility assessment by in vitro cellular responses. *Mater Sci Eng C* 2013;33:2113–21.
- [45] Schroers J, Kumar G, Hodges TM, Chan S, Kyriakides TR. Bulk metallic glasses for biomedical applications. *JOM* 2009;61:21–9.
- [46] Li HF, Zheng YF. Recent advances in bulk metallic glasses for biomedical applications. *Acta Biomater* 2016;36:1–20.
- [47] Kumar G, Desai A, Schroers J. Bulk metallic glass: the smaller the better. *Adv Mater* 2011;23:461–76.
- [48] Ishida M, Takeda H, Nishiyama N, Kita K, Shimizu Y, Saotome Y, et al. Wear resistivity of super-precision microgear made of ni-based metallic glass. *Mater Sci Eng A* 2007;449–451:149–54.
- [49] Liquidmetal Technologies. Available from: [https://liquidmetal.com/wp-content/uploads/2021/05/LQM\\_ASoundDecision.pdf](https://liquidmetal.com/wp-content/uploads/2021/05/LQM_ASoundDecision.pdf). 2022.
- [50] Klement W, Willens RH, Duwez POL. Non-crystalline structure in solidified gold-silicon alloys. *Nature* 1960;187:869–70.
- [51] Zhang JY, Zhou ZQ, Zhang ZB, Park MH, Yu Q, Li Z, et al. Recent development of chemically complex metallic glasses: from accelerated compositional design, additive manufacturing to novel applications. *Materials Futures* 2022;1:012001.
- [52] Inoue A. Stabilization of metallic supercooled liquid and bulk amorphous alloys. *Acta Mater* 2000;48:279–306.
- [53] Ryu WH, Kim KJ, Yoo GH, Park ES. Alloy design strategy to improve fluidity of zr-based bulk metallic glass for near-net-shape manufacturing. *J Alloy Compd* 2022;896:162680.
- [54] Mukherjee S, Schroers J, Zhou Z, Johnson WL, Rhim WK. Viscosity and specific volume of bulk metallic glass-forming alloys and their correlation with glass forming ability. *Acta Mater* 2004;52:3689–95.
- [55] Schuh CA, Hufnagel TC, Ramamurty U. Mechanical behavior of amorphous alloys. *Acta Mater* 2007;55:4067–109.
- [56] Greer AL, Cheng YQ, Ma E. Shear bands in metallic glasses. *Mater Sci Eng R Rep* 2013;74:71–132.
- [57] Inoue A, Takeuchi A. Recent progress in bulk glassy, nanoquasicrystalline and nanocrystalline alloys. *Mater Sci Eng A* 2004;375–377:16–30.
- [58] Inoue A, Takeuchi A. Recent development and application products of bulk glassy alloys. *Acta Mater* 2011;59:2243–67.
- [59] Nishiyama N, Takenaka K, Miura H, Saidoh N, Zeng Y, Inoue A. The world's biggest glassy alloy ever made. *Intermetallics* 2012;30:19–24.
- [60] Amorphous Metal Cores Market Outlook (2022–2032). 2023 Available at: <https://www.futuremarketinsights.com/reports/amorphous-metal-cores-market> Accessed 22 Nov 2023.
- [61] Bulk Metallic Glass Market - A Global and Regional Analysis. 2022 Available at: <https://bisresearch.com/industry-report/bulk-metallic-glass-market.html> Accessed 22 Nov 2023.
- [62] Steel Market Size, Share, Analysis and Forecast to 2031. 2023 Available at: <https://stratificresearch.com/report/steel-market> Accessed 22 Nov 2023.
- [63] Duwez P, Willens RH, Klement Jr W. Continuous series of metastable solid solutions in silver-copper alloys. *J Appl Phys* 2004;31:1136–7.
- [64] Tkatch VI, Limanovskii AI, Denisenko SN, Rassolov SG. The effect of the melt-spinning processing parameters on the rate of cooling. *Mater Sci Eng A* 2002;323:91–6.
- [65] Hagiwara M, Inoue A. Production techniques of alloy wires by rapid solidification. In: Liebermann HH, editor. *Rapidly Solidified Alloys*. New York: Dekker; 1993. p. 139–55.
- [66] Yi J, Xia XX, Zhao DQ, Pan MX, Bai HY, Wang WH. Micro-and nanoscale metallic glassy fibers. *Adv Eng Mater* 2010;12:1117–22.
- [67] Wang W. Metallic glassy fibers. *SCIENCE CHINA Physics, Mechanics & Astronomy* 2013;56:2293–301.
- [68] Schroers J, Lohwongwatana B, Johnson WL, Peker A. Precious bulk metallic glasses for jewelry applications. *Mater Sci Eng A* 2007;449–451:235–8.
- [69] Miller SA, Murphy RJ. A gas-water atomization process for producing amorphous powders. *Scr Metall* 1979;13:673–6.
- [70] Suryanarayana C. Mechanical alloying and milling. *Prog Mater Sci* 2001;46:1–184.
- [71] Liebermann HH. The dependence of the geometry of glassy alloy ribbons on the chill block melt-spinning process parameters. *Mater Sci Eng* 1980;43:203–10.
- [72] Smith MT, Saletore M. Simple, low-cost planar flow casting machine for rapid solidification processing. *Rev Sci Instrum* 1986;57:1647–53.
- [73] Sohrabi S, Arabi H, Beitollahi A, Gholamipour R. Planar flow casting of Fe71Si13.5B9Nb3Cu1Al1.5Ge1 ribbons. *J of Materi Eng and Perform* 2013;22:2185–90.
- [74] Calin M, Grahl H, Adam M, Eckert J, Schultz L. Synthesis and thermal stability of ball-milled and melt-quenched amorphous and nanostructured al-ni-nd-co alloys. *J Mater Sci* 2004;39:5295–8.
- [75] Suryanarayana C, Inoue A. Bulk metallic glasses. CRC Press; 2011.
- [76] Soares Barreto E, Wegner J, Frey M, Kleszczynski S, Busch R, Uhlenwinkel V, et al. Influence of oxygen in the production chain of Cu–Ti-based metallic glasses via laser powder bed fusion. *Powder Metall* 2023;1–12.
- [77] Theisen EA, Weinstein SJ. An overview of planar flow casting of thin metallic glasses and its relation to slot coating of liquid films. *J Coat Technol Res* 2022;19:49–60.
- [78] Su Y-G, Chen F, Wu C-Y, Chang M-H, Chung C-A. Effects of Manufacturing Parameters in Planar flow casting process on ribbon formation and puddle evolution of Fe–Si–B alloy. *ISIJ Int* 2015;55:2383–90.
- [79] Willard MA, Daniil M. Nanostructured soft magnetic materials. In: Liu JP, Fullerton E, Gutfleisch O, Sellmyer DJ, editors. *Nanoscale Magnetic Materials and Applications*. New York: Springer Science; 2009.
- [80] Metglas, Inc. Available at: <https://metglas.com/metal-joining-brazing-foils-and-preforms/>. 2023.
- [81] Wegner J, Frey M, Piechotta M, Neuber N, Adam B, Platt S, et al. Influence of powder characteristics on the structural and the mechanical properties of additively manufactured zr-based bulk metallic glass. *Mater Des* 2021;209:109976.

- [82] Liu CT, Chisholm MF, Miller MK. Oxygen impurity and microalloying effect in a zr-based bulk metallic glass alloy. *Intermetallics* 2002;10:1105–12.
- [83] Ouyang D, Zhang P, Zhang C, Liu L. Understanding of crystallization behaviors in laser 3D printing of bulk metallic glasses. *Appl Mater Today* 2021;23:100988.
- [84] Koga GY, Bolfarini C, Kiminami CS, Jorge AM, Botta WJ. An overview of thermally sprayed fe-cr-nb-b metallic glass coatings: from the alloy development to the coating's performance against corrosion and Wear. *J Therm Spray Technol* 2022;31:923–55.
- [85] Chen X, Xiao J, Zhu Y, Tian R, Shu X, Xu J. Micro-machinability of bulk metallic glass in ultra-precision cutting. *Mater Des* 2017;136:1–12.
- [86] Gao M, Wang C, Dong J, Huan Y, Bai HY, Wang WH. Macroscopic tensile plasticity of zr-based bulk metallic glass with surface screw thread shaped structure. *Mater Sci Eng A* 2016;673:417–22.
- [87] Wang T, Wu X, Zhang G, Chen Y, Xu B, Ruan S. Study on surface roughness and top burr of micro-milled zr-based bulk metallic glass in shear dominant zone. *Int J Adv Manuf Technol* 2020;107:4287–99.
- [88] Maroju NK, Yan DP, Xie B, Jin X. Investigations on surface microstructure in high-speed milling of zr-based bulk metallic glass. *J Manuf Process* 2018;35:40–50.
- [89] Bakkal M, Shih AJ, McSpadden SB, Liu CT, Scattergood RO. Light emission, chip morphology, and burr formation in drilling the bulk metallic glass. *Int J Mach Tool Manu* 2005;45:741–52.
- [90] Bakkal M, Nakşiler V, Derin B. Machinability of bulk metallic glass materials on milling and drilling. *Adv Mat Res* 2010;83–86:335–41.
- [91] Boothroyd G, Knight WA. Fundamentals of machining and machine tools. New York: Marcel Dekker; 1989.
- [92] Fujita K, Morishita Y, Nishiyama N, Kimura H, Inoue A. Cutting Characteristics of bulk metallic glass. *Mater Trans* 2005;46:2856–63.
- [93] Chen SH, Ge Q, Zhang JS, Chang WJ, Zhang JC, Tang HH, et al. Low-speed machining of a zr-based bulk metallic glass. *J Manuf Process* 2021;72:565–81.
- [94] Xiong J, Wang H, Zhang G, Chen Y, Ma J, Mo R. Machinability and Surface generation of Pd40Ni10Cu30P20 bulk metallic glass in single-point diamond turning. *Micromachines* 2020;11.
- [95] Liu Y, Song Z, Liang Z, Cui X, Gong Y, Sun X, et al. Experimental investigations into groove bottom surface roughness for zr-based bulk metallic glass by using milling. *Int J Adv Manuf Technol* 2023.
- [96] Wang T, Wu X, Zhang G, Xu B, Chen Y, Ruan S. Experimental study on machinability of zr-based bulk metallic glass during micro milling. *Micromachines* 2020.
- [97] Xie B, Kumar MN, Yan DP, Jin X. Material behavior in micro milling of zirconium based bulk metallic glass. In: Tms TMM, Materials S, editors. TMS 2017 146th Annual Meeting & Exhibition Supplemental Proceedings. Cham: Springer International Publishing; 2017. p. 363–73.
- [98] Sakata S, Hayashi A, Terajima T, Nakao Y. Influence of cutting condition on Surface roughness in single point diamond turning of zr-based bulk metallic glass. ASME 2016 International Mechanical Engineering Congress and Exposition. 2016.
- [99] Jiang MQ, Dai LH. Formation mechanism of lamellar chips during machining of bulk metallic glass. *Acta Mater* 2009;57:2730–8.
- [100] Bakkal M, Shih AJ, Scattergood RO, Liu CT. Machining of a Zr–Ti–Al–Cu–Ni metallic glass. *Scr Mater* 2004;50:583–8.
- [101] Ding F, Wang C, Zhang T, Zhao Q, Zheng L. Light emission of zr-based bulk metallic glass during high-speed cutting: from generation mechanism to control strategies. *J Mater Process Technol* 2022;305:117598.
- [102] Wang M, Xu B, Zhang J, Dong S, Wei S. Experimental observations on surface roughness, chip morphology, and tool wear behavior in machining fe-based amorphous alloy overlay for remanufacture. *Int J Adv Manuf Technol* 2013;67:1537–48.
- [103] Kanani M, Sohrabi S, Ebrahimi R, Paydar MH. Continuous and ultra-fine grained chip production with large strain machining. *J Mater Process Technol* 2014;214:1777–86.
- [104] Liu C, Wan M, Zhang W, Yang Y. Chip formation mechanism of inconel 718: a review of models and approaches. *Chinese Journal of Mechanical Engineering* 2021;34:34.
- [105] Jawahir IS, van Luttervelt CA. Recent developments in Chip control Research and applications. *CIRP Ann* 1993;42:659–93.
- [106] Bakkal M, Shih AJ, Scattergood RO. Chip formation, cutting forces, and tool wear in turning of zr-based bulk metallic glass. *Int J Mach Tool Manu* 2004;44:915–25.
- [107] Chau SY, To S, Sun Z, Wu H. Twinned-serrated chip formation with minor shear bands in ultra-precision micro-cutting of bulk metallic glass. *Int J Adv Manuf Technol* 2020;107:4437–48.
- [108] Han DX, Wang G, Li J, Chan KC, To S, Wu FF, et al. Cutting Characteristics of zr-based bulk metallic glass. *J Mater Sci Technol* 2015;31:153–8.
- [109] Yan N, Li Z, Xu Y, Meyers MA. Shear localization in metallic materials at high strain rates. *Prog Mater Sci* 2020;100755.
- [110] Zeng F, Jiang MQ, Dai LH. Dilatancy induced ductile–brittle transition of shear band in metallic glasses. *Proceedings of the Royal Society A: Mathematical, Physical and Engineering Science*. 2018;474.
- [111] Maroju NK, Jin X. Mechanism of Chip segmentation in orthogonal cutting of zr-based bulk metallic glass. *J Manuf Sci Eng* 2019;141.
- [112] Deng Y, Wang C, Ding F, Zhang T, Wu W. Thermo-mechanical coupled flow behavior evolution of zr-based bulk metallic glass. *Intermetallics* 2023;152:107770.
- [113] He W, Wang D, Ming W, Ma J, Liu K, Du J. Research progress on cutting machining simulation technology of metallic glasses. *Int J Adv Manuf Technol* 2022;122:1167–93.
- [114] Avila KE, Vardanyan VH, Alabd Alhafez I, Zimmermann M, Kirsch B, Urbassek HM. Applicability of cutting theory to nanocutting of metallic glasses: atomistic simulation. *J Non Cryst Solids* 2020;550:120363.
- [115] Zhu P, Fang F. On the mechanism of material removal in nanometric cutting of metallic glass. *Appl Phys A* 2014;116:605–10.
- [116] Gilbert CJ, Ager III JW, Schroeder V, Ritchie RO, Lloyd JP, Graham JR. Light emission during fracture of a Zr–Ti–Ni–Cu–Be bulk metallic glass. *Appl Phys Lett* 1999;74:3809–11.
- [117] Sun B-R, Zhan Z-J, Liang B, Zhang R-J, Wang W-K. Light emission and dynamic failure mechanism of hypervelocity impact on zr-ti-ni-cu-be bulk metallic glass. *Chin Phys Lett* 2011;28:096102.
- [118] Date H, Ishiguro M, Futakawa M, Naoe T. Compressive strength and splitting tensile strength of Zr-based metallic glass. *Procedia Eng* 2011;10:857–62.
- [119] Bakkal M, Liu CT, Watkins TR, Scattergood RO, Shih AJ. Oxidation and crystallization of zr-based bulk metallic glass due to machining. *Intermetallics* 2004;12:195–204.
- [120] Tariq NH, Muhammad G, Awais HB. Effect of operating parameters on the drilling behavior of Zr57.5Cu11.2Ni13.8Al17.5 bulk metallic glass. *J Mater Res* 2013;28:3288–96.
- [121] Inoue A, Zhang T, Takeuchi A. Bulk amorphous alloys with high mechanical strength and good soft magnetic properties in Fe–TM–B (TM=IV–VIII group transition metal) system. *Appl Phys Lett* 1997;71:464–6.
- [122] Inoue A, Shen B, Koshiha H, Kato H, Yavari AR. Cobalt-based bulk glassy alloy with ultrahigh strength and soft magnetic properties. *Nat Mater* 2003;2:661–3.
- [123] Si JJ, Wang T, Wu YD, Cai YH, Chen XH, Wang WY, et al. Cr-based bulk metallic glasses with ultrahigh hardness. *Appl Phys Lett* 2015;106:251905.
- [124] Sarker S, Tang-Kong R, Schoeppner R, Ward L, Hasan NA, Van Campen DG, et al. Discovering exceptionally hard and wear-resistant metallic glasses by combining machine-learning with high throughput experimentation. *Appl Phys Rev* 2022;9:011403.
- [125] Bakkal M, Shih AJ, McSpadden SB, Scattergood RO. Thrust force, torque, and tool wear in drilling the bulk metallic glass. *Int J Mach Tool Manu* 2005;45:863–72.
- [126] Sohrabi S, Gholampour R. Glass transition kinetics and fragility of ZrCuAlNi(Nb) metallic glasses. *Intermetallics* 2022;145:107532.
- [127] Evenson Z, Busch R. Equilibrium viscosity, enthalpy recovery and free volume relaxation in a Zr44Ti11Ni10Cu10Be25 bulk metallic glass. *Acta Mater* 2011;59:4404–15.
- [128] Hu Q, Zeng X-R, Fu MW. Characteristic free volume change of bulk metallic glasses. *J Appl Phys* 2012;111:-.
- [129] Wang X, Gong P, Deng L, Jin J, Wang S, Li F. Sub-tg annealing effect on the kinetics of glass transition and crystallization for a ti-zr-be-fe bulk metallic glass. *J Non Cryst Solids* 2017;473:132–40.
- [130] Bragg WH, Bragg WL. The reflection of X-rays by crystals. *Proceedings of the Royal Society of London Series A, Containing Papers of a Mathematical and Physical Character*. 1913;88:428-38.

- [131] Valiev R, Gunderov D, Zhilyaev AP, Popov AG, Pushin. Nanocrystallization induced by severe plastic deformation of amorphous alloys. *J Metastable Nanocryst Mater* 2004;22:21–6.
- [132] Lee S-W, Huh M-Y, Fleury E, Lee J-C. Crystallization-induced plasticity of Cu–Zr containing bulk amorphous alloys. *Acta Mater* 2006;54:349–55.
- [133] Sun Y, Concustell A, Greer AL. Thermomechanical processing of metallic glasses: extending the range of the glassy state. *Nat Rev Mater* 2016;1:16039.
- [134] Ketov SV, Sun YH, Nachum S, Lu Z, Checchi A, Beraldin AR, et al. Rejuvenation of metallic glasses by non-affine thermal strain. *Nature* 2015;524:200–3.
- [135] Guo W, Shao Y, Zhao M, Lü S, Wu S. Varying the treating conditions to rejuvenate metallic glass by deep cryogenic cycling treatment. *J Alloy Compd* 2019;152997.
- [136] Lee S-C, Lee C-M, Lee J-C, Kim H-J, Shibutani Y, Fleury E, et al. Structural disordering process of an amorphous alloy driven by the elastostatic compression at room temperature. *Appl Phys Lett* 2008;92:151906.
- [137] Seung-Jae Lee B-GY. Jae-il jang, jae-chul lee irreversible structural change induced by elastostatic stress imposed on an amorphous alloy and its influence on the mechanical properties. *Met Mater Int* 2008;14:9–13.
- [138] Sohrabi S, Sun BY, Mahmoodan M, Sun YH, Gholamipour R, Wang WH. Rejuvenation by compressive elasto-static loading: the role of static stress on a zr-based metallic glass. *J Alloy Compd* 2023;933:167715.
- [139] Sohrabi S, Li MX, Bai HY, Ma J, Wang WH, Greer AL. Energy storage oscillation of metallic glass induced by high-intensity elastic stimulation. *Appl Phys Lett* 2020;116:081901.
- [140] Meng PQ, Tsuchiya K, li S, Yokoyama Y. Reversible transition of deformation mode by structural rejuvenation and relaxation in bulk metallic glass. *Appl Phys Lett* 2012;101:121914.
- [141] Stolpe M, Krucic JJ, Busch R. Evolution of shear bands, free volume and hardness during cold rolling of a zr-based bulk metallic glass. *Acta Mater* 2014;64:231–40.
- [142] Pham DT, Dimov SS, Bigot S, Ivanov A, Popov K. Micro-EDM—recent developments and research issues. *J Mater Process Technol* 2004;149:50–7.
- [143] Huang H, Yan J. On the surface characteristics of a zr-based bulk metallic glass processed by microelectrical discharge machining. *Appl Surf Sci* 2015;355:1306–15.
- [144] Huang Z, Liang X, Chang C, Ma J. WEDM-LS processing sophisticated and durable zr-based metallic glass mold insert for micro structure injection of polymers. *Biomed Microdevices* 2019;21:13.
- [145] Xu J, Pei Q, Lian Z, Yu P, Ma G, Yu H. Experimental study on wire-electrical discharge machining of zirconium-based metallic glass. *Mater Res Express* 2019;6:115214.
- [146] Pei Q, Xu J, Lian Z, Yu P, Ma G, Yu H. Experimental Study on Wire-Electrical Discharge Machining (WEDM) of Zirconium-based Metallic (MG) Glass Based on Orthogonal Test. 2019 IEEE International Conference on Manipulation, Manufacturing and Measurement on the Nanoscale (3M-NANO)2019. p. 16–9.
- [147] Hsieh S-F, Chen S-L, Lin M-H, Ou S-F, Lin W-T, Huang M-S. Crystallization and carbonization of an electrical discharge machined zr-based bulk metallic glass alloy. *J Mater Res* 2013;28:3177–84.
- [148] Chang W, Li X, Yang H, Zhang J, Zhang J, Tang H, et al. On the wire EDM of metastable atomic structured bulk metallic glasses. *Int J Adv Manuf Technol* 2022;120:5411–30.
- [149] Chen S, Gu H, Feng K, Zheng H, Chen K. A comparative study on the die-sinking EDM performance of bulk metallic glass composites under rough and refined conditions. *Int J Adv Manuf Technol* 2022;121:4865–83.
- [150] Xingchao Z, Yong Z, Hao T, Li Y, Xiaohua C, Guoliang C. Micro-electro-discharge Machining of Bulk Metallic Glasses. 2007 International Symposium on High Density packaging and Microsystem Integration2007. p. 1-4.
- [151] Yeo SH, Tan PC, Aligiri E, Tor SB, Loh NH. Processing of zirconium-based bulk metallic glass (BMG) using micro electrical Discharge machining (micro-EDM). *Mater Manuf Process* 2009;24:1242–8.
- [152] Xu B, Wu X-y, Ma J, Liang X, Lei J-g, Wu B, et al. Micro-electrical discharge machining of 3D micro-molds from Pd40Cu30P20Ni10metallic glass by using laminated 3D micro-electrodes. *J Micromech Microeng* 2016. 26:035004.
- [153] Liu C, Duong N, Jahan MP, Ma J, Kirwin R. Experimental investigation and numerical simulation of micro-EDM of bulk metallic glass with focus on crater sizes. *Procedia Manuf* 2019;34:275–86.
- [154] Huang H, Yan J. Microstructural changes of zr-based metallic glass during micro-electrical discharge machining and grinding by a sintered diamond tool. *J Alloy Compd* 2016;688:14–21.
- [155] Chen XH, Zhang XC, Zhang Y, Chen GL. Fabrication and characterization of metallic glasses with a specific microstructure for micro-electro-mechanical system applications. *J Non Cryst Solids* 2008;354:3308–16.
- [156] Kuriakose S, Patowari PK, Bhatt J. Effect of micro-EDM machining parameters on the accuracy of micro hole drilling in zr-based metallic glass. *Engineering Research Express* 2020;2:015001.
- [157] Tsui H-P, Hsu S-Y. Study on fe-based metallic glass micro hole machining by using micro-EDM combined with electrophoretic deposition polishing. *Processes* 2022.
- [158] Landolt D, Chauvy PF, Zinger O. Electrochemical micromachining, polishing and surface structuring of metals: fundamental aspects and new developments. *Electrochim Acta* 2003;48:3185–201.
- [159] Koza JA, Sueptitz R, Uhlemann M, Schultz L, Gebert A. Electrochemical micromachining of a zr-based bulk metallic glass using a micro-tool electrode technique. *Intermetallics* 2011;19:437–44.
- [160] Cole KM, Kirk DW, Singh CV, Thorpe SJ. Optimizing electrochemical micromachining parameters for zr-based bulk metallic glass. *J Manuf Process* 2017;25:227–34.
- [161] Horn S, Oswald S, Stoica M, Uhlemann M, Gebert A. Complex microshaping of bulk metallic glass surfaces by electrochemical means. *J Mater Res* 2015;30:3493–501.
- [162] Gebert A, Gostin PF, Sueptitz R, Oswald S, Abdi S, Uhlemann M, et al. Polarization studies of zr-based bulk metallic glasses for electrochemical machining. *J Electrochem Soc* 2014;161:E66–73.
- [163] Sharma V, Patel DS, Jain VK, Ramkumar J. Wire electrochemical micromachining: an overview. *Int J Mach Tool Manu* 2020;155:103579.
- [164] Meng L, Zeng Y, Fang X, Zhu D. Micro-shaping of metallic glass by wire electrochemical micro-machining with a reciprocating traveling workpiece. *J Alloy Compd* 2018;739:235–48.
- [165] Zeng Y, Meng L, Fang X. Surface Characteristics of ni-based metallic glass in wire electrochemical micro machining. *J Electrochem Soc* 2017;164:E408.
- [166] Hang Y, Zeng Y, Yang T, Meng L. The dissolution characteristics and wire electrochemical micromachining of metallic glass Ni82Cr7Si5Fe3B3. *J Manuf Process* 2020;58:884–93.
- [167] Guo C, Wu B, Xu B, Wu S, Shen J, Wu X. Investigation of pulse electrochemical machining of zr-based bulk metallic glasses in NaNO<sub>3</sub>-ethylene glycol electrolyte. *journal of the electrochemical. Society* 2021.
- [168] Meng L, Zeng Y, Zhu D. Wire electrochemical micromachining of ni-based metallic glass using bipolar nanosecond pulses. *Int J Mach Tool Manu* 2019;146:103439.
- [169] Meng L, Zeng Y, Zhu D. Investigation on wire electrochemical micro machining of ni-based metallic glass. *Electrochim Acta* 2017;233:274–83.
- [170] Meng L, Zeng Y, Fang X, Zhu D. Micropatterning of ni-based metallic glass by pulsed wire electrochemical micro machining. *Intermetallics* 2017;81:16–25.
- [171] Williams E, Lavery N. Laser processing of bulk metallic glass: a review. *J Mater Process Technol* 2017;247:73–91.
- [172] Wang X, Lu P, Dai N, Li Y, Liao C, Zheng Q, et al. Noncrystalline micromachining of amorphous alloys using femtosecond laser pulses. *Mater Lett* 2007;61:4290–3.
- [173] Browne DJ, Stratton D, Gilchrist MD, Byrne CJ. Bulk metallic glass multiscale tooling for molding of Polymers with micro to Nano features: a review. *Metall and Mat Trans A* 2013;44:2021–30.
- [174] Melkani U, Mullick S, Bhatnagar S, Pantangi R, Korimilli EP, Gollapudi S. Analysis of groove quality and machining behavior of zr-based metallic glass through laser grooving and electro-jet machining. *J Laser Appl* 2022;34:012030.

- [175] Aqida SN, Brabazon D, Naher S, Kovacs Z, Browne DJ. Laser micro-processing of amorphous and partially crystalline Cu45Zr48Al7 alloy. *Appl Phys A* 2010; 101:357–60.
- [176] Lin H-K, Lee C-J, Hu T-T, Li C-H, Huang JC. Pulsed laser micromachining of Mg–Cu–Gd bulk metallic glass. *Opt Lasers Eng* 2012;50:883–6.
- [177] Jia W, Peng Z, Wang Z, Ni X, Wang C-y. The effect of femtosecond laser micromachining on the surface characteristics and subsurface microstructure of amorphous FeCuNbSiB alloy. *Appl Surf Sci* 2006;253:1299–303.
- [178] Zhang P, Liu L, Yang W, Li D, Yu Y, Pan J, et al. Laser punching of soft magnetic fe-based amorphous ribbons. *Scr Mater* 2024;240:115839.
- [179] Li J-F, Soldatov I-V, Tang X-C, Sun B-Y, Schäfer R, Liu S-L, et al. Metallic Mimosa pudica: a 3D biomimetic buckling structure made of metallic glasses. *science. Advances* 2022;8:eabm7658.
- [180] Qiu P, Teraoka S, Gong Q, Xu S, Shimada K, Mizutani M, et al. Surface defect inhibition mechanisms of laser assisted microcutting on ni-P amorphous alloy. *J Manuf Process* 2020;60:644–53.
- [181] Williams E, Brousseau EB. Nanosecond laser processing of Zr41.2Ti13.8Cu12.5Ni10Be22.5 with single pulses. *J Mater Process Technol* 2016;232:34–42.
- [182] Li T, Guo Y, Mizutani M, Xu S. Surface smoothing of bulk metallic glasses by femtosecond laser double-pulse irradiation. *Surf Coat Technol* 2021;408:126803.
- [183] Park SS, Wei Y, Jin XL. Direct laser assisted machining with a sapphire tool for bulk metallic glass. *CIRP Ann* 2018;67:193–6.
- [184] Xu S, Osawa S, Kobayashi R, Shimada K, Mizutani M, Kuriyagawa T. Minimizing burrs and defects on microstructures with laser assisted micromachining technology. *Int J Automation Technol* 2016;10:891–8.
- [185] Khanna N, Pei Z, Ferreira PM. Experimental investigation of rotary ultrasonic grinding of ceramic disks. *Proceedings of the NAMRC XXIII Conference: SME*. 1995.
- [186] Yang Z, Zhu L, Zhang G, Ni C, Lin B. Review of ultrasonic vibration-assisted machining in advanced materials. *Int J Mach Tool Manu* 2020;156:103594.
- [187] Babitsky VI, Kalashnikov AN, Meadows A, Wijesundara A. Ultrasonically assisted turning of aviation materials. *J Mater Process Technol* 2003;132:157–67.
- [188] Amini S, Soleimani M, Paktinat H, Lotfi M. Effect of longitudinal– torsional vibration in ultrasonic-assisted drilling. *Mater Manuf Process* 2017;32:616–22.
- [189] Chen Z, Feng P, Wang J, Feng F, Zha H. Understanding the abnormal effects of ultrasonic vibration on tool wear and surface generation in zr-based bulk metallic glass cutting. *CIRP J Manuf Sci Technol* 2022;39:1–17.
- [190] Tsui H-P, Lee P-H, Yeh C-C, Hung J-C. Ultrasonic vibration-assisted electrical discharge machining on fe-based metallic glass by adding conductive powder. *Procedia CIRP* 2020;95:425–30.
- [191] Jahan M, Rahman M, Wong Y. A review on the conventional and micro-electrodischarge machining of tungsten carbide. *Int J Mach Tool Manu* 2011;51: 837–58.
- [192] Lee SH, Li X. Study of the surface integrity of the machined workpiece in the EDM of tungsten carbide. *J Mater Process Technol* 2003;139:315–21.
- [193] Lee HT, Tai TY. Relationship between EDM parameters and surface crack formation. *J Mater Process Technol* 2003;142:676–83.
- [194] Loc PH, Shiuu FJ. Abrasive water jet polishing on zr-based bulk metallic glass. *Adv Mat Res* 2012;579:211–8.
- [195] Wessels V, Grigoryev A, Dold C, Wyen C-F, Roth R, Weingärtner E, et al. Abrasive waterjet machining of three-dimensional structures from bulk metallic glasses and comparison with other techniques. *J Mater Res* 2012;27:1187–92.
- [196] Volkert CA, Donohue A, Spaepen F. Effect of sample size on deformation in amorphous metals. *J Appl Phys* 2008;103:083539.
- [197] Yang Y, Ye JC, Lu J, Liu FX, Liaw PK. Effects of specimen geometry and base material on the mechanical behavior of focused-ion-beam-fabricated metallic-glass micropillars. *Acta Mater* 2009;57:1613–23.
- [198] Saotome Y, Okaniwa S, Kimura H, Inoue A. Superplastic nanoforging of pt-based metallic glass with dies of zr-BMG and glassy Carbon fabricated by focused ion beam. *Mater Sci Forum* 2007;539–543:2088–93.
- [199] Joo B-Y, Rhim S-H, Oh S-I. Micro-hole fabrication by mechanical punching process. *J Mater Process Technol* 2005;170:593–601.
- [200] Sun F, Lin H, Fu J, Li Z, Luo F, Wang B, et al. Metallic glass based composites with precise tunable thermal expansion. *Appl Mater Today* 2022;29:101565.
- [201] Greer AL. Metallic glasses. *Science* 1995;31:1947–53.
- [202] Takahashi F, Nishimura T, Suzuki I, Kudo H. A method of blanking from amorphous alloy foils using rubber tool. *CIRP Ann* 1991;40:315–8.
- [203] Sano T, Takahashi M, Murakoshi Y, Matsuno K. Punchless blanking of an amorphous alloy. *Journal of Materials Processing Technology* 1992;30:341–50.
- [204] Cui J, Liu H, Ma Y, Li M, Gong J, Zhang Y, et al. Flexible microblanking of amorphous alloys under laser dynamic loading. *J Manuf Process* 2020;56:718–25.
- [205] Jeong HG, Kim WJ, Bae JC, Yoon DJ, Lim SJ, Na KH. Blanking of bulk amorphous alloy sheets fabricated by a squeeze casting method under hydraulics pressure. *J Metastable Nanocryst Mater* 2005;24–25:85–8.
- [206] Liu LF, Dai LH, Bai YL, B. C.W, Eckert J. characterization of rate-dependent shear behavior of zr-based bulk metallic glass using shear-punch testing. *Journal of Mater Res* 2006;21:153–61.
- [207] Guduru RK, Darling KA, Kishore R, Scattergood RO, Koch CC, Murty KL. Evaluation of mechanical properties using shear-punch testing. *Mater Sci Eng A* 2005; 395:307–14.
- [208] Murakoshi Y, Takahashi M, Terasaki M, Sano T, Matsuno K. High-speed blanking of an amorphous alloy. *J Mater Process Technol* 1992;30:329–39.
- [209] Jeong HG, Kim WJ, Bae JC, Yoon DJ, Choi SG, Na KH. Hole punching onto the Zr65Al10Ni10Cu15 BMG sheet fabricated by squeeze casting. *Mater Sci Forum* 2005;475–479:3423–6.
- [210] Huang Y, Wang D, Fan H, Sun J, Shen J, Mi J. Shear punching of a ti-based bulk metallic glass. *Mater Sci Eng A* 2013;561:220–5.
- [211] Li X, Wei D, Zhang JY, Liu XD, Li Z, Wang TY, et al. Ultrasonic plasticity of metallic glass near room temperature. *Appl Mater Today* 2020;21:100866.
- [212] Li Z, Huang Z, Sun F, Li X, Ma J. Forming of metallic glasses: mechanisms and processes. *Materials Today Advances* 2020;7:100077.
- [213] Yuan C, Lv Z, Pang C, Li X, Liu R, Yang C, et al. Ultrasonic-assisted plastic flow in a zr-based metallic glass. *Sci China Mater* 2021;64:448–59.
- [214] Luo F, Sun F, Li K, Gong F, Liang X, Wu X, et al. Ultrasonic assisted micro-shear punching of amorphous alloy. *Materials Research Letters* 2018;6:545–51.
- [215] Sun F, Wang B, Luo F, Yan YQ, Ke HB, Ma J, et al. Shear punching of bulk metallic glasses under low stress. *Mater Des* 2020;190:108595.
- [216] Li H, Yan Y, Sun F, Li K, Luo F, Ma J. Shear punching of amorphous alloys under high-frequency vibrations. *Metals* 2019;9.
- [217] Schroers J, Hodges TM, Kumar G, Raman H, Barnes AJ, Pham Q, et al. Thermoplastic blow molding of metals. *Mater Today* 2011;14:14–9.
- [218] Jagdale S, Javed A, Theeda S, Meduri CS, Hu Z, Hasan M, et al. Review of thermoplastic drawing with bulk metallic glasses. *Metals* 2022;12:518.
- [219] Busch R, Schroers J, Wang W. Thermodynamics and kinetics of bulk metallic glass. *MRS Bull* 2007;32:620–3.
- [220] Angell CA. Formation of glasses from liquids and biopolymers. *Science* 1995;267:1924–35.
- [221] Gallino I. On the fragility of bulk metallic glass forming liquids. *Entropy* 2017;19:483.
- [222] Li N, Chen W, Liu L. Thermoplastic micro-forming of bulk metallic glasses: a review. *JOM* 2016;68:1246–61.
- [223] Saotome Y, Imai K, Sawanobori N. Microformability of optical glasses for precision molding. *J Mater Process Technol* 2003;140:379–84.
- [224] Ma J, Yi J, Zhao D, Pan M, Wang W. Large size metallic glass gratings by embossing. *J Appl Phys* 2012;112:064505.
- [225] Kumar G, Tang HX, Schroers J. Nanomoulding with amorphous metals. *Nature* 2009;457:868–72.
- [226] Liu X, Shao Y, Li J-F, Chen N, Yao K-F. Large-area and uniform amorphous metallic nanowire arrays prepared by die nanoimprinting. *J Alloy Compd* 2014;605: 7–11.
- [227] Fu J, Li X, Li Z, Sun F, Wen W, Zhao J, et al. Strong absorption in ultra-wide band by surface nano engineering of metallic glass. *fundamental. Research* 2022.
- [228] Kumar G, Staffier PA, Blawdziewicz J, Schwarz UD, Schroers J. Atomically smooth surfaces through thermoplastic forming of metallic glass. *Appl Phys Lett* 2010;97:101907.
- [229] Li R, Chen Z, Datye A, Simon GH, Ketkaew J, Kinser E, et al. Atomic imprinting into metallic glasses. *Communications Physics* 2018;1:75.
- [230] Zhou C, Datye A, Chen Z, Simon GH, Wang X, Schroers J, et al. Atomic imprinting in the absence of an intrinsic length scale. *APL Mater* 2020;8:111104.
- [231] Schroers J. The superplastic forming of bulk metallic glasses. *JOM* 2005;57:35–9.
- [232] Wang D, Li Y, Sun B, Sui M, Lu K, Ma E. Bulk metallic glass formation in the binary Cu–Zr system. *Appl Phys Lett* 2004;84:4029–31.
- [233] Ponnambalam V, Poon SJ, Shiflet GJ. Fe-based bulk metallic glasses with diameter thickness larger than one centimeter. *J Mater Res* 2004;19:1320–3.
- [234] Wiest A, Duan G, Demetriou MD, Wiest LA, Peck A, Kaltenboeck G, et al. Zr–Ti-based be-bearing glasses optimized for high thermal stability and thermoplastic formability. *Acta Mater* 2008;56:2625–30.

- [235] Duan G, Wiest A, Lind ML, Li J, Rhim WK, Johnson WL. Bulk metallic glass with Benchmark thermoplastic processability. *Adv Mater* 2007;19:4272–5.
- [236] Schroers J, Johnson WL. Highly processable bulk metallic glass-forming alloys in the Pt–Co–Ni–Cu–P system. *Appl Phys Lett* 2004;84:3666–8.
- [237] Saotome Y, Imai K, Shioda S, Shimizu S, Zhang T, Inoue A. The micro-nanoformability of pt-based metallic glass and the nanofforming of three-dimensional structures. *Intermetallics* 2002;10:1241–7.
- [238] Zhang B, Zhao D, Pan M, Wang WH, Greer AL. Amorphous metallic plastic. *Phys Rev Lett* 2005;94:205502.
- [239] Zhang B, Zhao D, Pan M, Wang R, Wang W. Formation of cerium-based bulk metallic glasses. *Acta Mater* 2006;54:3025–32.
- [240] Inoue A, Nakamura T, Nishiyama N, Masumoto T. Mg–Cu–Y bulk amorphous alloys with high tensile strength produced by a high-pressure die casting method. *Mater Trans JIM* 1992;33:937–45.
- [241] Zhao Y-Y, Ma E, Xu J. Reliability of compressive fracture strength of Mg–Zn–Ca bulk metallic glasses: flaw sensitivity and weibull statistics. *Scr Mater* 2008;58:496–9.
- [242] Zhang W, Inoue A. Thermal stability and mechanical properties of cu-based bulk glassy alloys in Cu50 (Zr1-xHfx) 45Al5 system. *Mater Trans* 2003;44:2220–3.
- [243] Schroers J. On the formability of bulk metallic glass in its supercooled liquid state. *Acta Mater* 2008;56:471–8.
- [244] Li N, Xu X, Zheng Z, Liu L. Enhanced formability of a zr-based bulk metallic glass in a supercooled liquid state by vibrational loading. *Acta Mater* 2014;65:400–11.
- [245] Han G, Peng Z, Xu L, Li N. Ultrasonic vibration facilitates the micro-formability of a zr-based metallic glass. *Materials* 2018;11:2568.
- [246] Ding S, Liu Y, Li Y, Liu Z, Sohn S, Walker FJ, et al. Combinatorial development of bulk metallic glasses. *Nat Mater* 2014;13:494–500.
- [247] Hasan M, Kumar G. High-throughput drawing and testing of metallic glass nanostructures. *Nanoscale* 2017;9:3261–8.
- [248] Yan W, Richard I, Kurtuldu G, James ND, Schiavone G, Squair JW, et al. Structured nanoscale metallic glass fibres with extreme aspect ratios. *Nat Nanotechnol* 2020;15:875–82.
- [249] Mota RMO, Liu N, Kube SA, Chay J, McClintock HD, Schroers J. Overcoming geometric limitations in metallic glasses through stretch blow molding. *Appl Mater Today* 2020;19:100567.
- [250] Hu Z, Gorumlu S, Aksak B, Kumar G. Patterning of metallic glasses using polymer templates. *Scr Mater* 2015;108:15–8.
- [251] Fu J, Li Z, Li X, Sun F, Li L, Li H, et al. Hierarchical porous metallic glass with strong broadband absorption and photothermal conversion performance for solar steam generation. *Nano Energy* 2022;108019.
- [252] Wiest A, Harmon JS, Demetriou MD, Dale Conner R, Johnson WL. Injection molding metallic glass. *Scr Mater* 2009;60:160–3.
- [253] Wu Y, Kang Y, Xie Y, Xiang X, Shui L, Schroers J, et al. Fabrication of 3D metallic glass architectures by a mold-strain-set method. *Mater Des* 2022;218:110668.
- [254] Sarac B, Bera S, Spieckermann F, Balakin S, Stoica M, Calin M, et al. Micropatterning kinetics of different glass-forming systems investigated by thermoplastic net-shaping. *Scr Mater* 2017;137:127–31.
- [255] Liu X, Chen N, Gu J-L, Yang G-N, Mussler G, Yao K-F. Die imprinting of MGs: a one-step approach for large-area metallic photonic crystals. *Mater Des* 2015;87:1018–21.
- [256] Li N, Chen Y, Jiang M, Li D, He J, Wu Y, et al. A thermoplastic forming map of a zr-based bulk metallic glass. *Acta Mater* 2013;61:1921–31.
- [257] Carmo M, Sekol RC, Ding S, Kumar G, Schroers J, Taylor AD. Bulk metallic glass nanowire architecture for electrochemical applications. *ACS Nano* 2011;5:2979–83.
- [258] Sarac B, Ketkaew J, Popnoe DO, Schroers J. Honeycomb structures of bulk metallic glasses. *Adv Funct Mater* 2012;22:3161–9.
- [259] Hasan M, Schroers J, Kumar G. Functionalization of metallic glasses through Hierarchical patterning. *Nano Lett* 2015;15:963–8.
- [260] Chen N, Yang H, Caron A, Chen P, Lin Y, Louzguine-Luzgin D, et al. Glass-forming ability and thermoplastic formability of a pd 40 ni 40 si 4 p 16 glassy alloy. *J Mater Sci* 2011;46:2091–6.
- [261] Ma J, Zhang X, Wang D, Zhao D, Ding D, Liu K, et al. Superhydrophobic metallic glass surface with superior mechanical stability and corrosion resistance. *Appl Phys Lett* 2014;104:173701.
- [262] He Y, Peng Y, Li Z, Ma J, Zhang X, Liu K, et al. Bio-inspired multifunctional metallic glass. *Sci China Chem* 2016;59:271–6.
- [263] Li N, Xia T, Heng L, Liu L. Superhydrophobic zr-based metallic glass surface with high adhesive force. *Appl Phys Lett* 2013;102:251603.
- [264] Schroers J, Veazey C, Johnson WL. Amorphous metallic foam. *Appl Phys Lett* 2003;82:370–2.
- [265] Luo X, Meng M, Li R, Li Z, Cole IS, Chen X-B, et al. Honeycomb-like porous metallic glasses decorated by cu nanoparticles formed by one-pot electrochemically galvanostatic etching. *Mater Des* 2020;196:109109.
- [266] Liu D, Song Z, Cheng S, Wang Y, Saad A, Deng S, et al. Mesoporous IrNiTa metal glass ribbon as a superior self-standing bifunctional catalyst for water electrolysis. *Chem Eng J* 2022;431:134210.
- [267] Qiu H-J, Wang J, Liu P, Wang Y, Chen M. Hierarchical nanoporous metal/metal-oxide composite by dealloying metallic glass for high-performance energy storage. *Corros Sci* 2015;96:196–202.
- [268] Fu J, Li Z, Liu Z, Li X, Wen W, Sun F, et al. Manufacture of porous metallic glass using dissolvable templates. *Sci China Mater* 2022;65:2833–41.
- [269] Liu J, Sun F, Yu X, Zhang H, Huang J, Wang W, et al. Dissolution manufacturing strategy for designing tailorable porous glass surfaces. *Sci China Mater* 2023;66:4334–41.
- [270] Schroers J, Pham Q, Peker A, Paton N, Curtis RV. Blow molding of bulk metallic glass. *Scr Mater* 2007;57:341–4.
- [271] Kanik M, Bordeenithikasem P, Kim D, Selden N, Desai A, M'Closkey R, et al. Metallic glass hemispherical shell resonators. *J Microelectromech Syst* 2014;24:19–28.
- [272] Sarac B, Kumar G, Hodges T, Ding S, Desai A, Schroers J. Three-dimensional Shell fabrication using blow molding of bulk metallic glass. *J Microelectromech Syst* 2011;20:28–36.
- [273] Martinez R, Kumar G, Schroers J. Hot rolling of bulk metallic glass in its supercooled liquid region. *Scr Mater* 2008;59:187–90.
- [274] Chiu HM, Kumar G, Blawdziewicz J, Schroers J. Thermoplastic extrusion of bulk metallic glass. *Scr Mater* 2009;61:28–31.
- [275] Huang H, Yan J. Surface patterning of zr-based metallic glass by laser irradiation induced selective thermoplastic extrusion in nitrogen gas. *J Microchem Microeng* 2017;27:075007.
- [276] Kim YH, Lim KR, Kim WT, Kim DH, Choi YS, Na YS. Rapid heating blow molding of metallic glasses by infrared heating. *Results in Materials* 2019;3:100045.
- [277] Fu J, Huang Z, Yang J, Ma J, Shen J. Nano-forming of the rare earth la-based metallic glass. *J Non Cryst Solids* 2021;558:120682.
- [278] Hu Z, Meduri CS, Blawdziewicz J, Kumar G. Nanoshaping of glass forming metallic liquids by stretching: evading lithography. *Nanotechnology* 2018;30:075302.
- [279] Urata A, Nishiyama N, Amiya K, Inoue A. Continuous casting of thick fe-base glassy plates by twin-roller melt-spinning. *Mater Sci Eng A* 2007;449:269–72.
- [280] Scudino S, Jerliu B, Surreddi KB, Kühn U, Eckert J. Effect of cold rolling on compressive and tensile mechanical properties of Zr52. 5Ti5Cu18Ni14. 5Al10 bulk metallic glass. *J Alloy Compd* 2011;509:S128–30.
- [281] Park J, Lim H, Kim J-H, Chang H, Kim W, Kim D, et al. In situ crystallization and enhanced mechanical properties of the Zr41. 2Ti13. 8Cu12. 5Ni10Be22. 5 alloy by cold rolling. *Journal of non-crystalline solids*. 2005;351:2142–6.
- [282] Johnson WL, Kaltenboeck G, Demetriou MD, Schramm JP, Liu X, Samwer K, et al. Beating crystallization in glass-forming metals by Millisecond heating and processing. *Science* 2011;332:828–33.
- [283] Kaltenboeck G, Harris T, Sun K, Tran T, Chang G, Schramm JP, et al. Accessing thermoplastic processing windows in metallic glasses using rapid capacitive discharge. *Sci Rep* 2014;4:6441.
- [284] Kaltenboeck G, Demetriou MD, Roberts S, Johnson WL. Shaping metallic glasses by electromagnetic pulsing. *Nat Commun* 2016;7:10576.
- [285] Ma J, Huang Z, Zheng H, Gong F, Liang X. Controllable thermoplastic forming of bulk metallic glasses in milliseconds by resistance welding forming. *Mater Res Express* 2019;6:075210.
- [286] Mei L, Liu J, Huang Y, Lin J, Shen J, Tan J, et al. Experimental study on formability of bulk metallic glass as mold for microstructure replication. *Microelectron Eng* 2012;98:142–6.
- [287] Ma J, Zhang X, Wang WH. Metallic glass mold insert for hot embossing of polymers. *J Appl Phys* 2012;112.

- [288] Huang J, Fu J, Li L, Ma J. Mg-based metallic glass nanowires with excellent photothermal effect. *Scr Mater* 2023;222:115036.
- [289] Man Q, Inoue A, Dong Y, Qiang J, Zhao C, Shen B. A new CoFe-based bulk metallic glasses with high thermoplastic forming ability. *Scr Mater* 2013;69:553–6.
- [290] Sun F, Yang J, Fu J, Wang B, Ma J, Shen J. Hierarchical macro to nano press molding of optical glasses by using metallic glasses. *J Non Cryst Solids* 2022;594:121821.
- [291] Liu X, Mo R, Li K, Shen J, Ma J, Gong F. Manufacturing of 3D microlens Array Mold on bulk metallic glass by self-aligned multi-ball hot embossing. *International Journal of Precision Engineering and Manufacturing-Green Technology* 2020;8:1209–23.
- [292] Sekol RC, Carmo M, Kumar G, Gittleson F, Doubek G, Sun K, et al. Pd–Ni–Cu–P metallic glass nanowires for methanol and ethanol oxidation in alkaline media. *Int J Hydrogen Energy* 2013;38:11248–55.
- [293] Sekol RC, Kumar G, Carmo M, Gittleson F, Hardesty-Dyck N, Mukherjee S, et al. Bulk metallic glass micro fuel cell. *Small* 2013;9:2081–5.
- [294] Cheng S, Zhu J, Shen J, Wei X. Effects of yttrium addition on thermoplastic formability of zr-cu-ni-al amorphous alloy under non-isothermal condition. *J Alloy Compd* 2021;872.
- [295] Gong P, Wang S, Liu Z, Chen W, Li N, Wang X, et al. Lightweight ti-based bulk metallic glasses with superior thermoplastic formability. *Intermetallics* 2018;98:54–9.
- [296] Xu L, Shui L, Zhang Y, Peng Q, Xue L, Liu Z. Robust and reproducible fabrication of large area aluminum (Al) micro/nanorods arrays by superplastic nanomolding at room temperature. *Appl Phys Express* 2020;13:036503.
- [297] Hu Q, Fu MW, Zeng XR. Thermostability and thermoplastic formability of (Zr65Cu17.5Ni10Al7.5)100–xREx (x=0.25–3.25, RE: Y, Gd, Tb, Dy, Ho, Er, Tm, Yb, Lu) bulk metallic glasses. *Materials & Design*. 2014;64:301–6.
- [298] Wang X, Dai W, Zhang M, Gong P, Li N. Thermoplastic micro-formability of TiZrHfNiCuBe high entropy metallic glass. *J Mater Sci Technol* 2018;34:2006–13.
- [299] Gao S, Jia J, Chen S, Luan H, Shao Y, Yao K. Oxide-derived nanostructured metallic-glass electrodes for efficient electrochemical hydrogen generation. *RSC Adv* 2017;7:27058–64.
- [300] Gong P, Kou H, Wang S, Deng L, Wang X, Jin J. Research on thermoplastic formability and nanomoulding mechanism of lightweight ti-based bulk metallic glasses. *J Alloy Compd* 2019;801:267–76.
- [301] Uzun C, Kahler N, Grave de Peralta L, Kumar G, Bernussi AA. Photo-induced-heat localization on nanostructured metallic glasses. *J Appl Phys* 2017. 122:094306.
- [302] Uzun C, Meduri C, Kahler N, De Peralta LG, McCollum JM, Pantoya M, et al. Photoinduced heat conversion enhancement of metallic glass nanowire arrays. *J Appl Phys* 2019;125:015102.
- [303] Yashiro W, Noda D, Hattori T, Hayashi K, Momose A, Kato H. A metallic glass grating for X-ray grating interferometers fabricated by imprinting. *Appl Phys Express* 2014;7:032501.
- [304] Gravier S, Kapelski G, Suéry M, Blandin J-J. Thermoplastic forming of bulk metallic glasses. *Int J Appl Glas Sci* 2012;3:180–7.
- [305] Chen YC, Chu JP, Jang JSC, Wu CW. Thermoplastic deformation and micro/nano-replication of an au-based bulk metallic glass in the supercooled liquid region. *Mater Sci Eng A* 2012;556:488–93.
- [306] Arora HS, Xu Q, Xia Z, Ho Y-H, Dahotre NB, Schroers J, et al. Wettability of nanotextured metallic glass surfaces. *Scr Mater* 2013;69:732–5.
- [307] Doubek G, Sekol RC, Li J, Ryu WH, Gittleson FS, Nejtai S, et al. Guided evolution of bulk metallic glass nanostructures: a platform for designing 3D electrocatalytic Surfaces. *Adv Mater* 2016;28:1940–9.
- [308] Mridha S, Arora HS, Lefebvre J, Bhowmick S, Mukherjee S. High temperature in situ compression of thermoplastically formed Nano-scale metallic glass. *JOM* 2016;69:39–44.
- [309] Zhang N, Chu JS, Byrne CJ, Browne DJ, Gilchrist MD. Replication of micro/nano-scale features by micro injection molding with a bulk metallic glass mold insert. *J Micromech Microeng* 2012;22.
- [310] Xia T, Li N, Wu Y, Liu L. Patterned superhydrophobic surface based on pd-based metallic glass. *Appl Phys Lett* 2012;101.
- [311] Li N, Xu E, Liu Z, Wang X, Liu L. Tuning apparent friction coefficient by controlled patterning bulk metallic glasses surfaces. *Sci Rep* 2016;6:39388.
- [312] Liu X, Gu J-L, Yang G-N, Shao Y, Chen N, Yao K-F. Theoretical and experimental study of metallic glass die-imprinting for manufacturing large-size micro/nano structures. *J Mater Process Technol* 2022;307.
- [313] Liu Z, Schroers J. General nanomoulding with bulk metallic glasses 2015;26:145301.
- [314] Li J, Zhang W, Song Y, Yin W, Zhang T. Template transfer nanoimprint for uniform nanopores and nanopoles. *J Nanomater* 2016;2016:1–7.
- [315] Magagnosc DJ, Chen W, Kumar G, Schroers J, Gianola DS. Thermomechanical behavior of molded metallic glass nanowires. *Sci Rep* 2016;6:19530.
- [316] Tariqan HJ, Kahler N, Ramos NS, Kumar G, Bernussi AA. Low reflectance of nano-patterned pt-cu-ni-p bulk metallic glass. *Appl Phys Lett* 2015;107.
- [317] Shayan M, Padmanabhan J, Morris AH, Cheung B, Smith R, Schroers J, et al. Nanopatterned bulk metallic glass-based biomaterials modulate macrophage polarization. *Acta Biomater* 2018;75:427–38.
- [318] Ma J, Chan KC, Xia L, Chen SH, Wu FF, Li WH, et al. Multi-layer laminated pd-based metallic glass with enhanced plasticity. *Mater Sci Eng A* 2013;587:240–3.
- [319] Chen YC, Chu JP, Jang JSC, Hsieh CW, Yang Y, Li CL, et al. Replication of nano/micro-scale features using bulk metallic glass mold prepared by femtosecond laser and imprint processes. *J Micromech Microeng* 2013;23.
- [320] Hasan M, Warzywoda J, Kumar G. Decoupling the effects of surface texture and chemistry on the wetting of metallic glasses. *Appl Surf Sci* 2018;447:355–62.
- [321] Monfared A, Liu W, Zhang L. Metallic glass hardening after thermoplastic forming. *Mater Sci Eng A* 2018;725:181–6.
- [322] Sarac B, Bera S, Balakin S, Stoica M, Calin M, Eckert J. Hierarchical surface patterning of ni- and be-free ti- and zr-based bulk metallic glasses by thermoplastic net-shaping. *Mater Sci Eng C Mater Biol Appl* 2017;73:398–405.
- [323] Ma J, Huo LS, Zhao DQ, Wang WH. Micro mold filling kinetics of metallic glasses in supercooled liquid state. *J Appl Phys* 2013;113.
- [324] Sarac B, Soppu D, Park E, Hufenbach J, Oswald S, Stoica M, et al. Mechanical and structural investigation of porous bulk metallic glasses. *Metals* 2015;5:920–33.
- [325] Li JB, Zhang HZ, Jang JSC, Jian SR, Li C, Huang JC, et al. Viscous flow and thermoplastic forming ability of a zr-based bulk metallic glass composite with ta dispersoids. *J Alloy Compd* 2012;536:S165–70.
- [326] Mukherjee S, Carmo M, Kumar G, Sekol RC, Taylor AD, Schroers J. Palladium nanostructures from multi-component metallic glass. *Electrochim Acta* 2012;74:145–50.
- [327] Hasan M, Kumar G. High strain rate thermoplastic demolding of metallic glasses. *Scr Mater* 2016;123:140–3.
- [328] Liu X, Shao Y, Lu S-Y, Yao K-F. High-accuracy bulk metallic glass mold insert for hot embossing of complex polymer optical devices. *J Polym Sci B* 2015;53:463–7.
- [329] Kinser ER, Padmanabhan J, Yu R, Corona SL, Li J, Vaddiraju S, et al. Nanopatterned bulk metallic glass biosensors. *ACS Sens* 2017;2:1779–87.
- [330] Wang X, Xu J, Wang C, Sanchez Egea AJ, Li J, Liu C, et al. Bio-inspired functional surface fabricated by electrically assisted micro-embossing of AZ31 magnesium alloy. *Materials* 2020;13:412.
- [331] Wang F, Zhang H, Liang X, Gong F, Ma J. Fabrication of metallic glass micro grooves by thermoplastic forming. *J Micromech Microeng* 2017;27.
- [332] Zhu Z, Yi C, Shi T, Zhang Y, Gao Y, Liao G. Hot embossing of zr-based bulk metallic glass Micropart using stacked silicon dies. *Adv Mater Sci Eng* 2015;2015:1–8.
- [333] Zhang N, Srivastava AP, Browne DJ, Gilchrist MD. Performance of nickel and bulk metallic glass as tool inserts for the microinjection molding of polymeric microfluidic devices. *J Mater Process Technol* 2016;231:288–300.
- [334] Zhang W, Fang C, Li Y. Ferromagnetic fe-based bulk metallic glasses with high thermoplastic formability. *Scr Mater* 2013;69:77–80.
- [335] Xiaoyu L, Sharma P, Zhang Y, Makino A, Kato H. Nano-imprinting potential of magnetic FeCo-based metallic glass. *Nanotechnology* 2019;30.
- [336] Liang X, Sharma P, Zhang Y, Kato H. Nanoimprinting of magnetic FeCo-based metallic glass thin films. *J Magn Magn Mater* 2022;542.
- [337] Pan CT, Wu TT, Chen MF, Chang YC, Lee CJ, Huang JC. Hot embossing of micro-lens array on bulk metallic glass. *Sens Actuators, A* 2008;141:422–31.
- [338] Padmanabhan J, Kinser ER, Stalter MA, Duncan-Lewis C, Balestrini JL, Sawyer AJ, et al. Engineering Cellular response using nanopatterned bulk metallic glass. *ACS Nano* 2014;8:4366–75.

- [339] He JJ, Li N, Tang N, Wang XY, Zhang C, Liu L. The precision replication of a microchannel mould by hot-embossing a zr-based bulk metallic glass. *Intermetallics* 2012;21:50–5.
- [340] Hu Z, Meduri CS, Ingrole RS, Gill HS, Kumar G. Solid and hollow metallic glass microneedles for transdermal drug-delivery. *Appl Phys Lett* 2020;116:203703.
- [341] Yamada R, Yodoshi N, Nomura N, Saida J, Kawasaki A. Uniformity of the glassy state of iron-based metallic glassy particles and reproducibility of fabricating microparts. *Mater Des* 2020;191.
- [342] Shen B, Liu CY, Jia Y, Yue GQ, Ke FS, Zhao HB, et al. Molecular dynamics simulation studies of structural and dynamical properties of rapidly quenched al. *J Non Cryst Solids* 2014;383:13–20.
- [343] Sarac B, Gammmer C, Deng L, Park E, Yokoyama Y, Stoica M, et al. Elastostatic reversibility in thermally formed bulk metallic glasses: nanobeam diffraction fluctuation electron microscopy. *Nanoscale* 2018;10:1081–9.
- [344] Kumar G, Prades-Rodel S, Blatter A, Schroers J. Unusual brittle behavior of pd-based bulk metallic glass. *Scr Mater* 2011;65:585–7.
- [345] Sarac B, Spieckermann F, Rezvan A, Gammmer C, Krämer L, Kim J, et al. Annealing-assisted high-pressure torsion in Zr<sub>55</sub>Cu<sub>30</sub>Al<sub>10</sub>Ni<sub>5</sub> metallic glass. *J Alloy Compd* 2019;784:1323–33.
- [346] Zhao H, Sun F, Li X, Ding Y, Yan YQ, Tong X, et al. Ultrastability of metallic supercooled liquid induced by vibration. *Scr Mater* 2021;194:113606.
- [347] Lv Z, Yan Y, Yuan C, Huang B, Yang C, Ma J, et al. Making fe-si-b amorphous powders as an effective catalyst for dye degradation by high-energy ultrasonic vibration. *Mater Des* 2020;194:108876.
- [348] Huang J, Yu X, Li L, Wang W, Zhang H, Zhang Y, et al. Design of Light-Driven Biocompatible and Biodegradable Microrobots Containing mg-Based Metallic Glass Nanowires. *ACS Nano* 2024;18:2006–16.
- [349] Liang X, Liu Z, Fu J, Zhang H, Huang J, Ren S, et al. Dissolvable templates to prepare pt-based porous metallic glass for the oxygen reduction reaction. *Nanoscale* 2023;15:6802–11.
- [350] Wang YB, Li HF, Zheng YF, Wei SC, Li M. Correlation between corrosion performance and surface wettability in ZrTiCuNiBe bulk metallic glasses. *Appl Phys Lett* 2010;96.
- [351] Li Z, Ma J. Water-repellent surfaces of metallic glasses: fabrication and application. *Materials Today Advances* 2021;12:100164.
- [352] Liu X, Shao Y, Tang Y, Yao K-F. Highly uniform and reproducible surface enhanced raman scattering on air-stable metallic glassy nanowire array. *Sci Rep* 2014;4:5835.
- [353] Li M-X, Zhao S-F, Lu Z, Hirata A, Wen P, Bai H-Y, et al. High-temperature bulk metallic glasses developed by combinatorial methods. *Nature* 2019;569:99–103.
- [354] You R, Liu YQ, Hao YL, Han DD, Zhang YL, You Z. Laser fabrication of graphene-based flexible electronics. *Adv Mater* 2020;32:1901981.
- [355] Xie W, Li M, Cao J, Hu L, Wang C, Wang W-H, et al. Oxidation of a zr 46 cu 46 al 7 gd 1 bulk metallic glass detected via optical characterizations. *Sci China Mater* 2020;64:973–8.
- [356] McMillon-Brown L, Bordeenithikasem P, Pinnock F, Ketkaew J, Martin AC, Schroers J, et al. Measured optical constants of Pd<sub>77</sub>. 5Cu<sub>6</sub>Si<sub>16</sub>. 5 bulk metallic glass. *Optical Materials: X*. 2019;1:100012.
- [357] Cheng Z, Liu L, Xu S, Lu M, Wang X. Temperature dependence of electrical and thermal conduction in single silver nanowire. *Sci Rep* 2015;5:1–12.
- [358] Sun BA, Wang WH. The fracture of bulk metallic glasses. *Prog Mater Sci* 2015;74:211–307.
- [359] Liu YH, Wang G, Wang RJ, Zhao DQ, Pan MX, Wang WH. Super plastic bulk metallic glasses at room temperature. *Science* 2007;315:1385–8.
- [360] Lewandowski JJ, Greer AL. Temperature rise at shear bands in metallic glasses. *Nat Mater* 2006;5:15–8.
- [361] Maaß R, Löffler JF. Shear-band dynamics in metallic glasses. *Adv Funct Mater* 2015;25:2353–68.
- [362] Qiao JC, Wang Q, Pelletier JM, Kato H, Casalini R, Crespo D, et al. Structural heterogeneities and mechanical behavior of amorphous alloys. *Prog Mater Sci* 2019;104:250–329.
- [363] Spaepen F. A microscopic mechanism for steady state inhomogeneous flow in metallic glasses. *Acta Metall* 1977;25:407–15.
- [364] Argon A, Kuo H. Plastic flow in a disordered bubble raft (an analog of a metallic glass). *Mater Sci Eng* 1979;39:101–9.
- [365] Falk ML, Langer JS. Dynamics of viscoplastic deformation in amorphous solids. *Phys Rev E* 1998;57:7192.
- [366] Wang Z, Wang W-H. Flow units as dynamic defects in metallic glassy materials. *Natl Sci Rev* 2019;6:304–23.
- [367] Li Z, Li X, Huang Z, Zhang Z, Liang X, Liu H, et al. Ultrasonic-vibration-enhanced plasticity of an entropic alloy at room temperature. *Acta Mater* 2022;225.
- [368] Li X, Li L, Sohrabi S, Jn Fu, Li Z, Chen Z, et al. Ultrasonic vibration enabled under-liquid forming of metallic glasses. *Science Bulletin* 2024;69:163–6.
- [369] Ma J, Liang X, Wu X, Liu Z, Gong F. Sub-second thermoplastic forming of bulk metallic glasses by ultrasonic beating. *Sci Rep* 2015;5:17844.
- [370] Liang X, Ma J, Wu XY, Xu B, Gong F, Lei JG, et al. Micro injection of metallic glasses parts under ultrasonic vibration. *J Mater Sci Technol* 2017;33:703–7.
- [371] Li X, He Q, Lu W, Zhou Z, Tian J, Liang D, et al. Machine learning atomic dynamics to unfold the origin of plasticity in metallic glasses: from thermo- to acousto-plastic flow. *Sci China Mater* 2022;65:1952–62.
- [372] Xue R, Zhao L, Shi C, Ma T, Xi X, Gao M, et al. Enhanced kinetic stability of a bulk metallic glass by high pressure. *Appl Phys Lett* 2016;109:221904.
- [373] Wang WH, Zhuang YX, Pan MX, Yao YS. Glass transition behavior, crystallization kinetics, and microstructure change of zr 41 ti 14 cu 12.5 ni 10 be 22.5 bulk metallic glass under high pressure. *J Appl Phys* 2000;88:3914–8.
- [374] Luo P, Cao C, Zhu F, Lv Y, Liu Y, Wen P, et al. Ultrastable metallic glasses formed on cold substrates. *Nat Commun* 2018;9:1389.
- [375] Yu HB, Luo Y, Samwer K. Ultrastable metallic glass. *Adv Mater* 2013;25:5904–8.
- [376] Luo Q, Zhang B, Zhao D, Wang R, Pan M, Wang W. Aging and stability of cerium-based bulk metallic glass. *Appl Phys Lett* 2006;88:151915.
- [377] Lee S-C, Lee C-M, Yang J-W, Lee J-C. Microstructural evolution of an elastostatically compressed amorphous alloy and its influence on the mechanical properties. *Scr Mater* 2008;58:591–4.
- [378] Brechtel J, Wang H, Kumar N, Yang T, Lin Y-R, Bei H, et al. Investigation of the thermal and neutron irradiation response of BAM-11 bulk metallic glass. *J Nucl Mater* 2019;526:151771.
- [379] Dmowski W, Yokoyama Y, Chuang A, Ren Y, Umemoto M, Tsuchiya K, et al. Structural rejuvenation in a bulk metallic glass induced by severe plastic deformation. *Acta Mater* 2010;58:429–38.
- [380] Chen S, Li S, Ma J, Yu H, Liu H, Peng H. Ultrasonic vibration accelerated aging in la-based bulk metallic glasses. *J Non Cryst Solids* 2020;535:119967.
- [381] Lou Y, Xv S, Liu Z, Ma J. Rejuvenation of zr-based bulk metallic glasses by ultrasonic vibration-assisted elastic deformation. *Materials* 2020;13:4397.
- [382] Chen Z, Ren S, Zhao R, Zhu J, Li X, Zhang H, et al. Plasticity and rejuvenation of aged metallic glasses by ultrasonic vibrations. *J Mater Sci Technol* 2023.
- [383] Zhang Y, Zhao H, Yan Y, Tong X, Ma J, Ke H, et al. Ultrasonic-assisted fabrication of metallic glass composites. *J Non Cryst Solids* 2022;597:121894.
- [384] Yuan C, Liu R, Lv Z, Li X, Pang C, Yang C, et al. Softening in an ultrasonic-vibrated pd-based metallic glass. *Intermetallics* 2022;144:107527.
- [385] Wu K, Meng Y, Li X, Ma J, Zhang P, Li W, et al. Improved alkaline hydrogen evolution performance of a Fe<sub>78</sub>Si<sub>9</sub>B<sub>13</sub> metallic glass electrocatalyst by ultrasonic vibrations. *Intermetallics* 2020;125:106820.
- [386] Bletry M, Guyot P, Brechet Y, Blandin JJ, Soubeyroux JL. Homogeneous deformation of bulk metallic glasses in the super-cooled liquid state. *Mater Sci Eng A* 2004;387:1005–11.
- [387] Kawamura Y, Nakamura T, Kato H, Mano H, Inoue A. Newtonian and non-newtonian viscosity of supercooled liquid in metallic glasses. *Mater Sci Eng A* 2001;304–306:674–8.
- [388] Louzguine DV, Kawamura Y, Inoue A. Production of Si<sub>55</sub> Al<sub>20</sub> Fe<sub>10</sub> Ni<sub>5</sub> Cr<sub>5</sub> Zr<sub>5</sub> bulk amorphous alloy by hot pressing. *Mater Sci Technol* 1999;15:583–5.
- [389] Wang Z, Prashanth KG, Surreddi KB, Suryanarayana C, Eckert J, Scudino S. Pressure-assisted sintering of Al–Gd–Ni–Co amorphous alloy powders. *Materialia* 2018;2:157–66.
- [390] Lee P-Y, Hung S-S, Hsieh J-T, Lin Y-L, Lin C-K. Consolidation of amorphous Ni–Zr–Ti–Si powders by vacuum hot-pressing method. *Intermetallics* 2002;10:1277–82.
- [391] El-Eskandarany MS, Inoue A. Synthesis of new bulk metallic glassy Ti<sub>60</sub>Al<sub>15</sub>Cu<sub>10</sub>W<sub>10</sub>Ni<sub>5</sub> alloy by hot-pressing the mechanically alloyed powders at the supercooled liquid region. *Metall and Mat Trans A* 2006;37:2231–8.
- [392] Kang EY, Kim YB, Kim KY, Chung YH, Baik HK. Vacuum hot pressing of Fe–Si–B–Nb-based amorphous powder cores and their high-frequency magnetic properties. *J Appl Phys* 2006;99:08F111.

- [393] Wei X, Han F, Wang X, Wang X, Ce W. Fabrication of al-based bulk metallic glass by mechanical alloying and vacuum hot consolidation. *J Alloy Compd* 2010; 501:164–7.
- [394] El-Eskandarany MS, Ishihara S, Zhang W, Inoue A. Fabrication and characterizations of new glassy Co<sub>71</sub>Ti<sub>24</sub>B<sub>5</sub> alloy powders and subsequent hot pressing into a fully dense bulk glass. *Metall and Mat Trans A* 2005;36:141–7.
- [395] Saheb N, Iqbal Z, Khalil A, Hakeem AS, Al Aqeeli N, Laoui T, et al. Spark plasma sintering of metals and metal matrix nanocomposites: a review. *J Nanomater* 2012;2012:983470.
- [396] Cardinal S, Pelletier JM, Qiao JC, Bonnefont G, Xie G. Influence of spark plasma sintering parameters on the mechanical properties of Cu<sub>50</sub>Zr<sub>45</sub>Al<sub>5</sub> bulk metallic glass obtained using metallic glass powder. *Mater Sci Eng A* 2016;677:116–24.
- [397] He T, Ciftci N, Uhlenwinkel V, Scudino S. Synthesis of bulk Zr<sub>48</sub>Cu<sub>36</sub>Al<sub>8</sub>Ag<sub>8</sub> metallic glass by hot pressing of amorphous powders. *Journal of Manufacturing and Materials Processing* 2021.
- [398] Lee PY, Kao MC, Lin CK, Huang JC. Mg–Y–Cu bulk metallic glass prepared by mechanical alloying and vacuum hot-pressing. *Intermetallics* 2006;14:994–9.
- [399] Lee PY, Lo C, Jang JSC. Consolidation of mechanically alloyed Mg<sub>49</sub>Y<sub>15</sub>Cu<sub>36</sub> powders by vacuum hot pressing. *J Alloy Compd* 2007;434–435:354–7.
- [400] Lee PY, Liu WC, Lin CK, Huang JC. Fabrication of Mg–Y–Cu bulk metallic glass by mechanical alloying and hot consolidation. *Mater Sci Eng A* 2007;449–451: 1095–8.
- [401] Santana DA, Kiminami CS, Coury FG, Liberato LG, Gargarella P, Kaufman MJ. Consolidation of fe-based metallic glass powders by hot pressing. *Mater Res* 2019;22.
- [402] Börner I, Eckert J. Phase formation and properties of mechanically alloyed amorphous Al<sub>85</sub>Y<sub>8</sub>Ni<sub>5</sub>Co<sub>2</sub>. *Scr Mater* 2001;45:237–44.
- [403] Guillon O, Gonzalez-Julian J, Dargatz B, Kessel T, Schierning G, Räthel J, et al. Field-assisted sintering Technology/Spark plasma sintering: mechanisms, materials, and technology developments. *Adv Eng Mater* 2014;16:830–49.
- [404] Kelly JP, Graeve OA. Spark plasma sintering as an approach to Manufacture bulk materials: feasibility and cost savings. *JOM* 2015;67:29–33.
- [405] Nagireddi S, Babu DA, Srinivasarao B, Majumdar B. Processing of hf based bulk metallic glass through Spark plasma sintering (SPS) process. *J Alloy Compd* 2021;876:160057.
- [406] Zrodowski Ł, Wróblewski R, Choma T, Rygiel T, Rosiński M, Moronczyk B, et al. Ultrashort sintering and Near net shaping of zr-based AMZ4 bulk metallic glass. *Materials* 2021.
- [407] Xie G, Louzguine-Luzgin DV, Kimura H, Inoue A. Nearly full density Ni<sub>52</sub>Nb<sub>10</sub>Zr<sub>15</sub>Ti<sub>15</sub>Pt<sub>7.5</sub> bulk metallic glass obtained by spark plasma sintering of gas atomized powders. *Appl Phys Lett* 2007. 90:241902.
- [408] Perrière L, Champion Y, Bernard F. Spark plasma sintering of metallic glasses. In: Cavaliere P, editor. *Spark Plasma Sintering of Materials: Advances in Processing and Applications*. Cham: Springer International Publishing; 2019. p. 291–335.
- [409] Li XX, Yang C, Chen T, Fu ZQ, Li YY, Ivasishin OM, et al. Effective atomic diffusion coefficient dependence on applied pressure during spark plasma sintering. *Materialia* 2019;6:100334.
- [410] Zarazúa-Villalobos L, Mary N, Soo-Hyun J, Ogawa K, Kato H, Ichikawa Y. Microstructure and corrosion study of fe-based bulk metallic glass obtained by spark plasma sintering. *J Alloy Compd* 2021;880:160399.
- [411] Choi PP, Kim JS, Nguyen OTH, Kwon DH, Kwon YS, Kim JC. Al-la-ni-fe bulk metallic glasses produced by mechanical alloying and spark-plasma sintering. *Mater Sci Eng A* 2007;449–451:1119–22.
- [412] Suárez M, Fernández-González D, Díaz LA, Diolgent F, Verdeja LF, Fernández A. Consolidation and mechanical properties of ZrCu<sub>39.85</sub>Y<sub>2.37</sub>Al<sub>1.8</sub> bulk metallic glass obtained from gas-atomized powders by spark plasma sintering. *Intermetallics* 2021. 139:107366.
- [413] Xie G, Qin F, Zhu S, Inoue A. Ni-free ti-based bulk metallic glass with potential for biomedical applications produced by spark plasma sintering. *Intermetallics* 2012;29:99–103.
- [414] Dong Y, Liu J, Wang P, Zhao H, Pang J, Li X, et al. Study of bulk amorphous and nanocrystalline alloys fabricated by high-sphericity Fe<sub>84</sub>Si<sub>7</sub>B<sub>5</sub>C<sub>2</sub>Cr<sub>2</sub> amorphous powders at different Spark-plasma-sintering temperatures. *Materials* 2022.
- [415] Li XX, Yang C, Chen T, Zhang LC, Hayat MD, Cao P. Influence of powder shape on atomic diffusivity and resultant densification mechanisms during spark plasma sintering. *J Alloy Compd* 2019;802:600–8.
- [416] Liu LH, Yang C, Yao YG, Wang F, Zhang WW, Long Y, et al. Densification mechanism of ti-based metallic glass powders during spark plasma sintering process. *Intermetallics* 2015;66:1–7.
- [417] Ding H, Zhao Z, Jin J, Deng L, Gong P, Wang X. Densification mechanism of zr-based bulk metallic glass prepared by two-step spark plasma sintering. *J Alloy Compd* 2021;850:156724.
- [418] Nowak S, Perrière L, Dembinski L, Tusseau-Nenez S, Champion Y. Approach of the spark plasma sintering mechanism in Zr<sub>57</sub>Cu<sub>20</sub>Al<sub>10</sub>Ni<sub>8</sub>Ti<sub>5</sub> metallic glass. *J Alloy Compd* 2011;509:1011–9.
- [419] Perrière L, Thai MT, Tusseau-Nenez S, Ochin P, Bléry M, Champion Y. Spark plasma sintering for metallic glasses processing. *Rev Metall* 2012;109:5–10.
- [420] Xie G, Zhang W, Louzguine-Luzgin DV, Kimura H, Inoue A. Fabrication of porous Zr–Cu–Al–Ni bulk metallic glass by spark plasma sintering process. *Scr Mater* 2006;55:687–90.
- [421] Du P, Li K, Zhu B, Xiang T, Xie G. Development of non-toxic low-cost bioactive porous Ti–Fe–Si bulk metallic glass with bone-like mechanical properties for orthopedic implants. *J Mater Res Technol* 2022;17:1319–29.
- [422] Wu Z, Du P, Xiang T, Li K, Xie G. Ti-based bulk metallic glass implantable biomaterial with adjustable porosity produced by a novel pressure regulation method in spark plasma sintering. *Intermetallics* 2021;131:107105.
- [423] Xie G, Kanetaka H, Kato H, Qin F, Wang W. Porous ti-based bulk metallic glass with excellent mechanical properties and good biocompatibility. *Intermetallics* 2019;105:153–62.
- [424] Xie G, Qin F, Zhu S, Louzguine-Luzgin DV. Corrosion behaviour of porous ni-free ti-based bulk metallic glass produced by spark plasma sintering in hanks' solution. *Intermetallics* 2014;44:55–9.
- [425] Graeve OA, Saterlie MS, Kanakala R, de la Torre SD, Farmer JC. The kinetics of devitrification of amorphous alloys: the time–temperature–crystallinity diagram describing the spark plasma sintering of fe-based metallic glasses. *Scr Mater* 2013;69:143–8.
- [426] Jiang JZ, Olsen JS, Gerward L, Abdali S, Eckert J, Schlorke-de Boer N, et al. Pressure effect on crystallization of metallic glass Fe<sub>72</sub>P<sub>11</sub>C<sub>6</sub>Al<sub>5</sub>B<sub>4</sub>Ga<sub>2</sub> alloy with wide supercooled liquid region. *J Appl Phys* 2000;87:2664–6.
- [427] Lin CK, Lee PY. Consolidation of mechanically alloyed cu-zr-ti metallic glass powders. *Key Eng Mater* 2017;732:5–10.
- [428] Li K, Li B, Du P, Xiang T, Yang X, Xie G. Effect of powder size on strength and corrosion behavior of Mg<sub>66</sub>Zn<sub>30</sub>Ca<sub>4</sub> bulk metallic glass. *J Alloy Compd* 2022; 897:163219.
- [429] Harimkar SP, Paital SR, Singh A, Aalund R, Dahotre NB. Microstructure and properties of spark plasma sintered Fe–Cr–Mo–Y–B–C bulk metallic glass. *J Non Cryst Solids* 2009;355:2179–82.
- [430] Singh A, Harimkar SP. Spark plasma sintering of in situ and ex situ iron-based amorphous matrix composites. *J Alloy Compd* 2010;497:121–6.
- [431] Zhang L, Li B, Wu H, Wang W, Zhai S, Xu J, et al. Microstructure and property characterization of al-based composites reinforced with CuZrAl particles fabricated by mechanical alloying and spark plasma sintering. *Adv Powder Technol* 2018;29:1695–702.
- [432] Kelly JP, Fuller SM, Seo K, Novitskaya E, Eliasson V, Hodge AM, et al. Designing in situ and ex situ bulk metallic glass composites via spark plasma sintering in the super cooled liquid state. *Mater Des* 2016;93:26–38.
- [433] Xie G, Huang Z. Optimizing mechanical and electrical properties of cu-coated Cu–Zr–Al bulk metallic glass composites by adjusting glassy powder size. *Intermetallics* 2022;146:107570.
- [434] Huang Z, Wu Z, Cheng X, Zhang Z, Xie G. Bulk metallic glass composites with high strength and electrical conductivity by sintering cu-coated CuZrAl glassy powder. *J Alloy Compd* 2020;841:155723.
- [435] Gheiratmand T, Madaah Hosseini HR, Davami P, Sarafidis C. Fabrication of FINEMET bulk alloy from amorphous powders by spark plasma sintering. *Powder Technol* 2016;289:163–8.

- [436] Monson TC, Zheng B, Delany RE, Pearce CJ, Langlois ED, Lepkowski SM, et al. Soft magnetic multilayered fescrb-fe<sub>x</sub> metallic glass composites fabricated by Spark plasma sintering. *IEEE Magn Lett* 2019;10:1–5.
- [437] Zhao P, Luo Y, Yu D-B, Peng H-J, Yan W-L, Wang Z-L, et al. Preparation and properties of hot-deformed magnets processed from nanocrystalline/amorphous Nd-Fe-B powders. *Rare Met* 2021;40:2033–9.
- [438] Zhu J, Cai Y, Zhang Y, Liu X, Tian J, Ma J, et al. Particle-reinforced cu matrix composites fabricated by sintering core-shell-type amorphous/crystalline composite powders. *Mater Sci Eng A* 2022;854:143823.
- [439] Liang S-X, Wang X, Zhang W, Liu Y-J, Wang W, Zhang L-C. Selective laser melting manufactured porous fe-based metallic glass matrix composite with remarkable catalytic activity and reusability. *Appl Mater Today* 2020;19:100543.
- [440] Ma Z, Li J, Zhang J, He A, Dong Y, Tan G, et al. Ultrathin, flexible, and high-strength Ni/Cu/metallic glass/Cu/Ni composite with alternate magneto-electric structures for electromagnetic shielding. *J Mater Sci Technol* 2021;81:43–50.
- [441] Fu J, Yang J, Wu K, Lin H, Wen W, Ruan W, et al. Metallic glue for designing composite materials with tailorable properties. *Mater Horiz* 2021;8:1690–9.
- [442] Li H, Li Z, Yang J, Ke HB, Sun B, Yuan CC, et al. Interface design enabled manufacture of giant metallic glasses. *Sci China Mater* 2021;64:964–72.
- [443] Lin H, Yang J, Zhao H, Gou J, Zhang Y, Fu J, et al. Fabrication of magnetostrictive composites using metallic glass as glue. *Intermetallics* 2022;145:107561.
- [444] Chen D, Fu J, Huang S, Huang J, Yang J, Ren S, et al. Design of la-based MG-ta composite with high and tailorable properties for solid ta electrolytic capacitor. *Mater Des* 2024;238:112743.
- [445] Li B, Li ZY, Xiong JG, Xing L, Wang D, Li Y. Laser welding of Zr45Cu48Al7 bulk glassy alloy. *J Alloy Compd* 2006;413:118–21.
- [446] Kawahito Y, Terajima T, Kimura H, Kuroda T, Nakata K, Katayama S, et al. High-power fiber laser welding and its application to metallic glass Zr55Al10Ni5Cu30. *Mater Sci Eng B* 2008;148:105–9.
- [447] Li JF, Sun YH, Ding DW, Wang WH, Bai HY. Nanosecond-pulsed laser welding of metallic glass. *J Non Cryst Solids* 2020;537:120016.
- [448] Wang H-S, Li T-H, Chen H-G, Pan J-H, Jang J-S-C. Microstructural evolution and properties of laser spot-welded ZrAlCoTa bulk metallic glass under various initial welding temperatures. *Intermetallics* 2019;108:39–44.
- [449] Shen Y, Li Y, Tsai H-L. Effect of pre-existing nuclei on crystallization during laser welding of zr-based metallic glass. *J Non Cryst Solids* 2019;513:55–63.
- [450] Kim JH, Lee C, Lee DM, Sun JH, Shin SY, Bae JC. Pulsed nd:YAG laser welding of Cu54Ni6Zr22Ti18 bulk metallic glass. *Mater Sci Eng A* 2007;449–451:872–5.
- [451] Shao L, Datye A, Huang J, Ketkaew J, Woo Sohn S, Zhao S, et al. Pulsed laser beam welding of Pd43Cu27Ni10P20 bulk metallic glass. *Sci Rep* 2017;7:7989.
- [452] Wang G, Huang YJ, Shagiev M, Shen J. Laser welding of Ti40Zr25Ni3Cu12Be20 bulk metallic glass. *Mater Sci Eng A* 2012;541:33–7.
- [453] Chen M, Wei D, Li C, Liu L, Zhou Q, Wu F. Influence of laser pulse on solidification of molten pool during laser welding of dissimilar ti-based amorphous alloys. *Sci Technol Weld Join* 2021;26:264–72.
- [454] Chen B, Shi T, Liao G. Laser welding of Zr41Ti14Cu12Ni10Be23 bulk metallic glass and zirconium metal. *Journal of Wuhan University of Technology-Mater Sci Ed* 2014;29:786–8.
- [455] Wang H-S, Chiou M-S, Chen H-G, Jang J-S-C, Gu J-W. Microstructure evolution of the laser spot welded ni-free zr-based bulk metallic glass composites. *Intermetallics* 2012;29:92–8.
- [456] Chen M, Lin S, Xin L, Zhou Q, Li C, Liu L, et al. Microstructures of the pulsed laser welded TiZrBeCuMo composite amorphous alloy joint. *Opt Lasers Eng* 2020;134:106262.
- [457] Wang H-S, Chen H-G, Jang J-S-C, Lin D-Y, Gu J-W. Interfacial analysis of the ex-situ reinforced phase of a laser spot welded zr-based bulk metallic glass composite. *Mater Charact* 2013;86:242–9.
- [458] Wang H-S, Wu J-Y, Liu Y-T. Effect of the volume fraction of the ex-situ reinforced ta additions on the microstructure and properties of laser-welded zr-based bulk metallic glass composites. *Intermetallics* 2016;68:87–94.
- [459] Wang HS, Chen HG, Jang JSC, Chiou MS. Combination of a nd:YAG laser and a liquid cooling device to (Zr53Cu30Ni9Al8)Si0.5 bulk metallic glass welding. *Mater Sci Eng A* 2010;528:338–41.
- [460] Wang H-S, Su Y-Z, Shian-Ching Jang J, Chen H-G. A comparison of crystallization behaviors of laser spot welded Zr–Cu–Ag–Al and Zr–Cu–Ni–Al bulk metallic glasses. *Mater Chem Phys* 2013;139:215–9.
- [461] Wang H-S, Chiou M-S, Chen H-G, Jang J-S-C. The effects of initial welding temperature and welding parameters on the crystallization behaviors of laser spot welded zr-based bulk metallic glass. *Mater Chem Phys* 2011;129:547–52.
- [462] Chen B, Shi TL, Li M, Yang F, Yan F, Liao GL. Laser welding of annealed Zr55Cu30Ni5Al10 bulk metallic glass. *Intermetallics* 2014;46:111–7.
- [463] Liquidmetal® Design Guide 5.0 ,(Liquidmetal Technologies, 2021). Available at: [https://liquidmetal.com/wp-content/uploads/2021/05/LQM\\_DesignGuide.pdf](https://liquidmetal.com/wp-content/uploads/2021/05/LQM_DesignGuide.pdf). 2021.
- [464] Wang G, Huang Y, Cao W, Huang Z, Huttula M, Su Y, et al. Microstructure and crystallization mechanism of ti-based bulk metallic glass by electron beam welding. *J Manuf Process* 2018;32:93–9.
- [465] Kim J, Kawamura Y. Electron beam welding of zr-based BMG/Ni joints: effect of beam irradiation position on mechanical and microstructural properties. *J Mater Process Technol* 2008;207:112–7.
- [466] Kim J, Kawamura Y. Dissimilar welding of Zr41Be23Ti14Cu12Ni10 bulk metallic glass and stainless steel. *Scr Mater* 2011;65:1033–6.
- [467] Kagao S, Kawamura Y, Ohno Y. Electron-beam welding of zr-based bulk metallic glasses. *Mater Sci Eng A* 2004;375–377:312–6.
- [468] Kawamura Y, Kagao S, Ohno Y. Electron beam welding of zr-based bulk metallic glass to crystalline zr metal. *Mater Trans* 2001;42:2649–51.
- [469] Kawamura Y, Ohno Y. Successful electron-beam welding of bulk metallic glass. *Mater Trans* 2001;42:2476–8.
- [470] Kim J, Kawamura Y. Electron beam welding of the dissimilar zr-based bulk metallic glass and ti metal. *Scr Mater* 2007;56:709–12.
- [471] Tariq NH, Shakil M, Hasan BA, Akhter JI, Haq MA, Awan NA. Electron beam brazing of Zr62Al13Ni7Cu18 bulk metallic glass with ti metal. *Vacuum* 2014;101:98–101.
- [472] Swiston AJ, Hufnagel TC, Weihs TP. Joining bulk metallic glass using reactive multilayer foils. *Scr Mater* 2003;48:1575–80.
- [473] Swiston AJ, Besnoin E, Duckham A, Knio OM, Weihs TP, Hufnagel TC. Thermal and microstructural effects of welding metallic glasses by self-propagating reactions in multilayer foils. *Acta Mater* 2005;53:3713–9.
- [474] Trenkle JC, Weihs TP, Hufnagel TC. Fracture toughness of bulk metallic glass welds made using nanostructured reactive multilayer foils. *Scr Mater* 2008;58:315–8.
- [475] Maalekian M. Friction welding – critical assessment of literature. *Sci Technol Weld Join* 2007;12:738–59.
- [476] Uday MB, Ahmad Fauzi MN, Zuhailawati H, Ismail AB. Advances in friction welding process: a review. *Sci Technol Weld Join* 2010;15:534–58.
- [477] Kawamura Y, Ohno Y. Superplastic bonding of bulk metallic glasses using friction. *Scr Mater* 2001;45:279–85.
- [478] Inoue A, Zhang T. Fabrication of bulk glassy Zr55Al10Ni5Cu30 alloy of 30 mm in diameter by a suction casting method. *Mater Trans JIM* 1996;37:185–7.
- [479] Kawamura Y, Ohno Y. Metallurgical bonding of bulk metallic glasses. *Mater Trans* 2001;42:717–9.
- [480] Shin H-S, Jeong Y-J, Choi H-Y, Kato H, Inoue A. Joining of zr-based bulk metallic glasses using the friction welding method. *J Alloy Compd* 2007;434–435:102–5.
- [481] Wong CH, Shek CH. Friction welding of Zr41Ti14Cu12.5Ni10Be22.5 bulk metallic glass. *Scr Mater* 2003;49:393–7.
- [482] Shin H-S, Jeong Y-J, Choi H-Y, Kato H, Inoue A. Friction welding of Zr55Al10Ni5Cu30 bulk metallic glasses. *Mater Trans* 2005;46:2768–72.
- [483] Shoji T, Kawamura Y, Ohno Y. Friction welding of bulk metallic glasses to different ones. *Mater Sci Eng A* 2004;375–377:394–8.
- [484] Kawamura Y, Shoji T, Ohno Y. Welding technologies of bulk metallic glasses. *J Non Cryst Solids* 2003;317:152–7.
- [485] Wang G, Huang YJ, Makhanlall D, Shen J. Friction joining of Ti40Zr25Ni3Cu12Be20 bulk metallic glass. *J Mater Process Technol* 2012;212:1850–5.
- [486] Arora HS, Grewal HS, Mridha S, Singh H, Mukherjee S. Structural changes in amorphous metals from high-strain plastic deformation. *Mater Sci Eng A* 2014;617:175–8.
- [487] Sun Y, Ji Y, Fujii H, Nakata K, Nogi K. Microstructure and mechanical properties of friction stir welded joint of Zr55Cu30Al10Ni5 bulk metallic glass with pure copper. *Mater Sci Eng A* 2010;527:3427–32.

- [488] Sun YF, Fujii H. Microstructure and mechanical properties of dissimilar spot friction stir welded Zr55Cu30Al10Ni5 bulk metallic glass to pure copper. *Intermetallics* 2013;33:113–9.
- [489] Shin H-S, Jung Y-C. Characteristics of dissimilar friction stir spot welding of bulk metallic glass to lightweight crystalline metals. *Intermetallics* 2010;18:2000–4.
- [490] Ji YS, Fujii H, Sun Y, Maeda M, Nakata K, Kimura H, et al. Friction stir welding of Zr55Cu30Ni5Al10 bulk metallic glass. *Mater Trans* 2009;50:1300–3.
- [491] Hirano S, Park SHC. Friction stir welding of metallic glass. *Weld Int* 2011;25:497–500.
- [492] Ma X, Howard SM, Jasthi BK. Friction stir welding of bulk metallic glass Vitreloy 106a. *J Manuf Sci Eng* 2014;136(5):7.
- [493] Wang D, Xiao BL, Ma ZY, Zhang HF. Friction stir welding of Zr55Cu30Al10Ni5 bulk metallic glass to Al–Zn–Mg–Cu alloy. *Scr Mater* 2009;60:112–5.
- [494] Li FP, Zhang DC, Luo ZC, Tan CG, Lin JG. Microstructure and mechanical properties of friction stir welded joint of Zr46Cu46Al8 bulk metallic glass with pure aluminum. *Mater Sci Eng A* 2013;588:196–200.
- [495] Jamili-Shirvan Z, Haddad-Sabzevar M, Vahdati-Khaki J, Yao K-F. Mechanical and thermal properties of identified zones at a ti-based bulk metallic glass weld spot jointed by friction stir spot welding (FSSW). *J Non Cryst Solids* 2020;544:120188.
- [496] Shin H-S, Jung Y-C. Characteristics of friction stir spot welding of zr-based bulk metallic glass sheets. *J Alloy Compd* 2010;504:S279–82.
- [497] Hill A, Wallach ER. Modelling solid-state diffusion bonding. *Acta Metall* 1989;37:2425–37.
- [498] Hongchao K, Heng G, Jun W, Bin T, Jinshan L. Diffusion bonding between zr-based metallic glass and copper. *Rare Metal Mater Eng* 2016;45:42–5.
- [499] Somekawa H, Inoue A, Higashi K. Superplastic and diffusion bonding behavior on Zr–Al–Ni–Cu metallic glass in supercooled liquid region. *Scr Mater* 2004;50:1395–9.
- [500] Wang JG, Fan JC, Zhang YF, Wang G, Wang WH, Chan KC. Diffusion bonding of a zr-based metallic glass in its supercooled liquid region. *Intermetallics* 2014;46:236–42.
- [501] Kuo P-H, Wang S-H, Liaw PK, Fan G-J, Tsang H-T, Qiao D, et al. Bulk-metallic glasses joining in a supercooled-liquid region. *Mater Chem Phys* 2010;120:532–6.
- [502] Kim J, Lee T. Brazing method to join a novel Cu54Ni6Zr22Ti18 bulk metallic glass to carbon steel. *Sci Technol Weld Join* 2017;22:714–8.
- [503] Chen HY, Cao J, Song XG, Feng JC. Contributions of atomic diffusion and plastic deformation to the plasma surface activation assisted diffusion bonding of zirconium-based bulk metallic glass. *Appl Phys Lett* 2012;100.
- [504] Lin JG, Wang XF, Wen C. Theoretical study on behaviour of superplastic forming/diffusion bonding of bulk metallic glasses. *Mater Sci Technol* 2010;26:361–6.
- [505] Chen W, Liu Z, Schroers J. Joining of bulk metallic glasses in air. *Acta Mater* 2014;62:49–57.
- [506] Peng Q, Xie Y, Zhu B, Chen W, Schroers J, Chen M, et al. Joining mechanism of bulk metallic glasses in their supercooled liquid region. *J Mater Process Technol* 2020;279:116583.
- [507] Li T, Zheng G. Atomistic simulation on the mechanical properties of diffusion bonded zr-cu metallic glasses with oxidized interfaces. *Metall and Mat Trans A* 2021;52:1939–46.
- [508] Pilling J, Ridley N, Islam MF. On the modelling of diffusion bonding in materials: superplastic super Alpha-2. *Mater Sci Eng A* 1996;205:72–8.
- [509] Xu W, Li W, Chen S, Wang X, Li F. Superplastic diffusion bonding of metallic glasses by rapid heating. *Intermetallics* 2018;98:143–7.
- [510] Saadati A, Malekan M, Khodabakhshi F. Under glass transition temperature diffusion bonding of bulk metallic glass and aluminum. *Mater Chem Phys* 2021;269:124758.
- [511] Saadati A, Malekan M, Khodabakhshi F, Wilde G, Gerlich AP. Dissimilar diffusion bonding of bulk metallic glass: amorphous/crystalline atomic-scale interaction. *Mater Charact* 2023;195:112480.
- [512] Cao J, Chen HY, Song XG, Liu JK, Feng JC. Effects of ar ion irradiation on the diffusion bonding joints of Zr55Cu30Ni5Al10 bulk metallic glass to aluminum alloy. *J Non Cryst Solids* 2013;364:53–6.
- [513] Chen H, Cao J, Song X, Liu J, Feng J. Characterization, removal and evaluation of oxide film in the diffusion bonding of Zr55Cu30Ni5Al10 bulk metallic glass. *J Mater Sci Technol* 2014;30:722–30.
- [514] Chen HY, Cao J, Song XG, Si GD, Feng JC. Pre-friction diffusion hybrid bonding of Zr55Cu30Ni5Al10 bulk metallic glass. *Intermetallics* 2013;32:30–4.
- [515] Chen HY, Cao J, Song XG, Shi YL, Feng JC. Effect of pre-friction surface treatment on the pre-friction assisted diffusion bonding of Zr55Cu30Ni5Al10 bulk metallic glass to aluminum alloy. *Mater Lett* 2012;74:125–7.
- [516] Liao C, Liu M, Zhang Q, Dong W, Zhao R, Li B, et al. Low-temperature thermoplastic welding of metallic glass ribbons for in-space manufacturing. *Sci China Mater* 2021;64:979–86.
- [517] Zhou Y, Zhang Q, He G, Guo J. Connection of bulk amorphous alloy Zr55Al10Ni5Cu30 by high current density electropulsing. *Mater Lett* 2003;57:2208–11.
- [518] Fujiwara K, Fukumoto S, Yokoyama Y, Nishijima M, Yamamoto A. Weldability of Zr50Cu30Al10Ni10 bulk glassy alloy by small-scale resistance spot welding. *Mater Sci Eng A* 2008;498:302–7.
- [519] Yiu P, Jang JSC, Chang SY, Chen YC, Chu JP, Hsueh CH. Plasticity enhancement of zr-based bulk metallic glasses by direct current electropulsing. *J Alloy Compd* 2012;525:68–72.
- [520] Yang Y, Kong J, Dong K, Liu X, Wang Q, Song X, et al. A novel bulk metallic glass joining mechanism based on electro pulsive technology. *Intermetallics* 2022;144:107520.
- [521] Makhanlall D, Wang G, Huang YJ, Liu DF, Shen J. Joining of ti-based bulk metallic glasses using resistance spot welding technology. *J Mater Process Technol* 2012;212:1790–5.
- [522] Yang Y, Kong J, Dong K, Wang Q, Feng S, Liang Y, et al. Joining of dissimilar bulk metallic glasses with non-common supercooled liquid regions. *Mater Sci Eng A* 2023;864:144608.
- [523] Guo SF, Chan KC, Zhu ZQ, Wu ZR, Chen W, Song M. Microstructure and tensile behavior of small scale resistance spot welded sandwich bulk metallic glasses. *J Non Cryst Solids* 2016;447:300–6.
- [524] Lasocka M. The effect of scanning rate on glass transition temperature of splat-cooled Te85Ge15. *Mater Sci Eng* 1976;23:173–7.
- [525] Handbook ASM. *Welding, Brazing and Soldering Materials Park, Vol. 6.* OH: ASM International; 1993.
- [526] Li B, Zhu G, Liu J, Zhao S, Wang B, Wei P, et al. Electric pulse 3D printing of metallic glass ribbons. *Mater Lett* 2022;316:131965.
- [527] Kawamura Y, Ohno Y. Spark welding of Zr55Al10Ni5Cu30 bulk metallic glasses. *Scr Mater* 2001;45:127–32.
- [528] Watanabe M, Kumai S, Hagimoto G, Zhang Q, Nakayama K. Interfacial microstructure of aluminum/metallic glass lap joints fabricated by magnetic pulse welding. *Mater Trans* 2009;50:1279–85.
- [529] Watanabe M, Kumai S, Kimura H. Microstructural Characterization of intermediate layer produced at aluminum/metallic glass interface fabricated by magnetic pulse welding. *Mater Trans* 2012;53:951–8.
- [530] Wang D, Li N, Liu L. Magnetic pulse welding of a zr-based bulk metallic glass with aluminum plate. *Intermetallics* 2018;93:180–5.
- [531] Liang H, Luo N, Li X, Sun X, Shen T, Ma Z. Joining of Zr60Ti17Cu12Ni11 bulk metallic glass and aluminum 1060 by underwater explosive welding method. *J Manuf Process* 2019;45:115–22.
- [532] Liu WD, Liu KX, Chen QY, Wang JT, Yan HH, Li XJ. Metallic glass coating on metals plate by adjusted explosive welding technique. *Appl Surf Sci* 2009;255:9343–7.
- [533] Lazurenko DV, Ivannikov AA, Anisimov AG, Popov NS, Dovzhenko GD, Bataev IA, et al. Joining ti-based metallic glass and crystalline titanium by magnetic pulse welding. *J Non Cryst Solids* 2022;597:121912.
- [534] Findik F. Recent developments in explosive welding. *Mater Des* 2011;32:1081–93.
- [535] Liu KX, Liu WD, Wang JT, Yan HH, Li XJ, Huang YJ, et al. Atomic-scale bonding of bulk metallic glass to crystalline aluminum. *Appl Phys Lett* 2008;93.
- [536] Liang H, Luo N, Shen T, Sun X, Fan X, Cao Y. Experimental and numerical simulation study of zr-based BMG/Al composites manufactured by underwater explosive welding. *J Mater Res Technol* 2020;9:1539–48.
- [537] Chiba A, Kawamura Y, Nishida M. Explosive welding of ZrTiCuNiBe bulk metallic glass to crystalline metallic plates. *Mater Sci Forum* 2008;566:119–24.

- [538] Hokamoto K, Nakata K, Mori A, Tsuda S, Tsumura T, Inoue A. Dissimilar material welding of rapidly solidified foil and stainless steel plate using underwater explosive welding technique. *J Alloy Compd* 2009;472:507–11.
- [539] Jiang MQ, Huang BM, Jiang ZJ, Lu C, Dai LH. Joining of bulk metallic glass to brass by thick-walled cylinder explosion. *Scr Mater* 2015;97:17–20.
- [540] Feng J, Chen P, Zhou K. Investigation on explosive welding of Zr53Cu35Al12 bulk metallic glass with crystalline copper. *J of Materi Eng and Perform* 2018;27:2932–7.
- [541] Kreye H, Hammerschmidt M, Reiners GJSM. Ultrasonic welding of metallic alloy glass to copper 1978;12:1059–61.
- [542] Becker M, Kuball A, Ghavimi A, Adam B, Busch R, Gallino I, et al. Solid State Joining of a Cold Rolled Zr-Based Bulk Metallic Glass to a Wrought Aluminum Alloy by Power Ultrasonics 2022;15:7673.
- [543] Maeda M, Takahashi Y, Fukuhara M, Wang X, Inoue AJMS, B e.. Ultrasonic bonding of Zr55Cu30Ni5Al10 metallic glass 2008;148:141–4.
- [544] Li X, Liang X, Zhang Z, Ma J, Shen J. Cold joining to fabricate large size metallic glasses by the ultrasonic vibrations. *Scr Mater* 2020;185:100–4.
- [545] Neppiras E. Ultrasonic welding of metals. *Ultrasonics* 1965;3:128–35.
- [546] Tsujino J. Recent developments of ultrasonic welding. In: 1995 IEEE Ultrasonics Symposium Proceedings An International Symposium: IEEE; 1995. p. 1051–60.
- [547] Becker M, Kuball A, Ghavimi A, Adam B, Busch R, Gallino I, et al. Solid state joining of a cold rolled zr-based bulk metallic glass to a wrought aluminum alloy by power ultrasonics. *Materials* 2022.
- [548] Zhang X, Li D, Wang L, Wan C, Song L, Song K, et al. Ultrasonic brazing of zr-based bulk metallic glass and 1060 al alloy using zn-3Al filler metal. *Journal of Advanced Joining Processes* 2022;5:100095.
- [549] Ji H, Li L, Li M. Low-temperature joining of fe-based amorphous foil with aluminum by ultrasonic-assisted soldering with sn-based fillers. *Mater Des* 2015;84:254–60.
- [550] Zhao X, Pan J, Zhao M. Soldering zr metallic glass to ti alloy using pre-cladding ultrasonic processes. *Welding in the World* 2021;65:1225–34.
- [551] Matheny M, Graff K. Ultrasonic welding of metals. *Power ultrasonics*: Elsevier; 2015. p. 259–93.
- [552] Huang Z, Fu J, Li X, Wen W, Lin H, Lou Y, et al. Ultrasonic-assisted rapid cold welding of bulk metallic glasses 2021;65:255–62.
- [553] Li L, Li X, Huang Z, Huang J, Liu Z, Fu J, et al. Joining of metallic glasses in liquid via ultrasonic vibrations. *Nat Commun* 2023;14:6305.
- [554] Ma J, Yang C, Liu X, Shang B, He Q, Li F, et al. Fast surface dynamics enabled cold joining of metallic glasses. *science*. *Advances* 2019;5:eaa7256..
- [555] Lowhaphandu P, Lewandowski JJSM. Fracture toughness and notched toughness of bulk amorphous alloy: Zr-Ti-Ni-Cu-Be 1998;38:1811–7.
- [556] Harding D, Oliver W, Pharr G. Cracking during nanoindentation and its use in the measurement of fracture toughness 1994;356:663.
- [557] Xi X, Zhao D, Pan M, Wang W, Wu Y. Lewandowski JJPrI. Fracture of brittle metallic glasses: Brittleness or plasticity 2005;94:125510.
- [558] Vivek A, Presley M, Flores KM, Hutchinson NH, Daehn GS. Solid state impact welding of BMG and copper by vaporizing foil actuator welding. *Mater Sci Eng A* 2015;634:14–9.
- [559] Wen C, Shi T, Chen B, Zhu Z, Peng Y, Liao G. Diffusion bonding of Zr55Cu30Ni5Al10 bulk metallic glass to cu with al as transition layer. *Mater Des* 2015;83:320–6.
- [560] Astm. Standard terminology for additive manufacturing technologies: designation F2792–12A. West Conshohocken, PA: ASTM International; 2012.
- [561] DebRoy T, Wei HL, Zuback JS, Mukherjee T, Elmer JW, Milewski JO, et al. Additive manufacturing of metallic components – process, structure and properties. *Prog Mater Sci* 2018;92:112–224.
- [562] Svetlizky D, Zheng B, Vyatskikh A, Das M, Bose S, Bandyopadhyay A, et al. Laser-based directed energy deposition (DED-LB) of advanced materials. *Mater Sci Eng A* 2022;840:142967.
- [563] Pauly S, Löber L, Petters R, Stoica M, Scudino S, Kühn U, et al. Processing metallic glasses by selective laser melting. *Mater Today* 2013;16:37–41.
- [564] Chen C, Shen Y, Tsai H-L. A foil-based additive Manufacturing technology for metal parts. *J Manuf Sci Eng* 2016;139.
- [565] Shen Y, Li Y, Chen C, Tsai H-L. 3D printing of large, complex metallic glass structures. *Mater Des* 2017;117:213–22.
- [566] Gorodesky N, Sedghani-Cohen S, Altman M, Fogel O, Cohen-Taguri G, Flegler Y, et al. Concurrent formation of metallic glass during laser Forward transfer 3D printing. *Adv Funct Mater* 2020;30:2001260.
- [567] Kosiba K, Kononenko DY, Chernyavsky D, Deng L, Bednarcik J, Han J, et al. Maximizing vitrification and density of a zr-based glass-forming alloy processed by laser powder bed fusion. *J Alloy Compd* 2023;940:168946.
- [568] Mahbooba Z, Thorsson L, Unosson M, Skoglund P, West H, Horn T, et al. Additive manufacturing of an iron-based bulk metallic glass larger than the critical casting thickness. *Appl Mater Today* 2018;11:264–9.
- [569] Bordeenithikasem P, Stolpe M, Elsen A, Hofmann DC. Glass forming ability, flexural strength, and wear properties of additively manufactured zr-based bulk metallic glasses produced through laser powder bed fusion. *Addit Manuf* 2018;21:312–7.
- [570] Deng L, Gebert A, Zhang L, Chen HY, Gu DD, Kühn U, et al. Mechanical performance and corrosion behaviour of zr-based bulk metallic glass produced by selective laser melting. *Mater Des* 2020;189:108532.
- [571] Li XP, Roberts MP, O'Keefe S, Sercombe TB. Selective laser melting of zr-based bulk metallic glasses: processing, microstructure and mechanical properties. *Mater Des* 2016;112:217–26.
- [572] Deng L, Kosiba K, Limbach R, Wondraczek L, Kühn U, Pauly S. Plastic deformation of a zr-based bulk metallic glass fabricated by selective laser melting. *J Mater Sci Technol* 2021;60:139–46.
- [573] Zhang P, Zhang C, Liu L. Toughening 3D-printed zr-based bulk metallic glass via synergistic defects engineering. *Materials Research Letters* 2022;10:377–84.
- [574] Pauly S, Schrickler C, Scudino S, Deng L, Kühn U. Processing a glass-forming zr-based alloy by selective laser melting. *Mater Des* 2017;135:133–41.
- [575] Yang Z, Wang H, Krauß S, Huber F, Merle B, Schmidt M, et al. Evolution of an industrial-grade zr-based bulk metallic glass during multiple laser beam melting. *J Non Cryst Solids* 2022;589:121649.
- [576] Sohrabi N, Jhabvala J, Kurtuldu G, Stoica M, Parrilli A, Berns S, et al. Characterization, mechanical properties and dimensional accuracy of a zr-based bulk metallic glass manufactured via laser powder-bed fusion. *Mater Des* 2021;199:109400.
- [577] Li XP, Kang CW, Huang H, Zhang LC, Sercombe TB. Selective laser melting of an Al86Ni6Y4.5Co2La1.5 metallic glass: processing, microstructure evolution and mechanical properties. *Mater Sci Eng A* 2014;606:370–9.
- [578] Li XP, Kang CW, Huang H, Sercombe TB. The role of a low-energy-density re-scan in fabricating crack-free Al85Ni5Y6Co2Fe2 bulk metallic glass composites via selective laser melting. *Mater Des* 2014;63:407–11.
- [579] Ouyang D, Xing W, Li N, Li Y, Liu L. Structural evolutions in 3D-printed fe-based metallic glass fabricated by selective laser melting. *Addit Manuf* 2018;23:246–52.
- [580] Li N, Zhang J, Xing W, Ouyang D, Liu L. 3D printing of fe-based bulk metallic glass composites with combined high strength and fracture toughness. *Mater Des* 2018;143:285–96.
- [581] Jiang Q, Zhang P, Tan J, Yu Z, Tian Y, Ma S, et al. Influence of the microstructure on mechanical properties of SLM additive manufacturing fe-based bulk metallic glasses. *J Alloy Compd* 2022;894:162525.
- [582] Deng L, Wang S, Wang P, Kühn U, Pauly S. Selective laser melting of a ti-based bulk metallic glass. *Mater Lett* 2018;212:346–9.
- [583] Jang J-H, Kim H-G, Kim H-J, Lee D-G. Crystallization and Hardness change of the ti-based bulk metallic glass Manufactured by a laser powder bed fusion process. *Metals* 2021.
- [584] Zheng B, Zhou Y, Smugeresky JE, Lavernia EJ. Processing and behavior of fe-based metallic glass components via laser-engineered net shaping. *Metall and Mat Trans A* 2009;40:1235–45.
- [585] Yang G, Lin X, Liu F, Hu Q, Ma L, Li J, et al. Laser solid forming zr-based bulk metallic glass. *Intermetallics* 2012;22:110–5.
- [586] Lin X, Zhang Y, Yang G, Gao X, Hu Q, Yu J, et al. Microstructure and compressive/tensile characteristic of large size zr-based bulk metallic glass prepared by laser solid forming. *J Mater Sci Technol* 2019;35:328–35.
- [587] Xu H, Lu Y, Liu Z, Wang G. Laser 3D printing of zr-based bulk metallic glass. *J Manuf Process* 2019;39:102–5.
- [588] Lu Y, Huang Y, Wu J. Laser additive manufacturing of structural-graded bulk metallic glass. *J Alloy Compd* 2018.

- [589] Su S, Lu Y. Laser directed energy deposition of zr-based bulk metallic glass composite with tensile strength. *Mater Lett* 2019;247:79–81.
- [590] Lu Y, Su S, Zhang S, Huang Y, Qin Z, Lu X, et al. Controllable additive manufacturing of gradient bulk metallic glass composite with high strength and tensile ductility. *Acta Mater* 2021;206:116632.
- [591] Ma H, Qin D, Lu Y. Laser additive manufacturing of zr-based bulk metallic glass composite improved by TRIP effect. *Mater Lett* 2022;323:132593.
- [592] Yu Z, Zheng W, Li Z, Lu Y, Yun X, Qin Z, et al. Accelerated exploration of TRIP metallic glass composite by laser additive manufacturing. *J Mater Sci Technol* 2021;78:68–73.
- [593] Li Q, Qin D, Lu Y, Zhu X, Lu X. Laser additive manufacturing of ductile fe-based bulk metallic glass composite. *J Mater Sci Technol* 2022;121:148–53.
- [594] Hu W, Yu Z, Lu Y, Huo J, Qin Z, Lu X, et al. Enhanced plasticity in laser additive manufactured nb-reinforced bulk metallic glass composite. *J Alloy Compd* 2022;918:165539.
- [595] Cui X, Hu W, Lu X, Lu Y. Laser additive manufacturing of laminated bulk metallic glass composite with desired strength-ductility combination. *J Mater Sci Technol* 2023;147:68–76.
- [596] Bordeenithikasem P, Shen Y, Tsai H-L, Hofmann DC. Enhanced mechanical properties of additively manufactured bulk metallic glasses produced through laser foil printing from continuous sheetmetal feedstock. *Addit Manuf* 2018;19:95–103.
- [597] Li Y, Shen Y, Chen C, Leu MC, Tsai H-L. Building metallic glass structures on crystalline metal substrates by laser-foil-printing additive manufacturing. *J Mater Process Technol* 2017;248:249–61.
- [598] Li Y, Shen Y, Hung C-H, Leu MC, Tsai H-L. Additive manufacturing of zr-based metallic glass structures on 304 stainless steel substrates via V/Ti/Zr intermediate layers. *Mater Sci Eng A* 2018;729:185–95.
- [599] Ur Rehman Z, Yang F, Wang M, Zhu T. Fundamentals and advances in laser-induced transfer. *Opt Laser Technol* 2023;160:109065.
- [600] Gorodesky N, Sedghani-Cohen S, Fogel O, Silber A, Tkachev M, Kotler Z, et al. Improving compactness of 3D metallic microstructures printed by laser-induced Forward transfer. *Crystals* 2021;11:291.
- [601] Ouyang D, Li N, Liu L. Structural heterogeneity in 3D printed zr-based bulk metallic glass by selective laser melting. *J Alloy Compd* 2018;740:603–9.
- [602] Ouyang D, Li N, Xing W, Zhang J, Liu L. 3D printing of crack-free high strength zr-based bulk metallic glass composite by selective laser melting. *Intermetallics* 2017;90:128–34.
- [603] Chang Z, Ge Y, Sun L, Wang W, Zhou J. The micro-zones formation of zr-based bulk metallic glass composite fabricated by laser 3D printing. *J Manuf Process* 2022;76:167–74.
- [604] Lu Y, Huang Y, Wu J, Lu X, Qin Z, Daisenberger D, et al. Graded structure of laser direct manufacturing bulk metallic glass. *Intermetallics* 2018;103:67–71.
- [605] Yang Z, Markl M, Körner C. Predictive simulation of bulk metallic glass crystallization during laser powder bed fusion. *Addit Manuf* 2022;59:103121.
- [606] Lu Y, Zhang H, Li H, Xu H, Huang G, Qin Z, et al. Crystallization prediction on laser three-dimensional printing of zr-based bulk metallic glass. *J Non Cryst Solids* 2017;461:12–7.
- [607] Sun H, Flores KM. Spherulitic crystallization mechanism of a zr-based bulk metallic glass during laser processing. *Intermetallics* 2013;43:53–9.
- [608] Zhang Y, Lin X, Wang L, Wei L, Liu F, Huang W. Microstructural analysis of Zr55Cu30Al10Ni5 bulk metallic glasses by laser surface remelting and laser solid forming. *Intermetallics* 2015;66:22–30.
- [609] Best JP, Evenson Z, Yang F, Dippel A-C, Stolpe M, Gutowski O, et al. Structural periodicity in laser additive manufactured zr-based bulk metallic glass. *Appl Phys Lett* 2019;115.
- [610] Best JP, Nomoto K, Yang F, Li B, Stolpe M, Zeng L, et al. Advanced structural analysis of a laser additive manufactured zr-based bulk metallic glass along the build height. *J Mater Sci* 2022;57:9678–92.
- [611] Bian P, Shi J, Shao X, Du J. Evolution of cyclic thermal stress in selective laser melting of 316L stainless steel: a realistic numerical study with experimental verification. *Int J Adv Manuf Technol* 2019;104:3867–82.
- [612] Yan QD, Yu J, Lin X, Zhang YF, Chai HZ, Tan H, et al. An unusual solid state amorphization in a TiZr-base bulk metallic glass composite fabricated by laser powder bed fusion. *Mater Sci Eng A* 2023;862:144349.
- [613] Guo S, Wang M, Zhao Z, Zhang YY, Lin X, Huang WD. Molecular dynamics simulation on the micro-structural evolution in heat-affected zone during the preparation of bulk metallic glasses with selective laser melting. *J Alloy Compd* 2017;697:443–9.
- [614] Yang C, Zhang C, Xing W, Liu L. 3D printing of zr-based bulk metallic glasses with complex geometries and enhanced catalytic properties. *Intermetallics* 2018; 94:22–8.
- [615] Luo N, Scheitler C, Ciftci N, Galgon F, Fu Z, Uhlenwinkel V, et al. Preparation of fe-co-B-si-nb bulk metallic glasses by laser powder bed fusion: microstructure and properties. *Mater Charact* 2020;162:110206.
- [616] Marattukalam JJ, Pacheco V, Karlsson D, Riekehr L, Lindwall J, Forsberg F, et al. Development of process parameters for selective laser melting of a zr-based bulk metallic glass. *Addit Manuf* 2020;33:101124.
- [617] Jiang Q, Liu H, Li J, Yang D, Zhang Y, Yang W. Atomic-level understanding of crystallization in the selective laser melting of Fe50Ni50 amorphous alloy. *Addit Manuf* 2020;34:101369.
- [618] Wang WH. Roles of minor additions in formation and properties of bulk metallic glasses. *Prog Mater Sci* 2007;52:540–96.
- [619] Sohrabi S, Gholampour R. Effect of nb minor addition on the crystallization kinetics of zr-cu-al-ni metallic glass. *J Non Cryst Solids* 2021;560:120731.
- [620] Sohrabi S, Ri MC, Jiang HY, Gu L, Wen P, Sun YH, et al. Prominent role of chemical heterogeneity on cryogenic rejuvenation and thermomechanical properties of La–Al–Ni metallic glass. *Intermetallics* 2019;111:106497.
- [621] Sohrabi N, Schawe JEK, Jhabvala J, Löffler JF, Logé RE. Critical crystallization properties of an industrial-grade zr-based metallic glass used in additive manufacturing. *Scr Mater* 2021;199:113861.
- [622] Schawe JEK, Löffler JF. Existence of multiple critical cooling rates which generate different types of monolithic metallic glass. *Nat Commun* 2019;10:1337.
- [623] Vilaro T, Colin C, Bartout JD. As-fabricated and heat-treated microstructures of the ti-6Al-4V alloy processed by selective laser melting. *Metall and Mat Trans A* 2011;42:3190–9.
- [624] Qiu C, Adkins NJE, Attallah MM. Microstructure and tensile properties of selectively laser-melted and of HIPed laser-melted Ti–6Al–4V. *Mater Sci Eng A* 2013; 578:230–9.
- [625] Thijs L, Verhaeghe F, Craeghs T, Humbeeck JV, Kruth J-P. A study of the microstructural evolution during selective laser melting of Ti–6Al–4V. *Acta Mater* 2010;58:3303–12.
- [626] Hojjatzadeh SMH, Parab ND, Yan W, Guo Q, Xiong L, Zhao C, et al. Pore elimination mechanisms during 3D printing of metals. *Nat Commun* 2019;10:3088.
- [627] Kumar P, Ramamurty U. High cycle fatigue in selective laser melted ti-6Al-4V. *Acta Mater* 2020;194:305–20.
- [628] Jung HY, Choi SJ, Prashanth KG, Stoica M, Scudino S, Yi S, et al. Fabrication of fe-based bulk metallic glass by selective laser melting: a parameter study. *Mater Des* 2015;86:703–8.
- [629] Xing W, Ouyang D, Li N, Liu L. Insight into micro-cracking in 3D-printed fe-based BMGs by selective laser melting. *Intermetallics* 2018;103:101–6.
- [630] Xing W, Ouyang D, Chen Z, Liu L. Effect of energy density on defect evolution in 3D printed zr-based metallic glasses by selective laser melting. *Science China Physics, Mechanics & Astronomy* 2019;63:226111.
- [631] Hofmann DC, Bordeenithikasem P, Pate A, Roberts SN, Vogli E. Developing processing Parameters and Characterizing microstructure and properties of an additively Manufactured FeCrMoBC metallic glass forming alloy. *Adv Eng Mater* 2018;20:1800433.
- [632] Szczepański Ł, Bambach M, Jensch F, Ambroziak A, Kurzynowski T. Structural investigations of fe-zr-si-cu metallic glass with low glass-forming ability produced in laser powder bed fusion technology. *Mater Des* 2021;210:110112.
- [633] Frey M, Wegner J, Barreto ES, Ruschel L, Neuber N, Adam B, et al. Laser powder bed fusion of cu-ti-zr-ni bulk metallic glasses in the Vit101 alloy system. *Addit Manuf* 2023;66:103467.
- [634] Zou YM, Wu YS, Li KF, Tan CL, Qiu ZG, Zeng DC. Selective laser melting of crack-free fe-based bulk metallic glass via chessboard scanning strategy. *Mater Lett* 2020;272:127824.

- [635] Soares Barreto E, Frey M, Wegner J, Jose A, Neuber N, Busch R, et al. Properties of gas-atomized cu-ti-based metallic glass powders for additive manufacturing. *Mater Des* 2022;215:110519.
- [636] Zhang C, Li X-m, Liu S-Q, Liu H, Yu L-J, Liu L. 3D printing of zr-based bulk metallic glasses and components for potential biomedical applications. *J Alloy Compd* 2019;790:963–73.
- [637] Lu X, Nursulton M, Du Y, Liao W. Structural and mechanical Characteristics of Cu50Zr43Al7 bulk metallic glass fabricated by selective laser melting. *Materials* 2019;12:775.
- [638] Li Y, Shen Y, Leu MC, Tsai H-L. Mechanical properties of zr-based bulk metallic glass parts fabricated by laser-foil-printing additive manufacturing. *Mater Sci Eng A* 2019;743:404–11.
- [639] Wu M-W, Ni K, Lei Y, Xiong X-X, Chuang Y-T, Lin Q-E, et al. Mechanical behavior of CuZrAl metallic glass scaffolds fabricated by selective laser melting. *Mater Lett* 2023;341:134242.
- [640] Best JP, Ast J, Li B, Stolpe M, Busch R, Yang F, et al. Relating fracture toughness to micro-pillar compression response for a laser powder bed additive manufactured bulk metallic glass. *Mater Sci Eng A* 2020;770:138535.
- [641] Best JP, Ostergaard HE, Li B, Stolpe M, Yang F, Nomoto K, et al. Fracture and fatigue behaviour of a laser additive manufactured zr-based bulk metallic glass. *Addit Manuf* 2020;36:101416.
- [642] Shi J, Ma S, Wei S, Best JP, Stolpe M, Markert B. Connecting structural defects to tensile failure in a 3D-printed fully-amorphous bulk metallic glass. *Mater Sci Eng A* 2021;813:141106.
- [643] Qiao J, Jia H, Liaw PK. Metallic glass matrix composites. *Mater Sci Eng R Rep* 2016;100:1–69.
- [644] Luo N, Huber F, Ciftci N, Wahl L, Bezold A, Neumeier S, et al. Laser powder bed fusion of FeCoBSiNb-cu bulk metallic glass composites: processing, microstructure and mechanical properties. *Mater Sci Eng A* 2022;849:143405.
- [645] Zhang Y, Ma X, Lin X, Xia Z, Su X, Huang W. Tensile behavior of large size Zr-based bulk metallic glass composites prepared by selective laser melting. *Intermetallics* 2023;158:107895.
- [646] Gao X, Lin X, Yang H, Wang Y, Zhang S, Lu J, et al. The effect of al content on Ti/Zr-based bulk metallic glass composite by additive manufacturing. *Mater Sci Eng A* 2022;844:143162.
- [647] Zhang P, Zhang C, Ouyang D, Liu L. Enhancement of plasticity and toughness of 3D printed binary Zr50Cu50 bulk metallic glass composite by deformation-induced martensitic transformation. *Scr Mater* 2021;192:7–12.
- [648] Gao X, Liu Z, Li J, Liu E, Yue C, Zhao K, et al. Selective laser melting of CuZr-based metallic glass composites. *Mater Lett* 2020;259:126724.
- [649] Pauly S, Das J, Bednarcik J, Mattern N, Kim KB, Kim DH, et al. Deformation-induced martensitic transformation in Cu–Zr–(Al, ti) bulk metallic glass composites. *Scr Mater* 2009;60:431–4.
- [650] Gao X, Lin X, Yu J, Li Y, Hu Y, Fan W, et al. Selective laser melting (SLM) of in-situ beta phase reinforced Ti/Zr-based bulk metallic glass matrix composite. *Scr Mater* 2019;171:21–5.
- [651] Gao X, Lin X, Yan Q, Wang Z, Yu X, Zhou Y, et al. Effect of cu content on microstructure and mechanical properties of in-situ  $\beta$  phases reinforced Ti/Zr-based bulk metallic glass matrix composite by selective laser melting (SLM). *J Mater Sci Technol* 2021;67:174–85.
- [652] Zhang P, Ouyang D, Liu L. Enhanced mechanical properties of 3D printed zr-based BMG composite reinforced with ta precipitates. *J Alloy Compd* 2019;803:476–83.
- [653] Wang P, Lei Y, Ma J, Song K, Deng L, Liu Z, et al. Influence of mo micro-particles on crack formation, microstructure, and mechanical behaviour of laser powder bed fusion fabricated CuZrAl bulk metallic glass composites. *Virtual and Physical Prototyping* 2023;18:e2224307.
- [654] Zhang S, Hou P, Mooraj S, Chen W. Printability of Zr41.2Ti13.8Cu12.5Ni10.0Be22.5 metallic glass on steel by laser additive manufacturing: a single-track study. *Surf Coat Technol* 2021;428:127882.
- [655] Hehr A, Norfolk M. A comprehensive review of ultrasonic additive manufacturing. *Rapid Prototyp J* 2020;26:445–58.
- [656] Wu W, Jiang J, Li G, Fuh JYH, Jiang H, Gou P, et al. Ultrasonic additive manufacturing of bulk ni-based metallic glass. *J Non Cryst Solids* 2019;506:1–5.
- [657] Song XC, Zhu ZQ, Chen YF. Ultrasonic welding of Fe78Si9B13 metallic glass. *Mater Sci Forum* 2015;809–810:348–53.
- [658] Li G, Zhao J, Fuh JY, Wu W, Jiang J, Wang T, et al. Experiments on the ultrasonic bonding additive Manufacturing of metallic glass and crystalline metal composite. *Materials* 2019:12.
- [659] Wang Y, Yang Q, Liu X, Liu Y, Liu B, Misra RDK, et al. Microstructure and mechanical properties of amorphous strip/aluminum laminated composites fabricated by ultrasonic additive consolidation. *Mater Sci Eng A* 2019;749:74–8.
- [660] Liang X, Zhu X, Li X, Mo R, Liu Y, Wu K, et al. High-entropy alloy and amorphous alloy composites fabricated by ultrasonic vibrations. *Science China Physics, Mechanics & Astronomy* 2020;63:116111.
- [661] Liang X, Wu K, Fu J, Li L, Fan C, Wen W, et al. Fabrication of amorphous and high-entropy biphasic composites using high-frequency ultrasonic vibration. *J Non Cryst Solids* 2022;582:121458.
- [662] Gibson MA, Mykulowycz NM, Shim J, Fontana R, Schmitt P, Roberts A, et al. 3D printing metals like thermoplastics: fused filament fabrication of metallic glasses. *Mater Today* 2018;21:697–702.
- [663] Singh S, Singh G, Prakash C, Ramakrishna S. Current status and future directions of fused filament fabrication. *J Manuf Process* 2020;55:288–306.
- [664] Zhang C, Guo RQ, Yang Y, Wu Y, Liu L. Influence of the size of spraying powders on the microstructure and corrosion resistance of fe-based amorphous coating. *Electrochim Acta* 2011;56:6380–8.
- [665] Wang G, Huang Z, Xiao P, Zhu X. Spraying of fe-based amorphous coating with high corrosion resistance by HVAF. *J Manuf Process* 2016;22:34–8.
- [666] Kobayashi A, Kuroda T, Kimura H, Inoue A. Effect of spraying condition on property of zr-based metallic glass coating by gas tunnel type plasma spraying. *Mater Sci Eng B* 2010;173:122–5.
- [667] Guo W, Zhang J, Wu Y, Hong S, Qin Y. Fabrication and characterization of fe-based amorphous coatings prepared by high-velocity arc spraying. *Mater Des* 2015;78:118–24.
- [668] Joshi SS, Katakam S, Singh Arora H, Mukherjee S, Dahotre NB. Amorphous coatings and Surfaces on structural materials. *Crit Rev Solid State Mater Sci* 2016;41:1–46.
- [669] Zhang C, Wang W, Li Y-C, Yang Y-G, Wu Y, Liu L. 3D printing of fe-based bulk metallic glasses and composites with large dimensions and enhanced toughness by thermal spraying. *J Mater Chem A* 2018;6:6800–5.
- [670] Zhang C, Wang W, Xing W, Liu L. Understanding on toughening mechanism of bioinspired bulk metallic glassy composites by thermal spray additive manufacturing. *Scr Mater* 2020;177:112–7.
- [671] Concustell A, Henao J, Dosta S, Cinca N, Cano IG, Guilemany JM. On the formation of metallic glass coatings by means of cold gas spray technology. *J Alloy Compd* 2015;651:764–72.
- [672] Henao J, Concustell A, Dosta S, Bolelli G, Cano IG, Lusvarghi L, et al. Deposition mechanisms of metallic glass particles by cold gas spraying. *Acta Mater* 2017;125:327–39.
- [673] Yoon S, Lee C, Choi H, Jo H. Kinetic spraying deposition behavior of bulk amorphous NiTiZrSiSn feedstock. *Mater Sci Eng A* 2006;415:45–52.
- [674] Kang N, Coddet P, Liao H, Coddet C. The effect of heat treatment on microstructure and tensile properties of cold spray zr base metal glass/Cu composite. *Surf Coat Technol* 2015;280:64–71.
- [675] Yin S, Cavaliere P, Aldwell B, Jenkins R, Liao H, Li W, et al. Cold spray additive manufacturing and repair: fundamentals and applications. *Addit Manuf* 2018;21:628–50.
- [676] Fan N, Huang C, Wang Z, Yu P, Chen W, Lupoi R, et al. Interparticle bonding and interfacial nanocrystallization mechanisms in additively manufactured bulk metallic glass fabricated by cold spray. *Addit Manuf* 2022;58:103057.
- [677] List A, Gärtner F, Mori T, Schulze M, Assadi H, Kuroda S, et al. Cold spraying of amorphous Cu50Zr50 alloys. *J Therm Spray Technol* 2015;24:108–18.
- [678] Gong X, Anderson TL, Chou K. Review on powder-based electron beam additive manufacturing technology. 2012.
- [679] Körner C. Additive manufacturing of metallic components by selective electron beam melting — a review. *Int Mater Rev* 2016;61:361–77.

- [680] Tariq NH, Iqbal M, Shaikh MA, Akhter JI, Ahmad M, Ali G, et al. Evolution of microstructure and non-equilibrium phases in electron beam treated Zr55Cu30Al10Ni5 bulk amorphous alloy. *J Alloy Compd* 2008;460:258–62.
- [681] Drescher P, Seitz H. Processability of an amorphous metal alloy powder by electron beam melting. *RTEJournal - Fachforum für Rapid Technologie*. 2015.
- [682] Saadi MASR, Maguire A, Pottackal NT, Thakur MSH, Ikram MM, Hart AJ, et al. Direct ink writing: a 3D printing Technology for Diverse Materials. *Adv Mater* 2022;34:2108855.
- [683] Lewis JA. Direct ink writing of 3D functional materials. *Adv Funct Mater* 2006;16:2193–204.
- [684] Duoss E. Direct Ink Writing of Bulk Metallic Glasses (Annual Report in LLNL). Available at: <https://lrd-annual.llnl.gov/archives/lrd-annual-2017/materials/17-FS-005>. 2017.
- [685] Wu W, Du H, Sui H, Sun B, Wang B, Yu Z, et al. Study of printing parameters of pneumatic-injection 3D printing of fe-based metallic glass. *J Non Cryst Solids* 2018;489:50–6.
- [686] Wang N, Chang S, Li G, Dheen ST, Kumar AS, Wu W, et al. Effects of Various processing Parameters on mechanical properties and biocompatibility of fe-based bulk metallic glass processed via selective laser melting at constant energy density. *Chinese Journal of Mechanical Engineering: Additive Manufacturing Frontiers* 2022;1:100038.
- [687] Zhang L-C, Jia Z, Lyu F, Liang S-X, Lu J. A review of catalytic performance of metallic glasses in wastewater treatment: recent progress and prospects. *Prog Mater Sci* 2019;105:100576.
- [688] Larsson L, Marattukalam JJ, Paschalidou E-M, Hjörvarsson B, Ferraz N, Persson C. Biocompatibility of a zr-based metallic glass enabled by additive Manufacturing. *ACS Applied Bio Materials* 2022;5:5741–53.
- [689] Yang C, Zhang C, Chen Z-J, Li Y, Yan W-Y, Yu H-B, et al. Three-dimensional Hierarchical porous structures of metallic glass/copper composite catalysts by 3D printing for efficient wastewater treatments. *ACS Appl Mater Interfaces* 2021;13:7227–37.
- [690] Yang C, Zhang C, Liu L. Excellent degradation performance of 3D hierarchical nanoporous structures of copper towards organic pollutants. *J Mater Chem A* 2018;6:20992–1002.
- [691] Zou Y, Qiu Z, Zheng Z, Wang G, Yan X, Yin S, et al. Ex-situ additively manufactured FeCrMoCB/Cu bulk metallic glass composite with well wear resistance. *Tribol Int* 2021;162:107112.
- [692] Hofmann DC, Bordeenithikaseem P, Tosi LP, Hendry M, Yahnker C, Sunday C, et al. Towards additively manufacturing excavating tools for future robotic space exploration. *Engineering Reports* 2020;2:e12219.
- [693] Jannesari LL. Applications of artificial intelligence and machine learning in metal additive manufacturing. *Journal of Physics: Materials* 2021;4:042009.
- [694] Chernyavsky D, Kononenko DY, Han JH, Kim HJ, van den Brink J, Kosiba K. Machine learning for additive manufacturing: predicting materials characteristics and their uncertainty. *Mater Des* 2023;227:111699.
- [695] Frey M, Wegner J, Neuber N, Reiplinger B, Bochtler B, Adam B, et al. Thermoplastic forming of additively manufactured zr-based bulk metallic glass: a processing route for surface finishing of complex structures. *Mater Res* 2021;198:109368.
- [696] Ouyang D, Zheng Q, Wang L, Wang H, Yang C, Zhang P, et al. The brittleness of post-treatment of 3D printed zr-based metallic glasses in supercooled liquid state. *Mater Sci Eng A* 2020;782:139259.



**Sajad Sohrabi** is an associate researcher at the College of Mechatronics and Control Engineering, Shenzhen University, China. He holds a B. Sc. in materials science and engineering from Shiraz University (2009) and an M.Sc. in the same field from Iran University of Science and Technology (2012). He received his Ph.D. in condensed matter physics from the Institute of Physics, Chinese Academy of Sciences, in 2019, under the CAS-TWAS Presidential fellowship. He has published 20+ papers including *Appl Phys Lett*, *Intermetallics*, and *J Alloys Compd*. His current research focuses on advanced manufacturing and physical metallurgy of metallic glasses. ORCID iD: 0000-0003-0400-9988.



**Jianan Fu** received his B.S. degree from Jiangxi Agricultural University in 2019 and his master degree in mechanical engineering from Shenzhen University in 2022. He is currently a research assistant at the College of Mechatronics and Control Engineering, Shenzhen University. His research includes micro/nano-structure by the thermoplastic forming process and functional application of metallic glasses. ORCID iD: 0000-0001-9422-9073



**Luyao Li** received his MA degree from Shenzhen University in 2021. He is currently a Ph.D. candidate at the School of Materials Science and Engineering, Southeast University, China. His research interests include metallic glasses, high-entropy alloys, and advanced manufacturing. ORCID id: 0009-0000-9595-8139



**Yu Zhang** received his MA degree from Shenzhen University in 2022. He is currently a Ph.D. candidate at the School of Materials Science and Engineering, Wuhan University of Technology. His research interests include metallic glass, high-entropy alloys, and ultrasonic vibration assisted manufacturing. ORCID id: 0009-0009-0065-7823



**Xin Li** received his BSc degree in mechanical engineering from East China University of Technology in 2018 and MA degree from Shenzhen University, Shenzhen, China, in 2021. He is currently a Ph.D. candidate at the College of Mechanical, Electrical & Information Engineering, Shandong University in Weihai, China. His research includes metallic glasses and ultrasonic machining of metallic glass and high entropy alloys. ORCID id: 0000-0003-0348-5384



**Fei Sun** received his BSc degree in mechanical engineering from Wuhan Institute of Technology in 2015 and MA degree from Shenzhen University, Shenzhen, China, in 2019. He is currently a Ph.D. candidate at the College of Mechatronics and Control Engineering, Shenzhen University. His research includes metallic glasses and composite materials. ORCID id: 0000-0003-1871-3466



**Jiang Ma** is distinguished professor and director of the Advanced Materials Manufacturing Research Center (AMMRC) in Shenzhen University. He graduated from Southeast University with a bachelor's degree and Institute of Physics, Chinese Academy of Sciences with a doctor's degree. Winner of National Excellent Youth Fund (NSFC), the outstanding young scientist award in China's amorphous and High-entropy alloy field, high-level talents in Shenzhen, outstanding teachers in Shenzhen et al. He has published over 70 SCI papers as the first or corresponding author, such as *Science Advances*, *Nano Energy*, *Materials Horizons*, *Applied Catalyst B-Environmental*, *Acta Materials*, and authorized over 20 invention patents. He served as the Deputy Secretary General of the Amorphous Alloy Materials Application Branch of the China Electrical Industry Association, editorial board member of the academic journal *Materials Futures*, and young editorial board member of *Science China Materials* and *The Innovation*. ORCID iD: 0000-0003-0234-3210.



**Wei Hua Wang** is the director of the Songshan Lake Materials Laboratory in Dongguan, China, and a professor at the Institute of Physics, Chinese Academy of Sciences, Beijing, China since 1999. He earned his Ph.D. in condensed matter physics from the Chinese Academy of Sciences in 1993 and was a Humboldt fellow during 1995-1997. His research focuses on the structure, features, formation, mechanical, and physical properties of amorphous glassy materials. He has presented over 60 invited presentations and plenary talks at international conferences and delivered 50 invited lectures at renowned research centers in China and abroad. He has published 250+ papers in international journals, including *Science*, *Nature*, *PRL*, *Nature Mater.*, *Adv. Mater.*, *PRB*, *APL*, and authored 8 review papers in esteemed journals like *Adv. Mater.*, *Prog Mater Sci.*, and *Mater Sci & Eng R*. Google scholar link: <https://scholar.google.com/citations?hl=zh-CN&user=4ocukVMAAAAJ>